

# **The Characterization of Glycosaminoglycans and Metallic Dianions in the Gas Phase**

Christopher Taylor

A Thesis submitted to the University of York  
for the degree of Doctor of Philosophy

March 2010

## **Acknowledgements**

I would like to acknowledge the invaluable supervision provided by Dr Caroline Dessent during my four years within her research group at the University of York. I would also like to thank Dr William Boxford, Dr Ruth Burke and Dr Michael Nix for many helpful conversations.

---

## Abstract

Singly, doubly and triply deprotonated monosaccharide and disaccharide molecules of the Heparin family of Glycosaminoglycans (GAGs) have been studied in the gas phase to investigate their geometric structures and intrinsic stabilities. Low energy Collision Induced Dissociation (CID) in a quadrupole ion trap was used to investigate the relative stabilities of the systems along with high energy (50-150 keV) Mass Induced Kinetic Energy (MIKE) experiments. The related alkali metal cation complexes were also studied for comparison.

The detailed effects of the cations  $\text{Li}^+$ ,  $\text{Na}^+$  and  $\text{K}^+$  on the stabilities and low energy fragmentation pathways of these highly sulphated isomeric sugars have been determined, allowing suitable ionic fragments to be selected to assist in future analytical studies. High-energy MIKE experiments have provided information rich mass spectra which allow the locations of the biologically crucial sulphate groups to be unambiguously determined and are suggested as an alternative to Electron Detachment Dissociation (EDD).

The conformational space available to the prototypical monosaccharide residue Iduronic Acid has been investigated using a combined molecular mechanics and quantum chemical approach. Merck Molecular Force Field 94' has been utilized to generate candidate structures for higher level B3LYP, PW91PW91, M05-2X and MP2 calculations using the 6-31++G\*\* basis set. This method was used to explore the preferred low energy structures of this highly flexible sulphated sugar around the  ${}^1\text{C}_4$ ,  ${}^4\text{C}_1$ ,  ${}^2\text{S}_0$  and  ${}^1\text{S}_5$  sugar ring conformations and to assess the suitability of the various methods for studying this class of compounds. This work showed that M05-2X method compared very favourably to the MP2 results, and that it provided improved relative energies over B3LYP. Additionally, the results presented demonstrated the need to study the three dimensional space available to sub conformers when assessing the relative energies of ring conformations

---

Finally, the CID technique was also used to investigate the Potential Energy Surface of two multiply charged inorganic anions. The Dichromate dianion  $\text{Cr}_2\text{O}_7^{2-}$  was seen to fragment via electron loss and ionic fragmentation. Density Functional Theory was used to determine that the relative barrier height for electron loss was lower than that for ionic fragmentation. The gas phase stability of the  $\text{Re}_2\text{X}_8^{2-}$  ( $\text{X} = \text{Cl}, \text{Br}$ ) and  $\text{Re}_2\text{X}_n\text{Y}_{8-n}^{2-}$  ( $\text{X} = \text{Cl}, \text{Y}=\text{Br}, n=1-3$ ) metal-metal bond complexes were then studied. The *ab initio* calculations performed for  $\text{Re}_2\text{Cl}_8^{2-}$  and  $\text{Re}_2\text{Br}_8^{2-}$  indicated that  $\text{Re}_2\text{Cl}_8^{2-}$  was intrinsically stable in the gas-phase, while for  $\text{Re}_2\text{Br}_8^{2-}$ , loss of  $\text{Br}^-$  was an exothermic process. However, gas-phase  $\text{Re}_2\text{Br}_8^{2-}$  was rendered metastable due to the presence of the repulsive coulomb barrier on the fragmentation potential energy surface. The intrinsic gas-phase stability displayed by the dirhenium complexes studied indicated that they could be investigated using more quantitative CID measurements to obtain accurate metal-ligand binding energies.

---

# Contents

<b>Chapter 1. Studying Biological Molecules in the Gas Phase:</b>	
<b>Determining the Structures of the Glycosaminoglycans</b>	
1.1 Studying Biological Molecules in the Gas Phase	1
1.2 The Glycosaminoglycans	5
1.2.1 Transferring Glycosaminoglycans into the Gas Phase	5
1.2.2 Nomenclature of Fragments and Diversity of structures	7
1.2.3 The Biological Roles of Heparin and Related Glycosaminoglycans	9
1.3 Elucidating the Structures of Glycosaminoglycans in the Gas Phase	10
1.3.1 Mass Spectrometry	10
1.3.2 Energy Resolved Mass Spectrometry	14
1.3.3 Ion Mobility Mass Spectrometry	16
1.3.4 Ab Initio Techniques	17
1.3.5 Molecular Dynamics	19
1.4 Properties of Gas-Phase Multiply Charged Anions	20
1.5 Summary and Thesis Aims	22
References	24
<b>Chapter 2. Experimental Methods</b>	
2.1 Electrospray Ionization Mass Spectrometry in Quadrupole Ion Traps	30
2.1.1 The Nature of ESI	30
2.1.2 Theory and Operation of the 3-Dimensional Quadrupole Ion Trap	32
2.1.3 Mass Selective Axial Instability	34
2.1.4 Resonance ejection	35
2.1.5 Collision Induced Dissociation	36
2.2 Mass Analyzed Ion Kinetic Energy – MIKE	38
2.3. Ab initio and Molecular Mechanics	39
2.3.1 Quantum Mechanical versus Molecular Mechanical Methods	39

---

2.3.2 Force Fields and Carbohydrates	40
2.3.3 Molecular Mechanics – Spartan and Merck Molecular Force Field 94	42
2.3.4 Functional and Basis Set selection	43
References	46

### **Chapter 3. Investigating the role of charge state and counterion complexation in the fragmentation of Heparin disaccharides**

3.1 Introduction	49
3.2 Experimental Methods	53
3.3 Results and Discussion	53
3.3.1 Initial mass spectra of sodium salts	53
3.3.2 MS <sup>2</sup> on Heparin Disaccharide Dianions	56
3.3.3 MS <sup>2</sup> on Heparin Disaccharide Trianions	58
3.3.4 MS <sup>2</sup> on Heparin Disaccharide Dianion Salt Complexes	59
3.4 Further Discussion	65
3.4.1 Low Energy Fragmentation Pathways	65
3.4.2 Analytical Benefits	66
3.4.3 Energy Resolved Mass Spectrometry of Isomeric Heparin Disaccharides	67
3.5 Summary	70
References	71

### **Chapter 4. Structural Characterization of Negatively-Charged Glycosaminoglycans Using High-Energy (50-150 keV) Collisional Activation**

4.1 Introduction	73
4.2 Experimental Methods	75
4.2.1 Mass-analyzed ion kinetic energy (MIKE) spectrometry	75
4.2.2 Low-Energy Collision Induced Dissociation	76
4.3 Results and Discussion	77

---

4.3.1 Monosaccharides	77
4.3.2 Disaccharides	83
4.3.3 Sodiated clusters of the $\text{IH}^{2-}$ and $\text{IS}^{3-}$ disaccharides	89
4.4 Further Discussion	93
4.5 Summary	96
References	97

**Chapter 5. Computational Studies of the Gas-Phase Conformers of the Anionic Iduronate (2-O-sulfo- $\alpha$ -L-iduronate) Monosaccharide: Variation of sub-conformer versus ring conformer for a prototypical anionic sugar**

5.1 Introduction	100
5.2 Computational Methods	102
5.3 Results and Discussion	104
5.3.1 Sub-Conformer Structures	104
5.3.2 Energies	113
5.4 Calculated Infra-red Vibrational Frequencies	116
5.5 Further Discussion	122
5.6 Summary	123
References	125

**Chapter 6. On the Intrinsic Stability of the Isolated Dichromate Dianion: Collision Activated Dissociation of a Multiply Charged Anion via Electron Detachment**

6.1 Introduction	127
6.2 Experimental Methods	129
6.3 Computational Methods	130
6.4 Results and Discussion	131
6.4.1 Resonance Excitation of the $\text{Cr}_2\text{O}_7^{2-}$ Dianion	131
6.4.2 Stability of $\text{Cr}_2\text{O}_7^{2-}$ with Respect to Electron Detachment and Ionic Fragmentation	135

---

6.5 Further Discussion	138
6.6 Summary	140
References	141
<b>Chapter 7. Probing the Gas-Phase Stability of the <math>\text{Re}_2\text{X}_8^{2-}</math> (X = Cl, Br) and <math>\text{Re}_2\text{X}_n\text{Y}_{8-n}^{2-}</math> (X = Cl, Y=Br, <math>n=1-3</math>) Metal-Metal Bond Complexes</b>	
7.1 Introduction	143
7.2 Experimental Methods	144
7.3 Results and Discussion	145
7.3.1 Resonance excitation of the $\text{Re}_2\text{X}_8^{2-}$ (X = Cl, Br) and $\text{Re}_2\text{X}_n\text{Y}_{8-n}^{2-}$ (X = Cl, Y=Br, $n=1-3$ ) complexes	145
7.3.2 Cryospray Ion Source	149
7.3.3 Discussion of Ab initio calculations	150
7.4 Further Discussion	152
7.5 Summary	153
References	154
<b>Chapter 8: Summary and Future Work</b>	
8.1 Summary and further experiments	156
References	159
<b>Appendix 1: Glossary</b>	160

---

## List of Figures

- Figure 1.1:** Selection of known disaccharide members for the Glycosaminoglycan family displaying sites of sulphation and N-acetylation. 8
- Figure 1.2:** Short GAG disaccharide structural code proposed by Lawrence et al used to fully describe any member of the Glycosaminoglycan family 8
- Figure 1.3:** Fragment labelling scheme used in this work for a) monosaccharide and b) disaccharides. The A, B and C labels are used to indicate a fragment containing a non-reducing end of the GAG, while X, Y and Z denote fragments which include the reducing end of the sugar. (The reducing end is defined as the ring with a C1 carbon not involved in a glycosidic bond.) 11
- Figure 2.1:** Schematic diagram of a commercial quadrupole ion trap mass spectrometer, based on the layout of a Finnegan LCQ machine. Background pressures are displayed from atmospheric through to the Quadrupole Ion Trap. 32
- Figure 2.2:** Diagram of a Quadrupole Ion Trap showing a cut through the ring electrode illustrating the un-scaled dimensions  $z_0$  and  $r_0$ . 33

- 
- Figure 2.3:** Graph showing solutions of the Mathieu  $a_z$  and  $q_z$  parameters. Ions for which these solutions lie within the cross hatched line have stable trajectories within the trap. 34
- Figure 2.4:** An  $MS^2$  experiment carried out in a quadrupole ion trap demonstrating (a) the isolation of  $Cr_2O_7^-$  and (b) and (c) its resonant excitation to produce  $Cr_2O_6^-$  37
- Figure 2.5:** Diagram of the Sep 1 high energy magnetic sector instrument. 38
- Figure 3.1:** The chemical structure of the three Heparin derived glycosaminoglycans disaccharides studied in chapter 3. a) IH,  $\alpha$ - $\Delta$ UA-2S-[1 $\rightarrow$ 4]-GlcN-6S, b) IIS,  $\alpha$ - $\Delta$ UA-[1 $\rightarrow$ 4]-GlcNS-6S and c) IIIS  $\alpha$ - $\Delta$ UA-2S-[1 $\rightarrow$ 4]-GlcNS 52
- Figure 3.2:** Fragment labelling scheme used in this work for a) monosaccharide and b) disaccharides. The A, B and C labels are used to indicate a fragment containing a non-reducing end of the GAG, while X, Y and Z denote fragments which include the reducing end of the sugar. (The reducing end is defined as the ring with a C1 carbon not involved in a glycosidic bond.) 54

- 
- Figure 3.3:** MS<sup>1</sup> mass spectra of a) IH, b) IIS and c) IIS sprayed from sodium salts in Methanol yielding a mixture of negative charge states and counterion complexes. 55
- Figure 3.4:** MS<sup>2</sup> mass spectra of a) IH, b) IIS and c) IIS dianions at 8% CID energy. 57
- Figure 3.5:** MS<sup>2</sup> mass spectra of a) IH, b) IIS and c) IIS trianions at 6.4% CID energy. 59
- Figure 3.6:** MS<sup>1</sup> spectrum of IH disaccharide electrosprayed at 10<sup>-4</sup> M in methanol as a sodium salt in the presence of lithium chloride. 60
- Figure 3.7:** MS<sup>2</sup> mass spectra of [IH-2H.X<sup>+</sup>]<sup>-</sup> at 8.8 % CID energy, where X= a) Lithium, b) Sodium and c) Potassium. 61
- Figure 3.8:** MS<sup>2</sup> mass spectra of [IIS-2H.X<sup>+</sup>]<sup>-</sup> at 8.8 % CID energy, where X= a) Sodium and b) Potassium. 62
- Figure 3.9:** MS<sup>2</sup> mass spectra of [IIS-2H.X<sup>+</sup>]<sup>-</sup> at 8.8 % CID energy, where X= a) Lithium, b) Sodium and c) Potassium. 64
- Figure 3.10:** CID Fragmentation curves for the production of the <sup>0,2</sup>A<sub>2</sub><sup>-</sup> ion from the IH, IIS and IIS precursor dianions. 69
- Figure 4.1:** The chemical structures of the six sulphated sugars studied in this chapter. a) The A monosaccharide, GlcNS, b) the B monosaccharide, GlcNS-6S, c) the

---

C monosaccharide, GlcNS-3S, d) the IVA disaccharide,  $\alpha$ - $\Delta$ UA-[1 $\rightarrow$ 4]-GlcNAc, e) the IH trianionic disaccharide,  $\alpha$ - $\Delta$ UA-2S-[1 $\rightarrow$ 4]-GlcN-6S, and f) the IS disaccharide,  $\alpha$ - $\Delta$ UA-2S-[1 $\rightarrow$ 4]-GlcNS-6S. (The sugar names have been abbreviated as follows;  $\Delta$ UA = 4-deoxy-L-threo-hex-4-enopyranosyluronic acid; GlcN = D-glucosamine; Ac = Acetyl; NS, 2S, 3S and 6S, = N-sulfo, 2-sulfate, 3-sulfate and 6-sulfate respectively.) 74

**Figure 4.2:** Fragment labelling scheme used in this work for a) monosaccharide and b) disaccharides. The A, B and C labels are used to indicate a fragment containing a non-reducing end of the GAG, while X, Y and Z denote fragments which include the reducing end of the sugar. (The reducing end is defined as the ring with a C<sub>1</sub> carbon not involved in a glycosidic bond.) 77

**Figure 4.3:** (a) Low-energy CID mass spectrum of the A<sup>-</sup> (i.e. [A-H]<sup>-</sup>) monoanionic monosaccharide at 11.5% collision energy. (b) Negative-ion MIKE spectrum (50 keV) following high-energy collision of A<sup>-</sup> with Neon. 78

**Figure 4.4:** (a) Low-energy CID mass spectrum of the B<sup>2-</sup> (i.e. [B - 2H]<sup>2-</sup>) dianionic monosaccharide at 5% collision energy. (b) Negative-ion MIKE spectrum (100 keV) following high-energy collision of B<sup>2-</sup> with Neon. 80

- 
- Figure 4.5:** (a) Low-energy CID mass spectrum of the  $C^{2-}$  (*i.e.*  $[C - 2H]^{2-}$ ) dianionic monosaccharide at 6% collision energy. (b) Negative-ion MIKE spectrum (100 keV) following high-energy collision of  $C^{2-}$  with Neon. 81
- Figure 4.6:** (a) Low-energy CID mass spectrum of the  $IVA^-$  (*i.e.*  $[IVA - H]^-$ ) monoanionic disaccharide at 10.5% collision energy. (b) Negative-ion MIKE spectrum (50 keV) following high-energy collision of  $IVA^-$  with Neon. 84
- Figure 4.7:** (a) Low-energy CID mass spectrum of the  $IH^{2-}$  (*i.e.*  $[IH - 2H]^{2-}$ ) dianionic monosaccharide at 7.9% collision energy. (b) Negative-ion MIKE spectrum (100 keV) following high-energy collision of  $IH^{2-}$  with Neon. 86
- Figure 4.8:** (a) Low-energy CID mass spectrum of the  $IS^{3-}$  (*i.e.*  $[IS - 3H]^{3-}$ ) trianionic monosaccharide at 6.5% collision energy. (b) Negative-ion MIKE spectrum (150 keV) following high-energy collision of  $IS^{3-}$  with Neon. 87
- Figure 4.9:** (a) Low-energy CID mass spectrum of the  $Na^+ \cdot IH^{2-}$  sodiated cluster at 21.4% collision energy. (b) Negative-ion MIKE spectrum (50 keV) following high-energy collision of  $Na^+ \cdot IH^{2-}$  with Neon. 90
- Figure 4.10:** (a) Low-energy CID mass spectrum of the  $Na^+ \cdot IS^{3-}$  sodiated cluster at 10.7% collision energy. (b) Negative-ion MIKE spectrum (100 keV) following

---

high-energy collision of $\text{Na}^+\cdot\text{IS}^{3-}$ collision with Neon.	92
<b>Figure 5.1:</b> Doubly deprotonated Iduronic Acid (Methyl 2-O-sulfo- $\alpha$ -L-iduronate).	101
<b>Figure 5.2:</b> Sugar ring conformers for doubly deprotonated methyl 2-O-sulfo- $\alpha$ -L-iduronate illustrating the a) ${}^4\text{C}_1$ , b) ${}^2\text{S}_0$ , c) ${}^1\text{S}_5$ and d) ${}^1\text{C}_4$ conformations.	103
<b>Figure 5.3:</b> Optimized conformers (MP2/6-31++G**) of doubly deprotonated methyl 2-O-sulfo- $\alpha$ -L-iduronate grouped according to sugar ring conformation and displayed with increasing energy (within conformers) from left to right.	105
<b>Figure 5.4:</b> Energy distribution plots (a-c) MMFF94, B3LYP/6-31++G** and MP2/6-31++G**, for the doubly deprotonated iduronate conformers displayed in Fig. 5.3. The MMFF94 energies were obtained from the conformer search utility in Spartan, whereas the B3LYP and MP2 energies are for the fully optimized structures at the respective levels. Conformer names are given in accordance with the MP2 geometries (as in Fig. 5.3), but where conformers differ upon optimization at the B3LYP and MMFF94 levels, the new conformer-type is labelled in parentheses adjacent to the relevant energy point.	113

- 
- Figure 5.5:** Energy distribution plots (a-c) MP2/6-31++G\*\*, PW91PW91/6-31++G\*\* and MO5-2X/6-31++G\*\* for the doubly deprotonated iduronate conformers displayed in Fig. 5.3. The MP2, PW91PW91 and MO5-2X energies are for the fully optimized structures at the respective levels. Conformer names are given in accordance with the MP2 geometries (as in Fig. 5.3). 115
- Figure 5.6:** Calculated IR Spectra at the MP2/6-31++G\*\* level for conformers a)  ${}^4C_1$  I, b)  ${}^4C_1$  II and c)  ${}^4C_1$  III 117
- Figure 5.7:** Calculated IR Spectra at the MP2/6-31++G\*\* level for conformers a)  ${}^4C_1$  IV, b)  ${}^4C_1$  V, c)  ${}^4C_1$  VI and d)  ${}^4C_1$  VII 118
- Figure 5.8:** Calculated IR Spectra at the MP2/6-31++G\*\* level for conformers a)  ${}^2S_0$  I, b)  ${}^2S_0$  II and c)  ${}^2S_0$  III 119
- Figure 5.9:** Calculated IR Spectra at the MP2/6-31++G\*\* level for conformers a)  ${}^1S_5$  I, b)  ${}^1S_5$  II and c)  ${}^1S_5$  III 120
- Figure 5.10:** Calculated IR Spectra at the MP2/6-31++G\*\* level for conformers a)  ${}^1C_4$  I, b)  ${}^1C_4$  II, c)  ${}^1C_4$  III and d)  ${}^1C_4$  IV 121
- Figure 6.1:** Schematic potential energy curves for decay of an  $AB_2^{2-}$  dianion via (a) electron detachment, and (b) ionic fragmentation into  $AB^- + B^-$ . The RCBs (inner) and (outer) for electron detachment ( $RCB_{ed}$ ) and ionic fragmentation ( $RCB_{if}$ ) are illustrated 128

---

**Figure 6.2:** (a) Negative ion ESI-MS of the sodium salt of  $\text{Cr}_2\text{O}_7^{2-}$  obtained by tuning on  $m/z$  108 (*i.e.* optimising the ion optics to maximise the  $m/z$  108 signal). (b) Isolation of  $\text{Cr}_2\text{O}_7^{2-}$  in the quadrupole trap at 0% collision energy. (c) CID mass spectrum of  $\text{Cr}_2\text{O}_7^{2-}$  at 9% collision energy illustrating fragmentation of  $\text{Cr}_2\text{O}_7^{2-}$  primarily into  $\text{Cr}_2\text{O}_7^-$ . ( $\text{CrO}_4^-$  and  $\text{CrO}_3^-$  are also evident as product fragments; see text for a discussion.) 131

**Figure 6.3:** % Fragmentation curves for decay of the  $\text{Cr}_2\text{O}_7^{2-}$  parent dianion, with production of the  $\text{CrO}_4^-$  and  $\text{Cr}_2\text{O}_7^-$  fragment ions. Typical experimental errors (obtained from repeat runs) were  $\pm 3\%$ . 133

**Figure 6.4:** (a) Isolation of  $\text{Cr}_2\text{O}_7^-$  anion in the quadrupole trap at 0% collision energy. (b) CID mass spectrum of  $\text{Cr}_2\text{O}_7^-$  at 15% collision energy illustrating fragmentation of  $\text{Cr}_2\text{O}_7^-$  into  $\text{Cr}_2\text{O}_6^-$ . (c) % Fragmentation curves for decay of the  $\text{Cr}_2\text{O}_7^-$  parent monoanion, with production of the  $\text{Cr}_2\text{O}_6^-$  fragment ion. 134

**Figure 6.5:** The optimized  $C_{2v}$  symmetry structure of  $\text{Cr}_2\text{O}_7^{2-}$  obtained at the B3LYP/LANL2DZ level, with bond lengths and NPA atomic charges. 136

**Figure 6.6:** (a) Calculated potential energy curve calculated using B3LYP/LANL2DZ for the ionic fragmentation of  $\text{Cr}_2\text{O}_7^{2-} \rightarrow \text{CrO}_3^- + \text{CrO}_4^-$ , obtained as a function of the oxygen-chromium bond distance. (b) One-dimensional cut through  $\text{RCB}_{\text{ed}}$  of  $\text{Cr}_2\text{O}_7^{2-}$  calculated

---

using the point charge model at the B3LYP/LANL2DZ level. The direction of electron detachment is indicated. 137

**Figure 7.1:** (a) Isolation of  $\text{Re}_2\text{Cl}_8^{2-}$  in the quadrupole trap at 0% CID voltage. (b) CID mass spectrum of  $\text{Re}_2\text{Cl}_8^{2-}$  at 6.8% collision energy illustrating fragmentation of  $\text{Re}_2\text{Cl}_8^{2-}$  into  $\text{Re}_2\text{Cl}_7^-$ . 145

**Figure 7.2:** (a) Isolation of  $\text{Re}_2\text{Br}_8^{2-}$  in the quadrupole trap at 0% CID voltage. (b) CID mass spectrum of  $\text{Re}_2\text{Br}_8^{2-}$  at 3.2% collision energy illustrating fragmentation of  $\text{Re}_2\text{Br}_8^{2-}$  into  $\text{Re}_2\text{Br}_7^-$ . 146

**Figure 7.3:** (a) Fragmentation curves for decay of the  $\text{Re}_2\text{Br}_8^{2-}$  and  $\text{Re}_2\text{Cl}_8^{2-}$  with production of  $\text{Re}_2\text{Br}_7^-$  and  $\text{Re}_2\text{Cl}_7^-$ , respectively. (b) Fragmentation curves for decay of the  $\text{Re}_2\text{Br}_8^{2-}$  and  $\text{Re}_2\text{Cl}_n\text{Br}_{8-n}^{2-}$  ( $n=1-3$ ) ions with production of  $\text{Re}_2\text{Br}_7^-$  and  $\text{Re}_2\text{Cl}_n\text{Br}_{7-n}^-$  ( $n=1-3$ ), respectively (associated with loss of the  $\text{Br}^-$  fragment ion). Typical experimental errors (obtained from repeat runs) were  $\pm 3\%$ . 148

**Figure 7.4:** CID Fragmentation curves for decay of  $\text{Re}_2\text{Br}_8^{2-}$  with production of  $\text{Re}_2\text{Br}_7^-$ , produced both with and without cryospray. 149

**Figure 7.5:** Calculated potential energy curves at the (CASSCF(8,8)/LANL2DZ) level for the ionic fragmentation of  $\text{Re}_2\text{X}_8^{2-} \rightarrow \text{Re}_2\text{X}_7^- + \text{X}^-$  ( $\text{X}=\text{Cl}, \text{Br}$ ), obtained with geometries relaxed at each Re-X bond distance. The barrier heights for ionic fragmentation

of each complex are illustrated on the figure, along with the calculated  $D_{4h}$  global minimum energy structure for  $Re_2X_8^{2-}$ , and the Cs symmetry transition state structure and  $C_{2v}$  symmetry  $Re_2X_7^-$  final product.

---

## List of Tables

<b>Table 3.1:</b>	Product Ions resulting from collisional excitation of heparin disaccharides. Dianions were fragmented using 8% CID energy, trianions at 6.4%.	58
<b>Table 3.2:</b>	Product Ions from heparin dianion-counter ion complexes at 8.8% CID energy.	63
<b>Table 4.1:</b>	Fragment ions present in the low- and high-energy fragmentation spectra for the $A^-$ , $B^{2-}$ and $C^{2-}$ monosaccharide anions. $m/z$ values and fragment intensities (relative to the strongest fragment ion) are given in parentheses. Prominent, unassigned peaks are also included in the table, listed by their observed $m/z$ values.	83
<b>Table 4.2:</b>	Fragment ions present in the low- and high-energy fragmentation spectra of the $IVA^-$ , $IH^{2-}$ and $IS^{3-}$ disaccharide anions, and the $Na^+ \cdot IH^{2-}$ and $Na^+ \cdot IS^{3-}$ sodiated complexes. $m/z$ values and fragment intensities (relative to the strongest fragment ion) are given in parentheses. Prominent unassigned peaks are also included in the table, listed by their observed $m/z$ values	88
<b>Table 5.1:</b>	Key non-covalent interactions present in the MP2/6-31++G** level sub-conformers of $IA^{2-}$	107
<b>Table 5.2:</b>	Bond lengths (in Å) for the optimized sub-conformers of $IA^{2-}$ .	108

---

<b>Table 5.3:</b>	Selected bond angles (MP2/6-31++G**) of the sub-conformers of the ${}^4C_1$ , ${}^2S_0$ , ${}^1S_5$ , and ${}^1C_4$ ring-conformers of $IA^{2-}$ .	110
<b>Table 5.4:</b>	Selected bond angles (in degrees) for the lowest energy sub-conformers of the ${}^4C_1$ , ${}^2S_0$ , ${}^1S_5$ , and ${}^1C_4$ ring-conformers of $IA^{2-}$ .	110
<b>Table 5.5:</b>	Selected torsional angles (in degrees) for the lowest-energy sub-conformers of the ${}^4C_1$ , ${}^2S_0$ , ${}^1S_5$ , and ${}^1C_4$ ring-conformers of $IA^{2-}$ .	111
<b>Table 5.6:</b>	Table 5.6: Atomic partial charges from a Mulliken population analysis (MP2/6-31++G**) of the lowest energy ${}^4C_1$ , ${}^2S_0$ , ${}^1S_5$ , and ${}^1C_4$ sub-conformers of $IA^{2-}$ .	112
<b>Table 7.1:</b>	Ab initio calculated parameters for the calculated global minimum energy structures and ionic fragmentation potential energy surfaces of the $Re_2X_8^{2-}$ ( $X=Cl^-, Br^-$ ) dianions.	150

## **Publications arising from this Thesis**

The contents of Chapter 4 are published, ‘C. J. Taylor, R.M. Burke, B.H. Wu, S. Panja, S.B. Nielsen, C.E.H. Dessent, *Int. J. Mass Spec.* 285 (2009) 70’ The high energy mass spectrometry work reported was performed at the Department of Physics and Astronomy, University of Aarhus, part of the distributed LEIF infrastructure

The contents of Chapter 6 are published, ‘C.J. Taylor, B. Wu, C.E.H. Dessent, *Int. J. Mass Spec.* 276 (2008) 31’.

The contents of Chapter 7 are published ‘C.J. Taylor, B. Wu, M.G.D. Nix, C.E.H Dessent, *Chem. Phys. Lett.* 479 (2009) 184. Ab initio calculations supporting this work were carried out by Dr M.G.D. Nix.

## **Author's Declaration**

I certify that the work presented in this thesis was conducted by myself at the University of York, United Kingdom of Great Britain and Northern Ireland. Computational calculations to support the work reported in Chapter 7 were carried out by Dr Michael Nix, as detailed within the text.

Signed..... Date.....

# Chapter 1: Introduction

## Studying Biological Molecules in the Gas Phase: Determining the Structures of the Glycosaminoglycans

### 1.1 Studying Biological Molecules in the Gas Phase

Biologically active macromolecules typically exist in an environment far removed from the gas phase. They may form part of lipid bi-layers, aggregate to make up complex assemblies and are surrounded by water molecules, salts and chaperone proteins.<sup>1,2,3</sup> There is little doubt that a vast array of complex interactions effect many aspects of their functions. An important and controversial question therefore immediately arises; what is the biological relevance in studying any of this huge range of species outside of their normal environment? The roles that biological molecules fulfil in nature are highly dependent on their conformational flexibility and on the numerous possible interactions that they may engage in with other structures.<sup>4</sup> For this reason it is of great significance to determine whether the conformations that are available to these structures in solution are adhered to in the gas phase.

Electrospray Ionisation is the primary technique used in contemporary science to transfer biological molecules from solution to the gas phase. Tian and Kass have found that during the electrospraying of a tyrosine based anion, a mixture of phenoxide and carboxylate ions are formed,<sup>5</sup> where due to their relative acidities, the carboxylate ion is far more dominant in solution. This experiment demonstrates that for a relatively simple system, the phase change is a significant event. A larger example is that of the DNA duplex, and Collision Induced Dissociation studies have suggested they are capable of being transferred intact from solution to the gas phase.<sup>6,7</sup> Gidden et al have studied DNA duplexes using a combination of ESI, Ion Mobility Mass Spectrometry and Molecular Dynamics. They found that while smaller 4-mer and 6-mer examples of cytosine/guanine sections produced cross sections in line with calculated globular structures, the larger 14- and 18-mer

examples seemed to remain stable in the gas phase on a millisecond time scale.<sup>8</sup> More complex DNA based structures such as hairpins and pseudoknots have been observed via a similar method, although their stability seems to depend upon their overall charge state remaining low.<sup>9</sup>

The simulation program MELTING has been used to predict the stability of DNA helices in solution and has identified strands which have then been shown by experiment to have highly similar heating requirements for dissociation.<sup>10,11</sup> In this case strands with comparable solution stability that differed only in GC content were found to require markedly different amounts of energy upon collision induced dissociation, suggesting that their structural features have altered on transferral to the gaseous environment.

The fact that DNA based structures rely on non-covalent interactions for their stability makes their structurally unchanged transfer from solution to gas phase surprising. In peptides, Helices and  $\beta$ -sheets have also been proven to retain their secondary and tertiary structures from solution to the gas-phase through a combination of molecular dynamics and collisional cross section measurements.<sup>12</sup> Extended  $\beta$ -sheets are generally stable gas-phase structures as neutrals, while helices appear to require charged sites in order to retain their form. The exact changes that have occurred to the structures of these molecules following the ESI process are unknown in most cases since equivalent experiments to monitor their shapes in solution are not carried out. However from these studies, it does appear that some large biological molecules can maintain solution-phase structures upon transferral to the gas-phase environment.

Barran et al have highlighted the fact that the dielectric constant in a vacuum,  $\epsilon_{\text{vacuum}} = 1$  is far more similar to that of a membrane receptor type environment  $\epsilon_{\text{peptide/protein}} = 2-4$ ,<sup>13</sup> than that of water  $\epsilon_{\text{water}} = 80$ ,<sup>14</sup> (and the fact that gas phase experiments allow researchers to exercise a far greater degree of control over the energy imparted to the system under study.) They demonstrate the high sensitivity of

gas phase ion mobility studies and molecular modelling in observing structural changes caused by single amino acid alterations.

The interior of certain macromolecules can also provide an environment that has similarities to a gas-phase environment. Evidence supporting a hydrophobic nature in the interior of proteins has been gained from green fluorescent protein (GFP) chromophore absorption data.<sup>15</sup> In this case the predicted unperturbed vacuum absorption peak for the chromophore studied was expected at 399 nm, while that of the chromophore attached to the protein is 397 nm. At the time of writing further high level calculations are being carried out in order to further clarify the precise wavelength some of these relatively large species absorb at.<sup>16</sup>

Perhaps the principal benefit of isolated gas-phase studies on biological molecules is the ability to add water molecules, ions or other ligands to the biological system of interest to observe the intrinsic effect of complexation on the system. Where the difference between the solution and gas phase properties of a system are being considered it is highly instructive to study the effects of adding low numbers of water molecules. The majority of such studies have been conducted using laser spectroscopy combined with suitable computational methods (often using Density Functional Theory).<sup>17,18</sup> Using this approach, Simons et al have made detailed studies of neutral gas phase carbohydrates produced via supersonic jet expansion.<sup>19</sup> For the singly- hydrated structures of  $\alpha$ - and  $\beta$ -anomers of phenyl (or methyl) glucoside, galactoside and mannoside they have detected that the water molecules are typically bound around the hydroxymethyl group, and that multiply hydrated structures tend to form distinct hydrophobic and hydrophilic faces. This led them to suggest that the hydrophobic sections form water free pockets when stacked against aromatic sections in protein binding, lending further weight to the concept that the gas-phase can act like a protein interior.<sup>20</sup> Neutral Trimannoside sugar compounds have been studied in isolation and in the presence of a single water cluster using IR depletion spectroscopy and Density Functional theory<sup>21</sup>. The isolated sugar structure is held in a 'closed' conformation by a network of strong intramolecular hydrogen bonds. The addition of a single water molecule allows for the formation of a more

complex network of hydrogen bonding interactions which have a dramatic effect on the overall structure of the molecule, causing it to adopt a more compact shape. The effect of adding a water molecule to sugars containing plentiful OH groups is not always the formation of such intricate hydrogen bonding networks. Phenyl-tagged cellobiose contains numerous OH groups and yet when a single water is added the IR spectroscopic results suggest that it remains associated towards the outside of the sugar and does not appear to have a significant impact on its' structure.<sup>22</sup> A similar effect is observed in the study of  $\beta$ -D-glucopyranoside, with the two additional water molecules added associated with the outer regions of the molecular structure. It should be noted that in this case the opportunity to form hydrogen binding networks is limited due the lack of a second OH containing sugar ring.<sup>23</sup>

Work involving the hydrated amino acid Valine used Infrared Laser Spectroscopy in tandem with a B3LYP/6-31++G\*\* computational study has previously been used to examine the early water shell structures formed around a model peptide.<sup>24</sup> For a protonated Valine molecule, a distinct network of three water molecules builds up surrounding the  $\text{NH}_3^+$  group. Where the  $\text{NH}_2$  lithiated version of the molecule is studied, this small group of waters is present clustered around the  $\text{Li}^+$  - carboxylate complex. Photo-dissociation spectroscopy has been used to demonstrate that a single water molecule may stabilize the zwitterionic form of Arginine where previously the un-solvated lithiated version was non-zwitterionic.<sup>25</sup>

So far the examples given are of relatively small molecules on a biological scale. In order to study biologically relevant molecules in the gas phase, techniques must be available that allow for their effective characterisation. Rizzo et al have demonstrated well resolved IR spectra of peptides of approximately 7-8 amino acids in length and noted that in terms of the observing secondary protein structure, 10-12 amino acid subunits are likely to be needed.<sup>26</sup> For gas-phase studies of larger examples, both computational resources and the potentially large numbers of conformers are likely to provide a challenge to definitive assignments.

At present, no Laser Spectroscopic data exists for the negatively charged Glycosaminoglycan (GAG) families of sugars described below. This is a major

limiting factor where attempts are made to understand their detailed gas phase structures, especially for the development of force fields and quantum chemical methods. The lack of three dimensional gas phase data on GAG structures makes comparisons with X-ray crystal structure and NMR data a fruitless exercise at this time. A large volume of structural information that can be inferred by mass spectrometry using the methodologies for studying the primary and higher structures of this diverse family of molecules as described in section 1.3.

## 1.2 The Glycosaminoglycans

### **1.2.1 Transferring Glycosaminoglycans into the Gas Phase**

*Matrix assisted laser desorption/ionisation* (MALDI) is a soft ionization technique widely used in the study of peptides and proteins,<sup>27</sup> glycoproteins,<sup>28,29</sup> oligonucleotides,<sup>30,31</sup> that has found widespread use within the pharmaceutical industry for product ionization prior to mass spectrometric analysis, often via its coupling to time of flight based instruments.<sup>32</sup> MALDI is an exceptionally sensitive technique, with only femtomoles of sample necessary in certain circumstances to produce detailed mass spectra.<sup>33</sup>

MALDI sources typically use nitrogen or Nd:YAG lasers, with intensities of approximately  $10^6$  to  $10^7$  W cm<sup>-2</sup> being common. Samples are stored within a Matrix, traditional examples including 2,5-dihydroxybenzoic acid for peptides and nucleotides,<sup>34</sup> and 4-hydroxy-3-methoxycinnamic acid for proteins.<sup>35</sup> Sulphated sugars such as Heparin are not trivial targets to analyse via MALDI, primarily because the technique has a tendency to favour the generation of singly charged ions and neutral sulphate groups are easily lost from these species in the gas phase as discussed in section 1.3.<sup>36</sup> Progress using this method is likely to be reliant on improvements to the matrices used, combining peptides with sulphated sugars has be

shown to increase signal strength.<sup>37</sup> Additionally the use of Caesium salts has been proven to be an effective way to prevent sulphate loss where MALDI is used.<sup>38</sup> Recently work with 2-(4-hydroxyphenylazo) benzoic acid (HABA) based ionic liquid matrices has proven capable of transferring densely N- and O-sulphated octa-saccharides into the gas phase without loss of these fragile side groups.<sup>39</sup>

A second technique that is used for producing gas-phase biological molecules is ***Fast Atom Bombardment*** (FAB). This technique involves the exposure of a sample matrix to a beam of high energy atoms of an inert gas such as argon or xenon at energies of around 4-10 KeV in order to generate charged molecular fragments. FAB has fallen out of use for the analysis of GAG type molecules due to its increased sample consumption compared with either ESI or MALDI, in addition to problems with sodium counter ion contamination and excessive losses of sulphate groups.<sup>40</sup> Early mass spectrometry studies utilising FAB produced spectra that would be considered congested by modern standards.<sup>41</sup> (Although the transfer of relatively large sulphated tetrasaccharides into the gas phase was effectively accomplished in these studies).<sup>42</sup> Octa-saccharide size examples were later observed although baselines for these mass spectral studies were likewise very highly congested with peaks, most likely due to fragments of the prepared samples being complexed to the matrix materials during the ionization process.<sup>43</sup>

***Electrospray Ionisation*** (ESI) is currently the most widely used ionisation technique for transferring biological ions from solution into the gas-phase. This technique has been the method of choice for the transfer of GAG molecules, and specifically Heparin, into the gas phase. ESI has proven capable of generating large multiply charged heparin fragments, and with tailoring of source conditions, variable numbers of sodium counter ions and charge states.<sup>44</sup> The method is also capable of delivering intact the more densely sulphated Heparin examples, such as the biologically active ‘Arixtra’ Heparin pentasaccharide sequence.<sup>45</sup> The mechanism of the ESI process is described in Chapter 2, and the range of mass spectrometry, energy resolved mass

spectrometry and ion mobility mass spectrometry studies described in section 1.3 all utilize an ESI source.

### 1.2.2 Nomenclature of Fragments and Diversity of structures

The Glycosaminoglycans (GAGs) are a linear structurally diverse family of sugars found on the surfaces of most mammalian cells with molecular weights commonly found to vary between 10-100kDa.<sup>46</sup> The GAG family represent the major known group of anionic saccharides and may be principally divided into two main sub-groups, based on whether or not they display sulphation. Chondroitin and Hyaluronan are examples of GAGs that lack sulphates. The sulphated members of the GAG family include Dermatan Sulphate, Keratan Sulphate, Heparin and Heparan Sulphate. Figure 1.1 displays several disaccharides from the GAG family. GAG chains consist of disaccharide repeating units made up out of an Uronic Acid coupled to an Amino sugar.

The Uronic acid may be either D-glucuronic or L-Iduronic Acid, while the Amino sugar is D-Galactosamine or D-Glucosamine. It should be noted that Keratan Sulphate possesses a Galactose sugar in place of an Uronic acid. The amino sugar is commonly found to be sulphated at the fourth and sixth carbon, while the nitrogen side group may also be sulphated or acetylated. Similarly, the initial Uronic acid monosaccharide may be sulphated at the second, third or sixth carbon and may also possess a negatively charged carboxylate group. The glycosidic bonds linking these monosaccharide subunits also provides for further structural variation with  $\alpha$ - and  $\beta$ -linkages possible between the (1 $\rightarrow$ 4) and (1 $\rightarrow$ 3) positions.

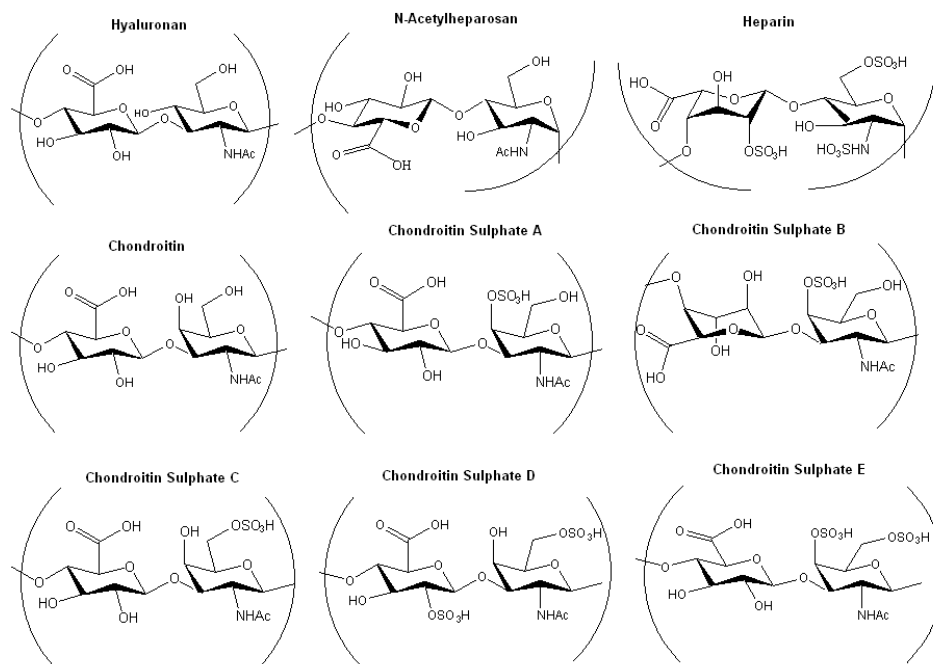


**Fig 1.1 Selection of disaccharide members of the Glycosaminoglycan family displaying sites of sulphation and N-acetylation.**

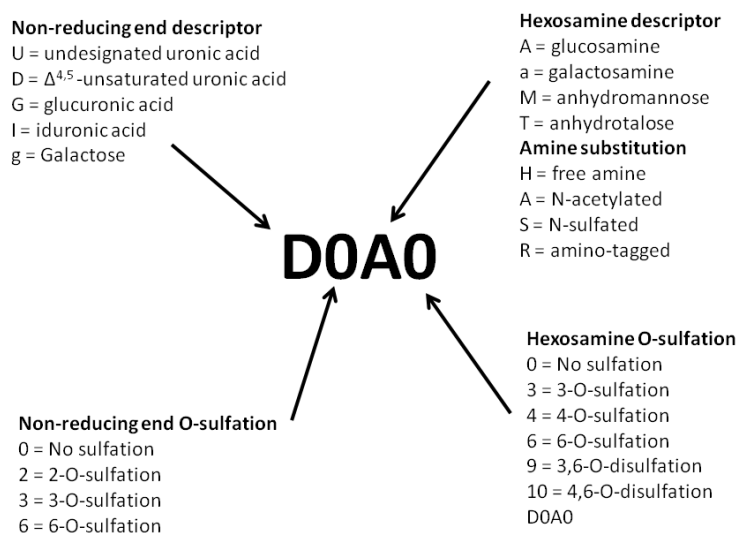


**Fig 1.2 Short disaccharide structure code proposed by Lawrence et al<sup>45</sup> used to fully describe any member of the Glycosaminoglycan family**

A common system of naming used specifically for Heparin is that of roman numerals to represent the 12 most commonly encountered disaccharides.<sup>47</sup> While this system is suitable short hand for this highly studied subset, a newer ‘disaccharide structure code’ has recently been proposed.<sup>48</sup> This elegant system has the advantage of being applicable without ambiguity to the entire GAG family, as well as being highly compact, representing each disaccharide sugar as a four character code, as shown in figure 1.2.

The Heparin fragmentation scheme used in this thesis is that of Domon and Costello and is explained fully in Chapter 3.<sup>49</sup>

### 1.2.3 The Biological Roles of Heparin and Related Glycosaminoglycans

The volume of published research into the interactions of Glycosaminoglycans with proteins and their involvement in biological functions is considerable, and several in depth reviews have been conducted in recent years.<sup>46,50</sup> The most well studied glycosaminoglycan-protein system is historically that of Heparin with Antithrombin, it was suggested in 1973 that the binding of these molecules was responsible for the conformational changes observed in Antithrombin, causing it to interact far more strongly with Thrombin and deactivating the complex.<sup>51</sup> Further research determined that a key penta-saccharide region in the Heparin chain was responsible for the Heparin - Antithrombin protein interaction,<sup>52</sup> and that this region contained an unusual 3-O-sulphation which was an absolute requirement for successful binding.<sup>53</sup> It is now known that the pattern of sulphate, amino-sulphate and carboxylate groups along this short chain is essential for effective binding to antithrombin with certain substituent groups being critical.<sup>54</sup> Additionally, the fourth monosaccharide in this structure is a highly flexible Iduronic acid, which may adopt several ring conformations in solution including  ${}^2S_0$ ,  ${}^1C_4$  and  ${}^4C_1$ .<sup>55</sup> Successful binding is reliant on the  ${}^2S_0$  conformation being present.<sup>51</sup> This feature is also present in the binding between a heparin tetrasaccharide and the annexin V protein, where interacting Iduronic acid residues are found in the  ${}^2S_0$  conformation while the non-interacting monomer remains as  ${}^1C_4$ . A review of conformations during protein

interactions has led Mancera et al to suggest that the role of the Iduronic acid monomer is to provide crucial flexibility for Heparin chains involved in protein binding.<sup>50</sup> Further discussion on the conformational nature of Iduronic acid is provided in Chapter 5.

In addition to the well known antithrombin interaction, the GAG family of molecules are linked to numerous clinically important processes, and as such are important drug development targets.<sup>56</sup> GAGs are implicated in tumour progression,<sup>57</sup> and are thought to play an important role in proteoglycans as receptors for growth factors such as the fibroblast growth factor (FGF) family.<sup>58</sup> GAGs play important roles in cell signalling,<sup>59</sup> in inflammation,<sup>60</sup> and in cancers.<sup>61</sup>

A marked increase in the presence of Heparin sulphate containing proteoglycans has been observed where the levels of  $\beta$ -amyloid proteins rise in the brain tissues of Alzheimer's sufferers.<sup>62</sup> The enormous range of potential GAG structures and the specificity with which they bind to cytokine proteins has led to the suggestion that they might become effective 'markers' in assays used to detect the presence of malignant tumours in patients.<sup>63</sup> Such a scheme would rely heavily on a detailed understanding of the structure-function relationship of GAGs, which in turn requires effective methods by which to sequence them. While the large range of processes in which GAGs are involved is a complex one, the need to obtain detailed structural information on these molecules is clear if we are to better understand their functions.

### 1.3 Elucidating the Structures of Glycosaminoglycans in the Gas Phase

#### **1.3.1 Mass Spectrometry**

The importance of Glycosaminoglycans (GAGs), particularly Heparin, in biological systems makes them an ideal target for primary structure determination by mass spectrometry. Knowledge of the GAG sequence is critical either where a new sample from a biological source is isolated or where a pharmaceutical product must be analysed for purity. The first problem to be overcome when analysing a GAG

from a biological source is in transporting a relatively pure sample to the gas phase. Sodium contamination from matrices, sample media and chromatography columns can produce highly complex spectra,<sup>64</sup> and this has led to the use of ammonium salts as alternative counter ions in ESI based analysis.<sup>65</sup> Once transferred to the gas phase, the generation of certain diagnostically useful product ions becomes critical. The retention of sulphate, carboxylate and acetylate groups along with production of cross ring and glycosidic fragmentation ions provides the maximum amount of information about the structure of the Heparin sugars.<sup>47</sup> For the 12 most common Heparin disaccharide molecules it was shown that from a mixture, the presence of each individual GAG compound could be unambiguously determined using a quadrupole ion trap MS<sup>2</sup> experiment, as described in Chapter 2. This study also highlighted the major problem with low to medium energy collision induced dissociation experiments, i.e. those carried out in ion traps and Time of Flight (TOF) instruments. While sufficient numbers of diagnostic product ions can be formed to distinguish isolated disaccharides, the fragmentation patterns for larger more complex examples are not sufficient for complete characterization.<sup>66,67,68</sup>

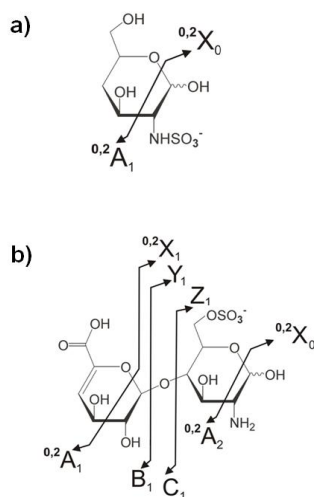


**Fig. 1.3** Fragment labelling scheme used in this work for a) monosaccharide and b) disaccharides. The A, B and C labels are used to indicate a fragment containing a non-reducing end of the GAG, while X, Y and Z denote fragments

**which include the reducing end of the sugar. (The reducing end is defined as the ring with a C1 carbon not involved in a glycosidic bond.)**

Additionally, neutral and charged sulphate groups are lost in high abundance, thus frustrating any attempts to sequence a larger chain. Earlier work carried out using collision induced dissociation has shown that B and Y type ions (an explanation of the Domon and Costello fragment naming system is given in Chapter 3 and in reference 46) may be formed with high efficiency across multiple negative charge states.<sup>69,70,71</sup>

These ‘backbone’ ions were formed without the loss of their fragile sulphates providing the majority of these groups were deprotonated.

The usefulness of studying small heparin disaccharides in isolation is highlighted by Meissen *et al.*<sup>72</sup> They have demonstrated the differences in fragmentation products produced when low-energy CID was performed on two heparin disaccharide fragments differing only in the position of a sulphate on the non-reducing ring. In one case, the third carbon of the ring was sulphated, in the other the sixth. An MS<sup>3</sup> experiment then determined the presence of a <sup>0,3</sup>X cross-ring fragment which only occurs where the third carbon is sulphated. This fragment was then used as a marker to examine the disaccharide enzymatic breakdown products of a series of larger sulphated octa-saccharides that bound effectively to a chemokine protein ligand. The role of the 3-O-sulphated region of the molecules in the binding process could be ruled out due to the absence of the <sup>0,3</sup>X fragment from the mass spectra of the larger saccharides seen binding effectively to the protein.

Zaia *et al.* also demonstrated the utility of CID in differentiating the epimers Iduronic and Glucuronic acid in Chondroitin Sulphate based on the ratios of <sup>0,2</sup>X<sub>n</sub> and Y<sub>n</sub> fragments produced. In this study the m/z ratios of the glycosidic and cross-ring product ions do not provide any information on the two epimers, however the abundance of Y<sub>5</sub><sup>3-</sup> and <sup>0,2</sup>X<sub>5</sub><sup>2-</sup> was significantly raised for the Iduronic acid containing GAG chain.<sup>71</sup>

Information about the relative composition of isomers in a GAG mixture may be obtained following enzymatic digestion to release the disaccharide content of a chain.<sup>71,73,74,75</sup> This method involves the use of pure isomeric standards to select product ions and to determine their contribution to the total ion current. Once the contribution of each isomer is known, a mixture of the two may be analysed for the intensity of these product ions and a system of equations used to reveal their ratio in the mixture. This method is further discussed in Chapter 3.

Studies on isolated disaccharides have provided sufficient data to distinguish isomers, epimers and their percentage contribution to a GAG chain. In order to fully characterise GAGs like Heparin, complete sequence information is required. At the time of writing one of the most successful ‘whole chain’ methods for GAG sequencing is Electron Detachment Dissociation (EDD). Electron detachment is achievable by means of high energy collisions with inert gas,<sup>76</sup> as described in Chapter 4. A more commonly used method is the irradiation of a multiply negatively charged ion with electrons in the 10-20eV kinetic energy range. Amster *et al* compared the results of EDD to Infrared Multi-Photon Dissociation (IRMPD) and Collision Induced Dissociation (CID) to demonstrate the benefits of the technique.<sup>77</sup> Their CID and IRMPD results for a non-sulphated carbohydrate showed that the majority of detected fragments were glycosidic in nature, with limited cross ring fragmentations. The EDD mass spectrum showed complete glycosidic bond fragmentation as well as a minimum of one cross-ring fragmentation per monosaccharide subunit of the tetramer studied. As well as producing comprehensive fragmentation patterns, the EDD technique has also been shown to distinguish GAG chains containing Iduronic and Glucuronic acids.<sup>78,79</sup>

EDD analysis has been applied to Dermatan Sulphate Oligosaccharides as long as 10 monosaccharide subunits,<sup>80</sup> involving molecules deprotonated at five sites. This size range means the technique is potentially highly suitable for the analysis of biologically relevant examples. The principal difference between these initial studies and biological GAGs is that the molecules studied contain a low number of sulphates when compared to those known to exist in nature.

The effects of charge state and sodium cation complexation have both been studied for the EDD process.<sup>81</sup> This that work it was determined that where the electron dissociation event occurs at a negatively charged sulphate group, the sulphate is often lost from the resulting fragment ions. Where a charged carboxylate group is the site of EDD, this problem is significantly reduced. Either selecting a higher charged species for isolation prior to irradiation, or using sodium cations to complex with the carboxylate groups, increases the overall charge on the molecule. Unfortunately it has also been shown that the increase in charged carboxylate side chains seems to be accompanied by a decrease in the number of glycosidic and cross ring fragmentations and so that experimental conditions must be carefully adapted to the specific species under study.

### 1.3.2 Energy Resolved Mass Spectrometry

Energy resolved mass spectrometry (ERMS) involves determining structural information based on the intensity of the fragment ion produced versus the kinetic energy used to effect fragmentation. It is directly analogous to the CID experiments described in Chapter 2, where a plot of product ion intensity versus percentage CID excitation voltage may be used to determine relative gas-phase stabilities of ions. The use of ERMS to determine additional information about gas-phase ions is a practical approach,<sup>82</sup> a clear example being in the study of stereo-isomers of hydroxycholesterol, which produce almost identical  $m/z$  fragments but are then distinguishable by varying the collisional energy used and monitoring the product ion intensities.<sup>83</sup> More recent studies by Kanie *et al* have shown that for sodiated hemiacetals, anomeric conformers may be distinguished based on ERMS data, and that this information can be used to determine to what extent anomerisation occurs in the gas phase.<sup>84</sup> This work has immediate applications in the mass spectrometric study of carbohydrate-based compounds where the  $\alpha$  or  $\beta$  position of a substituent group is important. ERMS studies may be compared to studies that involve a more straightforward spectral comparison, i.e. where a series of related anomeric or isomeric compounds produce very similar mass spectra that differ only in the

intensity of their peaks.<sup>86</sup> The energy-resolved approach produces more detailed information for comparison, differences in peak height may be negligible until studied under varying CID conditions. A comparison of an MS<sup>1</sup> CID experiment versus an ERMS study for 16 synthetic isomeric disaccharides including all anomeric combinations has shown that the former method was capable of distinguishing the structures of 7, while the latter produced unique curves for the entire sample.<sup>86</sup> The aim in this work was to attempt to produce a library of fragments that could be used to determine fragmentation characteristics useful in the analysis of other related sugars. While it seems that subtle anomeric differences between isomers can be clearly detected using this method, the extension of results specific to this compound set to more complex long chain examples would likely be highly challenging. Post-translational protein modifications, such as branched mannose-based oligosaccharides, are long-chain carbohydrate structures capable of a high degree of structural variation. ERMS has been demonstrated to produce subtly different curve shapes for these isomers, based on the location of the branched sections of the molecule.<sup>87</sup> The same methodology can be used in the study of gangliosides, where the fragment from the sugar part of the structure may be monitored to determine the location of the chain branching, avoiding the need to study the complex mass spectrum that would be produced by the dissociation of the entire molecule.<sup>88</sup>

The use of ERMS as a reliable test of product purity has been investigated for a wide range of sugars in the gas phase. This method is based on the premise that a first stage of MS isolation will reduce the ratio of the less stable species in a mixture. Even if the two species have identical  $m/z$  fragment patterns, the increased presence of the more stable ion at MS <sup>$n+1$</sup>  followed by resonant excitation will mean that the location of the 100 percent relative intensity of the product-ion curve will move to the right of the graph, i.e. more kinetic energy is required to reduce the precursor ion and raise the product ion values by a similar amount.<sup>89</sup>

### 1.3.3 Ion Mobility Mass Spectrometry

Ion-mobility mass spectrometry (IMMS) instruments are well established around the world for the detection and characterisation of a wide range of chemical species.<sup>90</sup> A ‘drift time’ IMMS instrument functions by recording the time it takes an ion to move through a buffer gas cell while in the presence of a magnetic field. The energy that the ions receive through collisions with the buffer gas is lower than that which they gain from the magnetic field and so the principal process is one of diffusion. Ion Mobility instruments have allowed isomeric and chiral compounds to be separated prior to the mass spectrometric stage and so have produced immediate analytical benefits. A proportionality constant (K), which relates the velocity of an ion to the electric field, forms part of the equation;

$$K = \left( \frac{3q}{16N} \right) \left( \frac{2\pi}{kT} \right)^{\frac{1}{2}} \left( \frac{m+M}{mM} \right)^{\frac{1}{2}} \left( \frac{1}{\Omega} \right) \quad [\text{Eq 1.1}]$$

where  $q$  is the ion charge,  $N$  is the number density of the buffer gas,  $k$  is Boltzmann’s constant,  $T$  is the absolute temperature,  $m$  is the mass of the buffer gas,  $M$  is the mass of the ion and the collisional cross section of the ion is represented as  $\Omega$ . A full review of the usefulness of this relationship in studying the gas phase structures of biological ions is outside the scope of this thesis and I discuss here instead its utility in the studies of glycosaminoglycans.

The immediate benefit of IMMS for GAG analysis is in its ability to separate mixtures of isomers and epimers prior to mass spectral analysis. Leary *et al* analysed a pair of suspected isomeric hexasaccharide GAGs which had been first isolated from a mixture via anion exchange chromatography.<sup>91</sup> An IMS tandem mass spectrometry approach was then used to examine two peaks from the chromatography stage. Distinct arrival times from the Ion mobility cell were noted (6.77 compared to 7.02 ms), although the ionic fragments generated at the mass spectrometry step were highly similar and differed only slightly in intensity. The use of partial enzymatic digestion and NMR analysis determined the difference to be an

axial versus equatorial position for a single carboxylate group, demonstrating the effectiveness of IMMS in differentiating closely related molecular structures. Ion-mobility drift times have also proven effective in separating a range of isomeric glycans where arrival times are found to vary with both epimeric and glycosidic linkage positions.<sup>92</sup>

One of the most valuable results of IMMS drift time measurements is the ability to extrapolate collisional cross sections for comparison with theoretical work. Jin *et al* have used molecular modelling to generate candidate structures for Heparin monosaccharides, a disaccharide and several tetrasaccharides.<sup>93</sup> While the monosaccharide calculated cross sections were found to be too similar to each other for experimental comparison, the larger anionic sugars results compared very favourably with drift time cross section results. An important result of this work was the observation that, as in the above study by Leary *et al*,<sup>91</sup> small changes in primary structure of the GAGs caused significant alterations in recorded collisional cross section. A similar approach has been used to study N-Linked glycans isolated from Ovalbumin after enzymatic digestion.<sup>94</sup> This study highlighted the large overlap that existed in the calculated collisional cross sections for three isomeric glycans, despite the authors attempts to alter their source ionization conditions to allow conformations to anneal into certain preferred low energy states.

### 1.3.4 Ab Initio Techniques

The large molecular size of GAGs, in addition to their flexibility and the presence of numerous heavy atoms within their structures make them challenging targets to study by computational methods. Simons *et al* have characterized neutral carbohydrate systems in the gas phase using laser spectroscopy,<sup>95</sup> however no data exists at present on negatively charged sugars with which to benchmark similar calculations. Remko and Leith have studied short sections of Heparin in detail, initially investigating the Iduronic acid monosaccharide 1,4-DiOMe IdoA2S.<sup>96</sup> This study, which was carried out at the B3LYP/6-311++G\*\* level, relied upon initial geometries based on the  ${}^2S_0$ ,  ${}^1C_4$  and  ${}^4C_1$  ring conformations commonly associated

with the Iduronic acid subunit of Heparin,<sup>50,51</sup> and determined that the most stable conformation of this structure as a neutral was  ${}^2S_0$ , whether in the gas phase or in solution. The lowest-energy conformation for the anionic form was found to be  ${}^1C_4$ . Further work by these authors involved larger trimeric and pentameric examples included the biologically active DEFGH sequence at the B3LYP/6-31G level.<sup>97</sup> One result of this study was the observation that sodium counter ions have a large effect on the calculated minimum energy structures, forming sodium ‘bridges’ between charged sulphate and carboxylate groups along the molecule’s length and causing it to form a far more compact structure than its uncomplexed anionic form. This formation of compacted structures has also been previously noted by Jin *et al*,<sup>93</sup> where the effect was studied by IMMS and is likely to be in part responsible for the changes in the lowest energy fragmentation pathways seen in the counter-ion complexed Heparin sugars studied in Chapter 3.

Remko *et al* have also studied the effects of solvation on some of the constituent monosaccharides that make up Heparin chains in nature.<sup>98</sup> They have found that the  ${}^2S_0$  conformation of Iduronic acid is the most stable conformer for the sodium salt complex in both the gas phase and in solution. The bare anionic form has  ${}^1C_4$  as its most stable conformation, again underlining the importance of counter-ion complexation in determining gas phase structures in negatively charged sugars. The principal weakness in these studies relates to the starting geometries. While the main ring conformations are well known in solution,<sup>50</sup> they are used here as the basis for gas-phase calculations including those involving counter ions. As discussed above, these counter-ion complexed structures differ significantly from the bare molecular ions. The complexity of the three-dimensional space available to the larger Heparin fragments suggests that a large number of minimum energy structures exist, and the method of Remko *et al* ignores the possibility of the existence of families of sub-conformers.

A similar study involving 2-O-sulfo-a-L-iduronate has been carried out using the B3LYP/6-311++G\*\* method, in which proton-proton and proton-carbon coupling constants were calculated and compared with time averaged NMR data.<sup>99</sup> In this

study the calculated coupling constants for a structure that was present as mainly  ${}^1\text{C}_4$  were in good agreement with those measured experimentally. The choice of the author to model this sugar only as a sodium cation-complexed system is of interest, since it implies that the solvated monosaccharide will always be paired. Recent work has suggested that one effect of solvation is to weaken carboxylate and sulphate ligand interactions with lithium and sodium cations,<sup>100</sup> and so a comparison with the uncomplexed anionic form of the sugar calculation is likely to be valuable in this context. Further studies involving proton-proton coupling constants examining the effect of incorporating the Iduronic acid into larger chains have shown that as the size of the molecule increased, the equilibrium values moved to favour the presence of the  ${}^2\text{S}_0$  conformer,<sup>101</sup> in agreement with work mentioned in section 1.2.2.

### 1.3.5 Molecular Dynamics

Force-field based methods are a far less computationally intensive route to obtaining structural information on a molecule than the wavefunction based techniques mentioned above. In order to better understand the reasons why the  ${}^2\text{S}_0$  conformation of Iduronic acid is more favoured in a chain, it is necessary to simulate the system using a molecular dynamics approach. Iduronic Acid has been known for some time to be a flexible subunit making up part of an equally flexible sugar chain.<sup>102,103</sup> Verli *et al.* have studied various combinations of Iduronic Acid with commonly found constituents of Heparin using the GROMOS96 force field in the Gromacs simulation suite.<sup>104</sup> Interestingly, this study showed it was less favourable energetically for a molecule to contain the  ${}^2\text{S}_0$  conformation instead of a chair based structure, due to a decrease in intramolecular hydrogen bonding. This result may not be representative of Iduronic Acid behaviour in a full chain since computational constraints limited the system studied to disaccharide size. Earlier work using the Gromacs program to study larger sections of a Heparin chain required the artificial restraining of the conformation of the Iduronate sugar ring to allow study of the  ${}^1\text{C}_4$  and  ${}^2\text{S}_0$  conformations, since the inter-conversion between the two was not well modelled by the force field used.<sup>105</sup> This study included the addition of numerous

sodium atoms to neutralise the negative charge sites along the chains structure and produced dihedral angles that were in many cases quite different from either NMR or X-Ray crystal data. Comparisons of the use of Löwdin, Mulliken and ESP charge fitting prior to molecular dynamics simulations have found Löwdin fitting to be an acceptable method.<sup>106</sup> These results highlighted the large relative energy changes that may be caused by the Iduronic acid monosaccharide, with the presence of the  ${}^1S_5$  conformation instead of  ${}^2S_0$  having a significant effect on the system studied.

The use of the Gromacs simulation suite to study the interaction of the antithrombin binding heparin pentasaccharide sequence DEFGH has produced results in good general agreement with known X-Ray crystal structures.<sup>107</sup> It should be noted that this study looked at both the  ${}^1C_4$  and  ${}^2S_0$  conformations of the Iduronic acid monomer and found that either conformation allowed effective binding, at odds with the work described in section 1.2.2. Pye et al have modelled short sections of Heparan Sulphate by Molecular Dynamics and compared their results to NMR spectroscopy. They note that an important consideration when using wavefunction based techniques is that hydrogen bonding between the sugar and its surrounding solvent molecules will be neglected if water molecules are not treated explicitly.<sup>108</sup>

The large size of the biologically significant GAG molecules means that Molecular Dynamics remains the only realistic means of simulation. The absence of spectroscopic data with which to compare results is likely to present a major difficulty in the benchmarking of newer force fields.<sup>109,110</sup>

#### 1.4 Properties of Gas-Phase Multiply Charged Anions

The Glycosaminoglycan family are commonly found as Multiply Charged Anions (MCAs) in the gas phase and are some of the most densely negatively charged molecules found in nature.<sup>46</sup> Gas-Phase MCAs display novel potential energy surfaces due to the presence of the Repulsive Coulomb Barrier (RCB). The existence of the RCB has a profound effect on the stability of MCAs since it can confer metastability on species that are exothermic for electron loss or ionic fragmentation.<sup>111</sup> Gas phase multiply charged anions may decay via either electron

loss or ionic fragmentation<sup>112,113,114</sup>. For the majority of systems studied within our group, the ionic fragmentation pathway will predominate,<sup>115,116</sup> and low energy collision induced dissociation may be used to determine the relative energies required to effect either route, as described in Chapter 2. Aside from Photoelectron Spectroscopy studies,<sup>117</sup> electron loss has been observed to occur spontaneously for  $\text{PtCl}_4^{2-}$  and fullerenes within FTICR mass spectrometers.<sup>118,119</sup> This pathway is also seen to occur in high energy collisions with noble gases.<sup>120</sup> Work carried out within our group has determined that in the case of small multiply negatively charged metal salts, the lowest energy fragmentation pathway for the cluster is identical to that of the bare MCA.<sup>121,122,123</sup>

Electron loss from a neutral atom results in the formation of a cation, and so the interactive force that exists is one of coulombic attraction. Where the precursor molecule is a multiply charged anion (MCA), the departing electron or anionic fragment will experience an electrostatic repulsion, in addition to the binding energy that needs to be supplied to remove it. This combination of forces leads to the unique shape of the Repulsive Coulomb Barrier (RCB).<sup>124</sup> It should be noted here that the barrier itself, examined from the point of view of a departing electron/anion is an attractive force to be overcome, lowered by the repulsion between two negative charges. Similarly, a negatively charged species moving towards a singly charged anion would experience the RCB as repulsive at first, with the potential energy of the system lowering from its maximum as its attraction to the nucleus began to dominate.

The existence of the RCB was conclusively proven by Wang et al when electrosprayed molecular dianions produced photo-detached electrons with kinetic energies in excess of the laser light energy used to produce them.<sup>125</sup> Chapter 6 reports the findings of study into the Dichromate dianion, which fragments via electron loss and ionic fragmentation under CID conditions and so may be considered atypical for a small molecular dianion.<sup>115,116</sup> Chapter 7 describes the findings of a similar study on the gas-phase stability of the  $\text{Re}_2\text{X}_8^{2-}$  ( $\text{X} = \text{Cl}, \text{Br}$ ) and

$\text{Re}_2\text{X}_n\text{Y}_{8-n}^{2-}$  ( $\text{X} = \text{Cl}$ ,  $\text{Y} = \text{Br}$ ,  $n=1-3$ ) metal-metal bond complexes which are seen to decay via ionic fragmentation.

### 1.5 Summary and Thesis Aims

The primary aim of the work presented in this thesis is to study the fragmentation pathways and conformational flexibility of Heparin Glycosaminoglycan anions. The principal experimental method used is collision induced dissociation (CID) based mass spectrometry.

Chapter 3 details the effects of cation complexation and varying charge states on the low energy fragmentation pathways for a typical isomeric set of three Heparin disaccharides. In addition to providing a better insight into the fragmentation routes for these species, this work is intended to assist in the selection of possible future ‘marker’ anionic products to assist in isomer identification in the presence of counter ion contamination during analysis. Chapter 4 demonstrates the first use of very high energy Mass Analysed Ion Kinetic Energy (MIKE) mass spectrometry to generate fragments from densely sulphated Heparin disaccharide fragments. Examples from this family have previously proven to be analytically challenging to study via mass spectrometry at low energies and via electron detachment dissociation (EDD). The method is assessed for its ability to generate the diagnostically important cross ring and glycosidic product ions, as well as in retaining the molecules substituent groups, specifically the fragile sulphates.

Chapter 5 explores the three dimensional space available to the Iduronic Acid monomer which has a crucial role in Heparin to protein binding. This study uses molecular mechanics to generate candidate structures that are then optimized using higher level quantum chemistry based techniques. The B3LYP, PW91PW91, MO5-2X model chemistries are compared at the 6-31++G\*\* level of theory and benchmarked against MP2 calculations to determine relative performance. This work is also intended to demonstrate the potentially large volume of conformational space available to this class of sulphated sugar.

Chapter 6 extends the application of the CID technique developed within our group to study the lowest energy fragmentation pathway for the isolated dichromate dianion  $\text{Cr}_2\text{O}_7^{2-}$ . The loss of an electron from this dianion represents a novel fragmentation route at low energy and the potential energy surface for electron loss versus ionic fragmentation is modelled using density functional theory. Chapter 7 demonstrates the use of this technique to probe the gas phase stability of  $\text{Re}_2\text{X}_8^{2-}$  ( $\text{X} = \text{Cl}, \text{Br}$ ) and  $\text{Re}_2\text{X}_n\text{Y}_{8-n}^{2-}$  ( $\text{X} = \text{Cl}, \text{Y}=\text{Br}, n=1-3$ ) metal-metal bond complexes with respect to the loss by ionic fragmentation of their halide atoms.

---

**References**

1. G. Rivas, F. Ferrone, J. Herzfeld, *EMBO reports* 5 (2004) 23
2. J. Spitzer, B. Poolman, *Microbiol. Mol. Biol. Rev.* 73 (2009) 371
3. R.J. Ellis, *Trends Biochem. Sci.* 26 (2001) 597
4. J.P. Simons, *Mol. Phys.* 107 (2009) 2435
5. Z. Tian and S.R. Kass, *J. Am. Chem. Soc.* 130 (2008) 10842
6. V. Gabelica, E. DePauw, *J. Mass Spectrom.* 36 (2001), 397
7. V. Gabelica, E. DePauw, *Int. J. Mass Spectrom.* 219 (2002) 151
8. J. Gidden, A. Ferzoco, E. Shammel Baker, M. T. Bowers, *J. Am. Chem. Soc.* 126 (2004) 15132
9. E. Shammel Baker, N.F. Dupuis, M.T. Bowers, *J. Phys. Chem. B* 113 (2009) 1722
10. N. Le Novere, *Bioinformatics* 17 (2001) 1226
11. S. Pan, X. Sun, J. K. Lee, *J. Am. Soc. Mass Spectrom.* 17 (2006) 1383
12. M.F. Jarrold, *Phys. Chem. Chem. Phys.* 9 (2007) 1659
13. P.E. Barran, N.C. Polfera, D.J. Campopiano, D.J. Clarke, P.R.R. Langridge-Smith, R.J. Langley, J.R.W. Govan, A. Maxwell, J.R. Dorin, R.P. Millard, M.T. Bowers, *Int. J. Mass Spectrom.* 240 (2005) 273
14. B. Turgut, K. Serdar, *Biophys. J.* 84 (2003) 2871
15. L. Lammich, M. Axman Petersen, M. Brøndsted Nielsen and L.H. Andersen, *Biophys. J.* 92 (2007) 201
16. J. Rajput, D.B. Rahbek, L.H. Andersen, T. Rocha-Rinza, O. Christiansen, K. B. Bravaya, A.V. Erokhin, A.V. Bochenkova, K.M. Solntsev, J. Dong, J. Kowalik, L.M. Tolbert, M. Axman Petersen, M. Brøndsted Nielsen, *Phys. Chem. Chem. Phys.* 11 (2009) 9996
17. J.P. Simons, R.A. Jockusch, P. ÇarÇabal, I. Hünig, R.T. Kroemer, N.A. Macleod, L.C. Snoek, *Int. Rev. Phys. Chem.* 24 (2005) 489
18. I. Hünig, A.J. Painter, R.A. Jockusch, P. ÇarÇabal, E.M. Marzluff, L.C. Snoek, D.P. Gamblin, B.G. Davis, J.P. Simons, *Phys. Chem. Chem. Phys.* 7 (2005) 2474.
19. J.P. Simons, B.G. Davis, E.J. Cocinero, D.P. Gamblin, E.C. Stanca-Kaposta, *Tetrahedron: Asymmetry* 20 (2009) 718
20. A.B. Boraston, D.N. Bolam, H.J. Gilbert, G.J. Davies, *Biochem. J.* 382 (2004) 769
21. E.C. Stanca-Kaposta, D.P. Gamblin, E.J. Cocinero, J. Frey, R.T. Kroemer, B.G. Davis, A.J. Fairbanks, J.P. Simons, *J. Am. Chem. Soc.* 130 (2008) 10691
22. E.J. Cocinero, D.P. Gamblin, B.G. Davis, J.P. Simons, *J. Am. Chem. Soc.* 131 (2009) 11117

23. J.P. Simons, *Mol. Phys.* 107 (2009) 2435
24. A. Kamariotis, O.V. Boyarkin, S.R. Mercier, R.D. Beck, M.F. Bush, E.R. Williams, T.R. Rizzo, *J. Am. Chem. Soc.* 128 (2006) 905
25. M.F. Bush, J.S. Prell, R.J. Saykally, E. R. Williams, *J. Am. Chem. Soc.* 129 (2007) 13544
26. T.R. Rizzo, J.A. Stearns, O.V. Boyarkin, *Int. Rev. Phys. Chem.* 28 (2009) 481
27. S.K. Drake, G.L. Hortin, *Int. J. Biochem. Cell Bio.* 42 (2010) 174
28. C.R. McAlpin, C.R. Cox, S.A. Matyi, K. J. Voorhees, *Rapid Commun. Mass Spectrom.* 24 (2010) 11
29. M. Kussmann, E. Nordhoff, H. Rehbek-Nielson, S. Haebel, M. Rossel-Larsen, L. Jakobsen, J. Gobom, E. Mirgorodskaya, A. Kroll-Kristensen, L.Palm, P. Roepstorff, *J. Mass Spectrom.* 32 (1997) 593
30. M. Zaitseva, D. Kaluzhny, A. Shchyolkina, O. Borisova, I. Smirnov, G. Pozmogova, *Biophys. Chem.* 146 (2010) 1
31. H. Gao, Y. Liu, M. Rumley, H. Yuan, B. Mao, *Rapid Commun. Mass Spectrom.* 23 (2009) 3423
32. W.C. Changa, L.C.L. Huanga, Y.-S. Wang, W.-P. Peng, H.C. Chang, N.Y. Hsueh, W. B. Yang, C.H. Chen, *Anal. Chim. Acta* 582 (2007) 1
33. MALDI MS: a practical guide to instrumentation, methods and applications, F. Hillenkamp, J. Peter-Katalinić, Wiley-VCH, 2007
34. K. Strupat, M. Karas, F. Hillenkamp, *Int. J. Mass Spectrom. Ion Processes* 72 (1991) 89
35. R.C. Beavis, B.T. Chait *Rapid Commun. Mass Spectrom.* 3 (1989) 432
36. D.P. Magparangalan, T.J. Garrett, D.M. Drexler, R.A. Yost, *Anal. Chem.* 82 (2010) 930
37. P. Juhasz, K. Biemann *Carbohydr. Res.* 270 (1995) 131
38. T.N. Laremore, R.J. Linhardt *Rapid Commun. Mass Spectrom.* 21 (2007) 1315
39. C. Przybylski, F. Gonnet, D. Bonnaffe, Y. Hersant, H. Lortat-Jacob, R. Daniel, *Glycobiology*, 20 (2010) 224
40. A. K. Korir, C.K. Larive, *Anal. Bioanal. Chem.* 393 (2009) 155
41. K.-H. Kboo, H.R. Morris, R.A. McDowell, A. Dell, M. Maccarana and U. Lindahl, *Carbohydr. Res.* 244 (1993) 205
42. L.M. Mallis, H.M. Wang, D. Loganathan, R.J. Linhardt, *Anal. Chem.* 61 (1989) 1453
43. R.J. Linhardt, H. M. Wang, D. Loganathan, D.J. Lamb, L.M. Mallis, *Carbohydr. Res.* 225 (1992) 137
44. J. J. Wolff, T. N. Laremore, A. M. Busch, R. J. Linhardt, I. J. Amster, *J. Am. Soc. Mass Spectrom.* 19 (2008) 790

45. H. Naimy, N. Leymarie, M. J. Bowman, J. Zaia, *Biochemistry* 47 (2008) 3155
46. I. Capila, R. J. Linhardt, *Angew. Chem. Int. Ed.* 41 (2002) 390
47. O. M. Saad, J.A. Leary, *J Am. Soc. Mass Spectrom.* 15 (2004) 1274
48. R. Lawrence, H. Lu, R.D. Rosenberg, J.D. Esko, L. Zhang, *Nat. Methods* 5 (2008) 291
49. B. Domon, C.E. Costello, *Glycoconjugate J.* 5 (1988) 397
50. N. S. Gandhi, R. L. Mancera, *Chem. Biol. Drug Des.* 72 (2008) 455
51. R. D. Rosenberg, P. S. Damus, *J. Biol. Chem.* 248 (1973) 6490
52. U. Lindahl, G. Backstrom, M. Hook, L. Thunberg, L. Fransson, A. Linker, *Proc. Natl. Acad. Sci. USA* 76 (1979) 3198
53. U. Lindahl, G. Backstrom, L. Thunberg, I. G. Leder, *Proc. Natl. Acad. Sci. USA* 77 (1980) 6551
54. M. Petitou, C.A.A. van Boeckel, *Angew. Chem. Int. Ed.* 43 (2004) 3118
55. C. A. A. van Boeckel, M. Petitou, *Angew. Chem.* 105 (1993) 1741
56. J. Kovensky, *Cur. Med. Chem.* 16 (2009) 2338
57. D. Liu, Z. Shriver, Y. Qi, G. Venkataraman, R. Sasisekharan, *Semin. Thromb. Hemost.* 28 (2002) 67
58. C.E. Bandtlow, D.R. Zimmermann *Physiol. Rev.* 80 (2000) 1267
59. R.J. Linhardt, T. Toida, *Acc. Chem. Res.* 37 (2004) 431
60. M. Gotte, *FASEB J.* 17 (2003) 575
61. G. Chatzinikolaou, D. Nikitovic, A. Berdiaki, A. Zafiroopoulos, P. Katonis, N. K. Karamanos G. N. Tzanakakis, *Cell Prolif.* 43 (2010) 9
62. H. Shimizu, M. Ghazizadeh, S. Sato, T. Oguro, O. Kawanami, *J. of Clin. Neurosci.* 16 (2009) 277
63. T. Muramatsu, H. Muramatsu *Proteomics* 8 (2008) 3350
64. W. Chai, H. Kogelberg, A. M. Lawson, *Anal Biochem.* 237 (1996) 88
65. W. Chai, J. Luo, C.K. Lim, A. M. Lawson, *Anal. Chem.* 70 (1998) 2060
66. A. Zamfir, D.G. Seidler, H. Kresse, Jasna Peter-Katalinić, *Rapid Commun. Mass Spectrom.* 16 (2002) 2015
67. A. Zamfir, D.G. Seidler, H. Kresse, Jasna Peter-Katalinić, *Glycobiology*, 13 (2003) 733
68. R. Daniel, L. Chevlot, M. Carrascal, B. Tissot, P.A.S. Mourão J. Abiand, *Carbohydr. Res.* 342 (2007) 826
69. J. Zaia and C. E. Costello, *Anal. Chem.* 75 (2003) 2445
70. O. M. Saad, J. A. Leary, *Anal. Chem.* 75 (2003) 2985
71. J. Zaia, X-Q Li, S-Y Chan, C. E. Costello, *J. Am. Soc. Mass Spectrom.* 14 (2003) 1270
72. J.K. Meissen, M.D. Sweeney, M. Girardi, R. Lawrence, J. D. Esko, J.A. Leary, *J. Am. Soc. Mass Spectrom.* 20 (2009) 652

73. O.M. Saad and J.A. Leary, *Anal. Chem.*, 75 (2003) 2985
74. H. Desaire and J. A. Leary, *J. Am. Soc. Mass Spectrom.* 11 (2000) 916
75. H. Desaire and J. A. Leary, *Anal. Chem.*, 71 (1999) 4142
76. B. Liu, P. Hvelplund, S.B. Nielsen, S. Tomita, *Int. J. Mass Spectrom.* 230 (2003) 19
77. J. J. Wolff, I.J. Amster, L. Chi and R.J. Linhardt, *J. Am. Soc. Mass Spectrom.* 18 (2007) 234
78. J. J. Wolff, T.N. Laremore, H. Aslam, R.J. Linhardt I. J. Amster, *J. Am. Soc. Mass Spectrom.* 19 (2008) 1449
79. J.J. Wolff, L. Chi, R.J. Linhardt, I. J. Amster, *Anal. Chem.* 79 (2007) 2015
80. J.J. Wolff, T. N. Laremore, A.M. Busch, R.J. Linhardt, I.J. Amster, *J. Am. Soc. Mass Spectrom.* 19 (2008) 294
81. J.J. Wolff, T.N. Laremore, A.M. Busch, R. J. Linhardt, I. J. Amster, *J. Am. Soc. Mass Spectrom.* 19 (2008) 790
82. D.-D. Fetterolf, R.-A. Yost, *Int. J. Mass Spec. Ion Phys.* 44 (1982) 37
83. D. Favretto, F. Guidugli, R. Seraglia, P. Traldi, F. Ursini, A. Sevanian, *Rapid Comm. Mass Spec.* 5 (1991) 240
84. O. Kanie, A. Kurimoto, Y. Kanie, S. Daikoku, A. Ohtake, K. Suzuki, *Proc. Jpn. Acad., Ser. B* 85 (2009) 204
85. S. Daikoku, T. Ako, A. Kurimoto, O. Kanie, *J. Mass Spectrom.* 42 (2007) 714
86. S. Daikoku, T. Ako, R. Kato, I. Ohtsuka, O. Kanie, *J. Am. Soc. Mass Spectrom.* 18 (2007) 1873
87. A. Kurimoto, O. Kanie, *Rapid Commun. Mass Spectrom.* 21 (2007) 2770
88. Y. Shioiri, A. Kurimoto, T. Ako, S. Daikoku, A. Ohtake, H. Ishida, M. Kiso, K. Suzuki, O. Kanie, *Anal. Chem.* 81 (2009) 139
89. S. Daikoku, A. Kurimoto, S Mutsuga, T. Ako, T. Kanemitsu, Y. Shioiri, A. Ohtake, R. Kato, C. Saotome, I. Ohtsuka, S. Koroghi, S. K. Sarkar, A.Tobe, S. Adach, K. Suzuki, O Kanie, *Carbohydr. Res.* 344 (2009) 384
90. A.B. Kanu, P. Dwivedi, M. Tam, L. Matz, H. H. Hill, *J. Mass Spectrom.* 43 (2008) 1
91. M.R. Schenauer, J.K. Meissen, Y. Seo, J.B. Ames, J.A. Leary, *Anal. Chem.* 81 (2009) 10179
92. B.H. Clowers, P. Dwivedi, W.E. Steiner, H.H. Hill, B. Bendiak, *J. Am. Soc. Mass Spectrom.* 16 (2005) 660
93. L. Jin, P.E. Barran, J.A. Deakin, M. Lyon, D. Uhrín, *Phys. Chem. Chem. Phys.* 7 (2005) 3464
94. M. Remko, M. Swart, F.M. Bickelhaupt, *J. Phys. Chem. B* 111 (2007) 2313
95. L. Drouin, E.C. Stanca-Kaposta, P. Saundh, A.J. Fairbanks, S. Kemper, T.D.W. Claridge, J.P. Simons, *Chem. Eur. J.* 15 (2009) 4057

96. Milan Remko, C-W von der Lieth, J. Chem. Inf. Model. 46 (2006) 1194
97. M. Remko, C.-W. von der Lieth, J. Phys. Chem. A 111 (2007) 13484
98. M. Remko, M. Swart, F.M. Bickelhaupt, J. Phys. Chem. B 111 (2007) 2313
99. M. Hricovíni, Carbohydr. Res. 341 (2006) 2575
100. M. Remko, P.T. Van Duijnen, C.-W. von der Lieth, J. Mol. Struct Theo. 814 (2007) 119
101. M. Hricovíni, F. Bízík, Carbohydr. Res. 342 (2007) 779
102. B. Mulloy and M. J. Forster, Glycobiology, 10 (2000) 1147
103. J. Angulo, P.M. Nieto, M. Martín-Lomas, Chem. Commun. 13 (2003) 1512
104. L. Pol-Fachina, H. Verli, Carbohydr. Res. 343 (2008) 1435
105. H. Verli, J. A. Guimarães, Carbohydr. Res. 339 (2004) 281
106. C.F. Becker, J. A. Guimarães, H. Verli, Carbohydr. Res. 340 (2005) 1499
107. H. Verli, J.A. Guimarães, J. Mol. Graphics Modell. 24 (2005) 203
108. K.J. Murphy, N. McLay, D.A. Pye, J. Am. Chem. Soc. 130 (2008) 12435
109. K. N. Kirschner, A.B. Yongye, S.M. Tschampel, J. González-Outeiriño, C. R. Daniels, B.L. Foley, R.J. Woods, J. Comput. Chem 29 (2008) 622
110. D.R. Ferro, P. Pumilia M. Massimo Ragazzi, J. Comp. Chem. 18 (1997) 351
111. W.E. Boxford, C.E.H. Dessent, Phys. Chem. Chem. Phys. 8 (2006) 5151
112. W. E. Boxford, C. E. H. Dessent, Phys. Chem. Chem. Phys. 8 (2006) 5151
113. M. K. Scheller, R. N. Compton, L. S. Cederbaum, Science 270 (1995) 1160
114. A. Dreuw, L. S. Cederbaum, Chem. Rev. 102 (2002) 181
115. W. E. Boxford, J. K. Pearce, C. E. H. Dessent, Chem. Phys. Lett. 399 (2004) 465
116. R. M. Burke, J. K. Pearce, W. E. Boxford, A. Bruckmann, C. E. H. Dessent, J. Phys. Chem. A 109 (2005) 9775
117. T. Waters, X. B. Wang, L. S. Wang, Coord. Chem. Rev. 251 (2007) 474
118. P. Weis, O. Hampe, S. Gilb, M. M. Kappes, Chem. Phys. Lett. 321 (2000) 426.
119. O. Hampe, M. Neumaier, M. N. Blom, M. M. Kappes, Chem. Phys. Lett. 354 (2002) 303.
120. W. E. Boxford, M. O. A. El Ghazaly, C. E. H. Dessent, S. Brøndsted Nielsen, Int. J. Mass Spectrom. 244 (2005) 60
121. R.M. Burke, W.E. Boxford, C.E.H. Dessent, J. Chem. Phys. 126 (2007) 064308
122. R.M. Burke, W.E. Boxford, C.E.H. Dessent, J. Chem. Phys. 125 (2006) 021105
123. W.E. Boxford, R.M. Burke, C.E.H. Dessent, Phys. Scripta 76 (2007) C56
124. A. Dreuw and L.S. Cederbaum, Phys. Rev. A. 63 (2000) 012501

125. X.-B. Wang and L.S. Wang, *Nature* 400 (1999) 245

## Chapter 2: Experimental Methods

### 2.1 Electrospray Ionization Mass Spectrometry in Quadrupole Ion Traps

#### 2.1.1 The Nature of ESI

Electrospray Ionization (ESI) is a highly effective technique for transferring large macromolecules from solution into the gas phase. This soft ionization technique was developed by Professor John Fenn who received a share of the 2002 Nobel Prize for Chemistry for his work.<sup>1</sup> A sample solution is introduced via a thin diameter fused silica capillary line to a needle, which is then either positively or negatively biased, depending on the charge on the ions to be studied. Voltages vary considerably on the solute and solvent employed however 2-5 kV may be considered standard values. The small size of the electrospray capillary leads to a high electric field in the air surrounding the tip. Placing a negative voltage on the needle tip will cause anions to accumulate at the surface, leading to the formation of a ‘Taylor Cone’ as the meniscus deforms.<sup>2</sup> From the tip of this cone a jet of droplets then emerges under the influence of the applied field. At this point, solvent evaporation causes charged droplets to start to shrink, until the Rayleigh stability limit is reached,<sup>3</sup> a point at which the electrostatic repulsion between the ions exceeds the force of surface stabilizing the droplet. The result is fission of the droplet, leading to increasingly smaller, highly-charged versions of the original.

Ion production from droplets is believed to proceed by one of two mechanisms, Coulomb Fission or Ion Evaporation. *Coulomb Fission*, or the Charged Residue Model (CRM),<sup>4</sup> describes a process in which increased charge density caused by solvent evaporation causes droplets to break into smaller and smaller units. Eventually a single ion contained in a very small droplet remains, and solvent evaporation from this species leads to the bare ion. *Ion Evaporation*,<sup>5</sup> suggests that the same increase in charge density leads to ions overcoming the surface tension of the droplet to allow ion release from the surface. The precise mechanism by which

the process occurs has been the subject of sustained debate and may vary depending on the solute involved.<sup>6</sup> Very high molecular weight ions, such as Poly-ethylene glycols of approximately 5MDa, may favour the Coulombic fission model,<sup>6,7</sup> although evidence exists that far smaller organic ions in the 1000-7000Da range may also enter the gas phase through the same route.<sup>8</sup> Fenn and Nguyen have added solvent vapour to the nitrogen background gas of an ESI and source and found that the intensity of desolvated ions increased, casting doubt on the Coulomb fission route.<sup>6</sup>

Modern mass spectrometers are equipped with several features to ensure that minimal solvent ion clusters survive to enter the mass selective region. The most common set up includes a heated capillary where the newly forming ion beam passes along a short heated section to aid solvent evaporation. Another common solution is the inclusion of drying gas, typically nitrogen, which is blown outwards from around the sampling orifice. A further refinement is to place the ESI needle tip at a right angle to the capillary region which has the effect of causing neutrals, such as bulk solvent to be lost as they are not affected by the voltage applied.

A schematic diagram of a Thermo-Finnegan LCQ mass spectrometer is shown below. In brief, this instrument is composed of an ESI source that is coupled to a quadrupole ion-trap. The ESI needle is immediately followed by a heated capillary which is approximately 11.5 cm long and has an internal diameter of 400 micrometers. The end of the heated capillary allows supersonic expansion of the gas and ions into the next chamber by means of a molecular beam skimmer. This is placed within the silent zone of the Mach disk formed at expansion, the ideal distance being given by

$$x_m = 0.67D_o\sqrt{P_0/P_1} \quad [\text{Eq 2.1}]$$

where  $D_o$  is the nozzle diameter,  $P_o$  is the atmospheric or higher pressure, and  $P_1$  is the lower pressure.<sup>9</sup> The skimmer collected ions then pass to the first octopole (Oct

1), operating as an ion guide in radiofrequency at 2.5 MHz and 400 V peak to peak. The ions then pass through an inter-octopole lens which, in addition to facilitating transmission, acts as an aid to the differential pumping necessary between atmosphere and analyzer region. The second octopole (Oct 2) is responsible for direct transmission of ions into the quadrupole ion trap. The second octopole (Oct 2) is responsible for direct transmission of ions into the quadrupole ion trap.

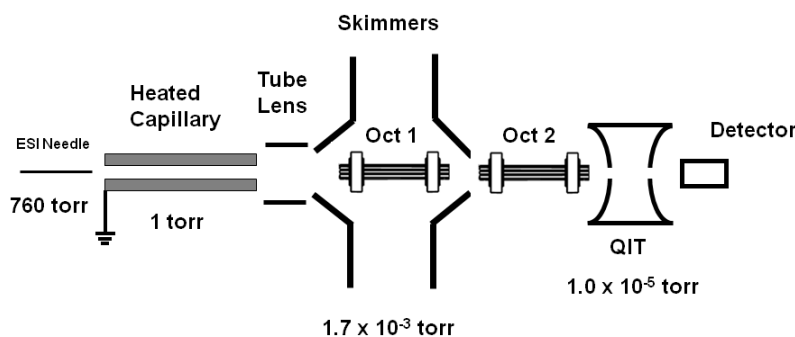


**Fig 2.1 Schematic representation of a commercial quadrupole ion trap mass spectrometer, based on the layout of the Finnegan LCQ**

Across the capillary, ion optics and the octopoles, the overall focussing voltages form a downhill gradient, so that a negative ion will experience a lowering of the relative positive bias as it moves through the instrument and hence is propelled towards the ion trap. Immediately prior to the trap is a ‘gate’ electrode which is used to control the density of ions present in this area. This function is required since too few ions contained means a loss of instrument sensitivity, while too many trapped ions lead to enhanced space charge effects, i.e. the high density of charged ions can lead to repulsive effects causing ion ejection and consequently increased background noise, including ghost peaks. More modern instruments include the option to raise and lower the target ion density within the trap and this can be a valuable tool when fragile species are studied.

### 2.1.2 Theory and Operation of the 3-Dimensional Quadrupole Ion Trap

The Quadrupole Ion Trap (QIT) or ‘Paul Trap’ was developed by Wolfgang Paul and Hans Dehmelt.<sup>10</sup> The device consists of three principal electrodes, a ring

electrode and two end-cap electrodes. Initially, work with these traps consisted of employing ‘mass selective stability mode’ in which the RF/DC ratio of voltages placed on the ring electrode were kept at an equal ratio and ramped across a range that determined at which mass-to-charge ratio value an ion would be confined within the trap. In this way the Paul Trap acted as the three-dimensional equivalent of a linear quadrupole mass filter operating in RF/DC mode.

The utility of this device was greatly increased in the early 1980’s when George Stafford working for Finnegan MAT developed the ‘mass instability mode’ of operation, relying on the principle of resonance ejection.<sup>11</sup> In practical terms this meant that ions of all masses introduced into the trap over a period of time were present, and were then ejected to obtain a spectrum. The ions contained in the trap may be visualized as performing a series of ‘figure of eight’ orbits as shown below.

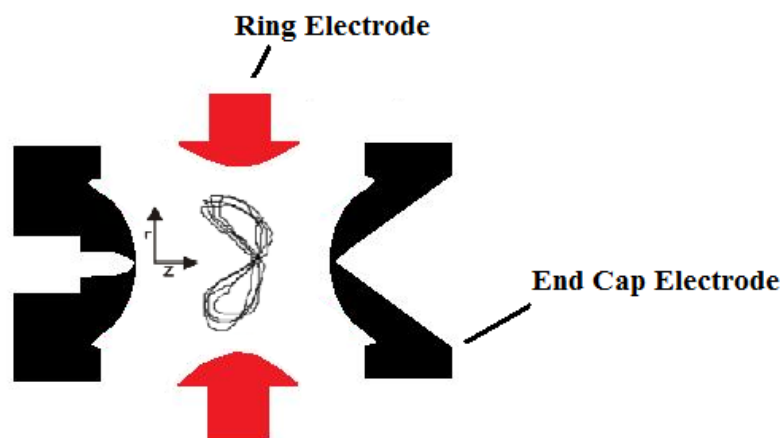


**Fig 2.2 Schematic Representation of a Quadrupole Ion Trap cut through the ring electrode, illustrating the directions of the r and z dimensions.**

Since trapped ions would tend to repel each other within the confines of the trap, this would lead to increasingly large trajectories and hence ion loss. To counter this problem, a background pressure of approximately  $10^{-4}$  Torr of Helium gas is maintained within the trap. As well as reducing the ion trajectory, collisions with the Helium are the basis for Collision Induced Dissociation (CID) experiments.

### 2.1.3 Mass Selective Axial Instability

The criteria for stable ion storage within a quadrupole ion trap are described by the Mathieu parameters  $a_z$  and  $q_z$  as detailed below.

$$a_z = \frac{-16ZeU}{m(r_0^2 + 2z_0^2)\Omega^2} \quad q_z = \frac{8ZeV}{m(r_0^2 + 2z_0^2)\Omega^2} \quad [\text{Eq 2.2}]$$

In the above equation for  $q_z$ ,  $Z$  represents the charge on the trapped ion,  $e$  is the elementary charge for one electron ( $1.602 \times 10^{-19}$  C),  $r_0$  and  $z_0$  refer to the dimensions of the trap as shown above,  $m$  is the mass of the ion,  $V$  is the amplitude of the RF frequency expressed in Volts and  $\Omega$  is the radial frequency ( $\text{rad s}^{-1}$ ).

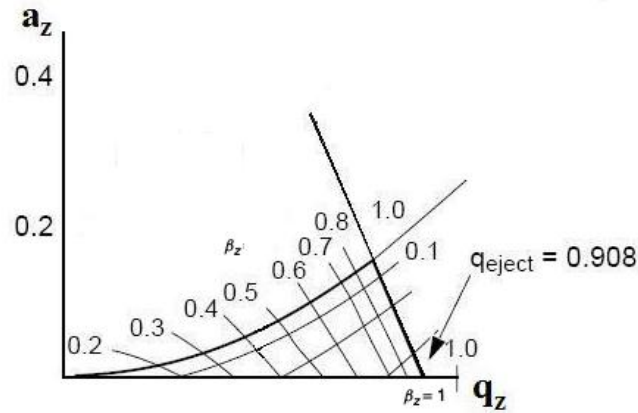


**Fig 2.3 Graph showing solutions of the above  $a_z$  and  $q_z$  equations. Ions for which these solutions lie within the cross hatched area have stable trajectories within the trap**

Ramping the RF amplitude will cause the  $q_z$  values for all ions within the trap to increase, until each reaches 0.908 where their stability is lost and they are ejected axially through the end cap electrodes. In this way a spectrum may be obtained as a function of the RF amplitude versus detected ion signal.

### 2.1.4 Resonance ejection

The secular frequency,  $f_z$ , at which an ion oscillates within a trap may be given by the equation;

$$f_z = \beta_z \nu / 2 \quad [\text{Eq 2.2}]$$

Each ion has its own secular frequency since a Radio frequency applied along the z axis must effect ions of differing masses, having different inertias, to greater or lesser extents. Knowing  $\beta_z$  and having supplied Radio frequency for a certain value of  $\nu$  it is then possible to determine at what secular frequency the chosen ion would oscillate at, and to apply a supplementary R<sub>f</sub> voltage to the end caps of the trap in order to resonantly excite this ion. In this way ions may acquire unstable trajectories without reaching the condition  $\beta_z = 1$  as described above. This process immediately makes possible MS/MS type experiments, a possible scheme is described below;

Ions are introduced to the trap. Initially all that fall within the selected  $q_z / a_z$  space have stable trajectories. Resonant excitation through the end caps is then used to expel all unwanted ions. Only ions of the desired m/z ratio are then present within the trap. The Rf voltage V (above, equation 2.1) and hence  $\beta_z$  is then altered to bring these ions in resonance with the supplementary voltage applied at the end caps. Product Ions may then be analysed by ejection at the mass stability limit.

The above points represent just one possible excitation and analysis scheme. Resonant ejection allows for the three-dimensional ion-trap to carry out repeated stages of tandem mass analysis in a time resolved manner. Briefly, undesired ions are resonantly ejected (broad spectrum of supplementary end-cap voltage frequencies at high amplitude), the ions corresponding to the m/z ratio of interest are then resonantly excited (narrow spectrum of frequencies, amplitude insufficient to

cause ejection, although sufficient kinetic energy is supplied to cause collision induced dissociation). Following resonant excitation the fragment ions produced may be analysed by resonant ejection once again. It is then possible to select another ion from the ionic fragments via the resonant ejection route, and carry out further stages of MS analysis.

### 2.1.5 Collision Induced Dissociation

Collision Induced Dissociation (CID), or Collision Activated Dissociation, describes the process of multiple collisions that an excited ion undergoes in the QIT with the background Helium gas.<sup>12</sup> While resonantly excited by the end cap radio frequency voltage the ions undergo a continuous acceleration and deceleration leading to a rate of approximately  $10^3$  collisions per second, with each thought to impart around 0.05eV of internal energy.<sup>13,14</sup> This situation is therefore different to the situation that pertains in a high energy collisional experiment where a small number of very high energy impacts would occur in a short space of time. The primary benefit of this is that the ion experiences activation akin to a thermal heating process, meaning that fragmentation occurs via the lowest energy pathway first. This collisional fragmentation process forms the basis for the majority of traditional gas phase studies carried out on GAG molecules as discussed in Chapter 1. In addition to CID carried out within linear quadrupoles

A CID curve consists of a plot of the applied supplementary end cap voltage used to effect resonance excitation versus the intensity of either the precursor or product ions.

Figure 2.4 demonstrates the utility of CID on a Finnegan LCQ mass spectrometer to study the fragmentation of  $\text{Cr}_2\text{O}_7^-$  to  $\text{Cr}_2\text{O}_6^-$  with the onset of fragmentation occurring at approximately 12 % of the 2.5 volts available on the instrument used. From this data we may assume neutral oxygen loss from the  $\text{Cr}_2\text{O}_7^-$  to be a major pathway, although loss of a singly negatively charged oxygen could not be comprehensively ruled out since its' product ions would be neutral, or too light in

mass to be detectable within the stability region for the instrument. CID curves represent plots of *relative* intensities for the isolated and product ions.

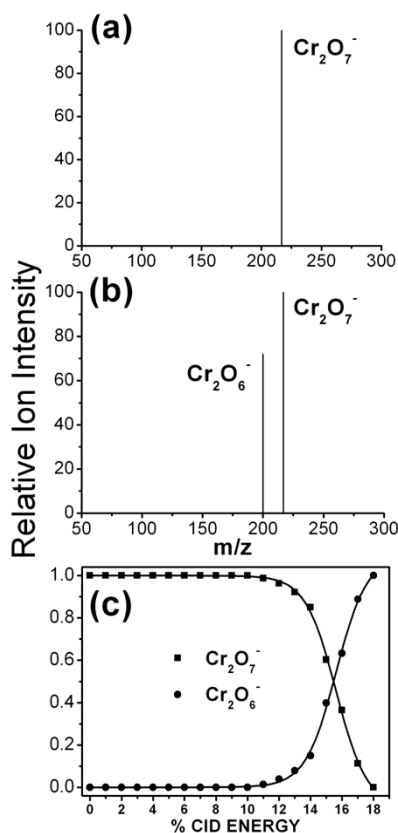


**Figure 2.4** An MS<sup>2</sup> experiment carried out in a quadrupole ion trap demonstrating (a) the isolation of Cr<sub>2</sub>O<sub>7</sub><sup>-</sup> and (b) and (c) its resonant excitation to produce Cr<sub>2</sub>O<sub>6</sub><sup>-</sup>

A chromatogram trace of the overall ion intensity in the trap will show that a significant total ion loss occurs as the percentage CID energy (given as a percentage of the maximum supplementary end cap voltage) increases. This is due to losses via resonant ejection and imperfect transmission from trap to detector. The kinetic energy supplied to a target molecule during CID is not well defined, and will naturally vary depending on the mass of the ion studied. This is in contrast to experiments carried out in linear quadrupole type instruments where ion beam energies may be accurately known and allow thermodynamic data on CID processes to be acquired.<sup>15</sup> It is generally accepted that where a relative energy of dissociation using CID is required, the ions studied should be within 100 atomic mass units of

each other and of the same charge.<sup>16</sup> Chapters 3 and 7 report experiments carried out using a Bruker-Daltonics Esquire 6000 quadrupole ion trap, while the data in Chapter 6 was recorded on a Thermo-Finnegan LCQ instrument. The essential layouts for these two mass spectrometers are identical to the schematic diagram shown in Figure 2.1.

## 2.2 Mass Analyzed Ion Kinetic Energy – MIKE

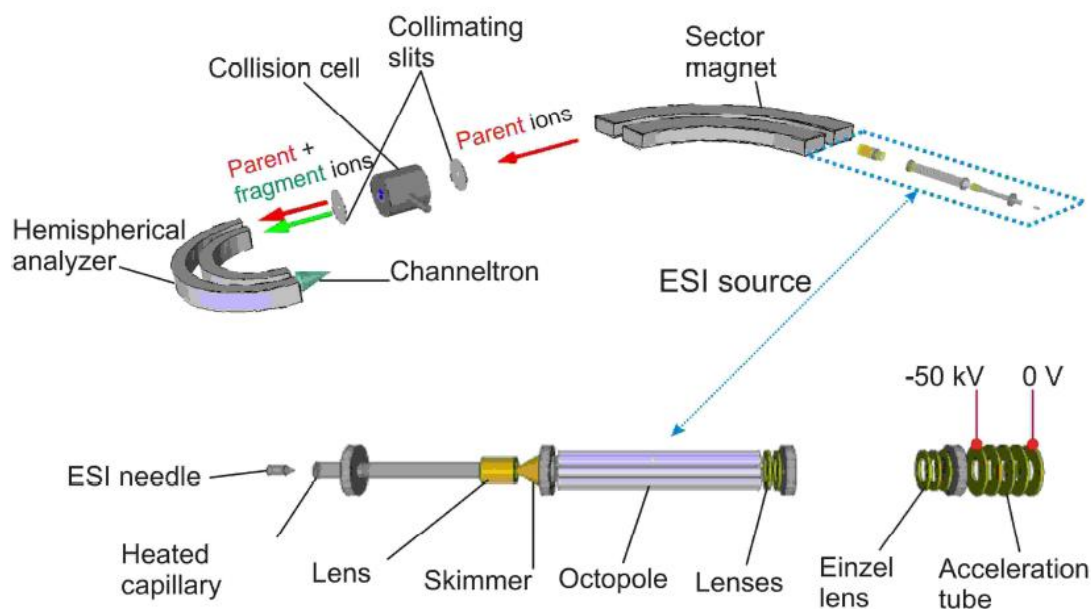


**Figure 2.5 Diagram of the Sep 1 high energy magnetic sector instrument.**

The high energy experiments described in Chapter 4 were conducted using the Sep 1 magnetic sector instrument located in the Department of Physics and Astronomy at the University of Aarhus. Figure 2.5 shows a schematic layout of the instrument which consists of an Electrospray ionisation source coupled to an acceleration tube with a potential difference of 50 kV. The accelerated ions are then separated by a 72° 2 meter radius sector magnet. The selected ions then enter a collision cell containing neon at approximately 0.2mTorr. An oven chamber is interfaced with the collision cell allowing for the introduction of Caesium gas if required for electron transfer studies. Mass analysed ion kinetic energy scans of the fragment ions are then

performed using a 15 cm radius 180° electrostatic analyser coupled to a channeltron ion detector.<sup>17</sup>

The Sep1 instrument has been previously used to study a wide range of high energy collision induced processes. These have included propensity of electron transfer from Caesium to Iridium halide complexes,<sup>18</sup> and the study of the gas phase fragmentation pathways for amino acid analogues.<sup>19</sup> The instrument may also be used in ‘two-step’ electron transfer studies, an example of which is electron transfer from Caesium to a peptide producing a radical and neutral fragments. Neutral peptide fragments may then accept an electron during a second collision event, allowing their detection.<sup>20</sup>

### 2.3. Ab initio and Molecular Mechanics

#### **2.3.1 Quantum Mechanical versus Molecular Mechanics Methods**

Quantum chemistry methods involve an attempt to find solutions to the Schrödinger equation;

$$\mathbf{H}\Psi = E\Psi$$

Unfortunately exact solutions are practically impossible for all but the smallest (i.e. one electron) systems without making certain mathematical approximations. One of these is the Born-Oppenheimer Approximation, wherein the electrons are judged to move at a far greater speed than that of the nuclei and so nuclear and electronic motion may be decoupled. The Adiabatic Approximation means that interactions between different electronic states are ignored, meaning that only the properties of the ground state are taken into account. At a very basic level solving the equation can be thought of as providing trial wave-functions upon which the Hamiltonian operator  $\mathbf{H}$  acts to return an energy for the system. The lower the returned energy calculated the closer to the ‘true’ wave-function the approximation is likely to be. True *ab initio* methods utilize only fundamental constants such as the speed of light,

Plank's constant, the mass and charge of electrons along with a chemical structure in order to compute chemical properties. Hartree-Fock Theory is possibly the simplest of these methods, although this technique completely ignores the effects of electron correlation. Moller-Plesset Perturbation Theory (MP2 in this Thesis) involves a calculation where the electrons are initially treated as in the ground state. Their wave-functions are then calculated in the excited state and the ground and excited state wave-functions combined to give a better account of electron interaction.

Molecular mechanics relies on Newtonian physics where atoms may be thought of as spheres bound together by 'springs' acting as described by Hooks Law;

$$F = -kx$$

Where  $F$  is the restoring force,  $x$  is the displacement and  $k$  is the force constant. These 'springs' are interaction potentials between atoms that have been determined from ab initio calculations and physical data, a collection of the constants that describe them are known as a Force Field. For a given set of atomic interactions this will include bonding, angle and dihedral force terms, in addition to terms to describe van der Waals and Electrostatic forces. It is important to note that electronic effects are not treated explicitly. Molecular Mechanics relies on relatively simple mathematical formulae meaning that extremely large molecular systems may be studied with relatively modest computational resources. In order to rigorously study a system it is necessary to have parameterised a force field that is suitable for all of the atom types and combinations of atoms within the molecule. Given the enormous size of the possible 'molecule space', that is to say the vast combinations of atoms possible in even small systems, Force Fields are in many cases using terms from known systems to simulate similar ones.

### **2.3.2 Force Fields and Carbohydrates**

Molecular mechanics represents the least computationally expensive route to obtaining information about the conformations of a bio-molecule. Even relatively

small monosaccharides can be associated with a very large three dimension space, with one study identifying more than 700 distinct possible conformations for one chair system alone.<sup>21</sup> The size and conformational flexibility of sulphated carbohydrates means that wavefunction-based studies are restricted to smaller examples of these sugars, and where larger analogues are examined, functionals and basis sets must be scaled back accordingly.<sup>22,23,24,25,26</sup> A great variety of force fields are available depending on the system to be studied.<sup>27,28</sup> A recent study into the suitability of different force fields for the analysis of disaccharide molecules found that older computer codes could often compete favourably with more modern simulations.<sup>29</sup> This study examined selected neutral sugar disaccharides predicted hydroxyl and glycosidic torsional angles and compared the results to x-ray crystal structures. The results showed that the GROMOS,<sup>30</sup> GLYCAM06,<sup>31</sup> OPLS-2005<sup>32</sup> and CSFF<sup>33</sup> codes produced results that were broadly similar and in good agreement with the known crystal structures. It is interesting to note that a significantly older force field, MM3 also produced data that compared well with the more modern methods reviewed.<sup>34</sup> Carbohydrate parameterization is a very active field of contemporary research with recent work involving additions for the CHARMM force field. These have included high-level wavefunction based calculations to support the development of this code for furanose rings, hexopyranoses and acyclic species.<sup>35,36,37</sup> While the calculations supporting the development of these force fields are at a high level they are again all limited to relatively small structures and have been restricted to neutral examples.

Jin et al have used the Parm99 force field running within Amber 7 with the Glycam\_2000 extension to model heparin anionic disaccharides in the gas phase<sup>38</sup>. This study required the use of parameters originally designed for phosphates from Parm99 to be incorporated to fill in for those not adapted for sulphates in the work of Huige and Altona.<sup>39</sup> Work to resolve the structures of N-Linked Glycans for a similar purpose has used Homan's carbohydrate parameters in the Amber suite of software, although this code was not designed for sulphated sugars.<sup>40</sup> At the present time there is no force field available to explicitly model sulphated sugars and this is

evidenced by the lack of large-scale molecular mechanics based simulations in the literature for Heparin.<sup>41</sup>

### 2.3.3 Molecular Mechanics – Spartan 04 and Merck Molecular Force Field 94

In this thesis, molecular mechanics is used as the basis for providing initial geometries for GAG and small inorganic molecular systems. As discussed above, the lack of a suitable force field for GAG molecules means that the Merck Molecular Force Field 94 (MMFF 94) implemented by Spartan 04 is used as a route to geometries that can be refined at a higher level of theory.<sup>42</sup> MMFF 94 was originally designed for the study of the interactions of proteins with a wide range of ligands. Due to this demanding task, the parameters for this force field were primarily drawn from *ab initio* calculations, and it was intended at the time of compilation that the code would be comparable to Allinger's MM3 work mentioned above. MMFF 94 has recently been assessed to provide the best performance from amongst the traditional fixed charge force fields for small charged peptides.<sup>43</sup>

Spartan uses an iterative energy minimization procedure wherein bond angles, torsions and lengths are subject to rotations of discrete values coupled to energy minimization. The calculations use a Monte Carlo based system to explore the potential energy surface of the system, starting from what is typically a high-energy conformation and moving lower in energy. This simulated annealing method uses a temperature ramp of the form shown below to generate random structures.

$$T = T_{final} + (T - T_{final}) \left(1 - \frac{I}{I_{max}}\right)^3 \quad [\text{Eq 2.3}]$$

Where T is the temperature, I is the number of iterations. Spartan uses a default starting temperature of 5000K moving down to 300K at completion. At lower temperatures the molecule is less inclined to move out of lower energy conformations and thus the more localised minima are explored. The number of

iterations may vary based upon the structural flexibility of the molecule, however, the maximum number of low energy structures is set to 100 by default. Low-energy conformers are judged to be those less than  $10 \text{ kcal mol}^{-1}$  above that of the lowest energy structure found.<sup>44,45</sup>

In order to more thoroughly sample the three dimensional space associated with the Iduronate molecule studied in Chapter 5 it was necessary to constrain the sugar ring into a  ${}^1C_4$  conformation prior to running the Spartan simulation. This was necessary due to the Merck force field's inability to generate this well known conformation, although both  ${}^4C_1$ ,  ${}^2S_0$  and  ${}^1S_5$  conformations were produced without further difficulty. Sugar ring conformations are discussed in further detail in Chapter 5.

### 2.3.4 Functional and Basis Set selection

The electronic structure techniques available for studying carbohydrates may be broadly classified as semi-empirical, *ab initio* and the density functional methods. Csonka *et al* have made a recent detailed study into the choice of functional and basis set for multiple conformations of a test set of three neutral carbohydrates.<sup>45</sup> Semi-empirical methods such as AM1 and PM3 are poorly suited to the study of carbohydrate compounds when compared to the hybrid density functional B3LYP.<sup>47,48</sup> They also note that the lack of electron correlation in Hartree-Fock methods causes generally unreliable results for carbohydrates, and while basis set superposition errors may sometimes cancel out this effect, it is not a reliable technique when larger sets are used.<sup>49</sup>

As discussed in Chapter 1, B3LYP is a popular choice for the study of large carbohydrate systems due to its computational efficiency.<sup>50</sup> Previous work to determine the best choice of basis set in the study of L-fucose used B3LYP/6-311++G\*\* results as a reference and compared the relative energies calculated.<sup>51</sup> Both 6-31G\* and 6-31G\*\* were suggested to be very poor choices when coupled with B3LYP. The use of diffuse functions was found to be crucial for heavy atoms although not necessary on hydrogen atoms where density functional methods are used.

A more recent study of a wide range of functionals and basis sets used the high level MP2/aug-cc-pVTZ method as a reference that takes into account the effects of electron correlation.<sup>46</sup> Relative energies calculated at this level were in good agreement with results obtained using the hybrid density functional MO5-2X. It was notable that this method outperformed B3LYP when compared to the reference calculations. The PW91PW91 functional has been previously shown to compare well with MP2 in systems where electron correlation plays a major role.<sup>52,53,54,55</sup>

The GLC4 test set used was selected by Csonka because it contains a high proportion of intramolecular hydrogen bonding interactions, and these are highly likely to be a key feature of GAG conformers due to their extensive numbers of OH groups.<sup>46</sup> It should be emphasised that the systems in that study were neutrals, and that a similarly in depth study of anionic structures is not available at present.

The methods chosen to study the anionic iduronate (2-O-sulfo- $\alpha$ -L-iduronate) molecule in Chapter 5 are therefore MP2, B3LYP, PW91PW91 and the newer functional MO5-2X using the 6-31++G\*\* basis set. All starting geometries were generated from the Spartan 04 program as described above. Calculations were carried out using GAUSSIAN 03, with the default convergence criteria applied to the geometry optimizations.<sup>52</sup> Vibrational frequencies were calculated for all the optimized structures to ensure that true stationary points were generated.

Chapter 6 presents an investigation of the relative barrier heights for the dissociation of the dichromate dianion via ionic fragmentation and electron loss. The B3LYP functional was used along with the LANL2DZ double- $\zeta$  basis set,<sup>57</sup> since this has been found to give reliable computational results for  $\text{Cr}_2\text{O}_7^{2-}$ .<sup>58</sup> The Gaussian 03 SCAN keyword was used to increase the chromium to central oxygen bond length in 0.5 Angstrom steps as the relative energies were recorded. In order to model the loss of an electron, the point-charge model of Dreuw and Cederbaum was used.<sup>59</sup> The point-charge model was found to describe the short-range interaction between the electron and the monoanion poorly and so the barrier height for electron detachment

---

was calculated as the sum of the  $\text{RCB}_{\text{ed}}$  (outer) and the vertical detachment energy (VDE). The VDE was calculated as the difference in energy between the molecule at the two different charge states with identical geometries.

Chapter 7 presents a study where the complete active space self consistent field (CASSCF) method with the LANL2DZ double- $\zeta$  basis set running in the MolPro<sup>60</sup> software suite is used to investigate the potential energy surfaces for ionic fragmentation of the  $\text{Re}_2\text{X}_8^{2-}$  ( $\text{X} = \text{Cl}, \text{Br}$ ) series of compounds. This work was carried out by Dr M.G.D. Nix and further computational details are given within the Chapter.

References

1. K. Markides, A. Gräslund, "Advanced information on the Nobel Prize in Chemistry 2002"
2. G. Taylor, Proc. Roy. Soc. London. Ser. A 280 (1964) 383
3. Rayleigh, Philos. Mag. 14 (1882) 184
4. M. Dole, L.L. Mack, R.L. Hines, R.C. Mobley, L.D. Ferguson, M.B. Alice, J. Chem. Phys. 49 (1968) 2240
5. J.V. Iribarne, B.A. Thomson, J. Chem. Phys. 64 (1975) 2287
6. S. Nguyen, J. B. Fenn, Proc. Natl. Acad. Sci. USA, 104 (2007) 1111
7. J.B. Fenn, T. Nohmi, J. Am. Chem. Soc. 114 (1992) 3241
8. J.F. de la Mora, Anal. Chim. Acta. 406 (2000) 93
9. R.J. Champargue, J. Phys. Chem. 88 (1984) 4466
10. W. Paul, Angew. Chem. Int. Ed. Engl. 29 (1990) 739
11. G.C. Stafford, P.E. Kelley, J.E.P. Syka, W.E. Reynolds, J.F.J. Todd, Int. J. Mass Spectrom. Ion Proc. 60 (1984) 85
12. A. Maccoll, Int. J. Mass Spectrom. Ion Process. 156 (1997) xviv-xxi
13. Practical Aspects of ion-trap Mass Spectrometry, Volumes I & II, eds. R. E. March and J. F. J. Todd, CRC Press, Boca Raton, 1995
14. K. J. Hart, S. A. McLuckey, J. Am. Soc. Mass Spectrom. 5 (1994) 250
15. P.B. Armentrout, J. Am. Soc. Mass Spectrom. **2002**, 13, 419
16. M. Satterfield, J. S. Brodbelt, Inorg. Chem. 40 (2001) 5393
17. J.U. Andersen, P. Hvelplund, S. Brøndsted Nielsen, S. Tomita, H. Wahlgreen, S.P. Møller, U.V. Pedersen, J.S. Forster, T.J.D. Jørgensen, Rev. Sci. Instrum. 73 (2002) 1284
18. R.M. Burke, W.E. Boxford, S. Panja, S.B. Nielsen, C.E.H. Dessent, Chem. Phys. Lett. 442 (2007) 201
19. J. A. Wyer, L. Feketeová, S.B. Nielsen, R.A.J. O'Hair, Phys. Chem. Chem. Phys. 11 (2000) 8752
20. P. Hvelplund, B. Liu, S.B. Nielsen, S. Panja, J.-C. Pouilly, K. Støchkel, Int. J. Mass Spec. 263 (2007) 66
21. C. J. Cramer, D. G. Truhlar, J. Am. Chem. Soc. 115 (1993) 5745
22. M. Remko, C-W von der Lieth J. Chem. Inf. Model. 46 (2006) 1194
23. M. Remko C-W von der Lieth J. Phys. Chem. A 111 (2007) 13484
24. M. Remko, M. Swart, F. Matthias-Bickelhaupt, J. Phys. Chem. B 111 (2007) 2313
25. M. Hricovini, Carbohydr. Res. 341 (2006) 2575
26. M. Hricovini, F. Bizik, Carbohydr. Res. 342 (2007) 779
27. C. J. Cramer, Essentials of Computational Chemistry: Theories and Models, Wiley, Chichester, 2002
28. F. Jensen, Introduction to Computational Chemistry, Wiley, Chichester, 1999
29. C. A. Stortz, G.P. Johnson, A. D. French, G. I. Csonka, Carbohydr. Res. 344 (2009) 2217
30. J.E.H. Koehler, W. Saenger, W.F. van Gunsteren, Eur. Biophys. J. 15 (1987) 97
31. K.N. Kirschner, A.B. Yongye, S.M. Tschampel, J. González-Outeriño, C.R. Daniels, B.L. Foley, R.J.J. Woods, J. Comput. Chem. 29 (2008) 622

32. G.A. Kaminski, R.A. Friesner, J. Tirado-Rives, W.J.J. Jorgensen, *J. Phys. Chem. B* 105 (2001) 6474
33. M. Kuttel, J.W. Brady, K.J.J. Naidoo, *J. Comput. Chem.* 23 (2002) 1236
34. N.L. Allinger, Y.H. Yuh, J.-H Lii, *J. Am. Chem. Soc.* 111 (1989) 8551
35. E. Hatcher, O. Guvench, A.D. MacKerell, *J. Phys. Chem. B* 113 (2009) 12466
36. O.Guvench, E. Hatcher, R.M. Venable, R.W. Pastor A.D. MacKerell, *J. Chem. Theory Comput.* 5 (2009) 2353
37. E. R. Hatcher, O. Guvench, A.D. MacKerell, *J. Chem. Theory Comput.* 5 (2009) 1315
38. L. Jin, P. E. Barran, J. A. Deakin, M. Lyon and D. Uhrin, *Phys. Chem. Chem. Phys.* 7 (2005) 3464
39. C. J. M. Huige, C. Altona *J. Comp. Chem.* 16 (1995) 56
40. S.W. Homans, *Biochemistry* 29 (1990) 9110
41. C.F. Becker, J.A. Guimaraes, H. Verli, *Carbohydr. Res.* 340 (2005) 1499
42. B.J. Deppmeier, A.J. Driessen, T.S. Hehre, W.J. Hehre, J.A. Johnson, P.E. Klunzinger, J.M. Leonard, W.S. Ohlinger, I.N. Pham, W.J. Pietro, J. Yu, *PC Spartan Pro*, Wavefunction, Inc. Irvine, CA, 2000
43. J. Kaminsky, F.J. Jensen, *J. Chem. Theory. Comput.* 3 (2007) 1774
44. SPARTAN Customer Support, Wavefunction, Inc
45. Spartan '04 Windows: Tutorial and Users guide, Wavefunction Inc. Irvine, 2001-2003
46. G.I. Csonka, A.D. French, G.P. Johnson, C.A. Stortz, *J. Chem. Theory Comput.* 5 (2009) 679
47. G.I. Csonka, J.G. Angyan, *J. Mol. Struct. (THEOCHEM)* 393 (1997) 31
48. G.I. Csonka, I.G. Csizmadia, *J. Comput. Chem.* 18 (1997) 330
49. S.E. Barrows, F.J. Dulles, C.J. Cramer, A.D. French, D.G. Truhlar, *Carbohydr. Res.* 276 (1995) 219
50. P.J. Stephens, F.J. Devlin, C.F. Chabalowski, M.J. Frisch, *J. Phys. Chem.* 98 (1994) 11623
51. G.I. Csonka, *J. Mol. Struct. (THEOCHEM)* 584 (2002) 1
52. S. Tsuzuki, H. P. Lüthi, *J. Chem. Phys.* 114 (2001) 3949
53. Y. Yang, W. Pan, W. Yang, *J. Chem. Phys.* 107 (1997) 7291
54. T.A. Wesolowski, O. Parisel, Y. Ellinger, J. Weber, *J. Phys. Chem. A* 101 (1997) 7818
55. M.D. Patey, C.E.H. Dessent, *J. Phys. Chem. A* 106 (2002) 4623
56. M.J. Frisch, et al. (2004) Gaussian 03, Revision C.01, Gaussian, Inc., Wallingford CT
57. P. J. Hay, W. R. Wadt, *J. Chem. Phys.* 82 (1985) 299
58. J. Mestres, M. Duran, P. M. Zarza, E. M. de la Rosa, P. Gili, *Inorg. Chem.* 32 (1993) 4708
59. A. Dreuw, L. S. Cederbaum, *J. Chem. Phys.* 112 (2000) 7400
60. MOLPRO, version 2006.1, a package of ab initio programs, H.-J. Werner, P.J. Knowles, R. Lindh, F.R. Manby, M. Schütz, P. Celani, T. Korona, G. Rauhut, R.D. Amos, A. Bernhardsson, A. Berning, D.L. Cooper, M.J.O. Deegan, A.J. Dobbyn, F. Eckert, C. Hampel and G. Hetzer, A.W. Lloyd, S.J.

McNicholas, W. Meyer and M.E. Mura, A. Nicklass, P. Palmieri, R. Pitzer,  
U. Schumann, H. Stoll, A.J. Stone, R. Tarroni and T. Thorsteinsson

## Chapter 3

### Investigating the role of charge state and counterion complexation in the fragmentation of Heparin disaccharides

#### 3.1 Introduction

The volume of known GAG to protein interactions is extensive and their role as mediators of complex biological mechanisms makes them ideal candidates for structural elucidation by mass spectrometry.<sup>1,2,3,4</sup> The principal advantages of Mass Spectrometry for GAG analysis are accuracy, speed and sensitivity. Whereas NMR based analysis may provide detailed three dimensional structural information, it is hampered by the requirement for significant sample volumes.<sup>5</sup> Heparin sugars exist as linear chains consisting of a hexuronic acid followed by a glucosamine. These disaccharide subunits display complex patterns of sulphation and N-acetylation in addition to epimerisation at the hexuronic acid.<sup>6</sup> The study of this class of sugars is complicated by the presence of isomers, low sample concentrations and the need to retain fragile sulphate groups intact if useful structural information is to be obtained from fragment ions.<sup>7</sup> Early tandem MS studies demonstrated the relative ease with which sulphate groups are lost, and while significant numbers of diagnostically useful glycosidic fragments were produced, cross ring fragments required to unambiguously locate the positions of sulphate groups proved more elusive.<sup>8,9,10,11</sup> An important result of work at this time was that the charge state of the precursor ions studied had a profound effect on the numbers of glycosidic fragments generated. Via collision induced dissociation (CID), the higher the number of negatively charged sulphate groups a precursor contained, the less likely sulphate losses were to occur with a concurrent increase in glycosidic products.<sup>8</sup>

Additionally, the pairing of calcium counter ions with the negatively charged sugars was an effective means to prevent sulphate loss.<sup>8</sup>

Amster et al have pioneered the use of Electron Detachment Dissociation (EDD) in the analysis of GAG tetrasaccharides and found the diagnostic fragments produced, i.e. those resulting from cross ring and glycosidic bond breakages, to compare highly favourably with IRMPD and CAD techniques.<sup>12</sup> This method was then shown capable of distinguishing between the Glucuronic and Iduronic epimers through the absence of marker fragments in the Iduronic acid mass spectrum.<sup>13</sup> The use of EDD on longer chain Dermatan Sulphate examples has produced fragment rich data for chains composed of four disaccharide subunits, although the losses of neutral sulphate and water molecules are evidenced in highly complex mass spectra.<sup>14</sup> Experiments to determine the effect of increasing chain length and charge state on the production of product ions by EDD have shown no decrease in the efficiency of the overall fragmentation process.<sup>15</sup> An increase in negatively charged sulphate groups will however lead to a higher proportion of EDD fragments where the sulphate group has been lost. The utilization of higher charge state precursor anions allows for an increase in electron detachment events occurring at carboxylate groups, although a concurrent fall in the numbers of glycosidic and cross ring fragments is observed.<sup>16</sup> An alternative, but conceptually related method, using high energy collision induced dissociation is discussed in Chapter 4.

While EDD techniques represent a promising solution for the complete sequencing of GAG chains, compositional profiling of Heparin mixtures is of importance where the purity of pharmaceutical products is concerned and in determining the relative amounts of disaccharides present in a mixture.<sup>17</sup> The MS<sup>2</sup> and MS<sup>3</sup> fragmentation patterns of isomeric disaccharides are typically sufficient to determine which isomers are present.<sup>7,18</sup> Quantitative information on a mixture may be obtained using total enzymatic digestion to release the disaccharide content of a chain.<sup>18,19,20,21</sup> This method involves the use of pure isomeric standards to select product ions and to determine their contribution to the total ion current. Once the

contribution of each isomer is known, a mixture of the two may be analysed for the intensity of these product ions and a system of equations used to reveal their ratio in the mixture. An concise summary of the technique is given in reference 20, where UA-GalNAc4S and UA-GalNAc6S both display product ions as  $m/z = 282$  and 300. Knowing the individual ion currents for these fragments in the isolated standards allows the equations

$$1.62*A + 57.1*B = C_{282} \quad [3.1a]$$

$$74.1*A + 2.05*B = C_{300} \quad [3.1b]$$

to be formed and hence the ratios of A and B, or UA-GalNAc4S and UA-GalNAc6S present in a mixture may be calculated once the ion current  $C_{282}$  and  $C_{300}$  is measured. The wider applications of this and related techniques depend on a detailed knowledge of the fragmentation pathways of disaccharide ions to be studied.

The isolation of pure samples of GAGs from biologically relevant sources is a non-trivial task and may require mass spectrometric analysis to be performed at low signal concentrations. Detailed knowledge of the fragmentation pathways of sulphated disaccharides will assist in the selection of potentially suitable product ions for their identification where the possibility of isomerism and contaminants exists. To this end, this study examines the effects of charge state and counter ion complexation on the low energy fragmentation pathways of the IH, IIS and IIS isomeric disaccharides of Heparin shown in figure 3.1, using a 3D quadrupole ion trap.

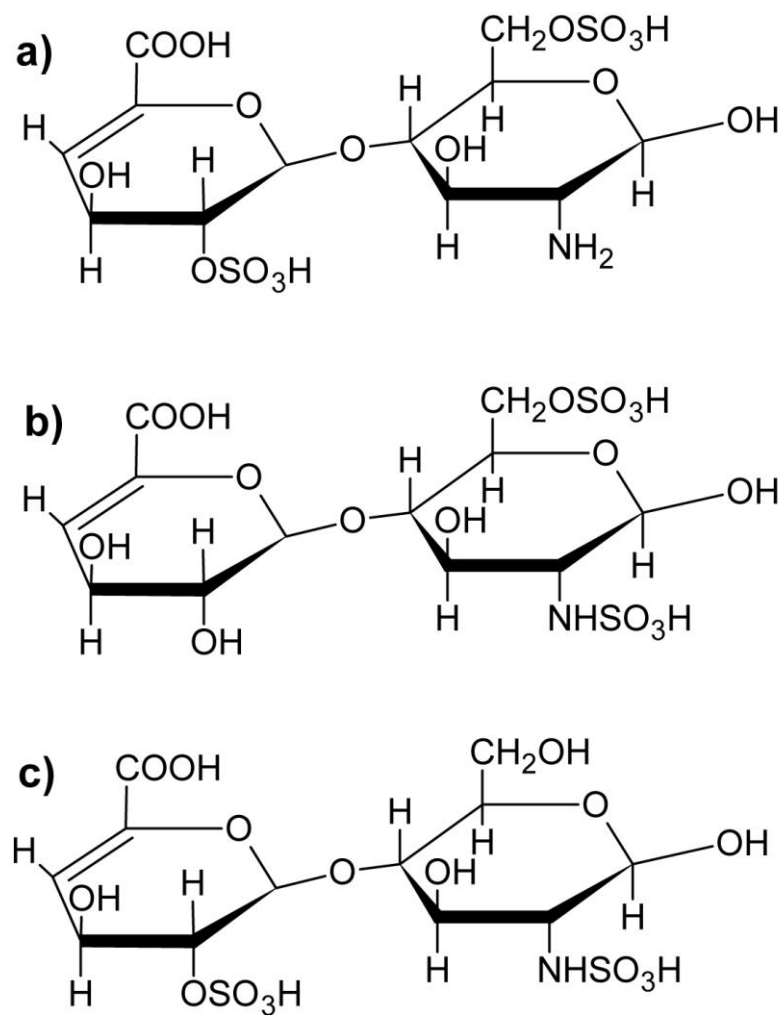


**Fig. 3.1** The chemical structure of the three Heparin derived glycosaminoglycans disaccharides studied in this chapter. a) IH,  $\alpha$ -DUA-2S-[1 $\rightarrow$ 4]-GlcN-6S, b) IIS,  $\alpha$ -DUA-[1 $\rightarrow$ 4]-GlcNS-6S and c) IIS  $\alpha$ -DUA-2S-[1 $\rightarrow$ 4]-GlcNS

## 3.2 Experimental Methods

Resonance excitation collision-induced dissociation (CID) was used to generate fragments from isolated anionic disaccharides and their counterion complexes. Experiments were performed as described in Chapter 2, using a Bruker Daltonics Esquire 6000 Electrospray Ionization (ESI) quadrupole ion-trap mass-spectrometer run in negative ion mode to record mass spectra and generate collision induced dissociation curves. CID energies are quoted as a percentage of 2.5 volts used for the resonance excitation step and ion intensities are quoted relative to the most intense peak in the spectrum in all cases. Signal optimization was performed using the instrument's automatic tuning feature, with the ESI needle biased at 4.2 kV and the capillary temperature set to 100°C. All disaccharide salts were purchased from Sigma Aldrich as sodium salts and sprayed as 10<sup>-4</sup>M solutions in Methanol. Lithium and Potassium counter ion complexes were generated via the addition of single drops of a 10<sup>-4</sup>M LiCl and KCl solution to 2.5ml of the above salt solution until the desired complex peaks were observed to be stable within the mass spectrum.

## 3.3 Results and Discussion

### **3.3.1 Initial mass spectra of sodium salts**

In this chapter, the fragment nomenclature first suggested by Domon and Costello<sup>23</sup> is adopted. This labelling scheme is illustrated in Figure 3.2. Figure 3.3 shows the initial MS<sup>1</sup> mass spectra for the three disaccharides studied in this chapter. In each case the doubly deprotonated [M-2H]<sup>2-</sup> (m/z = 247.4) and triply deprotonated [M-3H]<sup>3-</sup> (m/z = 164.7) species are present at high intensity, in addition to the single sodium complex of [M-3H]<sup>3-</sup> (m/z = 258.5). In the absence of isolation and resonance excitation, the IH disaccharide is the only species to display a significant

degree of fragmentation, producing a peak at  $m/z = 218$  which can be attributed to the  $^{0,2}A_2^{2-}$  fragment.

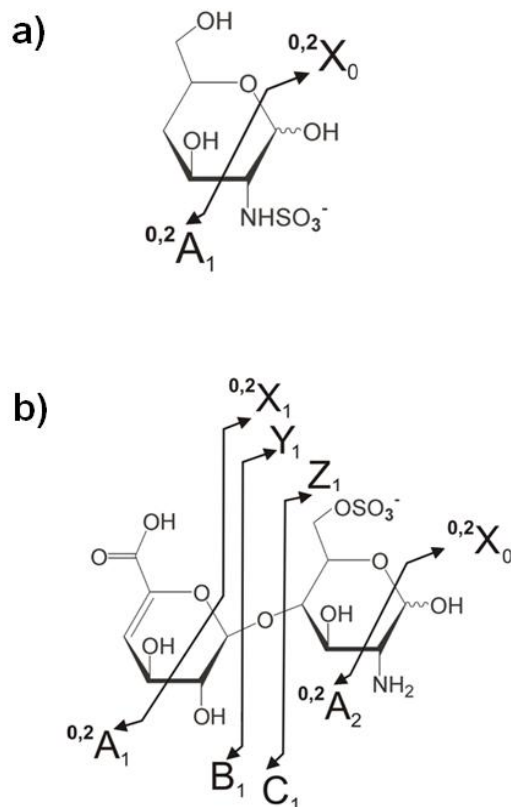


**Fig. 3.2** Fragment labelling scheme used in this work for a) monosaccharide and b) disaccharides. (This follows the scheme of Domon and Costello<sup>22</sup>.) The A, B and C labels are used to indicate a fragment containing a non-reducing end of the GAG, while X, Y and Z denote fragments which include the reducing end of the sugar. (The reducing end is defined as the ring with a C1 carbon not involved in a glycosidic bond.)

The associated  $^{0,2}X_0$  fragment is probably lost as a neutral due to its lack of a suitable site to accommodate a negative charge. Water losses from the  $[M-3H]^{3-}$  peaks are observed for both the IH and IIS species although not for the IIS species to any significant extent.

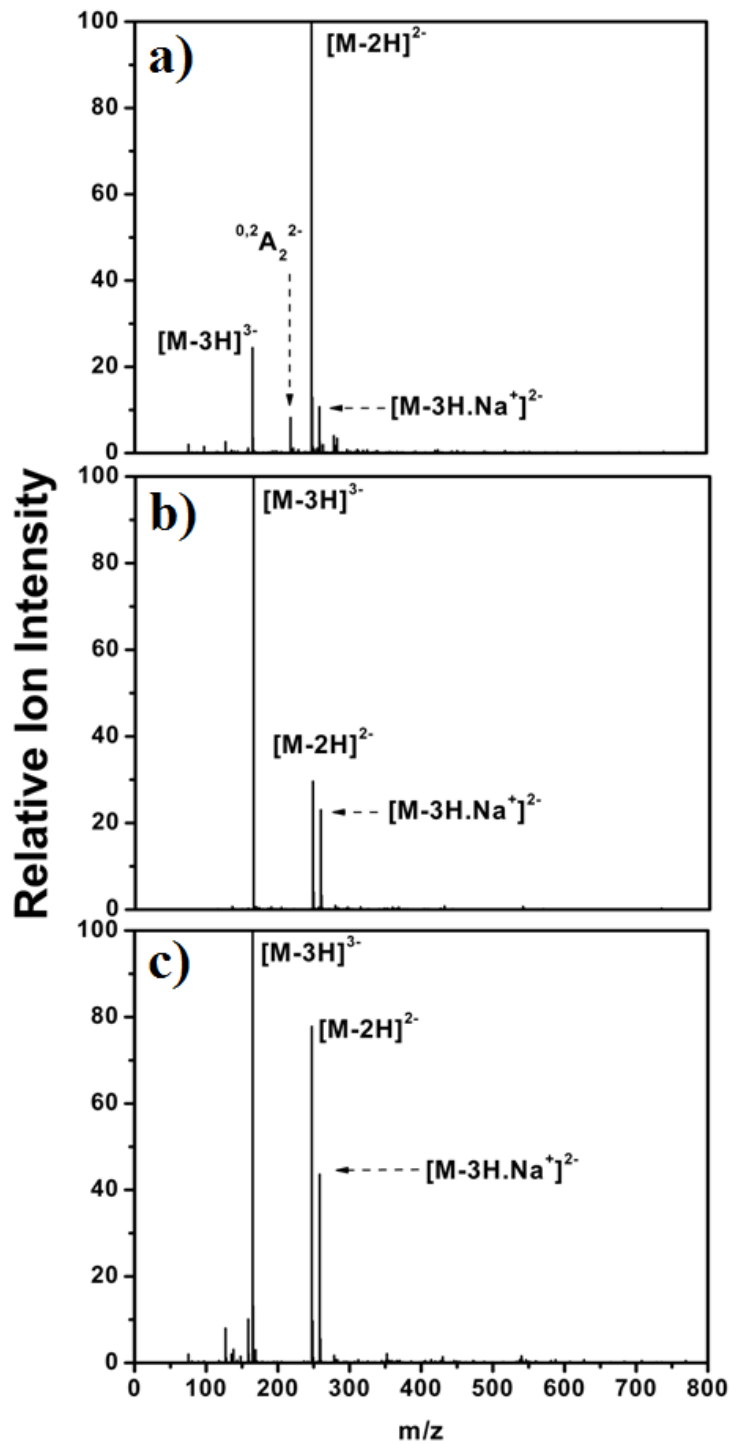


Fig. 3.3 MS<sup>1</sup> mass spectra of a) IH, b) IIS and c) IIS sprayed from sodium salts in methanol yielding a mixture of negative charge states and counterion complexes.

### 3.3.2 MS<sup>2</sup> on Heparin Disaccharide Dianions

The dianionic forms of IH, IIS and IIS have been previously studied using low energy collisions,<sup>7</sup> and are included here to allow for comparison with results at higher charge states and with counter ion complexes. Figure 3.4 (a) below shows the resulting MS<sup>2</sup> mass spectra of the dianionic forms of IH recorded at 8% CID energy. The major product peak is <sup>0,2</sup>A<sub>2</sub><sup>2-</sup> in agreement with previous analysis which has shown cross ring fragmentation to be the dominant pathway for low energy CID of this species.<sup>7</sup> Peaks present at m/z = 80 and 97, coupled with the lack of evidence of a fragment incorporating a COO<sup>-</sup> group strongly suggest that the sulphate side groups are the deprotonated ion sites for this sugar. This point is discussed further in Chapter 4. Loss of water from the precursor dianion is shown by production of a fragment at m/z = 239. A full summary of assigned product ions for the three dianionic species is given in Table 3.1.

Figure 3.4 (b) displays the 8% CID energy mass spectra for IIS. It is immediately apparent that a significantly larger number of product fragment ions are produced when compared to the IH result. In addition to the singly charged <sup>0,2</sup>A<sub>2</sub> fragment, the partner <sup>0,2</sup>X<sub>0</sub> fragment is visible due to the presence of the sulphate group on the second carbon atom of the reducing ring. The glycosidic bond breakage fragment Y<sub>1</sub> is present as both a singly and doubly negatively charged species, m/z = 338 and 169 respectively, indicating the presence of charges on both sulphate groups attached to the reducing ring. Both the B<sub>1</sub> (m/z = 157) and <sup>0,2</sup>A<sub>1</sub> (m/z = 115) singly charged-fragments are present, which suggests the COOH group on the non-reducing sugar ring is deprotonated in the parent ion. The peak at m/z = 300 is assigned to <sup>0,2</sup>X<sub>1</sub>-SO<sub>3</sub> and neutral water loss is again observed from the parent.

Figure 3.4 (c) shows the 8% CID energy MS<sup>2</sup> mass spectrum for IIS. Again, in contrast to the IH result, the spectrum contains a much higher proportion of product ions, with <sup>0,2</sup>A<sub>2</sub> and <sup>0,2</sup>X<sub>0</sub> singly negatively charged fragments are present as the most intense peaks at m/z = 357 and 138 respectively. Neutral loss of an SO<sub>3</sub> group as well as water loss from the parent are also observed. It is of interest to note that <sup>0,2</sup>A<sub>1</sub><sup>-</sup> is

also present as a fragment ion, consistent with the deprotonation of the carboxylate group in the parent ion.

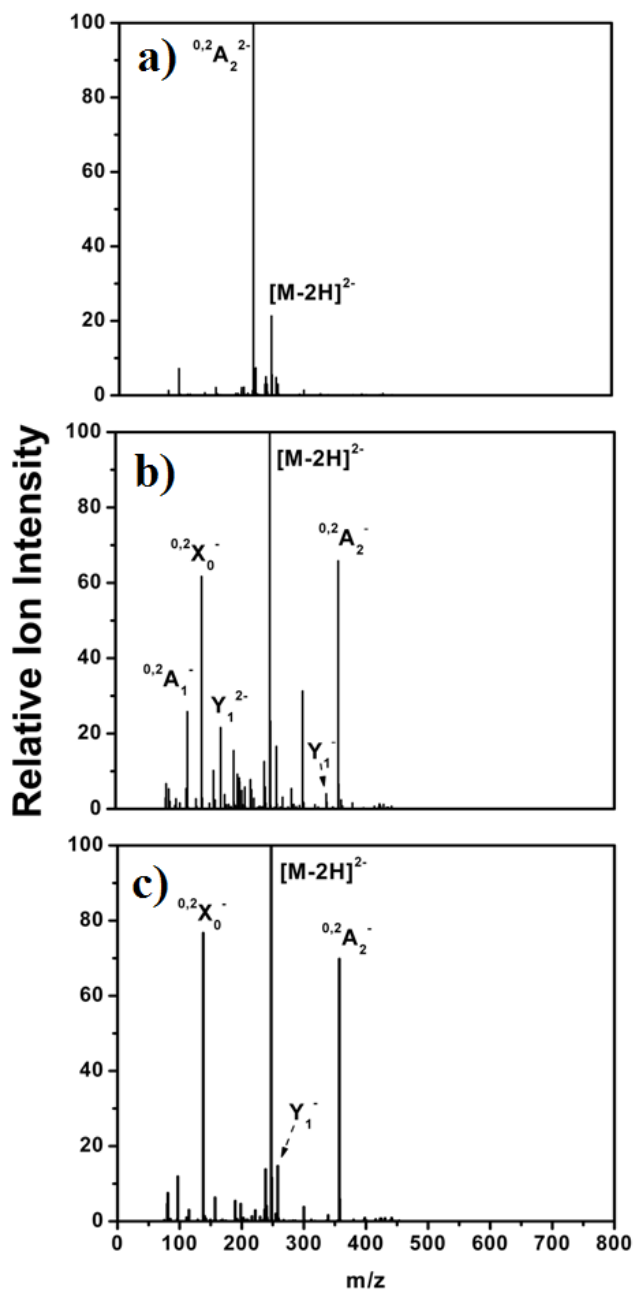


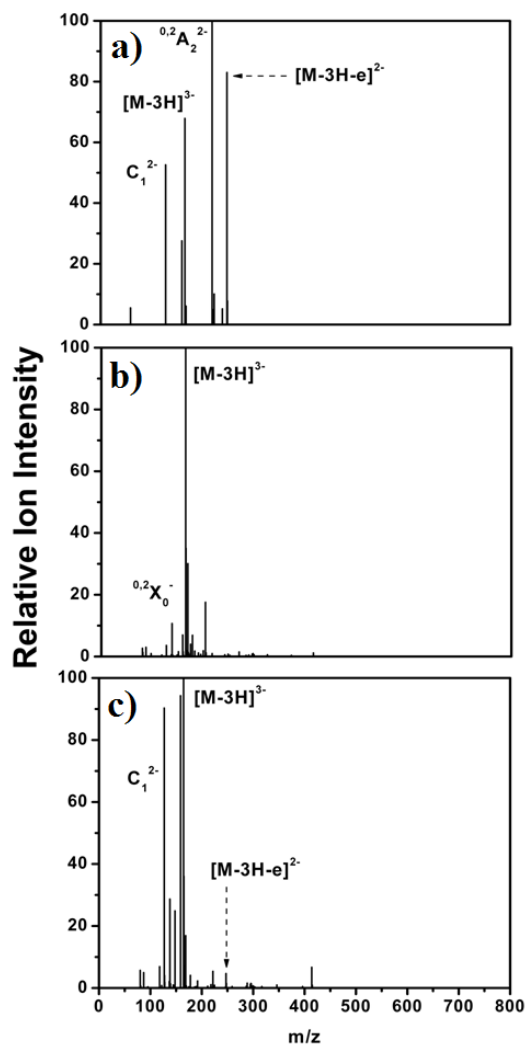
Fig. 3.4 MS<sup>2</sup> mass spectra of a) [IH-2H]<sup>2-</sup>, b) [IIS-2H]<sup>2-</sup> and c) [IIS-2H]<sup>2-</sup> dianions at 8% CID energy.

**Table 3.1 Product Ions resulting from collisional excitation of heparin disaccharides. Dianions were fragmented using 8% CID energy, trianions at 6.4%.**

Precursor Ion	Product Ions
[IH-2H] <sup>2-</sup>	<sup>0,2</sup> A <sub>2</sub> <sup>-</sup> (218), -H <sub>2</sub> O (238)
[IIS-2H] <sup>2-</sup>	<sup>0,2</sup> A <sub>2</sub> <sup>-</sup> (357), <sup>0,2</sup> X <sub>0</sub> <sup>-</sup> (138), <sup>0,2</sup> A <sub>1</sub> <sup>-</sup> (115), Y <sub>1</sub> <sup>-</sup> (338), Y <sub>1</sub> <sup>2-</sup> (168), B <sub>1</sub> <sup>-</sup> (157), <sup>0,2</sup> X <sub>1</sub> <sup>-</sup> -SO <sub>3</sub> (300), -H <sub>2</sub> O (238)
[IIS-2H] <sup>2-</sup>	<sup>0,2</sup> A <sub>2</sub> <sup>-</sup> (357), <sup>0,2</sup> X <sub>0</sub> <sup>-</sup> (138), <sup>0,2</sup> A <sub>1</sub> <sup>-</sup> (115), Y <sub>1</sub> <sup>-</sup> (258), <sup>0,2</sup> X <sub>1</sub> <sup>-</sup> -SO <sub>3</sub> (300), -H <sub>2</sub> O (238)
[IH-3H] <sup>3-</sup>	<sup>0,2</sup> A <sub>2</sub> <sup>2-</sup> (218), [M-3H-H <sub>2</sub> O] <sup>3-</sup> (159), [M-3H-e] <sup>2-</sup> (247), [M-3H-e-H <sub>2</sub> O] <sup>2-</sup> (238) C <sub>1</sub> <sup>2-</sup> (127)
[IIS-3H] <sup>3-</sup>	<sup>0,2</sup> X <sub>0</sub> <sup>-</sup> (138), [M-3H-H <sub>2</sub> O] <sup>3-</sup> (159), Y <sub>1</sub> <sup>2-</sup> (169)
[IIS-3H] <sup>3-</sup>	<sup>0,2</sup> X <sub>0</sub> <sup>-</sup> (138), [M-3H-H <sub>2</sub> O] <sup>3-</sup> (159), [M-3H-e] <sup>2-</sup> (247), C <sub>1</sub> <sup>2-</sup> (127), C <sub>1</sub> <sup>2-</sup> -H <sub>2</sub> O (118), Y <sub>1</sub> <sup>2-</sup> (169)

### 3.3.3 MS<sup>2</sup> on Heparin Disaccharide Trianions

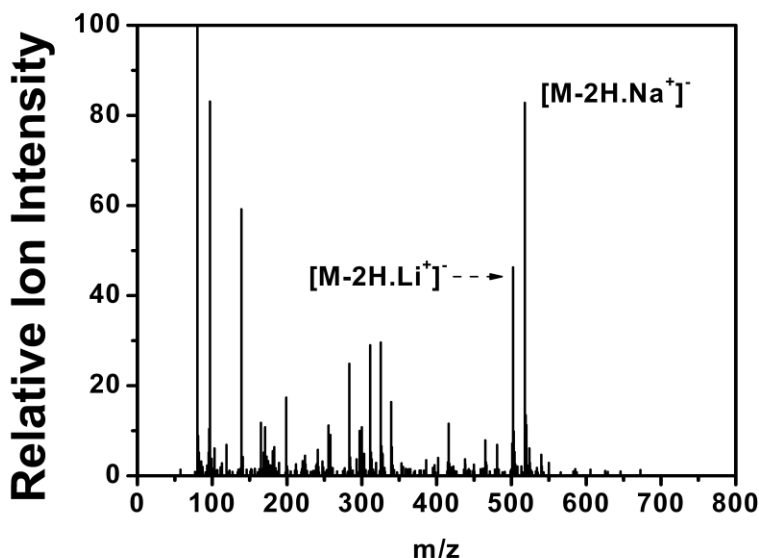
Figure 3.5 shows the MS<sup>2</sup> mass spectra for the trianion, or [M-3H]<sup>3-</sup>, state of the three disaccharides. Figures 3.5 a) and c) both show a peak at m/z = 247 which corresponds to the loss of a single electron from the precursor trianions of [IH-3H]<sup>3-</sup> and [IIS-3H]<sup>3-</sup>. This peak is not present above the signal/noise ratio for IIS in figure 3.5 b). Only IH displays loss of water from its oxidised product ion, i.e. [M-3H-e-H<sub>2</sub>O]<sup>2-</sup>, although all three parent trianions spectra display fragment peaks which can be assigned to neutral water loss. Both IIS and IIS produce <sup>0,2</sup>X<sub>0</sub><sup>-</sup> fragments not present in the [IH-3H]<sup>3-</sup> spectrum due to the lack of a sulphate group on the C2 position of its reducing ring. [IH-3H]<sup>3-</sup> uniquely displays a <sup>0,2</sup>A<sub>2</sub><sup>2-</sup> fragment for the same reason. The C<sub>1</sub><sup>2-</sup> fragment present for [IH-3H]<sup>3-</sup> is of note since it suggests that the COOH group is deprotonated. This fragment is not present in the [IIS-3H]<sup>3-</sup> spectrum, although the [IIS-3H]<sup>3-</sup> result indicates production of C<sub>1</sub><sup>2-</sup> and C<sub>1</sub><sup>2-</sup> - H<sub>2</sub>O. Both [IIS-3H]<sup>3-</sup> and [IIS-3H]<sup>3-</sup> produce a Y<sub>1</sub><sup>2-</sup> fragment. A full summary for the trianion product ions is provided in Table 3.1.



**Fig. 3.5** MS<sup>2</sup> mass spectra of a) [IH-3H]<sup>3-</sup>, b) [IIS-3H]<sup>3-</sup> and c) [IIS-3H]<sup>3-</sup> trianions at 6.4% CID energy.

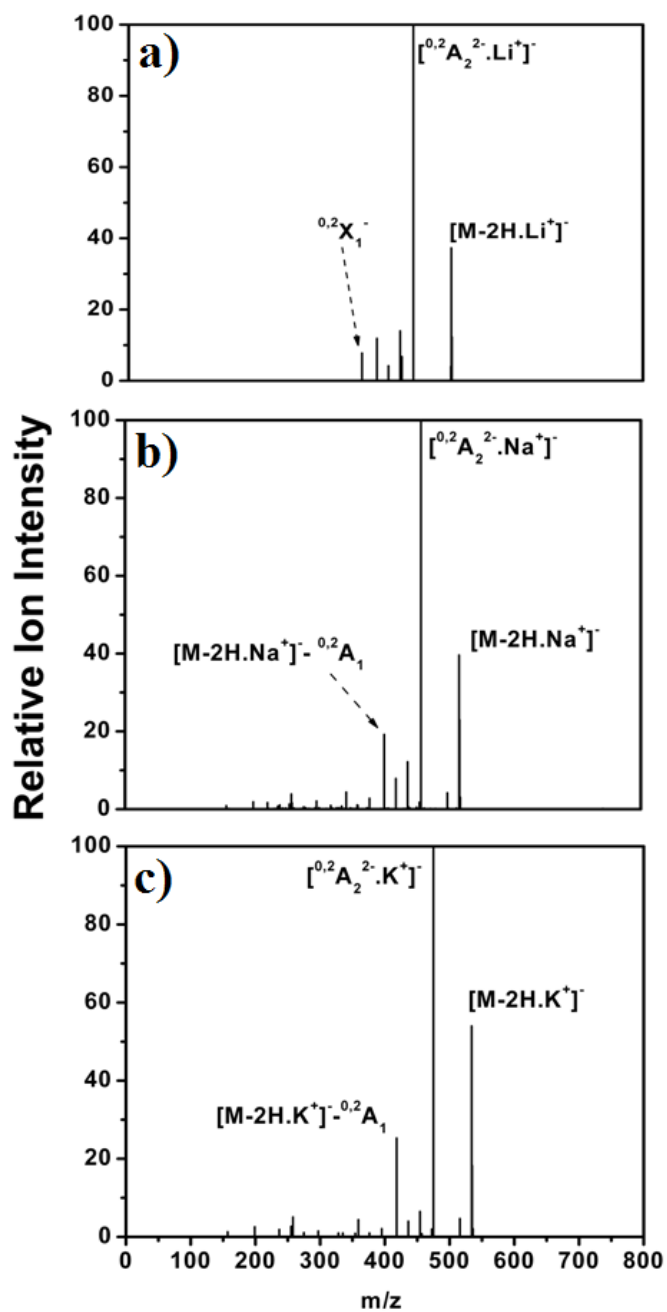
### 3.3.4 MS<sup>2</sup> on Heparin Disaccharide Dianion Salt Complexes

Figure 3.6 shows the spectrum resulting from spraying the [IH-2H]<sup>2-</sup> disaccharide in the presence of lithium chloride solution as described in Section 3.2. The [M-2H.Li<sup>+</sup>]<sup>-</sup> complex is clearly visible at  $m/z = 502$ , as is the sodium complex at  $m/z = 518$ .



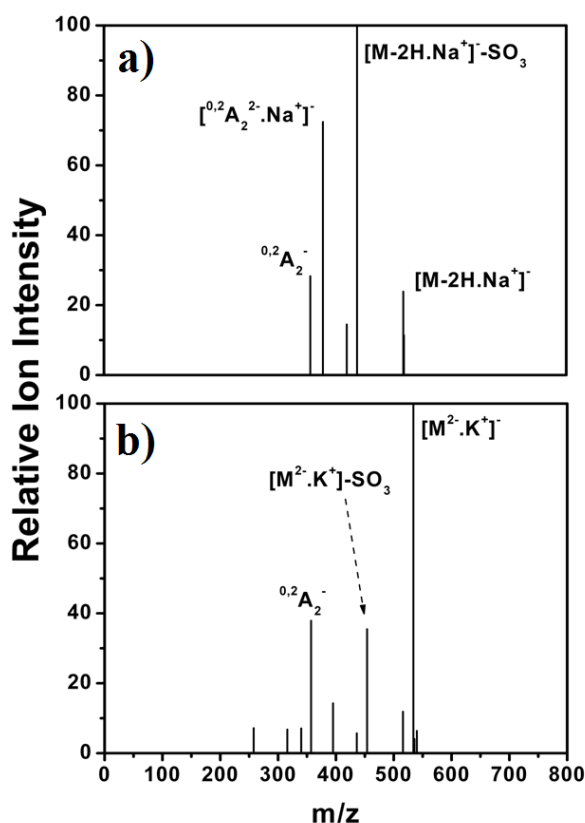
**Fig 3.6** MS<sup>1</sup> spectrum of [IH-2H]<sup>2-</sup> disaccharide electrosprayed at 10<sup>-4</sup> M in methanol as a sodium salt in the presence of lithium chloride.

Figure 3.7 displays the results of isolating the counter ion complexes of the IH<sup>2-</sup> disaccharide and resonantly exciting the isolated ions at 8.8 % CID energy. In each case the cross ring fragmentation pathway remains dominant with the alkali metal ion remaining complexed to the <sup>0,2</sup>A<sub>2</sub><sup>2-</sup> product ion. This behaviour is in good agreement with previous work which has determined that the low energy fragmentation pathways of multiply charged anions (MCAs) are the same as those of MCA - counterion complexes.<sup>23,24,25</sup> Loss of a neutral SO<sub>3</sub> is observed regardless of the counter ion complexed. Both [IH-2H.Na<sup>+</sup>]<sup>-</sup> and [IH-2H.K<sup>+</sup>]<sup>-</sup> complexes show loss of neutral water, while the lithium complex (Figure 3.7a) does not. All three disaccharide complexes also fragment with the loss of a neutral <sup>0,2</sup>A<sub>1</sub> fragment. A full list of observed fragments is given in Table 3.2.



**Fig 3.7** MS<sup>2</sup> mass spectra of [IH-2H.X<sup>+</sup>] at 8.8 % CID energy, where X = a) Lithium, b) Sodium and c) Potassium.

Figure 3.8 shows the MS<sup>2</sup> mass spectra for the IIS disaccharide counter ion complexes at 8.8% CID energy. The [IIS-2H.Li<sup>+</sup>]<sup>-</sup> complex was not observed at a sufficient intensity for isolation. Figure 3.8 a) illustrates the formation of <sup>0,2</sup>A<sub>2</sub><sup>-</sup> (m/z = 357) and <sup>0,2</sup>A<sub>2</sub><sup>2-</sup>.Na<sup>+</sup> (m/z = 379) fragment ions. The presence of the <sup>0,2</sup>A<sub>2</sub><sup>2-</sup>.Na<sup>+</sup> ions implies that the <sup>0,2</sup>X<sub>0</sub> fragment is lost as a neutral. This in turn suggests that the sulphate group on the C2 carbon of the reducing ring has not been deprotonated. The lack of <sup>0,2</sup>X<sub>0</sub><sup>-</sup> fragments in the spectrum, coupled with the presence of significant neutral SO<sub>3</sub> losses support this conclusion.



**Fig 3.8 MS<sup>2</sup> mass spectra of [IIS-2H.X<sup>+</sup>]<sup>-</sup> at 8.8 % CID energy, where X= a) Sodium and b) Potassium.**

Alternatively, the presence of the <sup>0,2</sup>A<sub>2</sub><sup>-</sup> peak may indicate that the sodium departs with the singly charged <sup>0,2</sup>X<sub>0</sub><sup>-</sup> fragment. A second explanation for the presence of the <sup>0,2</sup>A<sub>2</sub><sup>-</sup> could be breakdown of the <sup>0,2</sup>A<sub>2</sub><sup>2-</sup>.Na<sup>+</sup> species. Although an MS<sup>3</sup> experiment

would have determined to what extent, if any, extent this pathway was occurring, low ion signals for this peak made precursor ion isolation impractical. Neutral  $^{0,2}X_0$  loss is not observed where the bare IIS dianion is studied (section 3.3.2) and so it seems likely that the presence of the sodium cation favours the carboxylate group as the charge carrier. Alternative fragmentation routes include loss of a sulphate and water for both species, although only the potassium complex appears capable of single neutral water loss.

Figure 3.9 displays the MS<sup>2</sup> disaccharide fragmentation spectra for the [IIS-2H.X<sup>+</sup>]<sup>-</sup> counter ion complexes. The  $^{0,2}A_2$  pathway is again conserved irrespective of the counter ion, producing  $^{0,2}A_2^-$  as the dominant fragment. Both the lithium and the sodium complex spectra show loss of neutral sulphate groups from the precursor, while the potassium complex shows  $^{0,2}A_2^-$  as its sole product ion. The sodiated sugar is the only complex to show loss of neutral water, in addition to displaying a loss of mass equivalent to that of neutral  $^{0,2}A_2$ .

**Table 3.2 Product Ions from heparin dianion-counter ion complexes at 8.8% CID energy with m/z values given in parenthesis.**

Precursor Ion	Product Ions
[IH-2H.Li <sup>+</sup> ] <sup>-</sup>	$^{0,2}A_2^{2-} \cdot Li^+$ (443), [M-2H.Li <sup>+</sup> - SO <sub>3</sub> ] <sup>-</sup> (422), [M-2H.Li <sup>+</sup> - $^{0,2}A_1$ ] <sup>-</sup> (386), $^{0,2}X_1^-$ (363)
[IH-2H.Na <sup>+</sup> ] <sup>-</sup>	$^{0,2}A_2^{2-} \cdot Na^+$ (459), [M-2H.Na <sup>+</sup> - SO <sub>3</sub> ] <sup>-</sup> (438), [M-2H.Na <sup>+</sup> - $^{0,2}A_1$ ] <sup>-</sup> (402), [M-2H.Na <sup>+</sup> - SO <sub>3</sub> -H <sub>2</sub> O] <sup>-</sup> (420), [M-2H.Na <sup>+</sup> - H <sub>2</sub> O] <sup>-</sup> (500)
[IH-2H.K <sup>+</sup> ] <sup>-</sup>	$^{0,2}A_2^{2-} \cdot K^+$ (475), [M-2H.K <sup>+</sup> - SO <sub>3</sub> ] <sup>-</sup> (454), [M-2H.K <sup>+</sup> - $^{0,2}A_1$ ] <sup>-</sup> (418), [M-2H.K <sup>+</sup> - H <sub>2</sub> O] <sup>-</sup> (516)
[IIS-2H.Na <sup>+</sup> ] <sup>-</sup>	$^{0,2}A_2^{2-} \cdot Na^+$ (379), $^{0,2}A_2^-$ (357), [M-2H.Na <sup>+</sup> - SO <sub>3</sub> ] <sup>-</sup> (438), [M-2H.Na <sup>+</sup> - SO <sub>3</sub> - H <sub>2</sub> O] <sup>-</sup> (420)
[IIS-2H.K <sup>+</sup> ] <sup>-</sup>	$^{0,2}A_2^{2-} \cdot K^+$ (395), $^{0,2}A_2^-$ (357), [M-2H.K <sup>+</sup> - SO <sub>3</sub> ] <sup>-</sup> (454), [M-2H.K <sup>+</sup> - SO <sub>3</sub> - H <sub>2</sub> O] <sup>-</sup> (436) [M-2H.K <sup>+</sup> - H <sub>2</sub> O] <sup>-</sup> (516)
[IIS-2H.Li <sup>+</sup> ] <sup>-</sup>	$^{0,2}A_2^-$ (357), [M-2H.Li <sup>+</sup> - SO <sub>3</sub> ] <sup>-</sup> (422)
[IIS-2H.Na <sup>+</sup> ] <sup>-</sup>	$^{0,2}A_2^-$ (357), [M-2H.Na <sup>+</sup> - SO <sub>3</sub> ] <sup>-</sup> (438), [M-2H.Na <sup>+</sup> - $^{0,2}A_2$ ] <sup>-</sup> (402), [M-2H.Na <sup>+</sup> - H <sub>2</sub> O] <sup>-</sup> (500),
[IIS-2H.K <sup>+</sup> ] <sup>-</sup>	$^{0,2}A_2^-$ (357)

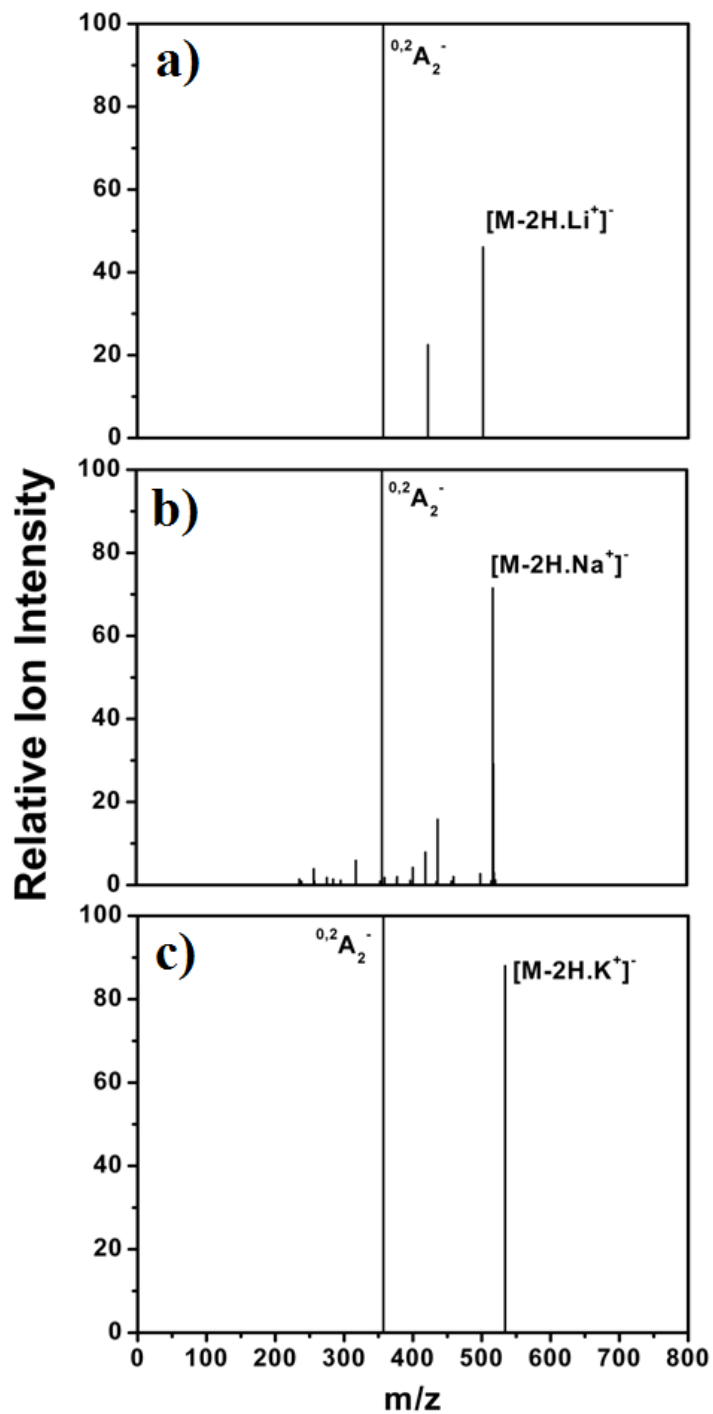


Fig 3.9 MS<sup>2</sup> mass spectra of  $[IIS-2H.X]^+$  at 8.8 % CID energy, where X = a) Lithium, b) Sodium and c) Potassium.

### 3.4 Further Discussion

#### **3.4.1 Low Energy Fragmentation Pathways**

The  $^{0,2}A_2$  fragment pathway is conserved throughout this study for the dianions and their cation complexes. This result is in good agreement with previous work which has shown that smaller cation-dianion complexes fragment in the same manner as the corresponding bare dianion, suggesting that the electronic structure of the dianion is not perturbed by the cation to any great extent.<sup>23,24,25</sup> The counter ion could have caused a significantly altered electron distribution throughout these precursor dianions, leading to alternative fragmentation pathways, this is not observed. The nature of the cation complexed to the disaccharide does appear to have some influence over the lesser fragmentation routes, for example the lithium complex of the IH dianion lacks a neutral water loss while the sodium and potassium complexes show a clear loss of 18 mass units. Since the GAG family of molecules are highly flexible gas-phase structures (see chapter 5) this result suggests that the  $[IH-2H.Li^+]$  complex adopts a conformation which makes the water loss pathway less favourable. The position of the sulphate groups on each disaccharide has a distinct effect on the location of the deprotonated or charged carrying region. The  $[IH-2H]^{2-}$  dianion displays no evidence of a charged  $COO^-$  group.  $IIS^{2-}$  has both its sulphate groups on the reducing ring, and shows evidence of the non-reducing ring  $COO^-$  group being present, in addition to displaying fragments indicating both of its sulphate groups being charged. From this data it is apparent that the proton ‘shared’ between these groups is mobile as discussed by Zaia et al.<sup>26</sup> The factors which allow the proton to occupy a certain position leading to distinct fragments in the mass spectrum are likely to be a combination of charge repulsion and the overall conformation in the gas phase that the disaccharide adopts, i.e. in certain cases the  $COOH$  group may be too distant from the sulphate groups to allow for proton exchange.

Fragments observed for both  $[IH-3H]^{3-}$  and  $[IIS-3H]^{3-}$  trianions suggest that the  $COOH$  side group has lost its proton at some stage of the fragmentation process. It is

of note that these sugars also show strong electron loss peaks, while IIS displays neither of these features.

### 3.4.2 Analytical Benefits

The results above clearly show a marked difference between the fragmentation patterns for the dianionic forms of the disaccharides. Both the IIS and IIS species fragment with the production of numerous cross-ring and glycosidic ions, while the IH products are limited to a single cross-ring fragment and a loss of neutral water. The fragments shown in Table 3.1 clearly provide a route by which the identity of the isomers present could be determined, with the fragments  $^{0,2}A_2^-$  ( $m/z = 218$ ),  $B_1^-$  ( $m/z = 157$ ) and  $Y_1^-$  ( $m/z = 258$ ) as being excellent ‘marker’ fragments for  $[IH-2H]^{2-}$ ,  $[IIS-2H]^{2-}$  and  $[IIS-2H]^{2-}$  respectively. The results of the trianionic study provide an additional diagnostic advantage via the loss of an electron from the  $IH^{3-}$  and  $IIS^{3-}$  species, but not from  $IIS^{3-}$ . As discussed in Section 3.1, compositional profiling of disaccharide *mixtures* relies upon the selection of suitable isomeric fragments from pure standards from which to construct solvable systems of equations. In order for the results of such a study to be meaningful it is necessary to select fragments which appear with a high intensity. Studying the IIS and IIS dianionic disaccharides, the  $^{0,2}A_2^-$  and  $^{0,2}X_0^-$  fragments are isomeric and clearly present in the spectrum, and I would suggest these fragments would form the basis for a “system of equations analysis” as used by Desaire and Leary.<sup>20</sup> This would allow the ratio of the IIS and IIS to be determined, although the IH fragment, if present, would require the use of fragments produced from the trianionic  $[M-3H]^{3-}$  species. From the results in Table 3.1 it would seem that the loss of neutral water ( $m/z = 158.6$ ) and of the electron ( $m/z = 246.8$ ) would provide suitable fragments for a comparison of IH and IIS. In summary, the ratios of mixtures of  $[IIS-2H]^{2-}$  to  $[IIS-2H]^{2-}$  could be known through an initial experiment using the fragments produced from CID of  $[M-2H]^{2-}$  ions. This would then be followed by repeating this step using the  $[M-3H]^{3-}$  trianions as precursors in an  $MS^2$  experiment to determine the ratio of  $[IH-3H]^{3-}$  to  $[IIS-3H]^{3-}$ .

The combination of these results would then allow the ratio of the three species from the original mixture to be calculated.

The related counter ion complexed dianions are less important in this context primarily because of the low intensities at which most of these species are observed. Detecting the presence of the three isomers in a mixture containing sodium cations could be accomplished using  $^{0,2}A_2^{2-}.Na^+$  ( $m/z = 459$ ),  $^{0,2}A_2^{2-}.Na^+$  ( $m/z = 379$ ) and  $^{0,2}A_2^-$  ( $m/z = 357$ ) fragments as markers for IH, IIS and IIS respectively. A common product ion observed throughout the complex series is the loss of a neutral sulphate. In the presence of significant sodium cation contamination it may be possible to compare this fragment i.e.  $[M-2H.Na^+-SO_3]^-$  ( $m/z = 438$ ) with that of  $[M-2H.Na^+-H_2O]^-$  ( $m/z = 500$ ) to determine the ratios of IH to IIS. The equivalent experiment with IIS and IIS would utilize  $^{0,2}A_2^-$  ( $m/z = 357$ ) and  $[M-2H.Na^+-SO_3]^-$  ( $m/z = 438$ ).

### 3.4.3 Energy Resolved Mass Spectrometry of Isomeric Heparin Disaccharides

Energy resolved mass spectrometry (ERMS) involves determining structural information based on the intensity of a selected fragment ion produced versus the kinetic energy used to effect fragmentation. This technique has been previously used in the construction of ERMS libraries for the analysis of glycans,<sup>27</sup> where all possible anomeric and linkage positions were studied for a test compound. This method relies upon the strict reproducibility of experimental data, since plotted curves of fragment ion intensity versus applied collisional energy are often highly similar between isomers. Additionally, the application of the technique to a wide range of glycans based on the results of one study is not feasible in cases where substituent groups such as sulphates and carboxylates would be expected to significantly affect the nature of the lowest energy fragmentation pathway. The generation of libraries of CID data for the GAG families of sugars would not be practical due to their structural complexity. ERMS has also been used to determine the purity of samples,<sup>28</sup> based on the comparison of curves generated at multiple stages of tandem MS, and in the identification of isomeric mannose-based post-

translational modifications to proteins.<sup>29</sup> Studies on the effect of collision energy on the fragments produced from chondroitin sulphates have highlighted the relationship between sulphate content and collisional energy, demonstrating that the choice of fragmentation parameters can be critical in obtaining the most useful balance of diagnostic product ions.<sup>26</sup> In a quadrupole ion-trap, ERMS is performed by isolation of an ion in an MS<sup>2</sup> experiment and monitoring its intensity relative to the fragments produced as the excitation voltage is increased. A more detailed description of this use of tandem mass spectrometry is given in Chapter 2.

Figure 3.10 below shows the result of a collision-induced dissociation experiment on the dianion isomers IH, IIS and IIS, monitoring the production of the  $^{0,2}A_2^-$  product ion. This result shows the order of gas-phase stability for the dianions to be IH < IIS < IIS, with IH distinctly less stable. This result is of interest since the IIS and IIS isomers both contain a sulphate substituent group at the C2 position of the reducing sugar ring, while IH possesses an NH<sub>2</sub> group at this position. The  $^{0,2}A_2$  route has been established as the dominant low-energy fragmentation pathway for these systems and it is likely that the sulphate group is involved in a charge stabilizing hydrogen-bonding network, examples of which are highlighted in Chapter 5. The ERMS result shown has a potential application as an efficient test of product purity in an MS<sup>2</sup> experiment, since IIS could be verified to be free of IIS/IH contamination based on the onset of the fragmentation curve. This data also suggests the suitability of these species for the analytical technique developed by Kanie et al, which depends on isomeric or anomeric compounds having significantly different gas phase stabilities.<sup>28</sup> Briefly, this technique relies on an MS<sup>2</sup> step on a mixture of isomeric compounds with the same predominant product ion producing a CID curve of a certain shape, i.e. with a 100% Product Ion Intensity at a specific Percentage CID Energy. Subsequent steps (MS<sup>3</sup>) on the remainder of the original isometric peak will then produce a second curve, with an identical shape if the original peak is pure. If a mixture is present the contribution of the other isomer, i.e. the one more stable in the gas phase will be increased since the ratio of the lower stability Isomer

will have been reduced in the MS<sup>2</sup> experiment. This would result in a movement of the CID curve to a higher Percentage CID value for its 100 Percent Product Ion Intensity.

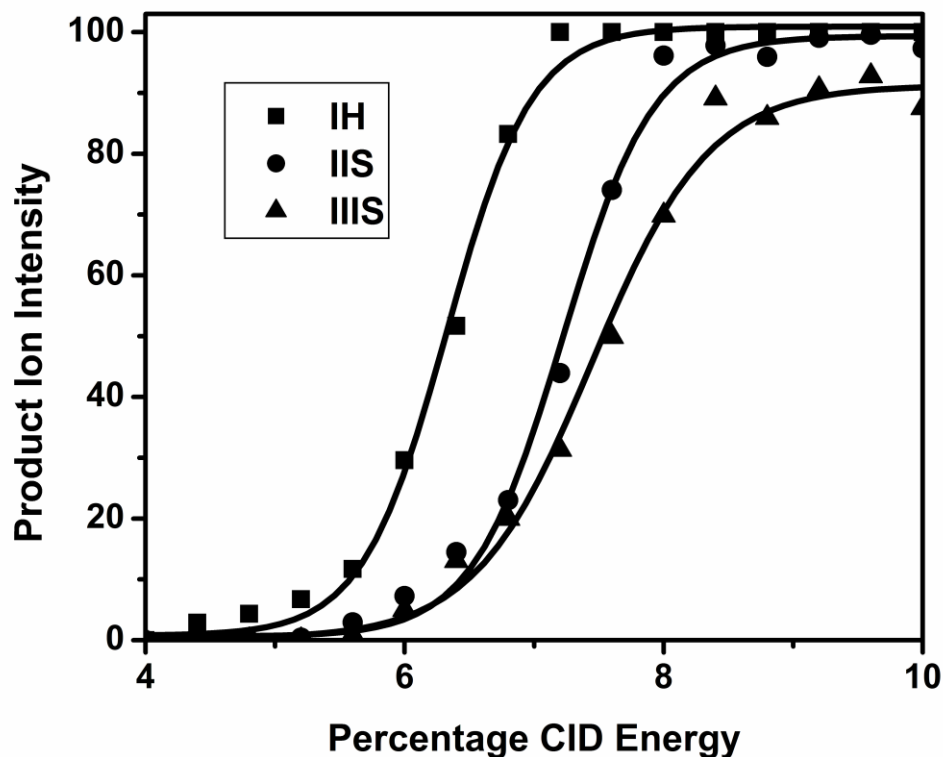


**Fig 3.10** Fragmentation curves for the production of the  $^{0,2}A_2^-$  ion from the IH, IIS and IIS precursor dianions.

The utility of ERMS for product analysis by this route depends upon the availability of fragment ions at high intensities that are common to all isomers present within the mixture. In this study the presence of  $Li^+$  or  $K^+$  generated densely populated mass spectra making the isolation of complexed disaccharides impractical in most cases due to the low signal intensities available for MS<sup>2</sup> experiments. The intensities of sodium cation disaccharide complexes are far higher than those of the lithium or potassium analogues since the sugars studied are supplied as sodium salts. However, as discussed in Section 3.3.4, while the presence of a counter ion still means the  $^{0,2}A_2$  fragmentation route is dominant, the mass of the product ions from each

species will vary due to the counter ion departing attached to different halves of the precursor anion, in addition to the differences in location of the sulphate groups for each isomer. To summarise, the disaccharide dianions present the most promising candidates for a practical ERMS experiment to determine purity, their counter ion complexes produce spectra likely to be too complex and with insufficient signal intensity for reliable analysis. While electron loss would be an effective test for contamination by unwanted disaccharides in a mixture through its presence or absence, it is not well suited for ERMS based studies due to its similarly low peak heights.

### 3.5 Summary

The low energy fragmentation results for the sulphated disaccharides IH, IIS and IIIS have been shown here to provide numerous potential ‘marker’ diagnostic product ions that could potentially aid heparin characterization in a mixture. The presence of cation contamination has been shown not to alter the principal low energy fragmentation route for these species. The locations of the charged sites at fragmentation are highly dependent on the positioning of the sulphate side groups and the overall total charge of the ions. Understanding the interplay between these factors and the fragments produced greatly enhances the diagnostic potential of this technique.

References

1. H. E. Conrad, Heparin-Binding Proteins; Academic Press: San Diego, CA, 1998; pp. 183–202
2. D. Shukla, J. Liu, P. Blaiklock, N.W. Shworak, X. Bai, J.D. Esko, G.H. Cohen, R.J. Eisenberg, R.D. Rosenberg and P.G. Spear, *Cell* 99 (1999) 13
3. C. I. Gama, L. C. Hsieh-Wilson, *Curr. Opin. Chem. Biol.* 9 (2005), 609
4. N. S. Gandhi, R. L. Mancera, *Chem Biol Drug Des.* 72 (2008) 455
5. V. A. Cummings, R. Esko, J. Freeze, H. Hart, G. Marth, *Essentials of Glycobiology*, Cold Spring Harbor Laboratory Press, Cold Spring Harbor, NY, 1999
6. R.J. Linhardt, T. Toida, *Acc. Chem. Res.* 37 (2004) 431
7. O.M. Saad, J.A. Leary, *J. Am. Soc. Mass Spectrom.* 15 (2004) 1274
8. J. Zaia, C. E. Costello, *Anal. Chem.* 75 (2003) 2445
9. J. Zaia, X-Q. Li, S-Y. Chan, C. E. Costello, *J. Am. Soc. Mass Spectrom.* 14 (2003) 1270
10. A. Zamfir, D. G. Seidler, H. Kresse, J. Peter-Katalinic, *Glycobiology*, 13 (2003) 733
11. A. Zamfir, D.G. Seidler, H. Kresse, J. Peter-Katalinic, *Rapid Comm. Mass Spec.* 16 (2002) 2015
12. J.J. Wolff, I.J. Amster, L. Chi, R.J. Linhardt, *J. Am. Soc. Mass Spec.* 18 (2007) 234
13. J.J. Wolff, I.J. Amster, L. Chi, R.J. Linhardt, *Anal. Chem.* 79 (2007) 2015
14. J.J. Wolff, T.N. Laremore, A.M. Busch, R.J. Linhardt, I.J. Amster, *J. Am. Soc. Mass Spec.* 19 (2008) 294
15. F.E. Leach III, J.J. Wolff, T.N. Laremore, R.J. Linhardt, I.J. Amster, *Int. J. Mass Spec.* 276 (2008) 110
16. J.J. Wolff, T.N. Laremore, A.M. Busch, R.J. Linhardt, I.J. Amster, *J. Am. Soc. Mass Spec.* 19 (2008) 790
17. A.K. Korir, C.K. Larive, *Anal. Bioanal. Chem.* 393 (2009) 155
18. O.M. Saad, J.A. Leary, *Anal. Chem.* 75 (2003) 2985
19. O.M. Saad, H. Ebel, K. Uchimura, S. D. Rosen, C. R. Bertozzi, J. A. Leary, *Glycobiology* 15 (2005) 818
20. H. Desaire, J. A. Leary, *J Am Soc Mass Spectrom.* 11(2000) 916
21. H. Desaire, J. A. Leary, *Anal. Chem.* 71 (1999) 4142
22. B. Domon, C.E. Costello, *Glycoconjugate J.* 5 (1988) 397
23. R.M. Burke, W.E. Boxford, C.E.H. Dessent, *J. Chem. Phys.* 126 (2007) 064308
24. R.M. Burke, W.E. Boxford, C.E.H. Dessent, *J. Chem. Phys.* 125 (2006) 021105
25. W.E. Boxford, R.M. Burke, C.E.H. Dessent, *Phys. Scripta* 76 (2007) C56
26. J. Zaia, M.J.C. Miller, J.L. Seymour, C.E. Costello, *J. Am. Soc. Mass Spectrom.* 18 (2007) 952
27. S. Daikoku, T. Ako, R. Kato, I. Ohtsuka, O. Kanie, *J Am Soc Mass Spectrom.*, 18 (2007) 1873

28. S. Daikoku, A. Kurimoto, S. Mutsuga , T. Ako, T. Kanemitsu , Y. Shioiri, A. Ohtake, R. Kato, C. Saotome, I. Ohtsuka , S. Koroghi, S. K. Sarkar, A. Tobe, S. Adachi, K. Suzuki, O. Kanie, *Carbohydr. Res.* 344 (2009) 384
29. A. Kurimoto, O. Kanie, *Rapid Commun. Mass Spectrom.* 21 (2007) 2770

## Chapter 4

### Structural Characterization of Negatively-Charged Glycosaminoglycans Using High-Energy (50-150 keV) Collisional Activation

#### 4.1 Introduction

Over recent years, the study of gas-phase biological molecules has developed into a rapidly expanding field of research, with considerable experimental and theoretical effort being expended to provide detailed insights into the geometric and electronic properties of isolated biomolecules.<sup>1-11</sup> While laser spectroscopy is particularly powerful at providing detailed geometric structures, there is also scope for applying other molecular physics techniques in this area.<sup>11-14</sup> Glycosaminoglycans (GAGs) are linear, sulfated polysaccharides found on the cell surfaces of a wide range of organisms. GAGs have been implicated in numerous biological roles including cell signaling, cancer progression, and in the regulation of the inflammatory immune response.<sup>15</sup> This study explores the possibility of structurally characterizing anionic GAGs by performing electron detachment *via* very high-energy collisions (50-150 keV ion kinetic energy prior to collision) with a noble gas. This high-energy collision technique has previously been applied to studying the structures and potential energy surfaces of a number of gas-phase chemical systems,<sup>16-21</sup> including multiply-charged oligonucleotide anions,<sup>20</sup> but is applied here to sugars for the first time. Low-energy collision-induced (CID) dissociation measurements obtained using resonance excitation in a quadrupole ion-trap are also presented for comparison, since low-energy CID is widely used to characterize the structures of oligosaccharides. Figure 4.1 illustrates the acidic sugars that have been investigated in this initial study, including three prototypical GAG disaccharides (IVA, IH and IS), and three monomer sugar units (which are denoted A, B and C). These sugars are deprotonated in solution, so that negative ion electrospray ionization produces deprotonated gas-phase anions. The selected sugars are more densely charged than

the related systems that have been studied previously using lower-energy activated dissociation.<sup>22-24</sup>

Determining the pattern of sulphate and acetylate substitution displayed on Heparin and Heparan Sulphate is a matter of particular biological importance as it is thought to be the key to their biochemical activity. The availability of samples is limited to naturally occurring species since GAGs cannot yet be routinely synthesized. For this reason, structural characterization by NMR is severely limited by the purity and volume of material available.<sup>25</sup> Enzymatic digestion and Capillary Electrophoresis/MS<sup>n</sup> based characterization techniques suffer from high sample consumption, low turnaround times, and low accuracy relative to mass spectrometry techniques, hence limiting the structural information that can be obtained from these methods.<sup>26</sup>

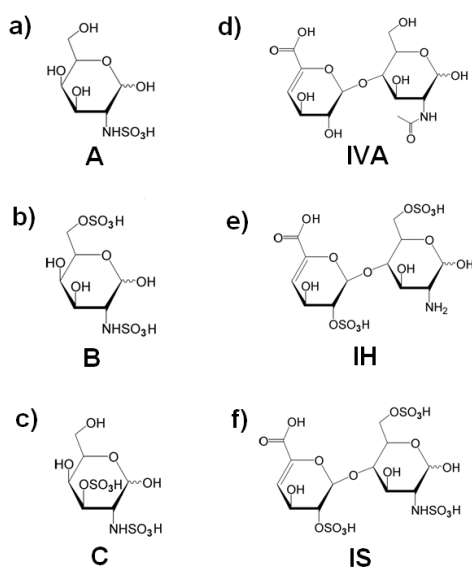


**Fig. 4.1** The chemical structures of the six sulphated sugars studied in this chapter. a) The A monosaccharide, GlcNS, b) the B monosaccharide, GlcNS-6S, c) the C monosaccharide, GlcNS-3S, d) the IVA disaccharide,  $\alpha$ - $\Delta$ UA-[1 $\rightarrow$ 4]-GlcNAc, e) the IH trianionic disaccharide,  $\alpha$ - $\Delta$ UA-2S-[1 $\rightarrow$ 4]-GlcN-6S, and f) the IS disaccharide,  $\alpha$ - $\Delta$ UA-2S-[1 $\rightarrow$ 4]-GlcNS-6S. (The sugar names have been abbreviated as follows;  $\Delta$ UA = 4-deoxy-L-threo-hex-4-enopyranosyluronic acid; GlcN = D-glucosamine; Ac = Acetyl; NS, 2S, 3S and 6S, = N-sulfo, 2-sulfate, 3-sulfate and 6-sulfate respectively.)

A full complement of cross-ring and glycosidic cleavage fragments is required to determine the sequence of the sugar polymer and the sulphation sites within the sugar units. The suitability of mass-spectral techniques for obtaining structural information on GAG systems is therefore strongly dependent on the method's ability to retain the fragile sulphate groups following molecular fragmentation.

Recent advances in the structural characterization of anionic saccharides have included the application of Electron Detachment Dissociation (EDD) to effect the fragmentation of GAG tetrasaccharides.<sup>22,23</sup> This method involves the irradiation of a multiply-charged anionic GAG with electrons of 15-20 eV, initiating electron detachment and subsequent fragmentation. Analysis of the resulting products has revealed the presence of fragments not seen by either low-energy CID or infrared multi-photon dissociation (IRMPD) techniques, and has shown an abundance of cross-ring and glycosidic cleavages. In addition, EDD was shown to be capable of distinguishing between the epimers iduronic and glucuronic acid based on the fragments produced.<sup>23</sup> To date however, experiments have been limited to model tetrasaccharides containing a lower level of sulfation than has been seen previously in biologically active GAG chains. High-energy ion collisions, such as the ones studied here, may also lead to EDD-type fragmentation of sugars and may therefore prove highly useful for performing structural characterization of GAGs.

## 4.2 Experimental Methods

### **4.2.1 Mass-analyzed ion kinetic energy (MIKE) spectrometry**

The experimental set-up of the SEP 1 accelerator mass spectrometer has been described in detail previously<sup>17</sup>, a summary of its design is given in Chapter 2. Monosaccharides (Dextra Laboratories) and disaccharides (Sigma Aldrich) were purchased as the sodium salt complexes. All compounds were used without further purification. The ions studied were prepared via ESI (negative ion mode) from 1:1 water-methanol solutions. The sugars studied were mass selected in the following charge states,  $A^-$ ,  $B^{2-}$ ,  $C^{2-}$ ,  $IVA^-$ ,  $IH^{2-}$  and  $IS^{3-}$ , where we denote  $A^-$  to be equivalent

to the more commonly used [A-H]<sup>-</sup>, etc, to simplify the labelling of the fragmentation mass spectra.

Accelerated ions of 50 keV (monoanions), 100 keV (dianions) and 150 keV (trianions) kinetic energy were mass selected by a magnet, and subjected to single-collision activation in a 3 cm collision cell containing neon gas at a pressure of approximately 0.2 mTorr. Mass analyzed ion kinetic energy scans of the anions exiting the collision cell were recorded using a 180° hemi-spherical electrostatic analyzer coupled to a channeltron detector. The flight time from the collision cell to the detector is a few microseconds, setting a limit on the time available for rearrangement of the parent or fragment ions following collision. We note that due to the design of the detector on the SEPI instrument, a peak is present below the parent ion. For dianionic species, this means that artificial peaks can mask the presence of (dianionic) fragment ions corresponding to loss of a neutral water unit from the parent ion.

#### **4.2.2 Low-Energy Collision Induced Dissociation**

A Finnigan LCQ electrospray quadrupole ion-trap mass spectrometer in negative ion mode was used to perform the low-energy CID experiments as described previously,<sup>27</sup> Further explanation of this technique is given in Chapter 2. Sample solution concentrations were 10<sup>-4</sup> M in methanol, prior to electrospraying in an 80:20 methanol/water solution. Signal optimization was performed using the LCQ automated tuning feature with the cone voltage set at 4.2 kV and a capillary temperature of 150°C. The sample flow rate was set to 5 µL/min.

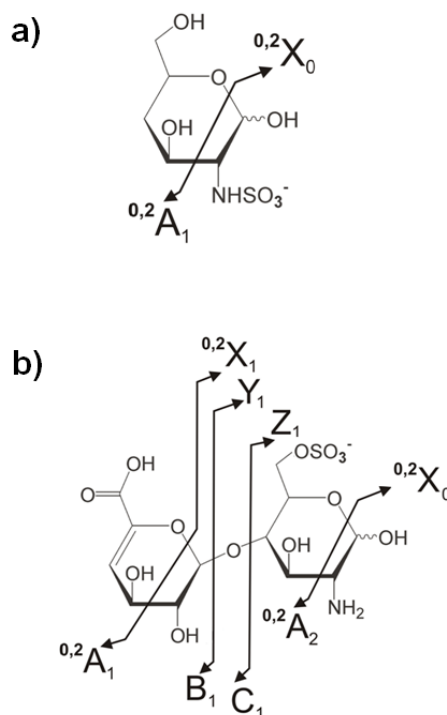


**Fig. 4.2** Fragment labelling scheme used in this work for a) monosaccharide and b) disaccharides. (This follows the scheme of Domon and Costello.<sup>28</sup>) The A, B and C labels are used to indicate a fragment containing a non-reducing end of the GAG, while X, Y and Z denote fragments which include the reducing end of the sugar. (The reducing end is defined as the ring with a C<sub>1</sub> carbon not involved in a glycosidic bond.)

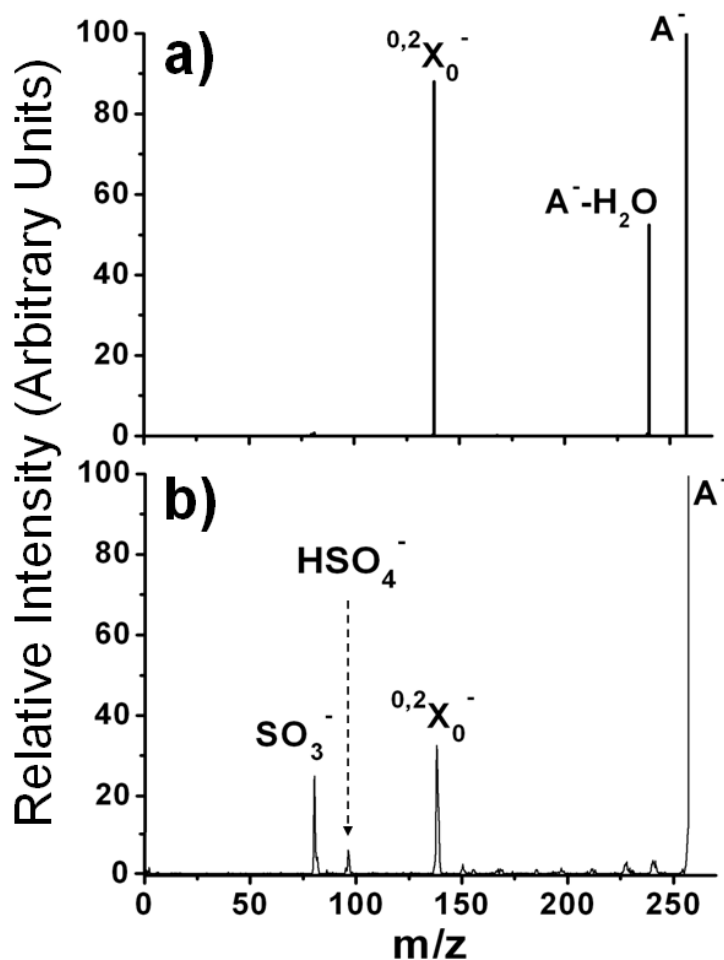
### 4.3 Results and Discussion

In this chapter, the fragment labelling scheme proposed by Domon and Costello to describe the fragmentation patterns of the disaccharide ions is adopted.<sup>28</sup> This scheme is extended to label the cross-ring fragmentations of the monosaccharide anions, with both the labelling schemes being illustrated in Fig. 4.2

#### 4.3.1 Monosaccharides

The low-energy CID fragmentation mass spectrum of the A<sup>-</sup> (GlcNS) monoanionic monosaccharide ( $m/z = 258$ ) is displayed in Fig. 4.3a (CID energy = 11.5%). The major fragment ion at  $m/z = 138$  is assigned to the <sup>0,2</sup>X<sub>0</sub><sup>-</sup> fragment (*i.e.* A<sup>-</sup>-<sup>0,2</sup>A<sub>1</sub>). A second fragment ion peak is present at  $m/z = 240$ , representing loss of a neutral

water molecule from the parent ion. Such fragments are a common feature of negative-ion Heparin mass spectra.<sup>29</sup>



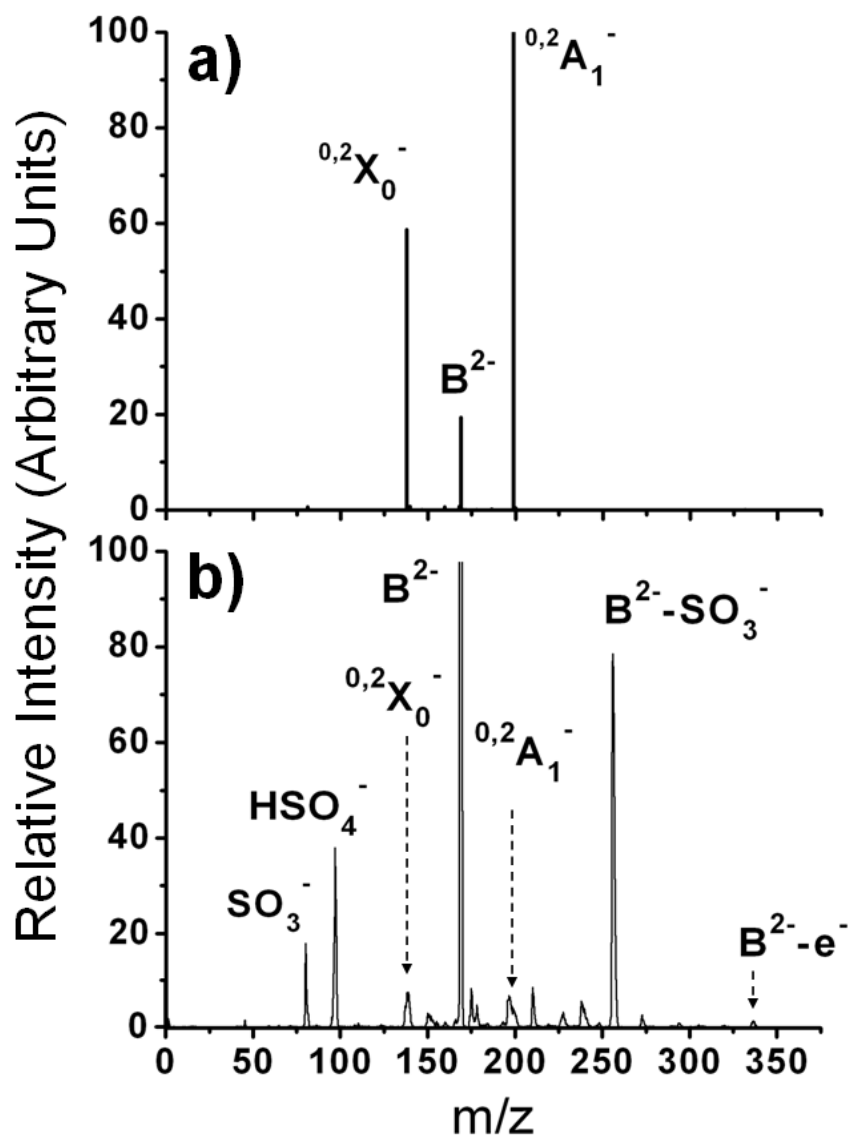
**Fig. 4.3 (a) Low-energy CID mass spectrum of the  $A^-$  (i.e.  $[A-H]$ ) monoanionic monosaccharide at 11.5% collision energy. (b) Negative-ion MIKE spectrum (50 keV) following high-energy collision of  $A^-$  with Neon.**

Fig. 4.3b displays the high-energy MIKE fragmentation spectrum of  $A^-$ . The number of fragment ions produced following high-energy collisional excitation is

considerably increased compared to the low-energy CID spectrum (Fig. 4.3a), even for this relatively simple molecular ion. As in the low-energy CID spectrum,  $^{0,2}X_0^-$  is the major fragment ion in the MIKE spectrum. The presence of this fragment is consistent with the sulphate group carrying the negative charge in the parent ion. The pair of peaks at  $m/z = 80.3$  and  $m/z = 97$  are assigned to the  $SO_3^-$  and  $HSO_4^-$  fragment ions, since this pair of ions are commonly observed in the low-energy CID of sulphated GAGs.<sup>29</sup> The appearance of the  $SO_3^-$  and  $HSO_4^-$  fragment-ion pair strongly indicates that the excess charge is located on the sulphate group in the parent ion.

Fig. 4.4a shows the low-energy CID fragmentation mass spectrum of the  $B^{2-}$  (GlcNS-6S) dianionic monosaccharide (CID energy = 5%). The low-energy fragmentation behaviour of  $B^{2-}$  mirrors that of other small molecular dianions, since it undergoes ionic fragmentation (or *Coulomb explosion*) with the production of two monoanionic species.<sup>30,31,32,33</sup> These fragment ions are assigned as  $^{0,2}X_0^-$  ( $m/z = 138$ ) and  $^{0,2}A_1^-$  ( $m/z = 199$ ), corresponding to a cross-ring fragmentation. It is notable that the dianionic  $B^{2-}$  fragments more efficiently at a lower CID energy than the monoanionic  $A^-$ , in line with the lower intrinsic stability of multiply charged ions.<sup>31</sup>

The high-energy MIKE fragmentation spectrum of  $B^{2-}$  (100 keV) is displayed in Figure 4.4b. The number of fragment ions produced following high-energy collisional excitation is again considerably increased compared to the low-energy CID spectrum (Fig. 4.4a). The most prominent fragment ion peak ( $m/z = 256$ ) corresponds to ionic fragmentation of the parent ion with loss of  $SO_3^-$ . As in the low-energy CID spectrum,  $B^{2-}$  again fragments across the saccharide ring with production of the  $^{0,2}X_0^-$  and  $^{0,2}A_1^-$  monoanions. The  $SO_3^-$  and  $HSO_4^-$  pair of fragments are also again evident in the MIKE spectrum, consistent with the excess charges being carried by the sulfate and aminosulfate groups in the parent ion.<sup>29</sup>



**Fig. 4.4** (a) Low-energy CID mass spectrum of the  $B^{2-}$  (*i.e.*  $[B - 2H]^{2-}$ ) dianionic monosaccharide at 5% collision energy. (b) Negative-ion MIKE spectrum (100 keV) following high-energy collision of  $B^{2-}$  with Neon.

Loss of water is a common fragmentation channel, with several peaks in the MIKE spectrum of  $B^{2-}$  being assigned to loss of water from either the parent or product ions. One of the most striking features of the  $B^{2-}$  high-energy fragmentation spectrum is the very low intensity of the electron detachment ion, *i.e.*  $B^{2-} - e^-$ . This contrasts with the high-energy fragment spectra of other molecular dianions, *e.g.*

deprotonated oligonucleotides, where the major fragment ion typically corresponds to electron detachment from the parent dianion.<sup>16-21</sup> We note that the parent ion -SO<sub>3</sub><sup>-</sup> fragment ion ( $m/z = 256$ ) may also result from initial electron loss, followed by loss of neutral SO<sub>3</sub>. This point will be addressed further in the discussion section.

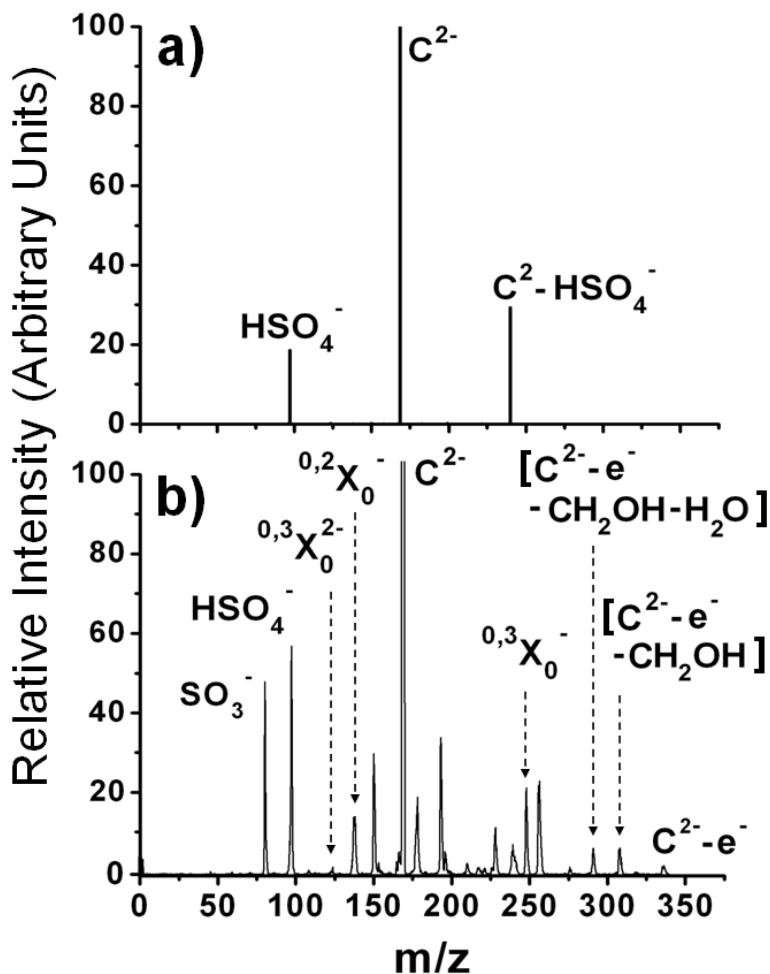


**Fig. 4.5 (a) Low-energy CID mass spectrum of the  $C^{2-}$  (*i.e.*  $[C - 2H]^{2-}$ ) dianionic monosaccharide at 6% collision energy. (b) Negative-ion MIKE spectrum (100 keV) following high-energy collision of  $C^{2-}$  with Neon.**

The low-energy CID fragmentation mass spectrum of the  $C^{2-}$  (GlcNS-3S) dianionic monosaccharide ( $m/z = 169$ ) is displayed in Fig. 4.5a (CID energy = 6%).  $C^{2-}$  again fragments efficiently at a relatively low CID energy, consistent with the intrinsic instability of small gas-phase dianions. Low-energy fragmentation of  $C^{2-}$  again proceeds *via* ionic fragmentation (*Coulomb explosion*) of the dianion, although this time with production of the  $HSO_4^-$  and  $[C^{2-} - HSO_4]^-$  pair of monoanions. This fragmentation pattern is notably different from that of  $B^{2-}$ , where ionic fragmentation occurred with cross-ring fragmentation, and reflects the fact that the two excess charges are held on adjacent position on the  $C^{2-}$  sugar ring.

The high-energy MIKE fragmentation spectrum of  $C^{2-}$  (100 keV) shown in Fig. 4.5b, exhibits similar fragmentation products to the corresponding spectrum of  $B^{2-}$ , consistent with the  $C^{2-}$  dianion fragmenting *via* Coulomb explosion upon high-energy collision. The  $SO_3^-$  and  $HSO_4^-$  pair of fragments is again prominent, consistent with the excess charges being carried by the sulfate and aminosulfate groups in the parent ion.<sup>29</sup> The  $^{0,2}X_0^-$  fragment is present, and both the singly and doubly-charged  $^{0,3}X_0^{n-}$  ( $n = 1,2$ ) ions are present. (The corresponding  $A^-$  set of fragments may be absent due to electron loss during or after the high-energy collision.) Fragments corresponding to loss of  $CH_2OH$  and  $H_2O$  units for either the parent ion or the product ions are common (Table 4.1). The fragment ion corresponding to electron detachment from the parent ion, *i.e.*  $C^{2-} - e^-$  ( $m/z = 337$ ), again appears with low intensity, although for  $C^{2-}$  it is also accompanied by loss of  $CH_2OH$  and  $CH_2OH + H_2O$ . A full list of the fragments observed in the low- and high-energy fragmentation spectra for the three monosaccharides studied is given in Table 4.1, with assignments.

**Table 4.1: Fragment ions present in the low- and high-energy fragmentation spectra for the A<sup>-</sup>, B<sup>2-</sup> and C<sup>2-</sup> monosaccharide anions. m/z values and fragment intensities (relative to the strongest fragment ion) are given in parentheses. Prominent, unassigned peaks are also included in the table, listed by their observed m/z values.**

Parent Ion	Low-Energy Fragment Ions	High-Energy Fragment Ions
A <sup>-</sup>	<sup>0,2</sup> X <sub>0</sub> <sup>-</sup> (138, <b>100%</b> ), A <sup>-</sup> - H <sub>2</sub> O (240, <b>60%</b> )	<sup>0,2</sup> X <sub>0</sub> <sup>-</sup> (138, <b>100%</b> ), SO <sub>3</sub> <sup>-</sup> (80, <b>77%</b> ), HSO <sub>4</sub> <sup>-</sup> (97, <b>19%</b> ), A <sup>-</sup> - H <sub>2</sub> O (240, <b>10%</b> ), A <sup>-</sup> - CH <sub>2</sub> OH (228, <b>9%</b> )
B <sup>2-</sup>	<sup>0,2</sup> A <sub>1</sub> <sup>-</sup> (199, <b>100%</b> ), <sup>0,2</sup> X <sub>0</sub> <sup>-</sup> (138, <b>59%</b> )	B <sup>2-</sup> - SO <sub>3</sub> <sup>-</sup> (256, <b>100%</b> ), HSO <sub>4</sub> <sup>-</sup> (97, <b>48%</b> ), SO <sub>3</sub> <sup>-</sup> (80, <b>22%</b> ), m/z = 175 ( <b>21%</b> ), B <sup>2-</sup> - CH <sub>2</sub> OSO <sub>3</sub> <sup>-</sup> - H <sub>2</sub> O (210, <b>11%</b> ), <sup>0,2</sup> X <sub>0</sub> <sup>-</sup> (138, <b>9%</b> ), B <sup>2-</sup> - SO <sub>3</sub> <sup>-</sup> - H <sub>2</sub> O (238, <b>7%</b> ), <sup>0,2</sup> A <sub>1</sub> <sup>-</sup> - H <sub>2</sub> O (178, <b>6%</b> ), <sup>0,2</sup> A <sub>1</sub> <sup>-</sup> (199, <b>8%</b> ), B <sup>2-</sup> - CH <sub>2</sub> OSO <sub>3</sub> <sup>-</sup> (228, <b>4%</b> ), B <sup>2-</sup> - e <sup>-</sup> (338, <b>1%</b> )
C <sup>2-</sup>	C <sup>2-</sup> - HSO <sub>4</sub> <sup>-</sup> (240, <b>100%</b> ), HSO <sub>4</sub> <sup>-</sup> (97, <b>64%</b> )	HSO <sub>4</sub> <sup>-</sup> (97, <b>100%</b> ), SO <sub>3</sub> <sup>-</sup> (80, <b>85%</b> ), C <sup>2-</sup> - HSO <sub>4</sub> <sup>-</sup> - CH <sub>2</sub> OH - H <sub>2</sub> O (193, <b>60%</b> ), m/z = 150.1 ( <b>53%</b> ), <sup>0,3</sup> X <sub>0</sub> <sup>-</sup> (247, <b>38%</b> ), C <sup>2-</sup> - SO <sub>3</sub> <sup>-</sup> (259, <b>36%</b> ), m/z = 178 ( <b>34%</b> ), <sup>0,2</sup> X <sub>0</sub> <sup>-</sup> (137, <b>25%</b> ), m/z = 228 ( <b>21%</b> ), C <sup>2-</sup> - e <sup>-</sup> - CH <sub>2</sub> OH - H <sub>2</sub> O (291, <b>11%</b> ), C <sup>2-</sup> - e <sup>-</sup> - CH <sub>2</sub> OH (306, <b>11%</b> ), C <sup>2-</sup> - HSO <sub>4</sub> <sup>-</sup> (240, <b>10%</b> ), C <sup>2-</sup> - CH <sub>2</sub> OH (153, <b>5%</b> ), <sup>0,3</sup> X <sub>0</sub> <sup>2-</sup> (123, <b>3%</b> ), C <sup>2-</sup> - HSO <sub>4</sub> <sup>-</sup> - CH <sub>2</sub> OH (210, <b>3%</b> ), C <sup>2-</sup> - e <sup>-</sup> (338, <b>3%</b> )

### 4.3.2 Disaccharides

Figure 4.6a displays the low-energy fragmentation mass spectrum of the IVA<sup>-</sup> monoanionic disaccharide (α-ΔUA-[1→4]-GlcNAc) obtained at 10.5 % CID energy. IVA<sup>-</sup> is distinctive amongst the sugars investigated in this study, since the excess charge cannot be held on a sulphate group. The most prominent fragment ions result from cross-ring cleavages of each sugar ring, producing <sup>0,2</sup>A<sub>2</sub><sup>-</sup> and <sup>0,2</sup>X<sub>1</sub><sup>-</sup>. A C<sub>1</sub><sup>-</sup>

fragment ion associated with Z cleavage is evident at  $m/z = 175$ , although the low peak intensity indicates that glycosidic cleavage is a minor channel at low collision-energy.

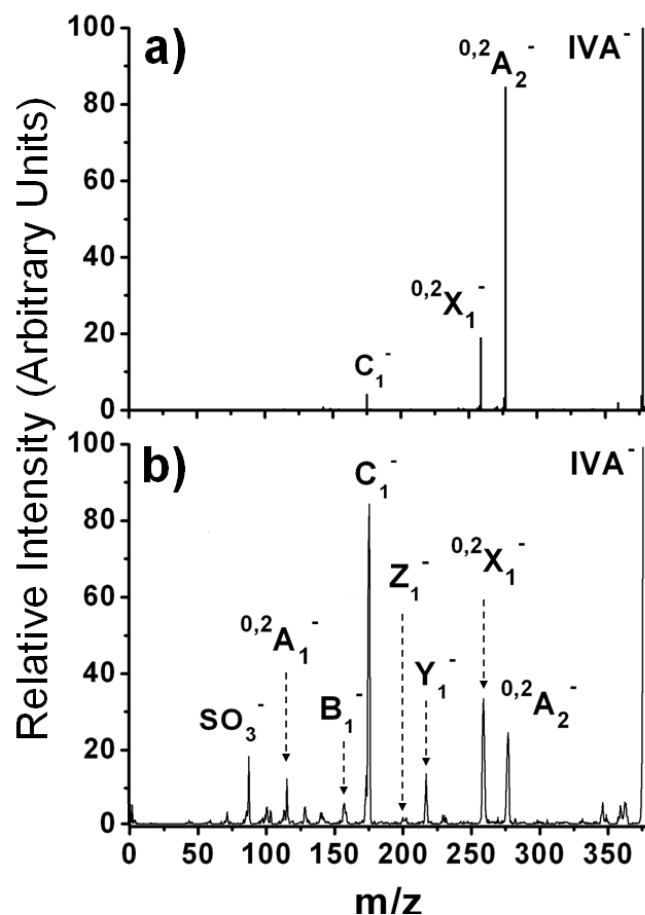


**Fig. 4.6 (a) Low-energy CID mass spectrum of the  $\text{IVA}^-$  (i.e.  $[\text{IVA} - \text{H}]^-$ ) monoanionic disaccharide at 10.5% collision energy. (b) Negative-ion MIKE spectrum (50 keV) following high-energy collision of  $\text{IVA}^-$  with Neon.**

The corresponding high-energy MIKE fragmentation spectrum (50 keV) of  $\text{IVA}^-$  is displayed in Fig. 4.6b. This spectrum displays the full complement of glycosidic fragments, with the  $\text{C}_1^-$  fragment ion now being the dominant product. In addition to the fragments associated with glycosidic cleavage ( $\text{C}_1^-$ ,  $\text{Z}_1^-$ ,  $\text{B}_1^-$ ,  $\text{Y}_1^-$ ),  $^{0,2}\text{A}_1^-$ ,  $^{0,2}\text{A}_2^-$  and  $^{0,2}\text{X}_1^-$  fragment ions corresponding to cross-ring fragmentations are also clearly present. Note that negatively charged fragments are observed for all the possible

glycosidic breakages (*i.e.* fragments are observed without the carboxylate part of the molecule carrying the negative charge ).

The low- and high-energy fragmentation mass spectra of the  $\text{IH}^{2-}$  dianionic disaccharide ( $\alpha$ - $\Delta$ UA-2S-[1 $\rightarrow$ 4]-GlcN-6S) are displayed in Fig. 4.7. The most prominent fragmentation channel in the low-energy CID fragmentation spectrum (Fig. 4.7a) corresponds to a cross-ring cleavage that results in production of the  $^{0,2}\text{A}_2^{2-}$  dianion ( $m/z = 218$ ). Fragmentation of a dianion with production of a smaller dianion and a neutral fragment is unusual for relatively small molecular dianions, and is generally driven by the production of a stable neutral molecule.<sup>30</sup> For  $\text{IH}^{2-}$ , fragmentation along the  $^{0,2}\text{X}_0$  cleavage produces  $\text{H}\text{NH}_2\text{C}=\text{CHOH}$ , consistent with this general picture. A  $\text{C}_1^-$  glycosidic-cleavage product ion ( $m/z = 255$ ) is again evident as a minor fragment, along with an ion associated with loss of water from  $\text{IH}^{2-}$  ( $m/z = 238$ ).

Upon high-energy collisional activation (Fig. 4.7b - 100 keV), the  $\text{IH}^{2-}$  dianionic disaccharide primarily fragments with production of  $\text{SO}_3^-$  and  $\text{HSO}_4^-$ , mirroring the behaviour of the  $\text{B}^{2-}$  and  $\text{C}^{2-}$  monosaccharides, which also possess  $\text{OSO}_3^-$  groups as charge carriers. The fragment ion corresponding to loss of  $\text{SO}_3^-$  from the parent dianion ( $m/z = 414$ ) is also evident, indicating that the parent dianion fragments via a coulombic explosion. Like the  $\text{B}^{2-}$  monosaccharide,  $\text{IH}^{2-}$  shows less propensity to undergo both cross-ring and glycosidic cleavages. In fact, any such peaks appear within the noise level of the spectrum. The electron detachment fragment ion,  $\text{IH}^{2-} \text{e}^-$ , again appears with very low intensity.

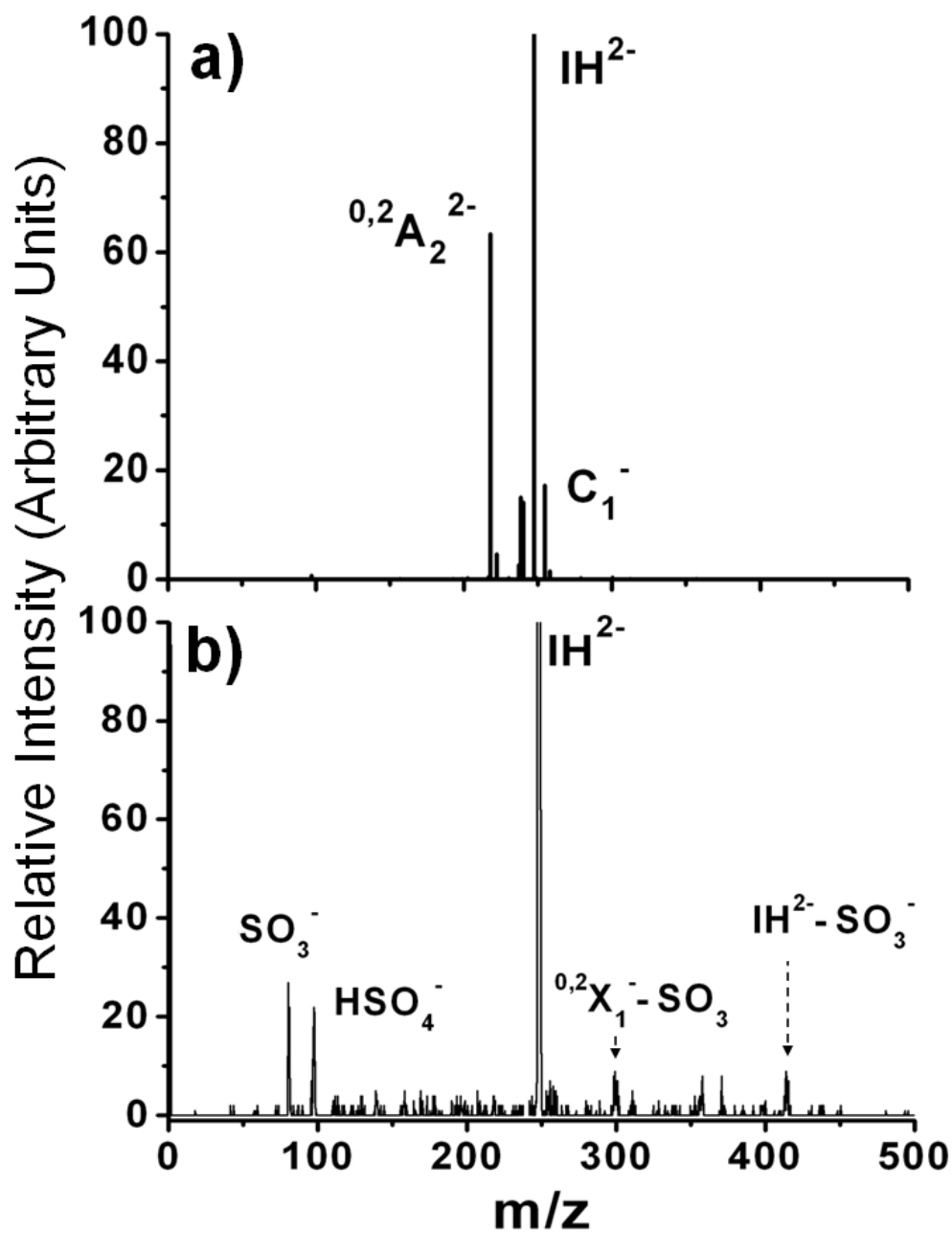
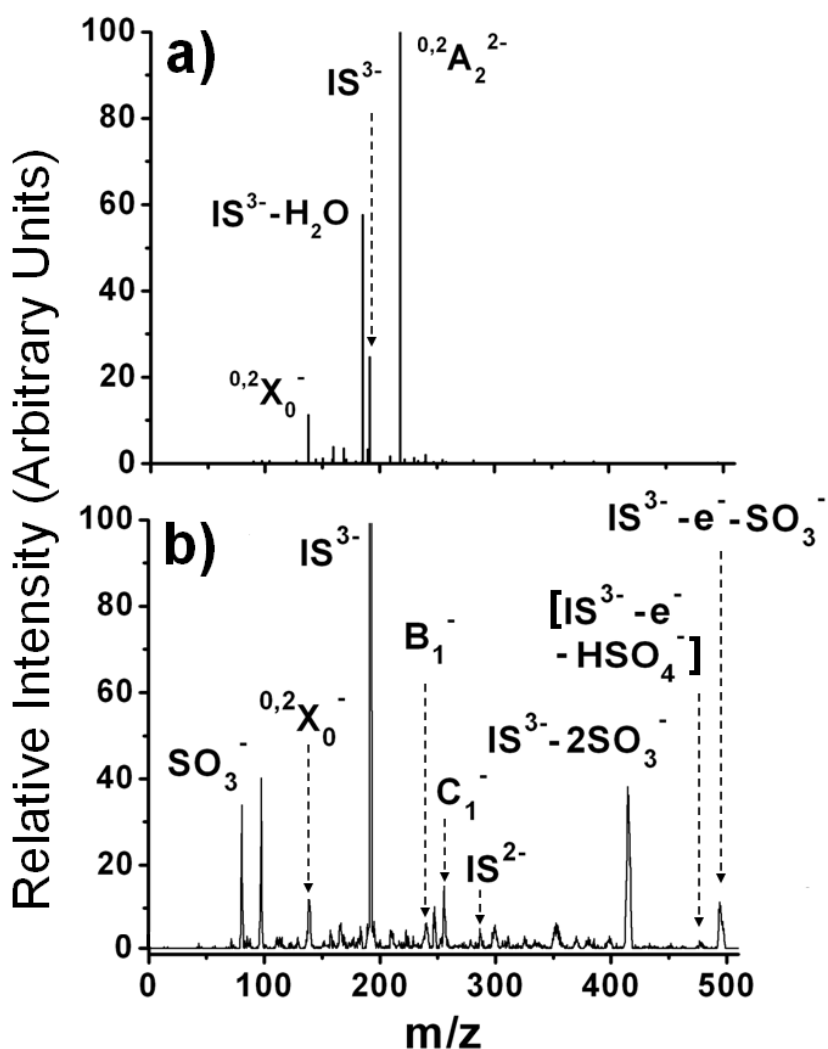


Fig. 4.7 (a) Low-energy CID mass spectrum of the  $IH^{2-}$  (*i.e.*  $[IH - 2H]^{2-}$ ) dianionic monosaccharide at 7.9% collision energy. (b) Negative-ion MIKE spectrum (100 keV) following high-energy collision of  $IH^{2-}$  with Neon.

Fig. 4.8a displays the low-energy CID fragmentation spectrum for the  $IS^{3-}$  trianionic disaccharide ( $\alpha$ - $\Delta$ UA-2S-[1 $\rightarrow$ 4]-GlcNS-6S) obtained at 6.5 % relative CID energy. The major low-energy fragmentation channel for the trianionic parent ion corresponds to ionic fragmentation via a cross-ring cleavage with production of the  $^{0,2}X_0^-$  and  $^{0,2}A_2^{2-}$  pair of anions. The fragmentation channel corresponding to loss of water from the parent ion is also prominent, while fragments associated with glycosidic cleavages are noticeably absent.



**Fig. 4.8** (a) Low-energy CID mass spectrum of the  $IS^{3-}$  (*i.e.*  $[IS - 3H]^{3-}$ ) trianionic monosaccharide at 6.5% collision energy. (b) Negative-ion MIKE spectrum (150 keV) following high-energy collision of  $IS^{3-}$  with Neon.

Parent Ion	Low-Energy Fragment Ions	High-Energy Fragment Ions
IVA <sup>-</sup>	<sup>0,2</sup> A <sub>2</sub> <sup>-</sup> (277, <b>100%</b> ), <sup>0,2</sup> X <sub>1</sub> <sup>-</sup> (259, <b>22%</b> ), C <sub>1</sub> <sup>-</sup> (175, <b>5%</b> ), IVA <sup>-</sup> - H <sub>2</sub> O (360, <b>2%</b> )	C <sub>1</sub> <sup>-</sup> (175, <b>100%</b> ), <sup>0,2</sup> X <sub>1</sub> <sup>-</sup> (258, <b>39%</b> ), <sup>0,2</sup> A <sub>2</sub> <sup>-</sup> (277, <b>29%</b> ), Y <sub>1</sub> <sup>-</sup> (217, <b>16%</b> ), <sup>0,2</sup> A <sub>1</sub> <sup>-</sup> (115, <b>14%</b> ), IVA <sup>-</sup> - H <sub>2</sub> O (360, <b>7%</b> ), IVA <sup>-</sup> - CH <sub>2</sub> OH (346, <b>7%</b> ), B <sub>1</sub> <sup>-</sup> (157, <b>7%</b> ), Z <sub>1</sub> <sup>-</sup> (203, <b>2%</b> )
IH <sup>2-</sup>	<sup>0,2</sup> A <sub>2</sub> <sup>2-</sup> (218, <b>100%</b> ), C <sub>1</sub> <sup>-</sup> (255, <b>27%</b> ), IH <sup>2-</sup> - H <sub>2</sub> O (238, <b>24%</b> )	SO <sub>3</sub> <sup>-</sup> (80, <b>100%</b> ), HSO <sub>4</sub> <sup>-</sup> (97, <b>82%</b> ), IH <sup>2-</sup> - SO <sub>3</sub> <sup>-</sup> (414, <b>33%</b> ), <sup>0,2</sup> X <sub>1</sub> <sup>-</sup> - SO <sub>3</sub> (299, <b>33%</b> ), m/z = 358 ( <b>30%</b> ), m/z = 370 ( <b>30%</b> ), C <sub>1</sub> <sup>-</sup> (255, <b>26%</b> ), m/z = 311 ( <b>19%</b> ), <sup>0,2</sup> A <sub>2</sub> <sup>-</sup> (438, <b>8%</b> ), <sup>0,2</sup> A <sub>1</sub> <sup>-</sup> (118, <b>7%</b> ), IH - e <sup>-</sup> - CO <sub>2</sub> (450, <b>7%</b> ), <sup>0,2</sup> X <sub>1</sub> <sup>-</sup> (380, <b>7%</b> ), IH <sup>2-</sup> - e <sup>-</sup> (496, <b>4%</b> )
IS <sup>3-</sup>	<sup>0,2</sup> A <sub>2</sub> <sup>2-</sup> (218, <b>100%</b> ), IS <sup>3-</sup> - H <sub>2</sub> O (185, <b>58%</b> ), <sup>0,2</sup> X <sub>0</sub> <sup>-</sup> (138, <b>11%</b> )	HSO <sub>4</sub> <sup>-</sup> (97, <b>100%</b> ), IS <sup>3-</sup> - 2SO <sub>3</sub> <sup>-</sup> (415, <b>95%</b> ), SO <sub>3</sub> <sup>-</sup> (80, <b>84%</b> ), C <sub>1</sub> <sup>-</sup> (256, <b>39%</b> ), <sup>0,2</sup> X <sub>0</sub> <sup>-</sup> (139, <b>34%</b> ), IS <sup>3-</sup> - SO <sub>3</sub> <sup>-</sup> - e <sup>-</sup> (494, <b>27%</b> ), IS <sup>3-</sup> - SO <sub>3</sub> <sup>-</sup> (247, <b>21%</b> ), m/z = 352 ( <b>15%</b> ), IS <sup>3-</sup> - SO <sub>3</sub> <sup>-</sup> - SO <sub>3</sub> (166, <b>15%</b> ), m/z = 300 ( <b>14%</b> ), IS <sup>3-</sup> - e <sup>-</sup> (286, <b>11%</b> ), B <sub>1</sub> <sup>-</sup> - SO <sub>3</sub> (158, <b>11%</b> ), B <sub>1</sub> <sup>-</sup> (238, <b>7%</b> ), IS <sup>3-</sup> - CO <sub>2</sub> (176, <b>6%</b> ), IS <sup>3-</sup> - e <sup>-</sup> - HSO <sub>4</sub> <sup>-</sup> - SO <sub>3</sub> (397, <b>5%</b> ), IS <sup>3-</sup> - e <sup>-</sup> - HSO <sub>4</sub> <sup>-</sup> (477, <b>4%</b> )
Na <sup>+</sup> ·IH <sup>2-</sup>	Na <sup>+</sup> · <sup>0,2</sup> A <sub>2</sub> <sup>2-</sup> (459, <b>100%</b> ), <sup>0,2</sup> A <sub>2</sub> <sup>2-</sup> - 2H <sub>2</sub> O (402, <b>25%</b> ), <sup>0,2</sup> A <sub>2</sub> <sup>2-</sup> (438, <b>16%</b> ), Na <sup>+</sup> ·IH <sup>2-</sup> - H <sub>2</sub> O (500, <b>7%</b> ), <sup>0,2</sup> A <sub>2</sub> <sup>2-</sup> - H <sub>2</sub> O (420, <b>6%</b> ),	<sup>0,2</sup> A <sub>2</sub> <sup>-</sup> - 2H <sub>2</sub> O (401, <b>100%</b> ), Y <sub>1</sub> <sup>-</sup> (258, <b>94%</b> ), m/z = 342 ( <b>72%</b> ), m/z = 361 ( <b>66%</b> ), Na <sup>+</sup> ·IH <sup>2-</sup> - CO <sub>2</sub> (473, <b>65%</b> ), IH <sup>2-</sup> (248, <b>53%</b> ), Na <sup>+</sup> · <sup>0,2</sup> A <sub>2</sub> <sup>2-</sup> (459, <b>53%</b> ), m/z = 200 ( <b>53%</b> ), <sup>0,2</sup> A <sub>2</sub> <sup>2-</sup> (217, <b>50.0%</b> ), m/z = 413 ( <b>50%</b> ), IH <sup>2-</sup> - H <sub>2</sub> O (240, <b>34%</b> ), <sup>0,2</sup> A <sub>2</sub> <sup>2-</sup> (459, <b>34%</b> ), HSO <sub>4</sub> <sup>-</sup> (97, <b>25%</b> ), SO <sub>3</sub> <sup>-</sup> (80, <b>19%</b> )
Na <sup>+</sup> ·IS <sup>3-</sup>	Na <sup>+</sup> · <sup>0,2</sup> A <sub>2</sub> <sup>2-</sup> (459, <b>100%</b> ), <sup>0,2</sup> X <sub>0</sub> <sup>-</sup> (138, <b>19%</b> ), m/z = 216 ( <b>11%</b> ), m/z = 531 ( <b>7%</b> )	Na <sup>+</sup> ·IS <sup>3-</sup> - SO <sub>3</sub> <sup>-</sup> (516, <b>100%</b> ), Na <sup>+</sup> ·IS <sup>3-</sup> - HSO <sub>4</sub> <sup>-</sup> (500, <b>14%</b> ), Na <sup>+</sup> ·IS <sup>3-</sup> - SO <sub>3</sub> <sup>-</sup> - CO <sub>2</sub> (472, <b>13%</b> ), m/z = 401 ( <b>13%</b> ), HSO <sub>4</sub> <sup>-</sup> (97, <b>10%</b> ), Na <sup>+</sup> ·Z <sub>1</sub> <sup>2-</sup> (343, <b>8%</b> ), Na <sup>+</sup> · <sup>0,2</sup> A <sub>2</sub> <sup>2-</sup> (459, <b>7%</b> ), IS <sup>3-</sup> - 2SO <sub>3</sub> <sup>-</sup> (414, <b>7%</b> ), m/z = 313 ( <b>6%</b> ), m/z = 200 ( <b>6%</b> ), <sup>0,2</sup> X <sub>0</sub> <sup>-</sup> (140, <b>6%</b> ), m/z = 240 ( <b>5%</b> ), Na <sup>+</sup> ·Y <sub>1</sub> <sup>2-</sup> (360, <b>5%</b> ), Na <sup>+</sup> ·B <sub>1</sub> <sup>2-</sup> (259, <b>5%</b> ), SO <sub>3</sub> <sup>-</sup> (80, <b>4%</b> ), B <sub>1</sub> <sup>2-</sup> (120, <b>4%</b> ), Na <sup>+</sup> ·IS <sup>3-</sup> - CO <sub>2</sub> (277, <b>3%</b> ), m/z = 533 ( <b>3%</b> ), Na <sup>+</sup> ·IS <sup>3-</sup> - e <sup>-</sup> (597, <b>1%</b> )

**Table 4.2: Fragment ions present in the low- and high-energy fragmentation spectra of the IVA<sup>-</sup>, IH<sup>2-</sup> and IS<sup>3-</sup> disaccharide anions, and the Na<sup>+</sup>·IH<sup>2-</sup> and Na<sup>+</sup>·IS<sup>3-</sup> sodiated complexes. m/z values and fragment intensities (relative to the strongest fragment ion) are given in parentheses. Prominent unassigned peaks are also included in the table, listed by their observed m/z values**

Fig. 4.8b displays the high-energy collision fragmentation spectrum (150 keV) of  $\text{IS}^{3-}$ . Coulomb explosion decay of the trianion is again evident in the prominent production of the  $\text{SO}_3^-$  and  $[\text{IS}^{3-} - \text{SO}_3^-]$  fragment pair as in the MIKE spectra of  $\text{IH}^{2-}$ . The corresponding  $[\text{IS}^{3-} - 2\text{SO}_3^-]$  fragment also appears as the major fragment ion. In contrast to the low-energy CID spectrum, the high-energy collision fragmentation spectrum shows both the  $\text{C}_1^-$  ( $m/z = 256$ ) and  $\text{B}_1^-$  ( $m/z = 238$ ) glycosidic product ions. The single cross-ring cleavage is also evident through the production of the  $^{0,2}\text{X}_0^-$  fragment. The fragment ion corresponding to electron detachment, i.e.  $\text{IS}^{3-} - \text{e}^-$  ( $m/z = 286$ ) again appears with only low intensity, although the fragment corresponding to electron detachment coupled with  $\text{SO}_3^-$  loss (i.e.  $\text{IS}^{3-} - \text{e}^- - \text{SO}_3^-$   $m/z = 494$ ) appears more prominently. A minor fragment corresponding to electron loss accompanied by  $\text{HSO}_4^-$  loss (i.e.  $\text{IS}^{3-} - \text{e}^- - \text{HSO}_4^-$   $m/z = 477$ ) is also present at low intensity. A full list of fragments observed in the low- and high-energy fragmentation spectra for the disaccharides studied is given in Table 4.2, with assignments.

### 4.3.3 Sodiated clusters of the $\text{IH}^{2-}$ and $\text{IS}^{3-}$ disaccharides

To compare the fragmentation patterns observed, the sodiated clusters of the  $\text{IH}^{2-}$  and  $\text{IS}^{3-}$  disaccharides were also investigated using the high-energy collision technique. Fig. 4.9 displays the low-energy (21.4% CID energy) and high-energy fragmentation spectra for  $\text{Na}^+ \cdot \text{IH}^{2-}$ . The most prominent fragment in the low collision-energy spectrum (Fig. 4.9a) corresponds to loss of the neutral  $^{0,2}\text{X}_0$  fragment from the parent cluster, producing  $\text{Na}^+ \cdot ^{0,2}\text{A}_2^{2-}$  ( $m/z = 439$ ). This behaviour mirrors the low-energy fragmentation patterns of other dianion-cation complexes we have investigated,<sup>34-36</sup> where fragmentation of the cluster occurs by the same pathway as for the bare dianion.

The high-energy MIKE spectrum is shown in Fig. 4.9b, and displays much higher signal/noise than the corresponding unsodiated spectrum (Fig. 4.7b) due to the low initial intensity of the  $m/z$  channel selected for CID. As in the low-energy spectrum,

a product ion is evident at  $m/z = 459$  corresponding to loss of neutral  $^{0,2}X_0$  from the parent ion. In addition, the high-energy spectrum displays a  $Y_1^-$  glycosidic fragmentation product ion. Loss of  $Na^+$  from the parent ion is evident through the appearance of  $IH^{2-}$  ( $m/z = 248$ ).

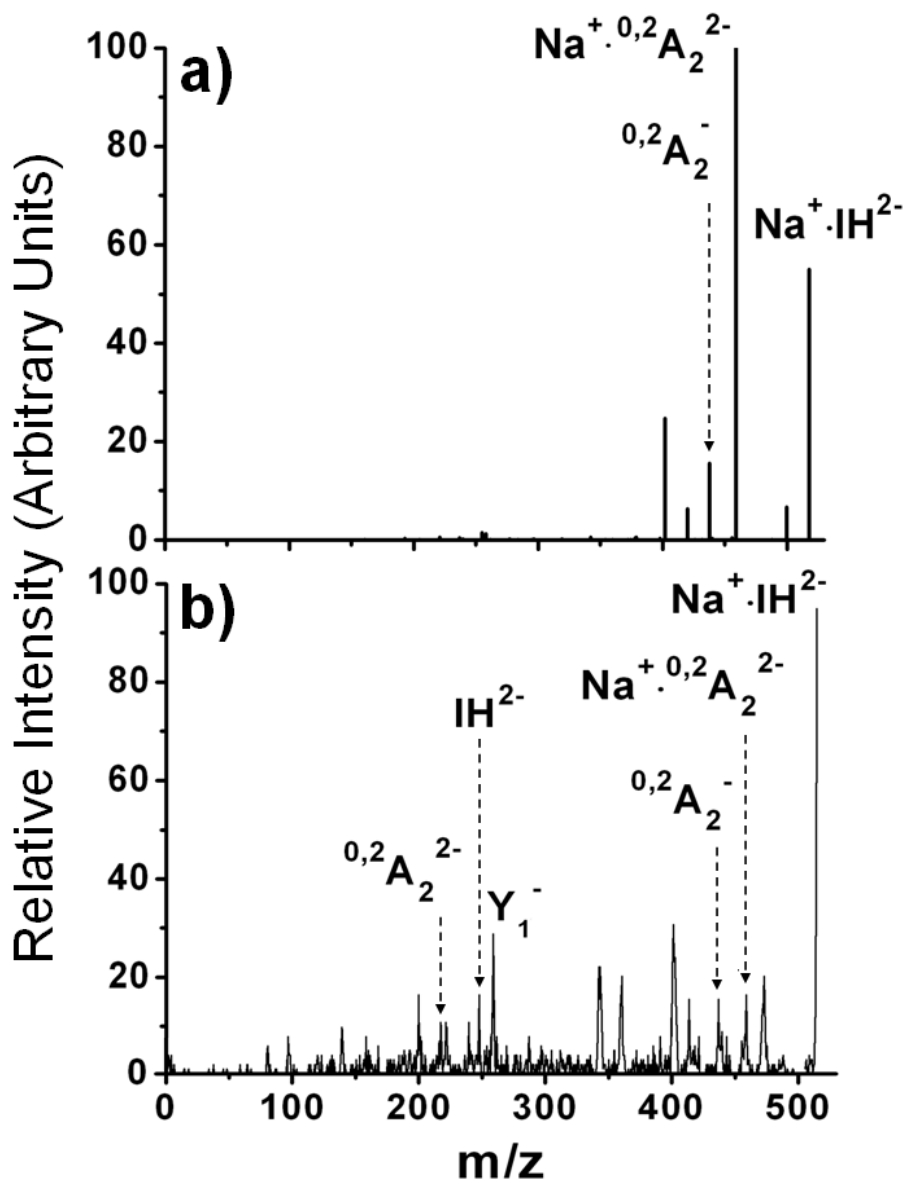


**Fig. 4.9** (a) Low-energy CID mass spectrum of the  $Na^+ \cdot IH^{2-}$  sodiated cluster at 21.4% collision energy. (b) Negative-ion MIKE spectrum (50 keV) following high-energy collision of  $Na^+ \cdot IH^{2-}$  with Neon.

The high-energy MIKE spectrum is shown in Fig. 4.9b, and displays much higher signal/noise than the corresponding unsodiated spectrum (Fig. 4.7b). As in the low-energy spectrum, a product ion is evident at  $m/z = 459$  corresponding to loss of neutral  ${}^{0,2}\text{X}_0$  from the parent ion. In addition, the high-energy spectrum displays a  $\text{Y}_1^-$  glycosidic fragmentation product ion. Loss of  $\text{Na}^+$  from the parent ion is evident through the appearance of  $\text{IH}^{2-}$  ( $m/z = 248$ ).

Finally, the  $\text{Na}^+\cdot\text{IS}^{3-}$  low- and high-energy fragmentation mass spectra are displayed in Fig. 4.10. Low-energy fragmentation of  $\text{IS}^{3-}\cdot\text{Na}^+$  (Fig. 10a) occurs with production of the  ${}^{0,2}\text{X}_0^-$  and  $\text{Na}^+\cdot{}^{0,2}\text{A}_2^{2-}$  pair of fragments, indicating that the multiply charged anion,  $\text{IS}^{3-}$ , is again fragmenting within the cluster by the same pathway as for the bare ion. This behaviour reflects the fact that the sodiated sugar complexes are true ion-pairs,<sup>34-36</sup> where the counterion only weakly perturbs the electronic structure of the multiply-charged saccharide anion. The  ${}^{0,2}\text{X}_0^-$  and  $\text{Na}^+\cdot{}^{0,2}\text{A}_2^{2-}$  pair of fragments are again evident in the high-energy MIKE spectrum (Fig. 4.10b), along with a variety of other product ions corresponding to both  $\text{C}_1$  and  $\text{B}_1$  glycosidic ring cleavages. Once again, the fragment ion corresponding to electron detachment from the  $\text{Na}^+\cdot\text{IS}^{3-}$  parent dianion is a very minor fragment.

The variety of fragment ions observed in the high-energy spectra of the  $\text{Na}^+\cdot\text{IS}^{3-}$  sodiated complex is of key interest, since they suggest that the three excess charges in  $\text{IS}^{3-}$  are distributed across the four acidic groups. For example, the occurrence of the  $\text{B}_1^{2-}$  fragment indicates that excess charges are located on the carboxylate and sulphate group of the  $\text{B}_1$  ring in some of the disaccharides, while the  $\text{Na}^+\cdot\text{Z}_1^{2-}$  and  $\text{Na}^+\cdot\text{Y}_1^{2-}$  fragments indicate that excess charges are located on the sulphate and  $\text{NHSO}_3$  groups of the  $\text{Z}_1$  ring. The simplest explanation of these observations is that the excess charges are distributed across the four acidic groups, and the high-energy experiment on the sodiated cluster therefore provides insight into the charge localization in the trianion. The distribution of charge across the four acidic groups of IS is initially surprising given that the  $\text{pK}_a$  value of the carboxylate group is higher

( $\sim 5$ )<sup>37</sup> than the value for a  $-\text{OSO}_3\text{H}$  or  $-\text{NHSO}_3\text{H}$  group (0.25 and 1.0, respectively).<sup>38-40</sup>

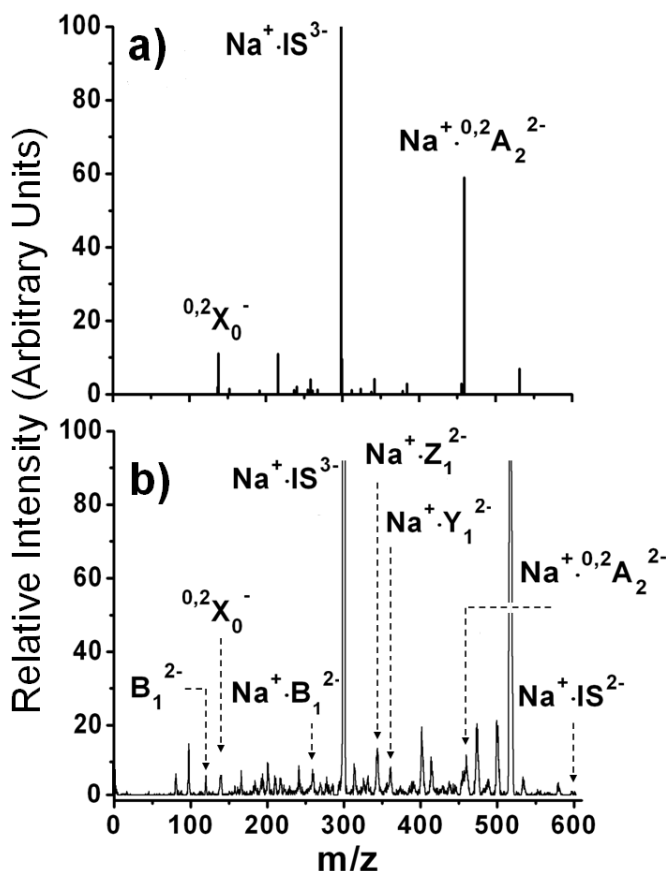


**Fig. 4.10 (a) Low-energy CID mass spectrum of the  $\text{Na}^+\cdot\text{IS}^{3-}$  sodiated cluster at 10.7% collision energy. (b) Negative-ion MIKE spectrum (100 keV) following high-energy collision of  $\text{Na}^+\cdot\text{IS}^{3-}$  collision with Neon.**

However, Tian and Kass have recently studied the deprotonation sites of the gas-phase tyrosine monoanion (carboxylate or phenoxide), and have found that deprotonation is highly dependent on the electrospray solvent used to spray the anion.<sup>41</sup> This study highlighted the fact that Tyrosine is normally found deprotonated at its carboxyl position in solution, although when deprotonated in the gas phase and allowed to equilibrate a 70:30 mixture of phenoxide:carboxylate anions are observed. Altering the solvent used to electrospray the Tyrosine to increase the ratio of Methanol to Acetonitrile caused a corresponding increase in

Phenoxide ions detected, which they attribute to the Methanol acting in a dual role to protonate the carboxylate group while abstracting the phenolic proton. This work clearly demonstrates not only that the gas phase structure of Tyrosine can differ from that of its aqueous form, but also that solvent plays a crucial role. It should be noted that the sugars in this Chapter were electrosprayed with methanol/water mixtures and a similar mechanism may be occurring.

The high-energy fragmentation behaviour of the  $\text{Na}^+\cdot\text{IS}^{3-}$  system is notably different from the analogous  $\text{Na}^+\cdot\text{IH}^{2-}$  cluster where only the  $\text{Y}_1^-$  glycosidic fragment is observed. This may be due to the presence of an  $\text{NH}_2$  group at the C2 position of  $\text{IH}^{2-}$ , where  $\text{IS}^{3-}$  has an acidic  $\text{NHSO}_3\text{H}$  group. A full list of fragments, with assignments, is given in Table 4.2 for the sodiated clusters of  $\text{IH}^{2-}$  and  $\text{IS}^{3-}$ .

#### 4.4 Further Discussion

In general, the anionic monosaccharides and disaccharides investigated in this work fragment along pathways that are primarily determined by their excess charges. In the low-energy CID studies, the monoanions are relatively stable compared to the multiply charged saccharides which fragment at much lower relative collision energies. This reflects the intrinsic instability of small, multiply charged molecular ions in the gas-phase. In both the high-energy and low-energy collision experiments, the dianionic and trianionic saccharides are susceptible to fragmenting *via* Coulombic explosion, which is typically the lowest barrier pathway for activated decay of gas-phase multiply charged anions.

Decay *via* electron detachment of the multiply-charged saccharide anions is also evident in the high-energy collision experiments. This contrasts with the low-energy CID experiments, where electron detachment from small multiply-charged anions is not generally observed.<sup>30</sup> Initial electron loss is often followed by further fragmentation, leading to ions that are not formed in low-energy CID. One of the striking features about the data obtained for the multiply-charged saccharide anions is that the electron detachment fragment ions appear with very low intensity, in

contrast to other multiply charged anions that have been studied in high-energy collision experiments.<sup>16-21</sup> For example, in a study of the  $[\text{d}(\text{A})_x - n\text{H}]^{n-}$  ( $x = 7,5$  and  $n = 1-6$ ) oligonucleotides, the single electron loss fragment ions were dominant in the fragment ion mass spectrum.<sup>20</sup>

The low intensity of the electron detachment fragments for the multiply-charged saccharide anions is likely due to the fact that these systems are susceptible to further rapid fragmentation following electron loss. It is useful, in this context to compare the high-energy collision results obtained here with electron detachment dissociation (EDD) results for similar systems.<sup>22,42</sup> In EDD experiments on  $[\text{M}-2\text{H}]^{2-}$  sulphated sugars, the electron detachment product ions are indeed also small, a fact that was attributed to electron loss occurring from the sulphate group, leaving a sulphate radical that is susceptible to  $\text{SO}_3$  loss. This loss channel would appear to be evident in the systems studied here where fragment ions are observed corresponding to loss of an  $\text{SO}_3^-$  unit (equivalent to loss of  $e^-$  followed by loss of neutral  $\text{SO}_3$ ).<sup>43</sup> It is interesting to note that in EDD experiments on sugars that contained deprotonated carboxylate and sulphate groups, no electron loss was observed from the sulphate group. Electron loss, followed by decarboxylation, is thought to occur preferentially from the carboxylate group since the electron binding energy of sulphate is considerably higher than that of carboxylate. In the high-energy collisions studied here, however, systems such as  $\text{IH}^{2-}$  with both deprotonated carboxylates and sulphate groups, do not decay preferentially by electron loss followed by decarboxylation, presumably due to the higher energy available in the collision. This illustrates one way in which the high-energy CID experiments performed in this study can complement EDD measurements.

The fragmentation patterns of the sodiated-multiply charged sugar clusters are characteristic of smaller cation-dianion clusters that have been studied previously.<sup>34-36</sup> In these simpler complexes (*e.g.*  $\text{K}^+\cdot\text{Pt}(\text{CN})_4^{2-}$ ), the cluster fragmentation is characteristic of the dianion, for example when the dianion fragments with production of  $\text{Pt}(\text{CN})_3^-$  and  $\text{CN}^-$ ,



the related cation-dianion cluster fragments as follows,



These results indicate that the electronic structure of the dianion is not significantly perturbed within the cation-dianion complex and hence the clusters represent true ion-pairs. Since the sodiated-multiply charged sugar clusters studied here also appear to correspond to ion-pairs, it is reasonable to assume that similar sodiated-anionic sugar complexes will fragment in a manner that can be straightforwardly interpreted. This could be useful from an analytical perspective since sodiated-anionic sugar complexes are frequently more dominant in ESI-MS than the unsodiated analogues,<sup>45</sup> and are intrinsically more robust due to the reduced overall charge of the complex.

Unsurprisingly, high-energy collisional activation does produce a greater number of fragment ions than low-energy CID. This should be beneficial for obtaining diagnostic information about the saccharide structures, but the nature of the fragment ions is also important. In particular, it is desirable that the fragment ions retain the crucial sulphate groups. The high-energy results obtained in this study are promising in this respect. For the A, B<sup>2-</sup>, and C<sup>2-</sup> monosaccharides, the high-energy fragmentation mass spectra display ions associated with cross-ring fragmentation with retained sulphate groups. In addition, the <sup>0,3</sup>X<sub>0</sub><sup>-</sup> cross-ring fragment is also evident for C<sup>2-</sup> but not for B<sup>2-</sup>. This is of particular interest since it suggests that this fragment may represent a high-energy diagnostic fragment for identifying the location of the sulphate group. The presence of the <sup>0,2</sup>X<sub>0</sub><sup>-</sup> fragment in both the B<sup>2-</sup> and C<sup>2-</sup> spectra demonstrates the general utility of the high-energy technique, since it is present irrespective of the sulphate position and without loss of the sulphate group.

Another example of the diagnostic utility of the high-energy fragmentation technique for providing crucial structural information is illustrated by the  $\text{IH}^{2-}$  disaccharide results. This molecular anion shares its  $m/z$  value with the related  $\text{IIS}^{2-}$  and  $\text{IIIS}^{2-}$  Heparin sub-units, which are often found together in mixtures with  $\text{IH}^{2-}$ .<sup>46</sup> Low-energy CID of  $\text{IH}^{2-}$  results in production of  $^{0,2}\text{A}_2^{2-}$  as the major fragment ion, along with  $\text{C}_1^-$  (glycosidic cleavage) and  $[\text{IH}^{2-} - \text{H}_2\text{O}]$ , a set of fragments that are insufficient to structurally characterize the disaccharide. In contrast, the high-energy spectrum of  $\text{IH}^{2-}$  displays singly-charged  $^{0,2}\text{A}_1^-$  and  $^{0,2}\text{X}_1^-$  cross-ring fragments, which are highly-diagnostic since they reveal the placement of the sulphate group on the uronic acid.

#### 4.5 Summary

The high-energy collision results for anionic monosaccharides and disaccharides presented in this Chapter illustrate that significantly more structural information can be obtained to characterize the saccharide structures compared to low-energy CID. The fragmentation patterns observed also appear to provide important complementary information to electron detachment dissociation measurements. More generally, the MIKE results illustrate how the application of novel molecular physics techniques can be useful for characterizing the structures of gas-phase biological ions, supplementing more traditional mass spectrometric techniques.

References

1. E.G. Robertson, J.P. Simons, *Phys. Chem. Chem. Phys.* 3 (2001) 1
2. T. Wyttenbach, M.T. Bowers, *Top. Curr. Chem.* 225 (2003) 207
3. P.E. Barran, N.C. Polfer, D.J. Campopiano, D.J. Clarke, P.R.R. Langridge-Smith, R.J. Langley, J.R.W. Govan, A. Maxwell, J.R. Dorin, R.P. Millar, M.T. Bowers, *Int. J. Mass Spectrom.* 240 (2005) 273
4. E. Nir, I. Hünig, K. Kleinermanns, M.S. de Vries, *Phys. Chem. Chem. Phys.* 5 (2003) 4780
5. M. Gerhards, C. Unterberg, A. Gerlach, A. Jansen, *Phys. Chem. Chem. Phys.* 6 (2004) 2682
6. S. Ullrich, G. Tarczay, X. Tong, C.E.H. Dessent, K. Müller-Dethlefs, *Angew. Chem. Int. Ed.* 41 (2002) 166
7. X. Tong, S. Ullrich, C.E.H. Dessent, K. Müller-Dethlefs, *Phys. Chem. Chem. Phys.* 4 (2002) 3578
8. J.A. Stearns, S. Mercier, C. Seaiby, M. Guidi, O.V. Boyarkin, T.R. Rizzo, *J. Am. Chem. Soc.* 129 (2007) 11814
9. S. Wiedemann, A. Metsala, D. Nolting, R. Weinkauf, *Phys. Chem. Chem. Phys.* 6 (2004) 2641
10. S. Brøndsted Nielsen, J.U. Andersen, P. Hvelplund, B. Liu, S. Tomita, *J. Phys. B-At. Mol. Opt. Phys.* 37 (2004) R25
11. S. Denifl, F. Zappa, A. Mauracher, F.F. daSilva, A. Bacher, O. Echt, T.D. Mark, D.K. Bohme, P. Scheier, *ChemPhysChem* 9 (2008) 1387
12. F. Alvarado, J. Bernard, B. Li, R. Bredy, L. Chen, R. Hoekstra, S. Martin, T. Schlatholter, *ChemPhysChem*, 9 (2008) 1254
13. T. Schlathölter, F. Alvarado, S. Bari, A. Lecointre, R. Hoekstra, V. Bernigaud, B. Manil, J. Rangama, B. Huber, *ChemPhysChem* 7 (2006) 2339
14. B.P. Marinković, F. Blanco, D. Šević, V. Pejčev, G. Garcia, D.M. Filipović, D. Pavlović, N.J. Mason, *Int. J. Mass Spectrom.* 277 (2008) 300
15. R.J. Linhardt, T. Toida, *Acc. Chem. Res.* 37 (2004) 431
16. A.B. Nielsen, P. Hvelplund, B. Liu, S. Brøndsted Nielsen, S. Tomita, *J. Am. Chem. Soc.* 125 (2003) 9592
17. M.O. Larsson, P. Hvelplund, M.C. Larsen, H. Shen, H. Cederquist, H.T. Schmidt, *Int. J. Mass Spectrom.* 177 (1998) 51
18. R.M. Burke, W.E. Boxford, S. Panja, S. Brøndsted Nielsen, C.E.H. Dessent, *Chem. Phys. Lett.* 442 (2007) 201
19. W.E. Boxford, M.O.A. El Ghazaly, C.E.H. Dessent, S. Brøndsted Nielsen, *Int. J. Mass Spectrom.* 244 (2005) 60
20. B. Liu, P. Hvelplund, S. Brøndsted Nielsen, S. Tomita, *Int. J. Mass Spectrom.* 230 (2003) 19; P. Hvelplund, B. Liu, S. Brøndsted Nielsen, S. Panja, J.-C. Pouilly, K. Støchkel, *Int. J. Mass Spectrom.* 263 (2007) 66
21. S.Y. Ovchinnikov, J. Macek, A.A. Tuiman, J.D. Steill, R.N. Compton, P. Hvelplund, A.I.S. Holm, S. Brøndsted Nielsen, M.B. Nielsen, *Phys. Rev. A* 73 (2006) 064704

22. J.J. Wolff, I.J. Amster, L. Chi, R.J. Lindhardt, *J. Am. Soc. Mass Spectrom.* 18 (2007) 234
23. J.J. Wolff, L. Chi, R.J. Linhardt, I.J. Amster, *Anal. Chem.* 79 (2007) 2015
24. J.T. Adamson, K. Håkansson, *Anal. Chem.* 79 (2007) 2901
25. A. Varki, R. Cummings, J. Esko, H. Freeze, G. Hart, J. Marth, *Essentials of Glycobiology*, Cold Spring Harbor Laboratory Press, 1999
26. O.M. Saad, J.A. Leary, *Anal. Chem.* 75 (2003) 2985
27. W.E. Boxford, J.K. Pearce, C.E.H. Dessent, *Chem. Phys. Lett.* 399 (2004) 465
28. B. Domon, C.E. Costello, *Glycoconjugate J.* 5 (1988) 397
29. O.M. Saad, J.A. Leary, *J. Am. Soc. Mass Spectrom.* 15 (2004) 1274
30. W.E. Boxford, C.E.H. Dessent, *Phys. Chem. Chem. Phys.* 8 (2006) 5151
31. R.M. Burke, J.K. Pearce, W.E. Boxford, A. Bruckmann, C.E.H. Dessent, *J. Phys. Chem. A* 109 (2005) 9775
32. M.K. Scheller, R.N. Compton, L.S. Cederbaum, *Science* 270 (1995) 116
33. D. Schröder, *Ang. Chem. Int. Ed.* 43 (2004) 1329
34. R.M. Burke, W.E. Boxford, C.E.H. Dessent, *J. Chem. Phys.* 126 (2007) 064308
35. R.M. Burke, W.E. Boxford, C.E.H. Dessent, *J. Chem. Phys.* 125 (2006) 021105
36. W.E. Boxford, R.M. Burke, C.E.H. Dessent, *Phys. Scripta* 76 (2007) C56
37. D.R. Hide (ed), *Handbook of chemistry and physics*, CRC Press, Boca Raton (2000)
38. E.P. Serjeant and B. Dempsey, *Ionization Constants of Organic Acids in Solution*, Iupac Chemical Data Series No. 23, Pergamon Press, Oxford, U.K., 1979
39. H.P. Hopkins, C.H. Wu, L.G. Hepler, *J. Phys. Chem.* 69 (1965) 2244
40. The quoted  $pK_a$  values are for bulk aqueous solution. The gas-phase  $pK_a$ s are unavailable for these species. Ref [41] discusses the issue of solution versus gas-phase deprotonation in electrospray.
41. Z.X. Tian, S.R. Kass, *J. Am. Chem. Soc.* 130 (2008) 10842
42. J.J. Wolff, T.N. Laremore, A.M. Busch, R.J. Linhardt, I.J. Amster, *J. Am. Soc. Mass Spectrom.* 19 (2008) 790
43. The product ion peaks corresponding to loss of  $SO_3^-$  from parent ions that are observed in our MIKE experiments may correspond to loss of either an  $SO_3^-$  ion from the parent or for electron detachment followed by loss of neutral  $SO_3$ . We anticipate that both processes occur: the fragment ions corresponding to electron detachment from the parent appear with such low intensity, implying that  $e^- + SO_3$  loss is common. We also observe the  $SO_3^-$  ion as a product ion, suggesting that direct  $SO_3^-$  loss occurs. However, the kinetic energy release for formation of  $SO_3^-$  and the corresponding (parent ion –  $SO_3^-$ ) fragment ion is low,<sup>44</sup> which indicates that this pair of anions are not formed in the same dynamical process.
44. G. Bojesen, P. Hvelplund, T.J.D. Jørgensen, S. Brøndsted Nielsen, *J. Chem. Phys.* 113 (2000) 6608

45. L. Jin, P.E. Barran, J.A. Deakin, M. Lyon, D. Uhrin, *Phys. Chem. Chem. Phys.* 7 (2005) 3464
46. J. R. Behr, Y. Matsumoto, F.M. White, R. Sasisekharan, *Rapid Commun. Mass Spectrom.* 19 (2005) 2553

## Chapter 5

### **Computational Studies of the Gas-Phase Conformers of the Anionic Iduronate (2-O-sulfo- $\alpha$ -L-iduronate) Monosaccharide: Variation of sub-conformer versus ring conformer for a prototypical anionic sugar.**

#### 5.1 Introduction

Complex oligosaccharides play crucial roles in the extracellular environment, for example, controlling cell adhesion and regulating growth mechanisms.<sup>1,2</sup> Characterization of the conformations of oligosaccharides is essential for understanding their biological activity, and therefore represents an area of intense current scientific activity. For *neutral* sugar systems, Simons and co-workers have recently used IR spectroscopy to successfully characterize a number of small carbohydrate molecules.<sup>3</sup> Such experimental work is of crucial importance since the data obtained allows for benchmarking of computational results obtained for these systems. However, there are currently no gas-phase laser spectroscopy studies of *charged* sugars, despite the fact that negatively charged sugars are constituents of a great number of extremely important biological systems. Glycosaminoglycans (GAGs), which include the heparin and heparin sulphate biopolymers,<sup>4</sup> represent an important class of biologically active anionic sugar molecules found on the surface of almost all animal cells.<sup>5</sup> GAGs are characterized by possessing strongly acidic carboxylic and sulphate groups that are readily deprotonated under physiological conditions so that the systems typically carry multiple negative charges.<sup>2</sup> It should be noted that there have been numerous mass-spectrometric studies of heparin and heparin sulphate species, which have focussed on the saccharides' primary structures.<sup>6-10</sup> In addition, a small number of gas-phase studies have employed mass spectrometric techniques to probe the physical chemistry of these systems.<sup>11-12</sup>

Due to the fact that there have been only very limited spectroscopic and thermodynamic studies of saccharide molecules in the gas-phase, theoretical approaches to studying saccharides are currently hampered by significant uncertainties in the semi-empirical parameters required for molecular mechanics calculations.<sup>13</sup> Simons et. al. have previously used the B3LYP and MP2 methods to interpret their spectroscopic data for neutral sugars<sup>14</sup> with recent computational work highlighting the need for a proper treatment of dispersion interactions in these systems. Modifications to traditional DFT functionals to address this issue have also been investigated.<sup>15,16</sup>

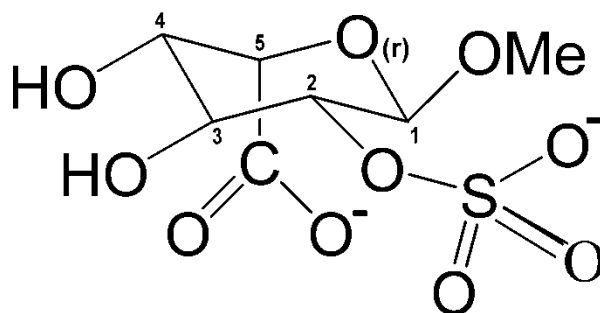


**Fig. 5.1** Doubly deprotonated Iduronic Acid (Methyl 2-O-sulfo- $\alpha$ -L-iduronate).

In this Chapter, computational methods are used to explore the conformational isomerism of the prototypical monomeric anionic sugar, doubly deprotonated iduronate (Methyl 2-O-sulfo- $\alpha$ -L-iduronate or IdoA2S), which is illustrated in Fig. 5.1. There have been a small number of previous studies of related anionic saccharides using density functional theory, with Hricovini having performed B3LYP/6-311++G\*\* calculations on the disodium salt of doubly deprotonated methyl 2-O-sulfo- $\alpha$ -L-iduronate,<sup>17</sup> and Remko and von der Lieth studying the doubly deprotonated dianions and disodium salts of the methylated 1,4 DiOMe IdoA2S derivative.<sup>18</sup> In this work the isolated anions have been selected for study, rather than the counterion complexed species, as there is evidence to suggest that these sugars behave more like independent ions in a biological environment, with

the counterions located around the multiply charged anions, rather than being tightly bound in a mixed-charge complex as in the gas phase. There are currently no higher-level wavefunction based computational studies of either these bare anions or their counterion complexes. The lack of higher-level calculations is surprising, given that calculations at the MP2 level have been shown to be necessary for characterizing the conformational energies of neutral saccharides.<sup>19</sup> Indeed, intersite electron correlation can be expected to play an important role in determining the structures of sugar molecules due to the presence of anomeric effects.<sup>20</sup> In this study the first fully optimized MP2 calculations of prototypical anionic saccharide monomers have therefore been performed, along with selective DFT calculations for comparison. In particular, the performance of the PW91PW91 and MO5-2X functionals against MP2 is evaluated since these functionals are expected to provide a better representation of van der Waals interactions than more common functionals such as B3LYP. The *ab initio* results presented will also be discussed in the context of MMFF94 molecular mechanics results for the same system, to allow some comparison against one of the most popular current force fields.

The three dimensional structure of a system such as  $IA^{2-}$  can primarily be described by the conformation adopted by the sugar ring, although sub-conformers that are associated with the conformational flexibility of the pendant functional groups also exist for each ring conformer. The existence of such sub-conformers has been largely ignored in the previous DFT studies of anionic monosaccharides.<sup>17,18</sup> The extended conformational space of  $IA^{2-}$  is explored with full optimizations on all of the sub-conformers obtained being performed. This full set of optimizations is essential to allow a proper investigation of the importance of sub-conformers in obtaining reliable computational conclusions about such systems.

## 5.2 Computational Methods

Low energy conformers for  $IA^{2-}$  (doubly deprotonated Methyl 2-O-sulfo- $\alpha$ -L-iduronate) were generated via conformational searching as implemented in

SPARTAN.<sup>21</sup> The default parameters were used including an initial temperature of 5000K (all of the low energy conformers generated were saved). The initial starting structures were refined using molecular mechanics based on the Merck Molecular Force Field (MMFF94),<sup>22</sup> prior to performing the conformational searches. Calculations were conducted only for the doubly deprotonated tautomer corresponding to deprotonation at the carboxylate and sulphate groups (Fig. 5.1). Initial conformer searching failed to produce any  ${}^1C_4$  conformers, presumably due to inadequacies of the force field in relation to saccharides.<sup>13</sup> However, these conformers have been located as minimum energy structures in previous computational studies<sup>17,18</sup> and are known to play a crucial role in determining the strength of Heparin interactions with proteins.<sup>3</sup> To generate structures of  $IA^{2-}$  associated with the  ${}^1C_4$  conformation, ring structures were therefore constrained during conformer searching. It is highly likely that there will be inadequacies associated with any of the currently available force fields for generating low-energy conformers, although this should not adversely affect the primary goals of this study, *i.e.* to evaluate the energetic differences between conformers and sub-conformers of  $IA^{2-}$  at higher levels of theory and to compare the performance of the selected density functionals against MP2. (MMFF94 was the force-field chosen here due to its widespread application. Also, it has recently been assessed to provide the best performance from amongst the traditional fixed charge force fields for small, charged peptides.<sup>23</sup>)

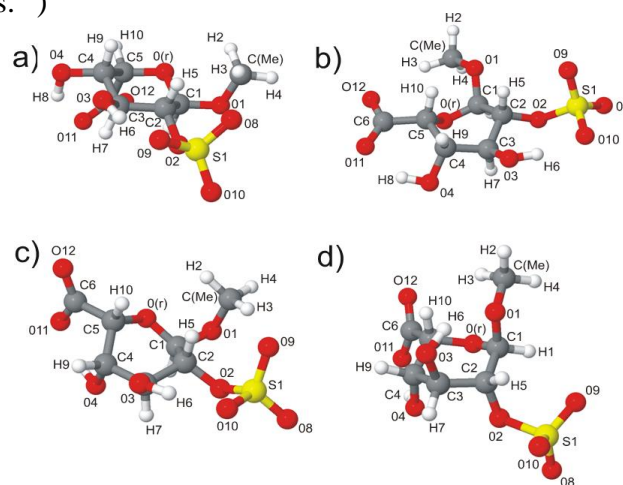


**Fig. 5.2 Sugar ring conformers for doubly deprotonated methyl 2-O-sulfo- $\alpha$ -L-iduronate illustrating the a)  ${}^4C_1$ , b)  ${}^2S_0$ , c)  ${}^1S_5$  and d)  ${}^1C_4$  conformations.**

Seventeen conformers of  $\text{IA}^{2-}$  were generated using the MMFF94 force field in SPARTAN as described in Section 5.2.  $\text{IA}^{2-}$  was found to exist in four ring-conformeric structures,  ${}^4\text{C}_1$  (Fig. 5.2a),  ${}^2\text{S}_0$  (Fig. 5.2b),  ${}^1\text{S}_5$  (Fig. 5.2c) and  ${}^1\text{C}_4$  (Fig. 5.2d) based on the orientation of the sugar-ring carbons and oxygen atom. S refers to a skew-boat type structure, with C referring to a chair structure; the superscripts and subscripts refer to the ring atoms that occupy the highest and lowest positions on the ring, respectively, with the ring-oxygen always counted as 0 and the other ring atom numbers defined relative to this atom in a clockwise direction.

Sub-conformers obtained by the conformational searching process described above were fully optimised using several *ab initio* methods. (It was not necessary to adopt the “family” grouping approach developed recently in our group<sup>24,25</sup>) Conformers were fully optimized at the B3LYP/6-31++G\*\*, PW91PW91/6-31++G\*\*, and MP2/6-31++G\*\* levels using Gaussian 03<sup>26</sup>, and frequency calculations were performed in all cases to ensure that the optimized structures corresponded to true minima. The PW91PW91 functional was selected since it has previously been shown to perform well against MP2 benchmark calculations for systems where correlation effects are important<sup>27-30</sup>. Finally, the conformers were also optimised at the MO5-2X/6-31++G\*\* level to compare the performance of the new MO5-2X functional<sup>31,32</sup> against the MP2 optimisations.

### 5.3 Results and Discussion

#### **5.3.1 Sub-Conformer Structures**

Fig. 5.3 displays all of the  $\text{IA}^{2-}$  sub-conformers (MP2/6-31++G\*\*) studied here to illustrate the structural variation within the conformeric groups. The  ${}^1\text{S}_5$  conformation does not appear to have been recognized for IA (or the methylated analogues) previously.<sup>17,18</sup> This figure illustrates that the majority of conformeric minima adopt a  ${}^4\text{C}_1$  geometry (generally an indicator that this is the lowest energy ring conformer). In general, structural changes were modest upon optimization at the different levels of theory employed, particularly between the *ab initio* calculated

structures. Referencing all calculated structures to those found at the MP2 level, one of the  ${}^2S_0$  structures at the MP2 level became a  ${}^1S_5$  structure with B3LYP whilst one  ${}^1C_4$  (MP2) structure rearranged to a  ${}^2S_0$  conformer with B3LYP. In addition, two of the MP2  ${}^2S_0$  optimised structures were originally  ${}^1C_4$  conformers at the molecular mechanics (MMFF94) level.

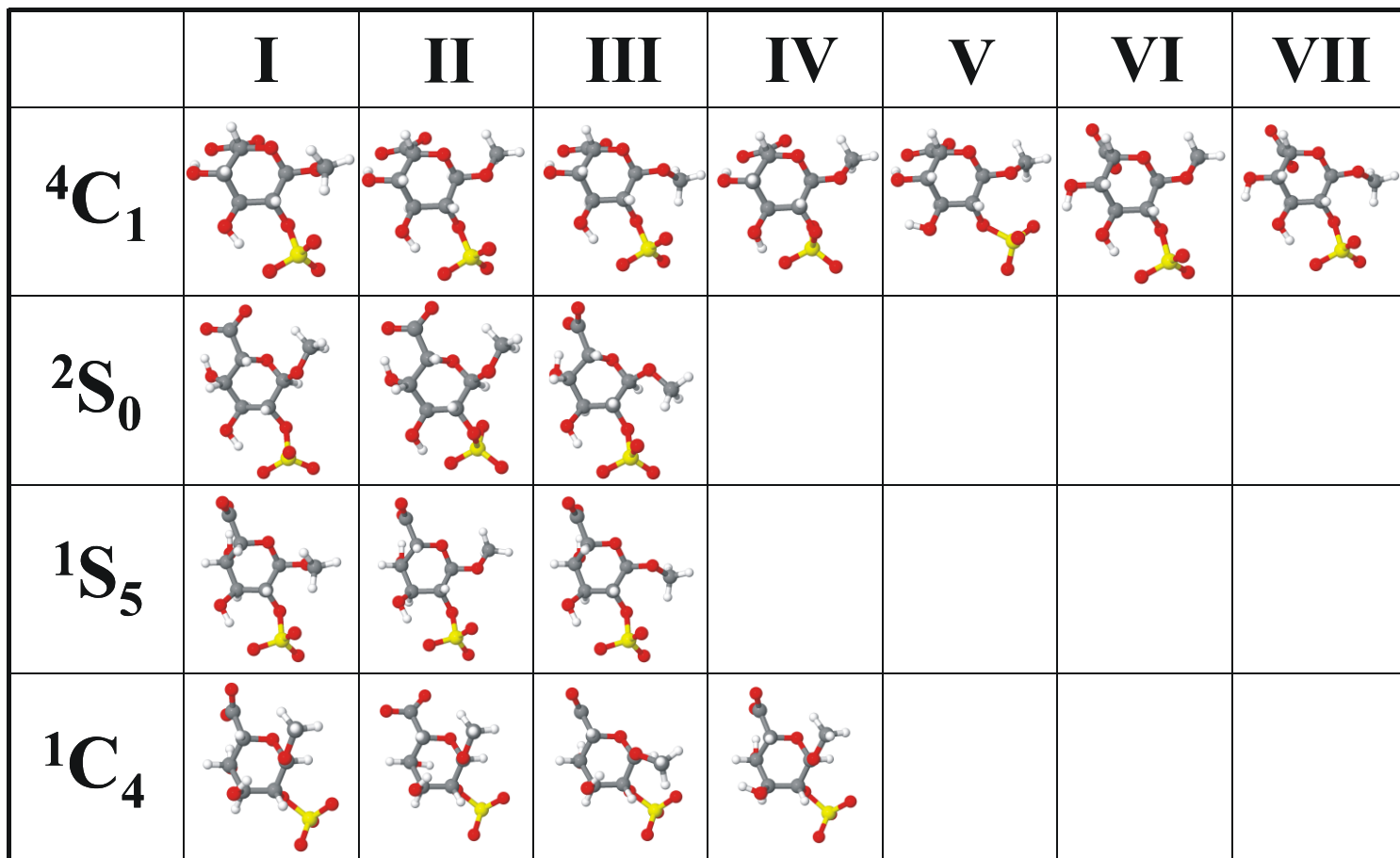


**Fig. 5.3** Optimized conformers (MP2/6-31++G\*\*) of doubly deprotonated methyl 2-O-sulfo- $\alpha$ -L-iduronate grouped according to sugar ring conformation and displayed with increasing energy (within conformers) from left to right.

Table 5.1 presents a list of some of the key hydrogen-bonding interactions that are present in the  $IA^{2-}$  sub-conformer structures, indicating which interactions are present in which conformer. The hydrogen-bonding interactions are classified as either typical (T) or loose (L) “hydrogen-bond-like” interactions.<sup>33,34</sup> Each

conformer is associated with a particular combination of either two or three hydrogen-bonds, with the strong electrostatic C(3)-OH $\cdots$ SO $_3^-$  and C(4)-OH $\cdots$ CO $_2^-$  interactions being the most prevalent. Remko and von der Leith have studied the dianions of methylated 1,4 DiOMe IndoA2S previously,<sup>18</sup> and found that the C(3)-OH group was involved in the key non-covalent interactions for each of the  $^4C_1$ ,  $^2S_0$ , and  $^1C_4$  conformers studied. This is in line with the results presented here since only the very high energy sub-conformer IV of  $^1C_4$  displays no interactions of the C(3)-OH. Table 5.1 will be discussed again in the context of the isomer energies in Section 5.3.2

Table 5.2 presents the key C(4)-OH $\cdots$ CO $_2^-$ , C(3)-OH $\cdots$ SO $_3^-$  and OMe $\cdots$ SO $_3^-$  hydrogen bond lengths, calculated at the various levels of theory employed. The short bond lengths observed for the C(4)-OH $\cdots$ CO $_2^-$  and C(3)-OH $\cdots$ SO $_3^-$  interactions ( $\sim 1.85$  and  $\sim 1.70$  Å, respectively, at the MP2 level) are characteristic of strong electrostatic hydrogen bonds. For the C(4)-OH $\cdots$ CO $_2^-$  interaction, the B3LYP values are generally within 0.01 Å of the MP2 values, with the PW91PW91 values being smaller than the MP2 values by an average of 0.09 Å. Similar trends are evident for the C(3)-OH $\cdots$ SO $_3^-$  values, indicating that B3LYP is performing well against the MP2 benchmark for these relatively tight hydrogen bonds. However, for the looser OMe $\cdots$ SO $_3^-$  interaction, where correlation may be more important, this trend is reversed with the PW91PW91 results being closer to the MP2 values than the B3LYP results. Comparison of the MO5-2X and MP2 results reveals that MO5-2X gives bond lengths that are impressively close to the MP2 values for both the C(3)-OH $\cdots$ SO $_3^-$  and OMe $\cdots$ SO $_3^-$  interactions.

**Table 5.1: Key non-covalent interactions present in the MP2/6-31++G\*\* level sub-conformers of IA<sup>2-</sup>.**<sup>a</sup>

	<sup>4</sup> C <sub>1</sub>	<sup>4</sup> C	<sup>4</sup> C <sub>1</sub>	<sup>1</sup> S <sub>5</sub>	<sup>1</sup> S <sub>5</sub>	<sup>1</sup> S <sub>5</sub>	<sup>2</sup> S <sub>0</sub>	<sup>2</sup> S <sub>0</sub>	<sup>2</sup> S <sub>0</sub>	<sup>1</sup> C <sub>4</sub>	<sup>1</sup> C <sub>4</sub>	<sup>1</sup> C <sub>4</sub>	<sup>1</sup> C <sub>4</sub>				
	I	II	III	IV	V	VI	VII	I	II	III	I	II	III	I	II	III	IV
<b>C(3)-OH...SO<sub>3</sub><sup>-</sup></b>	T	T	T	L		T	T	T	T	T	T	L					
<b>C(4)-OH...CO<sub>2</sub><sup>-</sup></b>	L	L	L	L	L			L	L	L	L	L	T	L		L	L
<b>OMe...CO<sub>2</sub><sup>-</sup></b>		L		L							L	L		L			L
<b>OMe...SO<sub>3</sub><sup>-</sup></b>	T		L		L		L	T		L			T			L	
<b>C(3)-OH...C(4)-OH</b>					L												
<b>C(4)-OH...C(3)-OH</b>						L	L										
<b>C(3)-OH...MeO</b>													T	L	L	L	
<b>C(4)-OH...SO<sub>3</sub><sup>-</sup></b>																L	

<sup>a</sup> T denotes a typical hydrogen-bonding interaction, while L denotes a loose “hydrogen-bond-like” interaction<sup>33,34</sup>

**Table 5.2: Bond lengths (in Å) for the optimized sub-conformers of IA<sup>2-</sup>.**

	<sup>4</sup> C <sub>1</sub>	<sup>1</sup> S <sub>5</sub>	<sup>1</sup> S <sub>5</sub>	<sup>1</sup> S <sub>5</sub>	<sup>2</sup> S <sub>0</sub>	<sup>2</sup> S <sub>0</sub>	<sup>2</sup> S <sub>0</sub>	<sup>1</sup> C <sub>4</sub>	<sup>1</sup> C <sub>4</sub>	<sup>1</sup> C <sub>4</sub>	<sup>1</sup> C <sub>4</sub>						
	I	II	III	IV	V	VI	VII	I	II	III	I	II	III	I	II	III	IV
<b>C(3)-OH<sup>•••</sup>SO<sub>3</sub><sup>-</sup></b>																	
MMFF	1.67	1.65	1.82	1.76		1.62	1.64	1.65	1.65	1.66		1.74					
B3LYP	1.85	1.83	1.85	1.88		1.77	1.79	1.83	1.82	1.84	1.83	1.88	1.83	1.83			
PW91	1.81	1.79	1.82	1.83		1.72	1.74	1.78	1.77	1.80	1.80	1.83	1.80				
MO5-2X	1.85	1.84	1.89	1.90		1.77	1.81	1.81	1.84	1.85	1.85	1.87	1.86				
MP2	1.85	1.84	1.87	1.90		1.78	1.81	1.82	1.82	1.66	1.84	1.87					
<b>C(4)-OH<sup>•••</sup>COO<sup>-</sup></b>																	
MMFF	1.81	1.78	1.64	1.74	1.71			1.74	1.71	1.72	1.76	1.68	1.73			1.74	1.76
B3LYP	1.68	1.69	1.69	1.67	1.65			1.69	1.7	1.69	1.69	1.68	1.67	1.67		1.71	1.69
PW91	1.63	1.64	1.64	1.61	1.59			1.63	1.63	1.63	1.64	1.62	1.61	1.66		1.64	1.62
MO5-2X	1.66	1.68	1.67	1.64	1.59			1.66	1.68	1.67	1.72	1.72	1.65	1.76		1.73	1.70
MP2	1.69	1.71	1.70	1.68	1.66			1.71	1.72	1.72	1.74	1.74	1.70	1.75		1.75	1.73
<b>OMe<sup>•••</sup>SO<sub>3</sub><sup>-</sup></b>																	
MMFF	2.63		3.33		3.02		3.02	2.67		2.77			2.91				2.89
B3LYP	2.39		3.35		2.46		3.43	2.45		3.44			2.46	2.46			2.91
PW91	2.34		3.33		2.43		3.45	2.41		3.40			2.42				2.91
MO5-2X	2.27		3.07		2.47		3.19	2.43		3.38			2.35				2.61
MP2	2.29		3.12		2.62		3.22	2.36		3.35			2.40				2.79

In general, the conformer-dependent variations in the bond lengths within the sugar ring are smaller than those of the non-covalent interactions, with the largest differences between ring parameters occurring in the C(1)-O(1) [0.065 Å], C(1)-O(r) [0.045 Å], and C(5)-O(r) [0.024 Å] bond lengths (MP2/6-31++G\*\*) associated with the anomeric O(1) and O(r).

Variations in the other geometrical parameters, bond angles and torsional angles (Tables 5.3, 5.4 and 5.5) were also largest in the anomeric part of the molecule [e.g. O(r)-C(1)-O(1), O(1)-C(1)-C(2), C(1)-O(1)-C(Me)]. A comparison of the bond and torsional angles obtained at the various levels of theory illustrates that the bond angles do not vary much at the different levels, whereas for the torsional angles, the MO5-2X and PW91PW91 functionals give better agreement with the MP2 results compared to B3LYP (Table 5.5).

The atomic charges from a Mulliken population analysis for the atoms of the lowest energy sub-conformers of IA<sup>2-</sup> (MP2/6-31++G\*\*) are displayed in Table 5.6 for reference. Differences in the partial charges between the various sub-conformers reflect the degree of non-covalent interactions present between groups attached to the ring. For example, the typical hydrogen-bonding 3OH...SO<sub>3</sub><sup>-</sup> interaction that exists in sub-conformer I of <sup>4</sup>C<sub>1</sub> is evident in the charges of the C(3), O(3), and O(9) atoms.

**Table 5.3: Selected bond angles (MP2/6-31++G\*\*) of the sub-conformers of the  ${}^4C_1$ ,  ${}^2S_0$ ,  ${}^1S_5$ , and  ${}^1C_4$  ring-conformers of IA $^{2-}$ .**

Bond Angle	${}^4C_1$	${}^1S_5$	${}^1S_5$	${}^1S_5$	${}^2S_0$	${}^2S_0$	${}^2S_0$	${}^1C_4$	${}^1C_4$	${}^1C_4$	${}^1C_4$						
	I	II	III	IV	V	VI	VII	I	II	III	I	II	III	I	II	III	IV
O(r)-C(1)-C(2)	109.1	110.1	110.4	107.1	112.6	110.9	110.7	110.2	112.2	112.0	113.2	111.9	113.6	114.5	113.7	115.1	114.3
O(r)-C(1)-O(1)	107.7	107.0	104.4	107.0	105.9	106.2	103.9	107.6	107.5	104.5	111.5	111.1	107.3	110.9	111.6	108.8	111.3
O(1)-C(1)-C(2)	114.3	109.7	110.9	110.4	108.5	108.7	110.7	114.3	112.2	112.0	107.2	106.6	112.0	105.3	105.9	107.2	107.2
C(1)-C(2)-C(3)	111.1	110.3	112.2	108.6	109.2	108.8	110.2	110.1	110.8	111.9	110.7	110.3	111.7	111.2	111.1	111.2	114.3
C(1)-O(1)-CMe	115.0	110.9	113.2	110.3	112.8	111.2	112.9	114.1	111.4	113.8	111.4	111.1	113.2	111.5	111.1	111.1	111.2
S(1)-O(2)-C(2)	118.0	118.0	118.3	120.7	119.7	117.9	118.2	116.6	116.3	116.7	119.0	121.1	119.4	112.7	113.8	111.8	113.5

**Table 5.4: Selected bond angles (in degrees) for the lowest-energy sub-conformers of the  ${}^4C_1$ ,  ${}^2S_0$ ,  ${}^1S_5$ , and  ${}^1C_4$  ring-conformers of IA $^{2-}$ .**

Bond Angle	B3LYP/6-31++G**				PW91/PW91/6-31++G**				MO5-2X/6-31++G**				MP2/6-31++G**			
	${}^4C_1$	${}^1S_5$	${}^2S_0$	${}^1C_4$	${}^4C_1$	${}^1S_5$	${}^2S_0$	${}^1C_4$	${}^4C_1$	${}^1S_5$	${}^2S_0$	${}^1C_4$	${}^4C_1$	${}^1S_5$	${}^2S_0$	${}^1C_4$
	I	I	I	I	I	I	I	I	I	I	I	I	I	I	I	I
O(r)-C(1)-C(2)	109.1	110.6	113.6	114.0	109.0	110.6	113.7	115.2	108.9	110.0	112.6	114.1	109.1	110.2	113.2	114.5
O(r)-C(1)-O(1)	108.0	107.9	111.6	107.3	107.8	107.7	111.7	111.3	108.1	108.0	111.1	110.6	107.7	107.6	111.5	111.0
O(1)-C(1)-C(2)	114.6	110.6	113.6	111.8	114.8	110.6	113.7	105.0	114.0	113.9	107.8	105.8	114.3	110.2	107.2	105.3
C(1)-C(2)-C(3)	111.2	110.1	111.6	113.2	111.1	109.9	111.5	110.6	110.6	109.9	110.7	111.2	111.1	110.1	110.7	111.2
C(1)-O(1)-CMe	116.9	116.1	113.6	115.4	115.9	115.0	112.2	112.4	115.6	114.7	112.0	112.0	115.1	114.1	111.4	111.5
S(1)-O(2)-C(2)	119.3	118.1	120.5	120.4	118.0	116.7	119.0	113.6	118.8	117.2	112.0	113.6	118.0	116.6	119.0	112.7

**Table 5.5: Torsional angles (in degrees) for the lowest-energy sub-conformers of the  ${}^4C_1$ ,  ${}^2S_0$ ,  ${}^1S_5$ , and  ${}^1C_4$  ring-conformers of  $IA^{2-}$ .**

Torsion Angle	B3LYP/6-31++G**				PW91/PW91/6-31++G**				MO5-2X/6-31++G**				MP2/6-31++G**			
	${}^4C_1$	${}^1S_5$	${}^2S_0$	${}^1C_4$	${}^4C_1$	${}^1S_5$	${}^2S_0$	${}^1C_4$	${}^4C_1$	${}^1S_5$	${}^2S_0$	${}^1C_4$	${}^4C_1$	${}^1S_5$	${}^2S_0$	${}^1C_4$
	I	I	I	I	I	I	I	I	I	I	I	I	I	I	I	I
O(r)-C(1)-O(1)-CMe	64.4	65.5	-54.1	-160.7	66.3	66.7	-52.2	-54.9	62.6	66.6	-50.6	-54.2	63.8	66.5	-52.0	-54.2
C(2)-C(1)-O(1)-CMe	-57.3	-58.2	-179.2	73.6	-55.3	-56.9	-177.3	179.8	-58.7	-55.8	-174.4	-178.2	-57.5	-56.3	-176.4	-178.6
C(3)-C(2)-O(2)-S(1)	-101.5	-94.7	-95.6	-95.8	-100.3	-94.1	-95.6	-141.9	-104.7	-92.3	-100.6	-137.8	-103.1	-93.3	-97.9	-138.0
C(1)-C(2)-O(2)-S(1)	137.3	144.6	143.7	141.9	138.4	145.2	143.7	94.8	135.1	147.4	139.8	99.1	136.2	146.3	142.6	99.1
O(r)-C(1)-C(2)-C(3)	55.4	62.6	17.4	27.8	56.3	63.6	15.5	-46.7	56.9	64.3	17.6	-46.5	56.3	64.0	18.5	-47.1
C(6)-C(5)-O(r)-C(1)	-68.1	-153.2	157.2	165.3	-67.5	-152.7	156.7	174.7	-66.3	-151.2	155.0	171.5	-65.8	-153.8	155.3	172.5
O(r)-C(1)-C(2)-O(2)	176.3	-176.1	137.6	148.2	177.5	-174.7	135.8	77.0	176.7	-174.3	136.6	76.3	176.6	-174.6	138.1	75.3

**Table 5.6: Atomic partial charges from a Mulliken population analysis (MP2/6-31++G\*\*) of the lowest energy  ${}^4C_1$ ,  ${}^2S_0$ ,  ${}^1S_5$ , and  ${}^1C_4$  sub-conformers of IA<sup>2-</sup>.**

	${}^4C_1$ I	${}^1S_5$ I	${}^2S_0$ I	${}^1C_4$ I
C(1)	-0.062	-0.086	-0.077	-0.117
C(2)	-0.260	-0.152	-0.163	-0.014
C(3)	0.471	0.218	0.190	0.027
C(4)	-0.461	0.208	0.173	0.156
C(5)	0.396	-0.180	-0.076	0.030
C(6)	0.489	0.671	0.698	0.597
CMe	0.039	0.044	0.031	0.027
O(1)	-0.408	-0.420	-0.397	-0.437
O(2)	-0.725	-0.712	-0.718	-0.642
O(3)	-0.645	-0.651	-0.643	-0.525
O(4)	-0.575	-0.655	-0.658	-0.602
O(r)	-0.462	-0.466	-0.415	-0.417
O(8)	-0.959	-0.856	-0.865	-0.864
O(9)	-1.019	-0.880	-0.839	-0.901
O(10)	-0.964	-0.935	-0.397	-0.880
O(11)	-1.027	-0.780	-0.788	-0.770
O(13)	-0.898	-0.716	-0.731	-0.735
S(1)	2.582	2.393	2.310	2.242
H(1)	0.195	0.130	0.123	0.162
H(2)	0.080	0.089	0.090	0.088
H(3)	0.145	0.125	0.149	0.132
H(4)	0.093	0.096	0.054	0.081
H(5)	0.120	0.173	0.214	0.153
H(6)	0.489	0.479	0.472	0.446
H(7)	0.115	0.138	0.132	0.144
H(8)	0.478	0.472	0.458	0.472
H(9)	0.089	0.134	0.115	0.093
H(10)	0.134	0.117	0.089	0.056

## 5.3.2 Energies

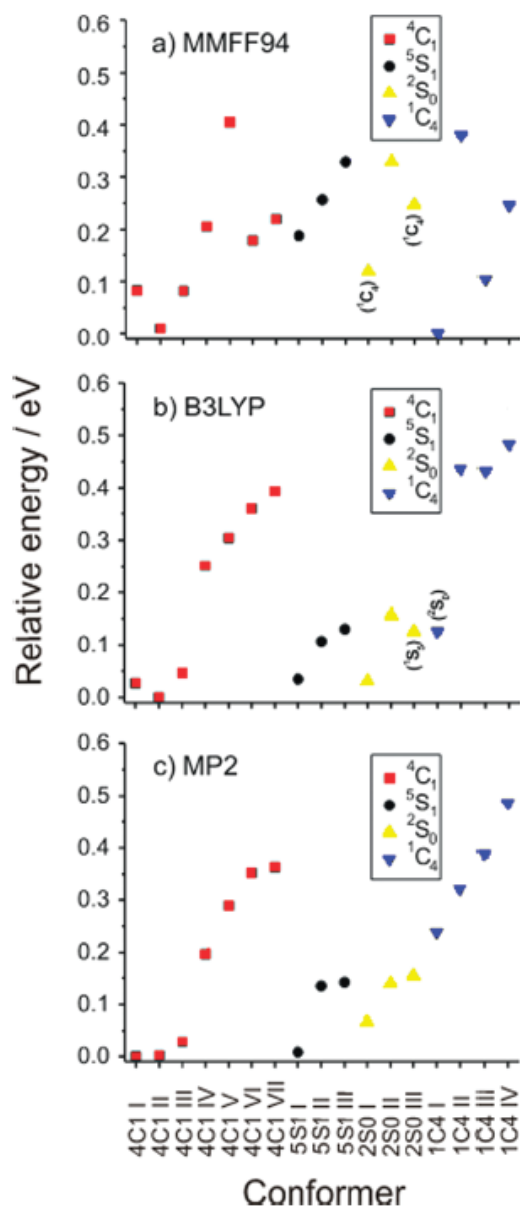


**Fig. 5.4** Energy distribution plots (a-c) MMFF94, B3LYP/6-31++G\*\* and MP2/6-31++G\*\*, for the doubly deprotonated iduronate conformers displayed in Fig. 5.3. The MMFF94 energies were obtained from the conformer search utility in Spartan, whereas the B3LYP and MP2 energies are for the fully optimized structures at the respective levels. Conformer names are given in accordance with the MP2 geometries (as in Fig. 5.3), but where conformers differ upon optimization at the B3LYP and MMFF94 levels, the new conformer-type is labelled in parentheses adjacent to the relevant energy point.

Fig. 5.4 displays energy distribution plots for the optimized iduronate structures, obtained at the MMFF94, B3LYP and MP2 levels. The results clearly demonstrate the need to compare the sub-conformers to obtain an accurate picture of the relative energies of the sugar ring conformers (something that has been neglected in previous work on such systems),<sup>17,18</sup> since the orientations of substituent groups around the sugar ring have a considerable effect on the final energies due to the making or breaking of various hydrogen bonding interactions. In the B3LYP and MP2 calculations, the sub-conformer energies are spread across ~0.5 eV, whereas the spread of energy between the lowest sub-conformers of the various ring-conformations is only ~0.2 eV. Unsurprisingly, there is considerable reorganization of the relative sub-conformer energy ordering between the MMFF94 and B3LYP/MP2 levels. The changes in the relative sub-conformer energetic ordering are much more modest between the B3LYP and MP2 calculations, with the relative energetic ordering of the  ${}^4C_1$  and  ${}^1S_5$  sub-conformers staying the same. (There is some reorganization of the  ${}^2S_0$  and  ${}^1C_4$  sub-conformers.)

Fig. 5.5 displays the energy distribution plots obtained at the MP2, PW91PW91 and MO5-2X levels. It is striking that both the PW91PW91 and MO5-2X calculations give very similar relative energies to the MP2 calculations, indicating that both of these functionals appear to provide a good energetic representation of the inter-site electron correlation in this system. MO5-2X is particularly successful in that it exactly replicates the MP2 energetic ordering of the sub-conformers, with very similar relative energies.

It should be emphasized that, uniquely amongst the DFT approaches used here, MO5-2X reproduces the relative energies of the most stable sub-conformer in each ring-class accurately relative to MP2. The MP2 calculations predict that the lowest energy  ${}^2S_0$  conformer lies ~0.06 eV above the global minimum, with the lowest energy  ${}^1S_5$  conformer at ~0.01 eV. MO5-2X reproduces these differences quantitatively, whereas B3LYP and PW91PW91 predict both the  ${}^2S_0$  and  ${}^1S_5$  conformers at ~0.02 eV relative energy, in poorer agreement with the MP2 results.

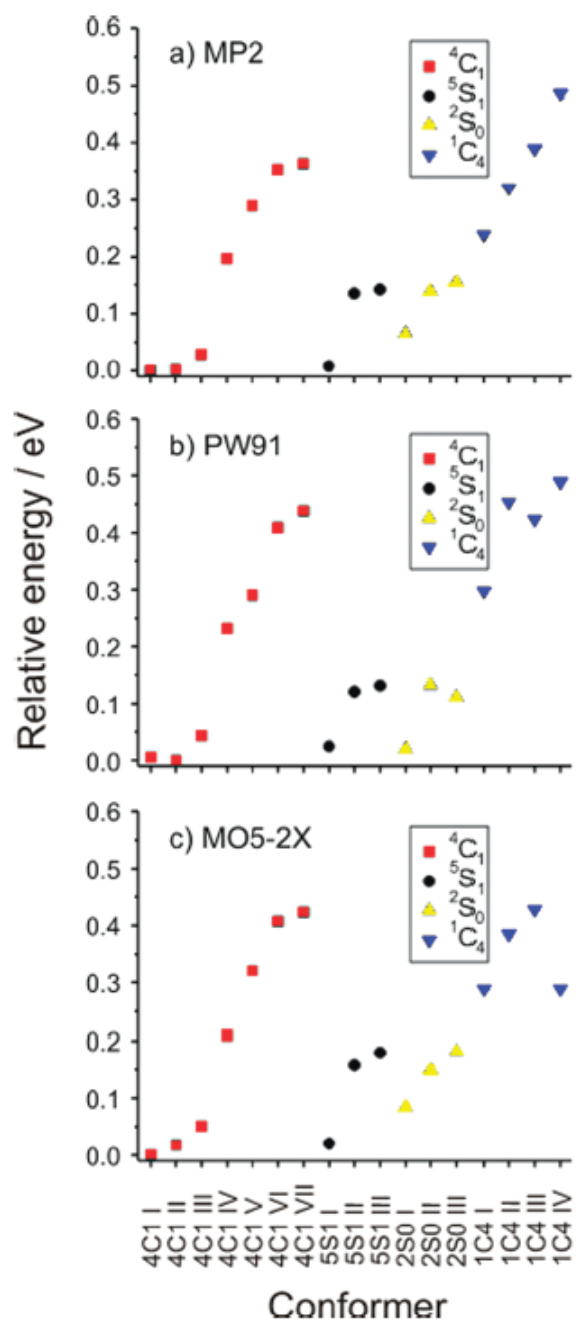


**Fig. 5.5** Energy distribution plots (a-c) MP2/6-31++G\*\*, PW91PW91/6-31++G\*\* and MO5-2X/6-31++G\*\* for the doubly deprotonated iduronate conformers displayed in Fig. 5.3. The MP2, PW91PW91 and MO5-2X energies are for the fully optimized structures at the respective levels. Conformer names are given in accordance with the MP2 geometries (as in Fig. 5.3).

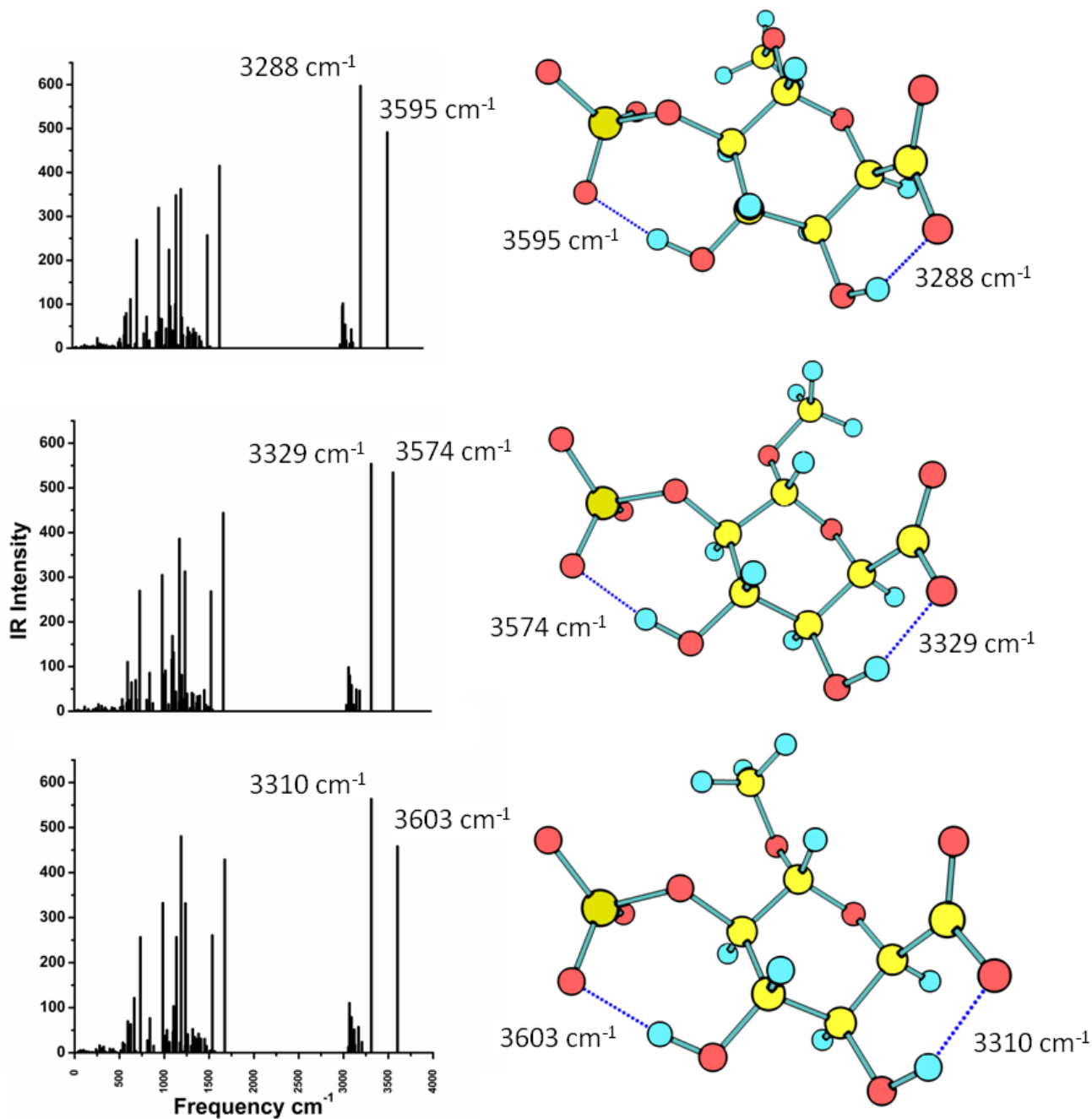
The dominant factor in determining ring conformer energies is the anomeric effect (which should have a minimal contribution to the energy difference between sub-conformers). Therefore it appears that MO5-2X is the most promising density functional studied here for investigating systems where anomeric effects occur.

A comparison of the MP2 relative energies of the sub-conformers (Fig. 5.5a) with the key intermolecular interactions presented in Table 5.1 reveals that in general, the lowest energy sub-conformers (*i.e.*  ${}^4C_1$  I,  ${}^4C_1$  II,  ${}^1S_5$  I, and  ${}^2S_0$  I) are associated with having the greatest number of typical and loose hydrogen-bonding type interactions, particularly those involving the anionic  $SO_3^-$  and  $CO_2^-$  groups. The higher-energy conformers (*e.g.* all of the  ${}^1C_4$  conformers, and sub-conformers V-VII of  ${}^4C_1$ ), in contrast, display proportionally less of these anionic hydrogen-bonding interactions.

#### 5.4 Calculated Infra-red Vibrational Frequencies

Vibrational frequencies were calculated for each conformer identified in order to facilitate future spectroscopic studies of the Iduronate molecule and to ensure that each structure represented a true local minimum. Highlighted here are the features most likely to usefully differentiate between the principal families, while avoiding the densely populated region of the spectrum, followed by those which would enable identification of the sub-families.

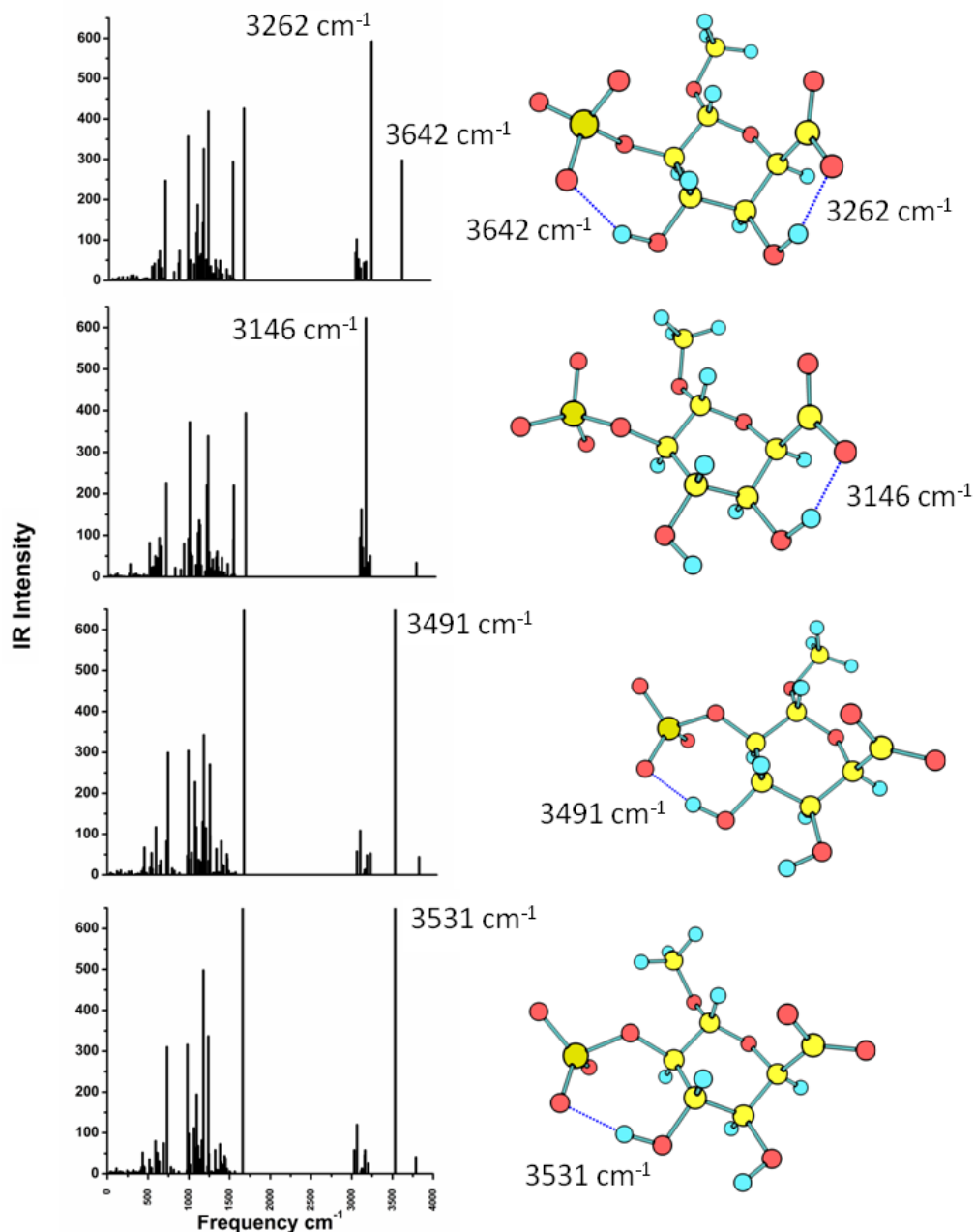
Figure 5.6 displays the calculated spectra for the  ${}^4C_1$  conformers I, II and III. The most prominent spectral features present are those in the hydrogen bonding regions associated with the OH to carboxylate and sulphate groups ( $3100-3800\text{ cm}^{-1}$ ). For  ${}^4C_1$  I to III the network of bonds between these groups is conserved across the three structures, with atom H6's interaction with the sulphate group at approximately  $3600\text{ cm}^{-1}$  and H8 to the carboxylate group at  $3300\text{ cm}^{-1}$ .



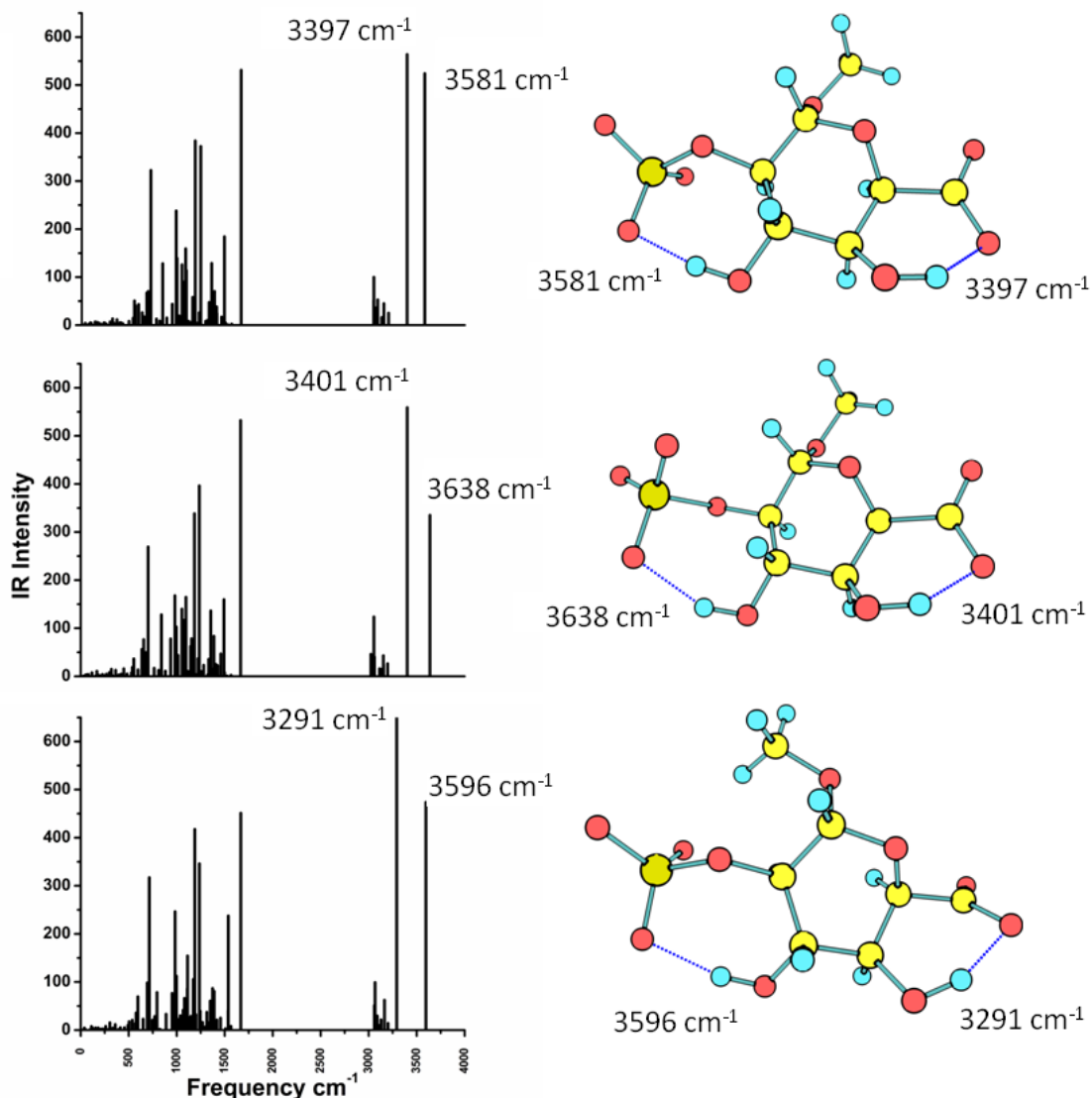
**Fig 5.6** Calculated IR Spectra at the MP2/6-31++G\*\* level for conformers a)  ${}^4C_1$  I, b)  ${}^4C_1$  II and c)  ${}^4C_1$  III

Figure 5.7 shows the calculated spectra for conformers  ${}^4C_1$  IV, V, VI and VII. A shift of the above values to 3642 and 3262 $\text{cm}^{-1}$  respectively occurs for  ${}^4C_1$  IV due to the slight reorientation of these interactions.  ${}^4C_1$  V is characterized by the movement of the H6 atom away from the sulphate group so that the interaction at 3600  $\text{cm}^{-1}$  is

no longer present in the spectra. The reverse is true of  ${}^4C_1$  VI where the sulphate interaction remains at  $3491\text{ cm}^{-1}$  and the carboxylate hydrogen bonding link is no longer present.  ${}^4C_1$  VII shows a similar bonding pattern to  ${}^4C_1$  VI, with the sulphate to H6 bond appearing at  $3531\text{ cm}^{-1}$ .



**Fig 5.7** Calculated IR Spectra at the MP2/6-31++G\*\* level for conformers a)  ${}^4C_1$  IV, b)  ${}^4C_1$  V, c)  ${}^4C_1$  VI and d)  ${}^4C_1$  VII



**Fig 5.8** Calculated IR Spectra at the MP2/6-31++G\*\* level for conformers a)  ${}^2S_0$  I, b)  ${}^2S_0$  II and c)  ${}^2S_0$  III

The calculated IR spectra for the  ${}^2S_0$  family, shown in figure 5.8, all contain the H6 to sulphate and H8 to carboxylate interactions mentioned above. The  ${}^2S_0$  I spectra predicts  $3581\text{ cm}^{-1}$  and  $3397\text{ cm}^{-1}$  for the H6 to sulphate and H8 to carboxylate hydrogen bonds respectively, with the same pair of interactions calculated at  $3638\text{ cm}^{-1}$  and  $3401\text{ cm}^{-1}$  for  ${}^2S_0$  II and  $3596\text{ cm}^{-1}$  /  $3291\text{ cm}^{-1}$  for  ${}^2S_0$  III.

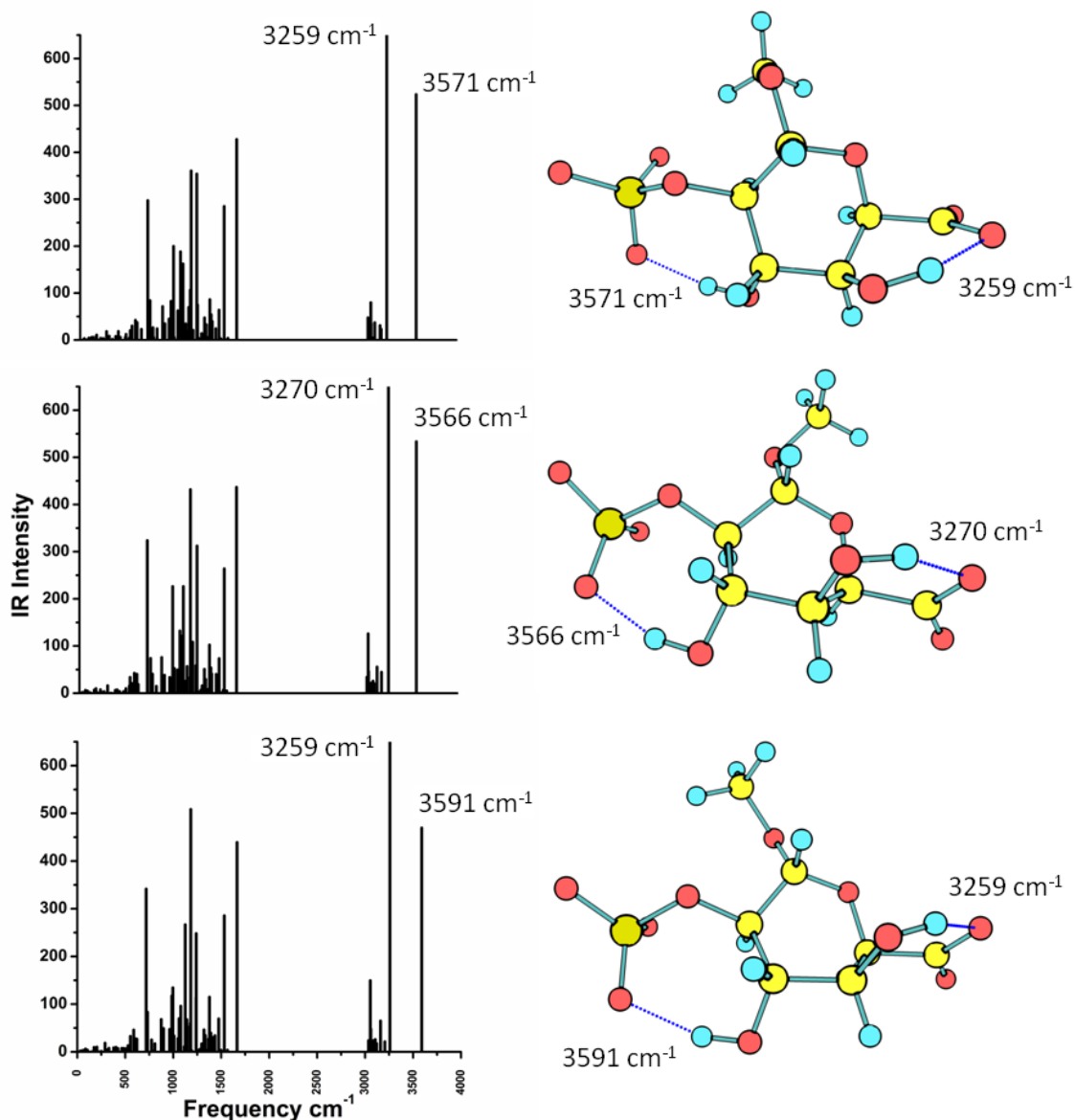


**Fig 5.9** Calculated IR Spectra at the MP2/6-31++G\*\* level for conformers a)  ${}^1S_5$  I, b)  ${}^1S_5$  II and c)  ${}^1S_5$  III

In a similar arrangement of hydrogen bonding, the calculated IR spectra for the  ${}^1S_5$  family members shown here in figure 5.9, all display frequencies associated with the H6 to sulphate and H8 to carboxylate structure. For  ${}^1S_5$  I, this is observed spectrally as the  $3571\text{ cm}^{-1}$  (H6 to sulphate) and  $3259\text{ cm}^{-1}$  (H8 to carboxylate) frequencies, with the same pair of interactions calculated at  $3566\text{ cm}^{-1}/3270\text{ cm}^{-1}$  and  $3591\text{ cm}^{-1}/3259\text{ cm}^{-1}$  for  ${}^1S_5$  II and  ${}^1S_5$  III respectively.

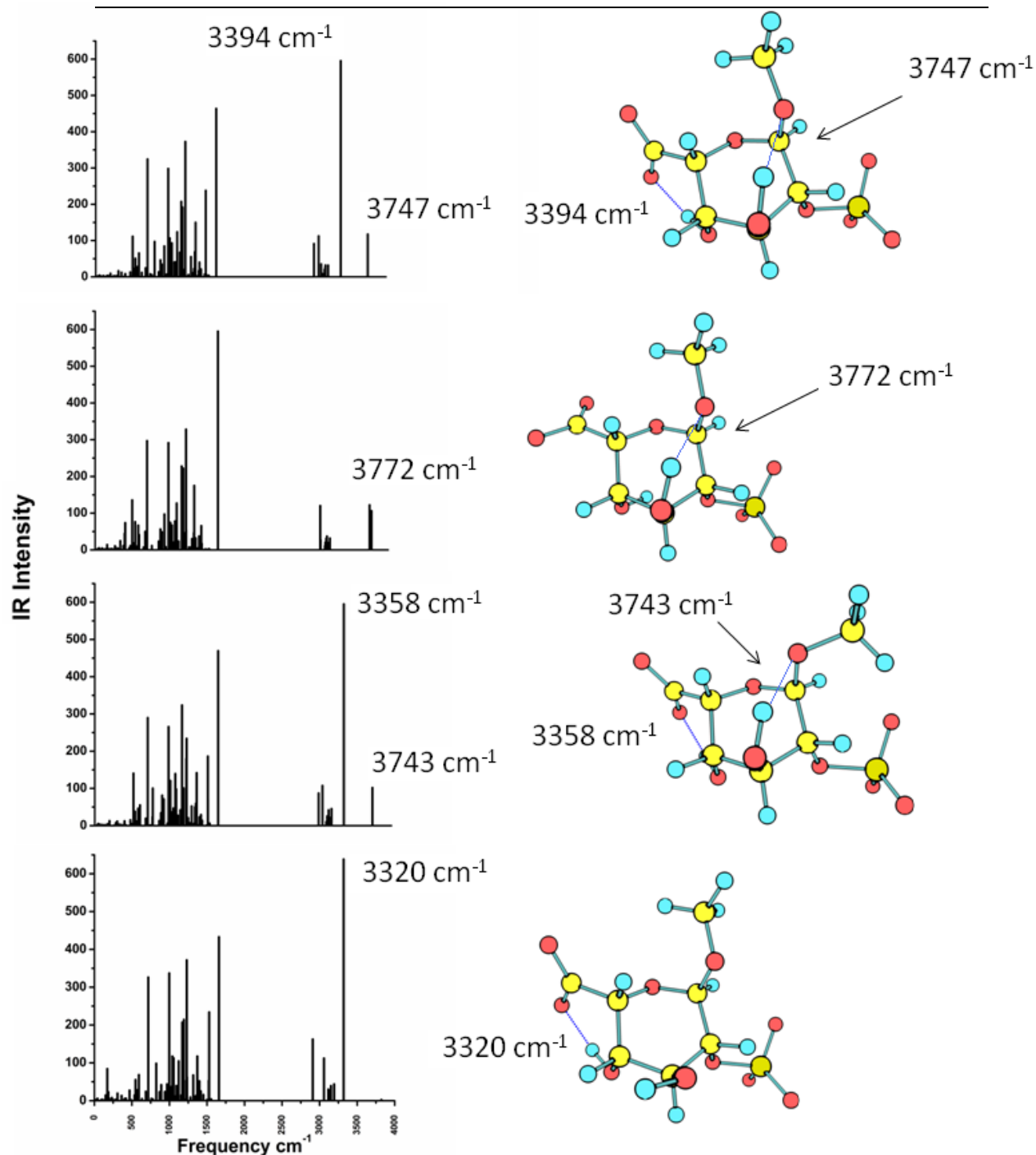


**Fig 5.10** Calculated IR Spectra at the MP2/6-31++G\*\* level for conformers a)  ${}^1C_4$  I, b)  ${}^1C_4$  II, c)  ${}^1C_4$  III and d)  ${}^1C_4$  IV

Conformers  ${}^1C_4$  I,  ${}^1C_4$  II and  ${}^1C_4$  III all share a common hydrogen bonding interaction between H6 and the OMe group which is reflected in the calculated spectra by the appearance of a peak in the region 3743 to 3747  $\text{cm}^{-1}$ . These

conformations may be readily distinguished from  ${}^1\text{C}_4$  IV since it does not display a peak in this area. The predicted spectra for  ${}^1\text{C}_4$  I and  ${}^1\text{C}_4$  II are significantly different since  ${}^1\text{C}_4$  I has an intense peak at  $3374\text{ cm}^{-1}$  caused by the H8 hydrogen interacting with the carboxylate group, which is lacking in  ${}^1\text{C}_4$  II. The principal difference between conformers  ${}^1\text{C}_4$  I and  ${}^1\text{C}_4$  III is the orientation of the OMe group, which interacts closely with the sulphate side group in  ${}^1\text{C}_4$  III. This change in orientation is not predicted to produce a spectral feature that would easily lend itself to identification, and so telling apart this pair of conformers is likely to be problematic due to their extremely similar spectra. As discussed above, the choice of the hydrogen bonding region for conformer identification is necessary to avoid the more congested regions of the spectra. Future success in studying this region will ultimately depend on the extent to which each conformer is populated and the resolution of the spectroscopic method used.

### 5.5 Further Discussion

The  $\text{IA}^{2-}$  results presented above illustrate that the new MO5-2X functional performs very favourably against the MP2 calculations. This reflects the overall results of the previous evaluations of MO5-2X against the S22 database of model complexes that display noncovalent interactions of biological importance,<sup>31,35</sup> and also against three test sets of monomeric saccharides.<sup>36</sup> All of the molecular systems within these test sets are, however, uncharged, in contrast to the system studied here. One of the notable results to emerge from the work on the neutral saccharide GLC4 test set which includes intramolecular H-bonds, was that MO5-2X did not perform so well compared to non-empirical functionals such as PBE.<sup>36</sup> Indeed, Csonka et al. go as far as recommending that MO5-2X should not be used for assessing carbohydrate conformational energy differences between  ${}^1\text{C}_4$  and  ${}^4\text{C}_1$  conformers. This is at odds with the results of the work on  $\text{IA}^{2-}$  presented here, where the relative energies of the  ${}^1\text{C}_4$  and  ${}^4\text{C}_1$  conformers are in good agreement for the MP2 and MO5-2X calculations.

In order to extend the computational methodology employed here to take account of higher order correlation effects, some exploratory single-point coupled cluster (CCSD and CCSD(T)) calculations were performed using the 6-31++G\*\* basis. Due to the computational cost, these calculations were restricted to the double zeta basis level, despite the well documented “gold-standard” performance of CCSD(T) with triple zeta basis. Only three of the sub-conformers were studied.<sup>37</sup> The results showed minimal changes in the relative energies between conformers, relative to MP2, whilst decreasing the absolute energies of all conformers slightly. It therefore appears that higher-order correlation is not critical in determining conformational preference in these anomeric sugars.

Heparin is widely used for the prevention and treatment of thrombosis, with its activity being linked to its ability to bond to antithrombins through a pentasaccharide sugar unit, DEFGH.<sup>38</sup> Through the investigation of the structure-activity relationships of this pentasaccharide fragment, it has been found that the sub-unit G (which is the methyl 2-O-sulfo- $\alpha$ -L-iduronate saccharide studied here) of the pentasaccharide DEFGH oscillated among the three conformations,  ${}^4C_1$ ,  ${}^2S_0$ , and  ${}^1C_4$ . Only the skewed boat conformation,  ${}^2S_0$ , of the G sub-unit allowed the pentasaccharide to bind effectively to antithrombin. It is of interest to note that this conformation does not appear to be favoured for the uncomplexed G sub-unit. The biological importance of the conformational structure of such saccharide units highlights the need for an improved understanding of the structural properties of such systems, as well as the need for the parameterization of a molecular mechanics force field to adequately reproduce all polysaccharide conformational features.

## 5.6 Summary

Hricovini has previously conducted a B3LYP/6-311++G\*\* level study of  $IA^{2-} \cdot 2Na^+$ ,<sup>17</sup> while Remko and von der Lieth have studied the doubly deprotonated dianion and neutral disodium salt of the methylated 1,4 DiOMe IndoA2S derivative.<sup>18</sup> While the relative energies of the ring conformers were investigated in

these studies ( ${}^4C_1$ ,  ${}^2S_0$ , and  ${}^1C_4$ ), neither study considered the influence of sub-conformer geometry on the relative energies obtained. However, the results presented in this work clearly illustrate the importance of surveying the sub-conformers to accurately assess the relative energies of the various ring conformers.

Comparison of various computational methodologies suggests that in these anionic saccharide systems, where dispersion and anomeric effects dominate, care must be taken to select an appropriate method. MP2 treats these effects well, but is already computationally expensive for systems of this size. The DFT methods are popular due to their speed and good scaling with molecular size, but careful selection of functional is crucial. For the prototype IA<sup>2-</sup> sugar, the recently developed M05-2X functional is able to provide much improved relative energies compared to B3LYP, due to its more accurate representation of dispersion interactions.<sup>39</sup>

References

1. M. Bernfield, M. Götte, P.W. Park, O. Reizes, M.L. Fitzgerald, J. Lincecum, M. Zako, *Annu. Rev. Biochem.* 68 (1999) 729
2. M. Berg, J.L. Tymoczko, L. Stryer, *Biochemistry*, Fifth Edition, W.H Freeman & Company, (2002)
3. L. Drouin, E.C. Stanca-Kaposta, P. Saundh, A.J. Fairbanks, S. Kemper, T.D.W. Claridge, J.P. Simons, *Chem. Eur. J.* 15 (2009) 4057
4. U. Lindahl, G. Backstrom, M. Hook, L. Thunberg, L.A., Fransson, A. Linker, *Proc. Natl. Acad. Sci. USA* 76 (1979) 3198
5. M. Petitou, C.A.A van Boeckel, *Angew. Chem. Int. Ed.* 43 (2004) 3118
6. Z. Shriver, R. Raman, G. Venkataraman, K. Drummond, J. Turnbull, T. Toida, R. Linhardt, K. Biemann and R. Sasisekharan, *Biochemistry* 97 (2000) 10359
7. R. M. Pope, C. S. Raska, S. C. Thorp and J. Liu, *Glycobiology* 11 (2001) 505
8. G. Venkataraman, Z. Shriver, R. Raman and R. Sasisekharan, *Science* 286 (1999) 537
9. B. Kuberan, M. Lech, L. Zhang, Z. L. Wu, D. L. Beeler and R. D. Rosenberg, *J. Am. Chem. Soc.* 124 (2002) 8707
10. H. Desaire and J. A. Leary, *J. Am. Soc. Mass Spectrom* 11 (2000) 916
11. L. Jin, P.E. Barran, J.A. Deakin, M. Lyon and D. Uhrin, *Phys. Chem. Chem. Phys.* 7 (2005) 3464
12. C.J. Taylor, R.M. Burke, B. Wu, S. Panja, S.B. Nielsen and C.E.H. Dessent, *Int. J. Mass. Spec.* 285 (2009) 70
13. R.J. Linhardt, I. Capila, *Angew. Chem. Int. Ed.* 41 (2002) 390
14. I. Hunig, A.J. Painter, R.A. Jockusch, P. Carcabal, E.M. Marzluff, L.C. Snoek, D.P. Gamblin, B.G. Davis and J.P. Simons, *Phys. Chem. Chem. Phys.* 7 (2005) 2474
15. R.K. Raju, A. Ramraj, I.H. Hillier, M.A. Vincent and N.A. Burton, *Phys. Chem. Chem. Phys.* 11 (2009) 3411
16. R.K. Raju, A. Ramraj, M.A. Vincent, I.H. Hillier and N.A. Burton, *Phys. Chem. Chem. Phys.* 10 (2008) 6500
17. M. Hricovini, *Carbohydr. Res.* 341 (2006) 2575
18. M. Remko, C-W. von der Lieth, *J. Chem. Inf. Model.* 46 (2006) 1194
19. L. Hemmingson, D.E. Madsen, A.L. Esbensen, L. Olsen, S.B. Engelsen, *Carbohydr. Res.* 339 (2004) 937
20. S.E. Barrows, F.J. Dulles, C.J. Cramer, A.D. French, D.G. Truhlar, *Carbohydr. Res.* 276 (1995) 219
21. B.J. Deppmeier, A.J. Driessen, T.S. Hehre, W.J. Hehre, J.A. Johnson, P.E. Klunzinger, J.M. Leonard, W.S. Ohlinger, I.N. Pham, W.J. Pietro, J. Yu, *PC Spartan Pro*, Wavefunction, Inc.: Irvine, CA, 2000.
22. T.A. Halgren, *J. Comp. Chem.* 17 (1996) 490
23. Kaminsky, J.; Jensen, F, *J. Chem. Theory. Comput.* 3 (2007) 1774
24. R.M. Burke, J.K. Pearce, W.E. Boxford, A. Bruckmann, C.E.H. Dessent, *J. Phys. Chem. A* 109 (2005) 9775

25. R. M. Burke, C. E. H. Dessent, *J. Phys. Chem. A* 113 (2009) 2683
26. M.J. Frisch et al. *Gaussian 03, Revision C.01*; Gaussian, Inc., Pittsburgh, PA, 2003.
27. S. Tsuzuki, H. P. Lüthi, *J. Chem. Phys.* 114 (2001) 3949
28. Y. Yang, W. Pan, W. Yang, *J. Chem. Phys.* 107 (1997) 7291
29. T. A. Wesolowski, O. Parisel, Y. Ellinger, J. Weber, *J. Phys. Chem. A* 101 (1997) 7818
30. M.D. Patey, C.E.H. Dessent, *J. Phys. Chem. A* 106 (2002) 4623
31. Y. Zhao, D. G. Truhlar, *J. Chem. Theory Comput.* 3 (2007) 289
32. Y. Zhao, N. E. Schultz, D. G. Truhlar, *J. Chem. Theory Comput.* 2 (2006) 364
33. The term “hydrogen bond” is applied to any pairwise interaction between an electron-pair donating atom and an electron-pair accepting hydrogen atom. **Error! Bookmark not defined.** We define typical hydrogen bonds as having bond lengths of  $<3\text{\AA}$  and bond angles of  $180 \pm 25^\circ$ , with loose “hydrogen-bond-like” interactions having bond lengths of  $<3.5\text{\AA}$  and bond angles of  $180 \pm 65^\circ$ .
34. D. Liu, T. Wyttenbach, C. J. Carpenter, M. T. Bowers, *J. Am. Chem. Soc.* 126 (2004) 3261
35. P. Jurecka, J. Sponer, J. Cerny, P. Hobza, *Phys. Chem. Chem. Phys.* 8 (2006) 1985
36. G.I. Csonka, A.D. French, G.P. Johnson, C.A. Stortz, *J. Chem. Theory Comput.* 5 (2009) 679
37. The three conformers studied at the CCSD and CCSD(T) level were  ${}^2S_0$ -I,  ${}^1S_5$ -II and  ${}^4C_1$ -V according to the naming scheme adopted in Fig. 3.
38. A. Raghuraman, A. Liang, C. Krishnasamy, T. Lauck, G.T. Gunnarsson, U.R. Desai, *Euro. J. Med. Chem.* 44 (2009) 2626
39. T. van Mourik, *J. Chem. Theory Comput.* 10 (2008) 1610



## Chapter 6

### **On the Intrinsic Stability of the Isolated Dichromate Dianion: Collision Activated Dissociation of a Multiply Charged Anion via Electron Detachment**

#### 6.1 Introduction

Gas-phase multiply charged anions (MCAs) represent a class of high-energy molecular ions that are prone to decay by either ionic fragmentation or electron detachment<sup>1-4</sup>, with the potential energy surfaces for decay *via* both of these channels being dominated by the presence of novel Repulsive Coulomb Barriers (RCBs). These features are of crucial importance in determining the intrinsic stability of a multiply charged ion since they can confer metastability on a system even when it is exothermic with respect to fragmentation<sup>5-7</sup>.

Over the last ten years, a number of important studies have been conducted to characterize the RCB surfaces of prototypical MCAs<sup>4,8-10</sup>. In our group, an innovative approach has been developed using resonance excitation (low energy collision-induced dissociation) of MCAs within a quadrupole ion-trap to evaluate whether the barrier height for decay is lower for the electron detachment or ionic fragmentation channel of a given MCA<sup>11</sup>. This technique is described in detail in Chapter 2, section 2.1.5. Fig. 6.1 displays a schematic diagram of the potential energy surfaces for decay of an  $AB_2^{2-}$  dianion with the barrier height for ionic fragmentation being labelled  $RCB_{if}(inner)$ , and the corresponding barrier for electron detachment labelled as  $RCB_{ed}(inner)$ . For the range of systems studied to date,  $RCB_{if}(inner)$  was always observed to lie below  $RCB_{ed}(inner)$ <sup>1,11-13</sup>, leading to the conclusion that ionic fragmentation will represent the preferred lowest energy decay pathway for transition metal complex dianions that can dissociate to form a pair of stable monoanions<sup>11</sup>.

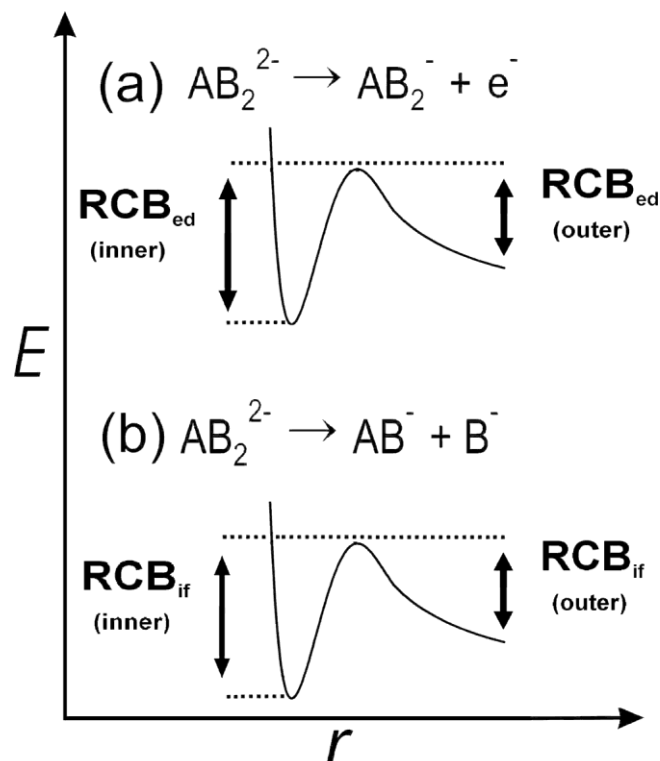


**Fig. 6.1** Schematic potential energy curves for decay of an  $AB_2^{2-}$  dianion via (a) electron detachment, and (b) ionic fragmentation into  $AB^- + B^-$ . The RCBs (inner) and (outer) for electron detachment ( $RCB_{ed}$ ) and ionic fragmentation ( $RCB_{if}$ ) are illustrated.

In an extension of this work, a number of small inorganic multiply charged systems that contain multiple metal atoms (e.g.  $Re_2Cl_8^{2-}$ ), have been studied as part of the work presented in this thesis (Chapter 7) to investigate the utility of resonance excitation as a technique for identifying metal-metal bonding within inorganic cluster ions. As a preliminary to the work on  $Re_2X_8^{2-}$  systems, the dichromate dianion,  $Cr_2O_7^{2-}$ , a well-known polyoxometalate anion that is stable in aqueous solution and crystalline compounds<sup>14,15</sup>, was investigated. Intriguingly, the dichromate dianion was observed to decay with electron loss upon resonance excitation, behaviour that contrasts with that of the other MCAs previously investigated<sup>1</sup>. In this chapter, the results of the resonance excitation experiments and *ab initio* calculations for  $Cr_2O_7^{2-}$  are presented to probe the intrinsic stability of

$\text{Cr}_2\text{O}_7^{2-}$  and investigate why this dianion displays atypical low-energy fragmentation behaviour. The mononuclear chromate oxoanions and dichromate species have been studied previously by Wang and co-workers using photodetachment spectroscopy<sup>16,17,18</sup>, with the positively-charged mononuclear analogues having been investigated by Schwarz and co-workers<sup>19</sup>.

The  $\text{Cr}_2\text{O}_7^{2-}$  dianion studied here represents the example of where a small molecular dianion which has been observed to decay with electron detachment following low-energy activation in a quadrupole ion-trap. This observation is of interest since it suggests that the repulsive coulomb barrier for electron detachment lies below that for ionic fragmentation in this system. It should be emphasised that this result is atypical for small molecular dianions<sup>1,11</sup>. There have, however, been numerous previous studies relating to electron detachment of MCAs and that electron detachment is the most commonly studied decay pathway<sup>3</sup>. For example, Wang and co-workers have used photodetachment spectroscopy to probe the properties of a very wide range of MCAs<sup>4,20</sup>. Kappes and co-workers have studied autodetachment of both fullerenes and small dianions such as  $\text{PtCl}_4^{2-}$  in an FTICR mass spectrometer<sup>21,22</sup>, with Herlert *et al.* observing delayed electron emission from gold cluster dianions<sup>23</sup>. Tuinman and Compton have probed the electron detachment potential energy surfaces of dianions through charge-exchange collisions of fullerenes<sup>10</sup>, while Nielsen and co-workers used electron scattering of p-benzoquinone to study autodetaching resonance states of dianions<sup>24</sup>. In addition, electron detachment has been recognized as a common decay channel in high-energy collisions of MCAs with noble gas atoms<sup>25</sup>.

## 6.2 Experimental Methods

The experiments were performed as described previously<sup>1,11</sup>. A Finnigan LCQ quadrupole ion-trap mass spectrometer run in negative ion mode was used to perform the experiments. Sample solution concentrations were  $\sim 1 \times 10^{-3}$  M (50:50 methanol/water), prior to electrospraying in pure methanol. The sodium salt

complex was purchased from Aldrich (*e.g.*  $\text{Na}_2\text{Cr}_2\text{O}_7$ ) and used without further purification.

Low-energy collision induced dissociation (CID) (or *resonance excitation*) was performed by applying an excitation AC voltage to the end caps of the trap to induce collisions of the isolated anions with the helium buffer gas ( $\sim 1 \times 10^{-4}$  Torr). A Mathieu  $q_z$  parameter of 0.25 was used for resonance excitation and ions were subject to a 30 ms excitation time. The excitation voltage amplitude was varied between 0 and 2.5V zero-to-peak resonant excitation potential. Measured minimum resonance excitation amplitudes for decomposition of polyatomic ions in the quadrupole ion-trap CID experiment have been shown to correlate with the literature critical dissociation energies; however, there is no straightforward conversion from the resonance excitation voltage to absolute dissociation energies<sup>26,27</sup>. This situation contrasts with other guided ion beam CID experiments<sup>28</sup>.

### 6.3 Computational Methods

The equilibrium geometry, energies, and harmonic vibrational frequencies of the ions studied in this work were calculated with the B3LYP hybrid exchange and correlation functional. The LANL2DZ double- $\zeta$  basis set<sup>29</sup> was used for all of the calculations since this has been found to give reliable computational results for  $\text{Cr}_2\text{O}_7^{2-}$ <sup>30</sup>. All of the calculations were carried out using GAUSSIAN 03, with the default convergence criteria applied to the geometry optimizations<sup>31</sup>. Partial charge distributions were calculated using the natural population analysis (NPA) method<sup>32</sup>. The potential energy surface for the lowest energy ionic fragmentation decay pathway was calculated by scanning the total energy as a function of the distance between the ionic fragments. The point charge model of Dreuw and Cederbaum was applied to model the potential energy surface for electron detachment<sup>33,34</sup>.

## 6.4 Results and Discussion

### 6.4.1 Resonance Excitation of the $\text{Cr}_2\text{O}_7^{2-}$ Dianion

Fig. 6.2a displays the negative-ion electrospray ionisation mass spectrum (ESI-MS) of  $\text{Cr}_2\text{O}_7^{2-}$ .  $\text{CrO}_4^- / \text{HCrO}_4^-$  (the instrument used for this work has an accuracy of approximately one  $m/z$  unit) is the major peak in the spectrum, with the  $\text{Na}^+ \cdot \text{Cr}_2\text{O}_7^{2-}$  and  $\text{Cr}_2\text{O}_7^{2-}$  ions also appearing with significant intensity.

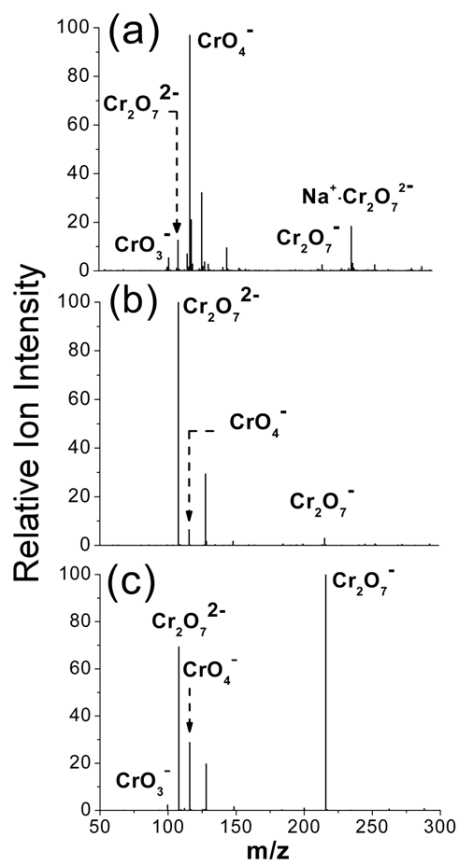
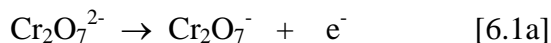


**Fig. 6.2** (a) Negative ion ESI-MS of the sodium salt of  $\text{Cr}_2\text{O}_7^{2-}$  obtained by tuning on  $m/z$  108 (*i.e.* optimising the ion optics to maximise the  $m/z$  108 signal). (b) Isolation of  $\text{Cr}_2\text{O}_7^{2-}$  in the quadrupole trap at 0% collision energy. (c) CID mass spectrum of  $\text{Cr}_2\text{O}_7^{2-}$  at 9% collision energy illustrating fragmentation of  $\text{Cr}_2\text{O}_7^{2-}$  primarily into  $\text{Cr}_2\text{O}_7^-$ . ( $\text{CrO}_4^-$  and  $\text{CrO}_3^-$  are also evident as product fragments; see text for a discussion.)

To investigate the lowest energy decay pathway, the  $\text{Cr}_2\text{O}_7^{2-}$  parent dianion was isolated in the quadrupole trap and activated using resonance excitation. At 0% collision energy (Fig. 6.2b),  $\text{Cr}_2\text{O}_7^{2-}$  is observed to decay with production of a number of ionic fragments. Similar effects have been observed in previous CID studies of multiply charged cluster ions<sup>11, 35</sup>, and were attributed to dissociation of metastable parent ions that are thermally or collisionally activated as they travel through the mass spectrometer. While such effects explain the appearance of the minor  $\text{CrO}_4^-$  and  $\text{Cr}_2\text{O}_7^-$  fragments, the  $m/z=128.5$  peak corresponds to a solvated cluster of dichromate, i.e.  $\text{Cr}_2\text{O}_7^{2-}\cdot\text{CH}_3\text{CN}$  which appear to arise due to complexation of the dianion with residual solvent in the ion trap<sup>36</sup>.

Fig. 6.2c displays a typical fragment ion mass spectrum obtained after activated collision-induced dissociation (9% collision energy).  $\text{Cr}_2\text{O}_7^{2-}$  can be seen to decay primarily with production of  $\text{Cr}_2\text{O}_7^-$ , i.e. via electron detachment;



$\text{CrO}_4^-$  is also evident as a minor fragment, with  $\text{CrO}_3^-$  also visible (ions with  $m/z < 100$  are not strongly detected by the LCQ instrument), indicating that decay of  $\text{Cr}_2\text{O}_7^{2-}$  is also occurring to a lesser extent *via* ionic fragmentation;



(I note that Cr is not known to adopt a +VII oxidation state, so that the  $\text{CrO}_4^-$  species is likely to have Cr in the +VI state, with one of the oxygen atoms being peroxidic.)

Fig. 6.3 displays % fragmentation curves (i.e. plots of fragment ion intensity *versus* collision energy) for decay of the  $\text{Cr}_2\text{O}_7^{2-}$  parent dianion upon resonance excitation, with production of the  $\text{CrO}_4^-$  and  $\text{Cr}_2\text{O}_7^-$  product ions. The onset of fragmentation for  $\text{Cr}_2\text{O}_7^{2-}$  occurs at ~ 8% CID energy, a value that is high compared to other transition metal complex dianions<sup>1,11</sup>. (For example,  $\text{IrCl}_6^{2-}$  has a fragmentation onset around 4% CID energy<sup>11</sup>.) The high fragmentation energy of  $\text{Cr}_2\text{O}_7^{2-}$  indicates

that the barrier to the lowest energy fragmentation pathway is relatively high in this system. While the fragmentation curve for production of  $\text{Cr}_2\text{O}_7^-$  rises very sharply above 8% CID energy, the curve for production of  $\text{CrO}_4^-$  has an onset of  $\sim 8.5\%$  and increases more gradually above this energy<sup>37</sup>. This suggests that production of  $\text{Cr}_2\text{O}_7^-$  is associated with decay of the  $\text{Cr}_2\text{O}_7^{2-}$  parent dianion *via* the lowest energy dissociative surface, and that  $\text{Cr}_2\text{O}_7^{2-}$  preferentially decays *via* electron detachment, i.e. equation [6.1a].

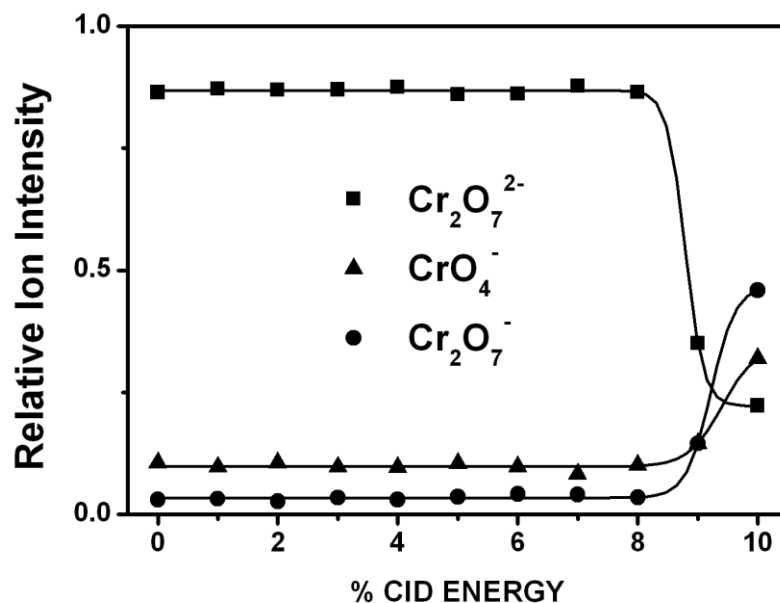


**Fig. 6.3 % Fragmentation curves for decay of the  $\text{Cr}_2\text{O}_7^{2-}$  parent dianion, with production of the  $\text{CrO}_4^-$  and  $\text{Cr}_2\text{O}_7^-$  fragment ions. Typical experimental errors (obtained from repeat runs) were  $\pm 3\%$ .**

It should be noted that it is possible that thermally excited (resonance excited)  $\text{Cr}_2\text{O}_7^{2-}$  may be decaying *via* electron tunnelling through the Coulomb Barrier<sup>4,9</sup>, so that from the experimental data it is not possible to unequivocally say that  $\text{RCB}_{\text{ed}}(\text{inner})$  lies below  $\text{RCB}_{\text{if}}(\text{inner})$  for this dianion. However, the data indicate that  $\text{RCB}_{\text{if}}(\text{inner})$  certainly does not lie substantially below  $\text{RCB}_{\text{ed}}(\text{inner})$ . We return to the relative heights of  $\text{RCB}_{\text{ed}}(\text{inner})$  and  $\text{RCB}_{\text{if}}(\text{inner})$  in section 6.4.2 where the barriers are calculated using *ab initio* methods.

To extend this study, the  $\text{Cr}_2\text{O}_7^-$  monoanion which was present in the parent ESI-MS of the sodium dichromate solution was also subjected to resonance excitation CID in the quadrupole ion-trap. Figures 6.4a and 6.4b display the mass spectra associated with isolation of  $\text{Cr}_2\text{O}_7^-$  in the ion-trap at 0% collision energy and excitation of  $\text{Cr}_2\text{O}_7^-$  at 15% excitation energy, respectively.

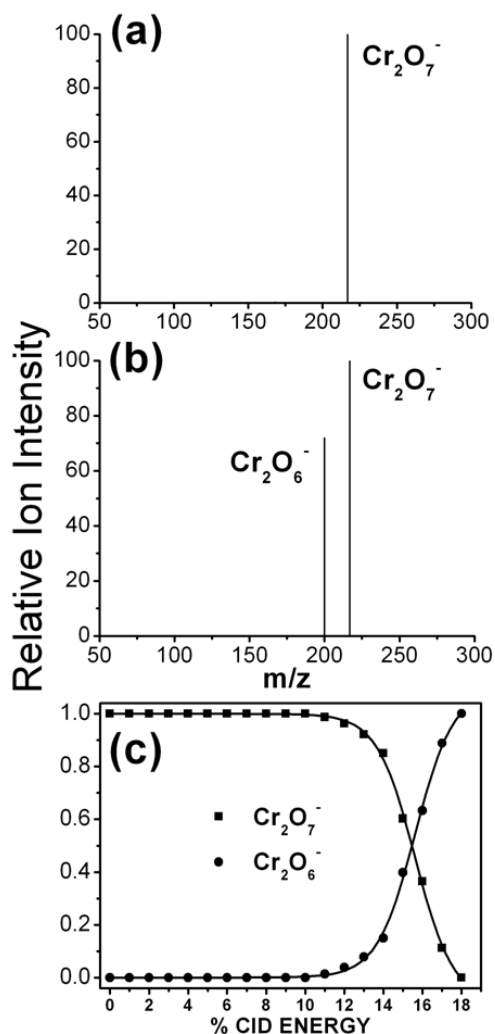


**Fig. 6.4** (a) Isolation of  $\text{Cr}_2\text{O}_7^-$  in the quadrupole trap at 0% collision energy. (b) CID mass spectrum of  $\text{Cr}_2\text{O}_7^-$  at 15% collision energy illustrating fragmentation of  $\text{Cr}_2\text{O}_7^-$  into  $\text{Cr}_2\text{O}_6^-$ . (c) % Fragmentation curves for decay of the  $\text{Cr}_2\text{O}_7^-$  parent monoanion, with production of the  $\text{Cr}_2\text{O}_6^-$  fragment ion.

Upon resonance excitation,  $\text{Cr}_2\text{O}_7^-$  can be seen to decay with production of  $\text{Cr}_2\text{O}_6^-$  *i.e.* via loss of a neutral oxygen atom. Figure 6.4c displays the % fragmentation curves for decay of the  $\text{Cr}_2\text{O}_7^-$  parent monoanion upon resonance excitation, with production of the  $\text{Cr}_2\text{O}_6^-$  product ion. The onset of fragmentation for  $\text{Cr}_2\text{O}_7^-$  occurs at  $\sim 12\%$  CID energy, a value that is somewhat higher than for  $\text{Cr}_2\text{O}_7^{2-}$ , indicating the higher intrinsic stability of the monoanion relative to the dianion.

The  $\text{Na}^+\cdot\text{Cr}_2\text{O}_7^{2-}$  cation-dianion cluster ( $m/z=239$ ) was also isolated in the quadrupole ion trap and subjected to resonance excitation. The ion was stable through the collisional energy range over which the bare  $\text{Cr}_2\text{O}_7^{2-}$  dianion decayed (8-12% CID energy). This behaviour mirrors that of other cation-dianion complexes<sup>38</sup>, and can be attributed to the  $\text{Na}^+$  cation electrostatically stabilizing the dianion. Above 18% CID energy, the parent-ion intensity decays rapidly, but without the clear production of any product ion fragments, consistent with the dianion within the ion-pair complex decaying with loss of an electron, *i.e.*



This behaviour is again in line with that of other cation-dianion complexes, which decay with production of fragments associated with the decay of the uncomplexed dianion<sup>42</sup>.

#### 6.4.2 Stability of $\text{Cr}_2\text{O}_7^{2-}$ with Respect to Electron Detachment and Ionic Fragmentation

To investigate the intrinsic stability of  $\text{Cr}_2\text{O}_7^{2-}$ , a series of *ab initio* calculations were performed to probe the potential energy surfaces for decay of the molecular dianion. Fig. 6.5 displays the optimized  $C_{2v}$  structure (B3LYP/LANL2DZ) of  $\text{Cr}_2\text{O}_7^{2-}$ , with the  $\text{CrO}_3$  groups oriented in an eclipsed configuration across the central oxygen atom. This structure agrees well with the known structure of the dianion<sup>30,39</sup>.

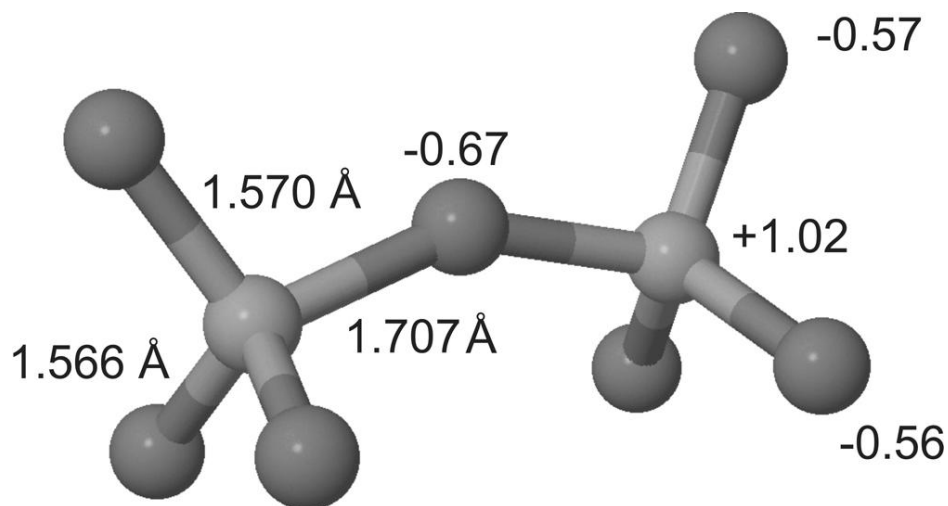


**Fig. 6.5** The optimized  $C_{2v}$  symmetry structure of  $\text{Cr}_2\text{O}_7^{2-}$  obtained at the B3LYP/LANL2DZ level, with bond lengths and NPA atomic charges.

Fig. 6.6a displays the calculated potential energy curve for ionic fragmentation of  $\text{Cr}_2\text{O}_7^{2-}$  into  $\text{CrO}_4^-$  and  $\text{CrO}_3^-$ , obtained as a function of the central Cr-O distance. (Only this channel is considered in this work since there is no evidence for ionic fragmentation of the dianion into  $\text{Cr}_2\text{O}_6^-$  and  $\text{O}^-$ .) The surface displays the expected RCB (barrier height = 3.6 eV) which is characteristic of an MCA, and indicates that the system is stable with respect to ionic fragmentation since dissociation of the dianion into the ionic fragments is endothermic.

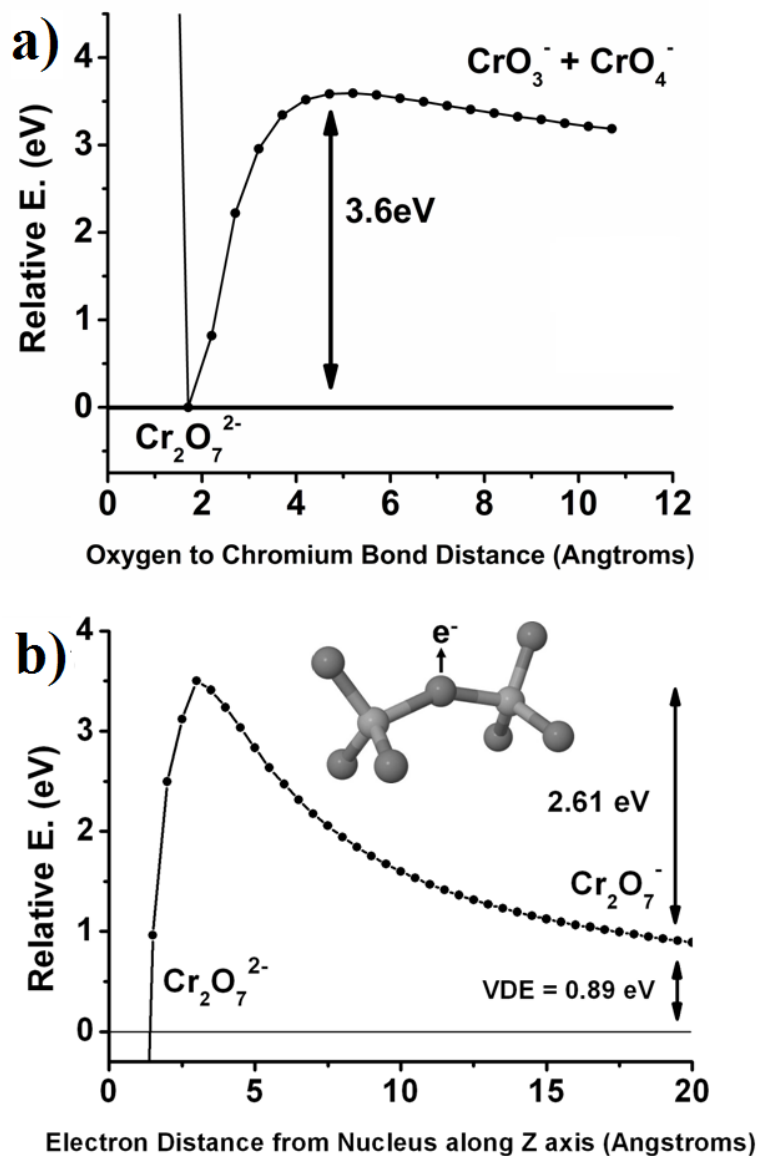


**Fig. 6.6** (a) Calculated potential energy curve (B3LYP/LANL2DZ) for the ionic fragmentation of  $\text{Cr}_2\text{O}_7^{2-} \rightarrow \text{CrO}_3^- + \text{CrO}_4^-$ , obtained as a function of the oxygen-chromium bond distance. (b) One-dimensional cut through  $\text{RCB}_{\text{ed}}$  of  $\text{Cr}_2\text{O}_7^{2-}$  calculated using the point charge model (see text) at the B3LYP/LANL2DZ level. The direction of electron detachment is indicated.

Calculations were also performed to investigate electron detachment decay of  $\text{Cr}_2\text{O}_7^{2-}$ , using the point charge model of Dreuw and Cederbaum<sup>33</sup>. Fig. 6.6b displays the 1D-cut along the electron detachment surface obtained for removal of the electron along the direction indicated, with the maximum value of  $V(r)$  representing the  $\text{RCB}_{\text{ed}}(\text{outer})$  height, *i.e.* the barrier measured from the  $\text{Cr}_2\text{O}_7^- + e^-$  asymptote. (The geometry of the dichromate ion is frozen across the electron detachment scan.) The point-charge method describes the short-range interaction rather poorly, so that the magnitude of  $\text{RCB}_{\text{ed}}(\text{inner})$  is more reliably obtained as the sum of the  $\text{RCB}_{\text{ed}}(\text{outer})$  of 2.61 eV and the calculated vertical detachment energy of 0.89 eV (VDE)<sup>37,38</sup>. Combining these values gives  $\text{RCB}_{\text{ed}}(\text{inner})$  as 3.5 eV. The  $\text{Cr}_2\text{O}_7^{2-}$  VDE and  $\text{RCB}_{\text{ed}}(\text{outer})$  values calculated in this work are in reasonable agreement with the experimental values of  $\sim 1.3$  eV and  $\sim 2.3$  eV, respectively, measured by Wang and co-workers using photodetachment photoelectron spectroscopy<sup>18</sup>.

## 6.5 Further Discussion

The calculations for  $\text{Cr}_2\text{O}_7^{2-}$  presented in Section 6.4.2 indicate that the dianion is intrinsically stable with respect to dissociation *via* either electron detachment or ionic fragmentation. The calculated values of 3.5 eV and 3.6 eV for  $\text{RCB}_{\text{ed}}(\text{inner})$  and  $\text{RCB}_{\text{if}}(\text{inner})$ , respectively, indicate that the lowest energy decay pathway for  $\text{Cr}_2\text{O}_7^{2-}$  should be *via* electron loss, with the barrier for decay *via* ionic fragmentation lying just higher in energy. This picture is in excellent agreement with the low-energy collision induced dissociation results. It is likely that electron detachment decay is occurring via electron tunnelling through the  $\text{RCB}_{\text{ed}}$  before the barrier energy is reached.

The similar values for  $\text{RCB}_{\text{ed}}(\text{inner})$  and  $\text{RCB}_{\text{if}}(\text{inner})$  observed here are surprising, since in previous studies of inorganic ions (*e.g.*  $\text{Pt}(\text{CN})_4^{2-}$  and  $\text{IrBr}_6^{2-}$ )  $\text{RCB}_{\text{if}}(\text{inner})$

has typically been considerably smaller than  $\text{RCB}_{\text{ed}}(\text{inner})$ . The unusual behaviour of  $\text{Cr}_2\text{O}_7^{2-}$  can be traced to its relatively high value of  $\text{RCB}_{\text{if}}(\text{inner})$ , 3.6 eV, compared to values of  $\sim 2$  eV for  $\text{MX}_6^{2-}$  dianions, where  $\text{M}=\text{Ir}, \text{Os}, \text{Re}, \text{Pt}$ , and  $\text{X}=\text{Cl}, \text{Br}$ <sup>11</sup>. Since  $\text{RCB}_{\text{if}}(\text{inner})$  is relatively high for  $\text{Cr}_2\text{O}_7^{2-}$ , it occurs in the same region as the barrier for electron detachment. It has previously been proposed within our group that  $\text{RCB}_{\text{if}}(\text{inner})$  for an  $\text{MX}_6^{2-}$  dianion should be associated with the purely attractive binding energy of an  $\text{X}^-$  ion to the  $\text{MX}_5^-$  moiety, *i.e.*

$$\text{RCB}_{\text{if}}(\text{inner}) = \Delta E (\text{MX}_5^- + \text{X}^-) - \text{intramolecular Coulomb repulsion} \quad [6.3a]$$

By analogy, the corresponding expression for the dichromate dianion will be;

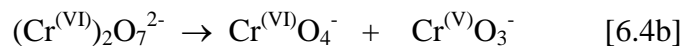
$$\text{RCB}_{\text{if}}(\text{inner}) = \Delta E (\text{CrO}_4^- + \text{CrO}_3^-) - \text{intramolecular Coulomb repulsion} \quad [6.3b]$$

Comparing  $\text{Cr}_2\text{O}_7^{2-}$  with an  $\text{MX}_6^{2-}$  dianion such as  $\text{IrBr}_6^{2-}$ , the intramolecular Coulomb repulsion should be broadly similar for both dianions, so that the high value of  $\text{RCB}_{\text{if}}(\text{inner})$  for  $\text{Cr}_2\text{O}_7^{2-}$  can be attributed to a comparatively stronger intramolecular bond. This is consistent with the known structural differences of  $\text{Cr}_2\text{O}_7^{2-}$  and  $\text{MX}_6^{2-}$  type-dianions, since  $\text{Cr}_2\text{O}_7^{2-}$  is regarded as a covalent molecular ion composed of two corner-sharing tetrahedral chromate units<sup>39</sup>, whereas  $\text{MX}_6^{2-}$  ions are more correctly viewed as weakly associated complex anions. (The calculated bond dissociation energy of  $\text{Cr}_2\text{O}_7^{2-}$  into  $\text{CrO}_4^- + \text{CrO}_3^-$  is 3.1eV at the B3LYP/LANL2DZ level, whereas the corresponding calculated value for ionic fragmentation of  $\text{IrCl}_6^{2-}$  is -0.20 eV<sup>34</sup>.)

Finally, the atypical fragmentation behaviour of  $\text{Cr}_2\text{O}_7^{2-}$  can also be viewed as arising from the stoichiometry of the system. A metal halide dianion such as  $\text{PtCl}_4^{2-}$  does not change its valence state upon ionic fragmentation, *i.e.*,



whereas ionic fragmentation of  $\text{Cr}_2\text{O}_7^{2-}$  requires a single electron transfer process to produce a (peroxidic) Cr(VI) and a Cr(V):



The thermochemical location of the ionic fragmentation exit channel is therefore considerably less favourable, as reflected by the *ab initio* calculations presented above.

## 6.6 Summary

$\text{Cr}_2\text{O}_7^{2-}$  displays atypical behaviour for an inorganic MCA since it preferentially decays with electron loss upon low-energy collision activated dissociation in a quadrupole ion trap. This is the first such system observed to decay via electron loss under these conditions, and therefore illustrates that the resonance excitation technique is suitable for identifying electron detachment as well as ionic fragmentation pathways. Finally, the relatively high barrier for ionic fragmentation that is present for  $\text{Cr}_2\text{O}_7^{2-}$  is indicative of the relatively strong covalent bonding within this anion. This is important since it illustrates the utility of low-energy CID studies within quadrupole ion traps for probing structural features of inorganic cluster ions.

## 6.7 References

1. W. E. Boxford, C. E. H. Dessent, *Phys. Chem. Chem. Phys.* 8 (2006) 5151.
2. M. K. Scheller, R. N. Compton, L. S. Cederbaum, *Science* 270 (1995) 1160.
3. A. Dreuw, L. S. Cederbaum, *Chem. Rev.* 102 (2002) 181.
4. L. S. Wang, *Comm. Mod. Phys.* 2 (2001) 207.
5. D. Schröder, H. Schwarz, *J. Phys. Chem. A* 103 (1999) 7385.
6. D. Schröder, *Angew. Chem. Int. Ed.*, 43 (2004) 1329.
7. S. D. Price, *Phys. Chem. Chem. Phys.* 5 (2003) 1717.
8. J. Friedrich, S. Gilb, O. T. Ehrler, A. Behrendt, M. M. Kappes, *J. Chem. Phys.* 117 (2002) 2635.
9. D. Löffler, J. M. Weber, M. M. Kappes, *J. Chem. Phys.* 123 (2005) 224308.
10. A. A. Tuinman, R. N. Compton, *Phys. Rev. A* 65 (2002) 052724.
11. W. E. Boxford, J. K. Pearce, C. E. H. Dessent, *Chem. Phys. Lett.* 399 (2004) 465.
12. R. M. Burke, J. K. Pearce, W. E. Boxford, A. Bruckmann, C. E. H. Dessent, *J. Phys. Chem. A* 109 (2005) 9775.
13. X. Yang, X.B Wang, L.S. Wang, *Int. J. Mass Spectrom.* 228 (2003) 797.
14. R. J. Errington, M. D. Kerlogue, D. G. Richards, *J. Chem. Soc. Chem. Commun.* 7 (1993) 649.
15. M. Å. Dahlborg, G. Svensson, M. Valkeapää, *J. Solid State Chem.* 167 (2002) 525.
16. H. J. Zhai, S. Li, D. A. Dixon, L. S. Wang, *J. Am. Chem. Soc.* 130 (2008) 5167.
17. H. J. Zhai, L. S. Wang, *J. Chem. Phys.* 125 (2006) 164315.
18. H. J. Zhai, X. Huang, T. Waters, X. B. Wang, R. A. J. O'Hair, A. G. Wedd, L. S. Wang, *J. Phys. Chem. A* 109 (2005) 10512.
19. A. Fiedler, I. Kretzschmar, D. Schröder, H. Schwarz, *J. Am. Chem. Soc.* 118 (2006) 9941.
20. T. Waters, X. B. Wang, L. S. Wang, *Coord. Chem. Rev.* 251 (2007) 474.
21. O. Hampe, M. Neumaier, M. N. Blom, M. M. Kappes, *Chem. Phys. Lett.* 354 (2002) 303.
22. P. Weis, O. Hampe, S. Gilb, M. M. Kappes, *Chem. Phys. Lett.* 321 (2000) 426.
23. A. Herlert, L. Schweikhard, *Int. J. Mass Spectrom.* 252 (2006) 151; A. Herlert, L. Schweikhard, M. Vogel, *Int. J. Mass Spectrom.* 213 (2002) 157.
24. M. O. A. El Ghazaly, A. Svendsen, H. Bluhme, S. Brøndsted Nielsen, L. H. Andersen, *Chem. Phys. Lett.* 405 (2005) 278.
25. W. E. Boxford, M. O. A. El Ghazaly, C. E. H. Dessent, S. Brøndsted Nielsen, *Int. J. Mass Spectrom.* 244 (2005) 60.
26. A. Colorado and J. Brodbelt, *J. Am. Soc. Mass Spectrom.* 7 (1996) 116.
27. K. J. Hart, S. A. McLuckey, *J. Am. Soc. Mass Spectrom.* 5 (1994) 250.
28. P. B. Armentrout, *J. Am. Soc. Mass Spectrom.* 13 (2002) 419.
29. P. J. Hay, W. R. Wadt, *J. Chem. Phys.* 82 (1985) 299.

30. J. Mestres, M. Duran, P. M. Zarza, E. M. de la Rosa, P. Gili, *Inorg. Chem.* 32 (1993) 4708.
31. M. J. Frisch, et al., 2004, Gaussian 03, Revision C.01, Gaussian, Inc., Wallingford CT.
32. A. E. Reed, R. B. Weinstock, F. Winhold, *J. Chem. Phys.* 83 (1985) 735.
33. A. Dreuw, L. S. Cederbaum, *J. Chem. Phys.* 112 (2000) 7400.
34. W. E. Boxford, C. E. H. Dessent, *J. Phys. Chem. A* 109 (2005) 5836.
35. M. P. Ince, B. A. Perera, M. J. Van Stipdonk, *Int. J. Mass Spectrom.* 207 (2001) 41.
36. J. R. Wickens, R. Sleeman, B. J. Keeley, *Rapid Comm. Mass Spectrom.* 21 (2002) 2491.
37. The relative ion intensity for  $\text{CrO}_3^-$  as a function of %CID energy mirrors that of  $\text{CrO}_4^-$ , but since the intensity of the  $\text{CrO}_3^-$  fragment is low, the onset curve is not plotted as it is not reliable in the context of the experimental accuracy ( $\pm 3\%$  for repeat runs).
38. R. M. Burke, W. E. Boxford, C. E. H. Dessent, *J. Chem. Phys.* 126 (2007) 064308.
39. N. N. Greenwood and A. Earnshaw, *Chemistry of the Elements*, Second edition, Elsevier, 1997.

## Chapter 7

### Probing the Gas-Phase Stability of the $\text{Re}_2\text{X}_8^{2-}$ ( $\text{X} = \text{Cl}, \text{Br}$ ) and $\text{Re}_2\text{X}_n\text{Y}_{8-n}^{2-}$ ( $\text{X} = \text{Cl}, \text{Y}=\text{Br}$ , $n=1-3$ ) Metal-Metal Bond Complexes

#### 7.1 Introduction

The identification of the metal-metal quadruple bond in  $\text{Re}_2\text{Cl}_8^{2-}$  has stimulated intensive research in the area of transition metal chemistry over the last 40 years.<sup>1</sup> Metal-metal bonding is now recognized as one of the characteristic features of the chemistry of low oxidation state transition metals, and the understanding of metal-metal multiple bonds and metal-metal interactions is of widespread fundamental and applied interest.  $\text{Re}_2\text{Cl}_8^{2-}$  ( $d^4 - d^4$ ) is considered to be one of the most important dinuclear transition metal complexes since it contains a formal Re-Re quadruple bond,<sup>1</sup> and has been extensively studied using both theoretical<sup>2,3</sup> and experimental techniques.<sup>1,4,5</sup>

While the vast majority of experimental studies on metal-metal bonded transition metal complexes have been performed in the condensed phase,<sup>1</sup> it is also of interest to investigate these systems as isolated species in the gas-phase with the particular goal of obtaining data that can be directly compared with *ab initio* calculations.<sup>6,7</sup> Gas-phase studies also provide important insights into the fundamental stability of isolated inorganic species in the absence of bulk solvent and counterions.<sup>8-16</sup>

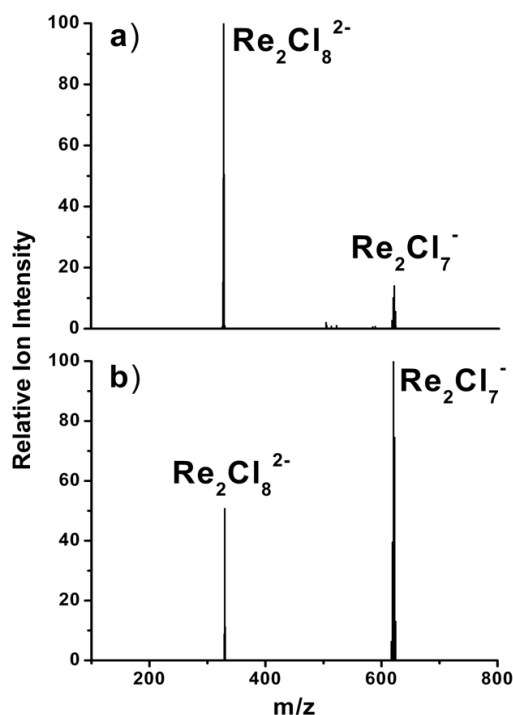
In a recent study, Wang and Wang used electrospray ionization (ESI) to produce the isolated  $\text{Re}_2\text{Cl}_8^{2-}$  anion in the gas-phase, then used photodetachment photoelectron spectroscopy to probe its electronic structure.<sup>17</sup> The photoelectron spectra obtained were interpreted in terms of the metal-ligand and metal-metal molecular orbitals, in this case verifying that the highest occupied molecular orbitals in  $\text{Re}_2\text{Cl}_8^{2-}$  were Metal-Metal bonds and that the order  $\delta > \pi > \sigma$ . The first spectral feature was

observed using an Nd:YAG laser at 355nm, suggesting an  $\text{RCB}_{\text{ed}}$  inner barrier height of 3.5 eV. As part of that work, preliminary investigations of the intrinsic gas-phase stability of  $\text{Re}_2\text{Cl}_8^{2-}$  were also conducted through studying the dianion in a quadrupole ion trap that forms part of their photoelectron spectrometer. They concluded that  $\text{Re}_2\text{Cl}_8^{2-}$  was intrinsically unstable in the gas-phase, and subject to decay with a half-life of  $\sim 150$  s, although the exact decay mechanism could not be identified. In this chapter, more detailed study of the gas-phase stability and lowest energy fragmentation channels of  $\text{Re}_2\text{Cl}_8^{2-}$  is presented to extend the previous work of Wang and Wang. In addition, results for the custom synthesised brominated analogue,  $\text{Re}_2\text{Br}_8^{2-}$ , and the mixed  $\text{Re}_2\text{Cl}_n\text{Br}_{8-n}^{2-}$  ( $n=1-3$ ) complexes are presented, allowing the first measurements to directly probe the relative stability of the Re-Cl and Re-Br bonds within these model dirhenium complexes.

## 7.2 Experimental Methods

Resonance excitation collision-induced dissociation (CID) within a quadrupole ion trap was used to probe the stability of the dirhenium complexes. This approach provides a cheap and straightforward means to investigate the intrinsic gas-phase stability of a molecular ion and its lowest potential energy surfaces.<sup>15,18</sup> Experiments were performed as described in Chapter 2, using a Bruker Daltonics Esquire 6000 Electrospray Ionization (ESI) quadrupole ion-trap mass-spectrometer run in negative-ion mode to record mass spectra and generate collision-induced dissociation curves. Data were acquired under normal electrospray conditions, and also using a cryospray source (with nebulizer gas set at  $-60^\circ\text{C}$ , and desolvation capillary at  $30-40^\circ\text{C}$ ). Dianion signals were optimized using the automatic tuning capabilities of the Esquire, with the capillary temperature at  $40^\circ\text{C}$ . The tetrabutylamine salt complex of  $\text{Re}_2\text{Cl}_8^{2-}$  (*i.e.*  $(\text{Bu}_4\text{N})_2\text{Re}_2\text{Cl}_8$ ) was purchased from Aldrich and used without further purification, while  $\text{Re}_2\text{Br}_8^{2-}$  was synthesised following a published method.<sup>19</sup> The  $\text{Re}_2\text{Cl}_n\text{Br}_{8-n}^{2-}$  ( $n=1-3$ ) species were produced as side products of the synthesis, and were straightforwardly isolated from the reaction mixture using ESI-mass spectrometry.

## 7.3 Results and Discussion

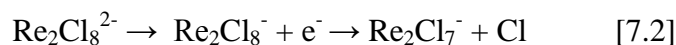
7.3.1 Resonance excitation of the  $\text{Re}_2\text{X}_8^{2-}$  ( $\text{X} = \text{Cl}$ ,  $\text{Br}$ ) and  $\text{Re}_2\text{X}_n\text{Y}_{8-n}^{2-}$  ( $\text{X} = \text{Cl}$ ,  $\text{Y}=\text{Br}$ ,  $n=1-3$ ) complexes

**Fig. 7.1 (a) Isolation of  $\text{Re}_2\text{Cl}_8^{2-}$  in the quadrupole trap at 0% CID voltage. (b) CID mass spectrum of  $\text{Re}_2\text{Cl}_8^{2-}$  at 6.8% collision energy illustrating fragmentation of  $\text{Re}_2\text{Cl}_8^{2-}$  into  $\text{Re}_2\text{Cl}_7^-$ .**

Fig. 7.1(a) displays the mass spectrum obtained upon isolation of  $\text{Re}_2\text{Cl}_8^{2-}$  in the quadrupole ion trap. Even at 0% CID voltage, the  $\text{Re}_2\text{Cl}_8^{2-}$  dianion is observed to fragment with production of the  $\text{Re}_2\text{Cl}_7^-$  fragment. Similar effects have been observed in previous CID studies of multiply charged cluster ions.<sup>15</sup>  $\text{Re}_2\text{Cl}_8^{2-}$  decays with production of the same  $\text{Re}_2\text{Cl}_7^-$  fragment (Fig. 7.1b) upon resonance excitation (low-energy CID) which is consistent with decay of the dianion *via* ionic fragmentation, *i.e.*



It is not possible to observe the  $\text{Cl}^-$  product ion since it falls outside the spectral window of the ion trap.<sup>15</sup> The possibility that  $\text{Re}_2\text{Cl}_7^-$  could be formed via a two step process, *i.e.*



may be discounted due to the lack of the  $\text{Re}_2\text{Cl}_8^-$  intermediate which would almost certainly be observed since the loss of a neutral Cl is likely to be endothermic.<sup>20</sup> Similar results were obtained for  $\text{Re}_2\text{Br}_8^{2-}$  (Fig. 7.2), with the dianion fragmenting into  $\text{Re}_2\text{Br}_7^-$  following resonance excitation. This again indicates decay *via* ionic fragmentation. The  $\text{Re}_2\text{Br}_7^-$  fragment peak that is evident in the isolation mass spectrum (Fig. 7.2a) is bigger than the  $\text{Re}_2\text{Cl}_7^-$  peak observed in the corresponding  $\text{Re}_2\text{Cl}_8^{2-}$  isolation spectrum, suggesting that  $\text{Re}_2\text{Br}_8^{2-}$  is more prone to decay than  $\text{Re}_2\text{Cl}_8^{2-}$ .

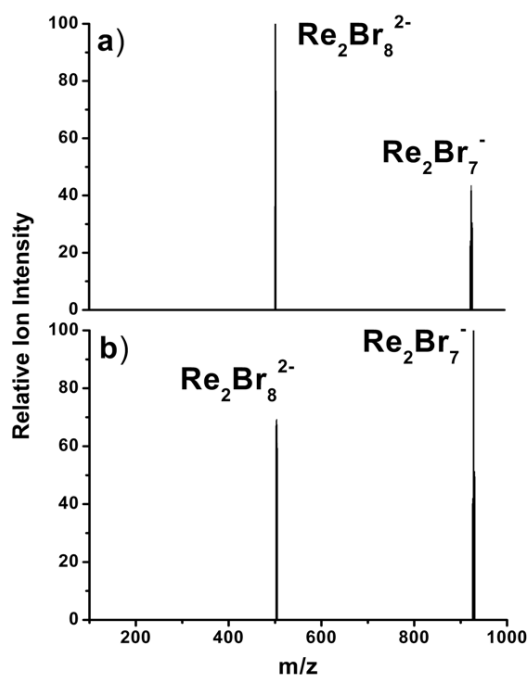


**Fig. 7.2** (a) Isolation of  $\text{Re}_2\text{Br}_8^{2-}$  in the quadrupole trap at 0% CID voltage. (b) CID mass spectrum of  $\text{Re}_2\text{Br}_8^{2-}$  at 3.2% collision energy illustrating fragmentation of  $\text{Re}_2\text{Br}_8^{2-}$  into  $\text{Re}_2\text{Br}_7^-$ .

Fig. 7.3a displays fragmentation curves (*i.e.* plots of the fragment ion intensity *versus* collision energy) for decay of the  $\text{Re}_2\text{Cl}_8^{2-}$  and  $\text{Re}_2\text{Br}_8^{2-}$  dianions, with production of the corresponding  $\text{Re}_2\text{X}_7^-$  monoanions. Such curves have been used to provide both qualitative and quantitative measures of gas-phase stability by subjecting an ion to increasing activation amplitude and monitoring the abundance of product ions as a function of collision energy.<sup>15,21</sup>

Comparison of the  $\text{Re}_2\text{Cl}_8^{2-}$  and  $\text{Re}_2\text{Br}_8^{2-}$  decay curves shows that the  $\text{Re}_2\text{Cl}_8^{2-}$  complex decays at much higher collision energies than  $\text{Re}_2\text{Br}_8^{2-}$ , consistent with a relatively stronger Re-Cl bond. Further evidence of this is provided by resonance excitation CID of the mixed halide dirhenium complexes  $\text{Re}_2\text{Cl}_n\text{Br}_{8-n}^{2-}$  ( $n=1-3$ ), where each complex is observed to decay exclusively with loss of a  $\text{Br}^-$  ligand to produce  $\text{Re}_2\text{Cl}_n\text{Br}_{7-n}^-$ , *e.g.*



No fragment ions consistent with loss of a  $\text{Cl}^-$  ion are observed. This indicates that the barrier height for fragmentation of a Re-Cl bond is higher than the barrier corresponding to Re-Br bond rupture in the mixed halide complexes, again consistent with a relatively stronger Re-Cl bond.

Fig. 7.3b displays the fragmentation curves for the mixed halide dirhenium complexes, along with the decay curve for  $\text{Re}_2\text{Br}_8^{2-}$ , *i.e.* for all of the complexes that decay with loss of a  $\text{Br}^-$  ligand. It is evident that all of these systems have decay curves that are clustered around 3% CID Energy, while the curve for decay of  $\text{Re}_2\text{Cl}_8^{2-}$  (the only complex to decay with loss of  $\text{Cl}^-$ ) lies at a considerably higher % CID Energy of ~7%. CID fragment ion intensities are influenced by the mass and degrees of freedom of the parent ion, and by kinetic shifts.<sup>21</sup>

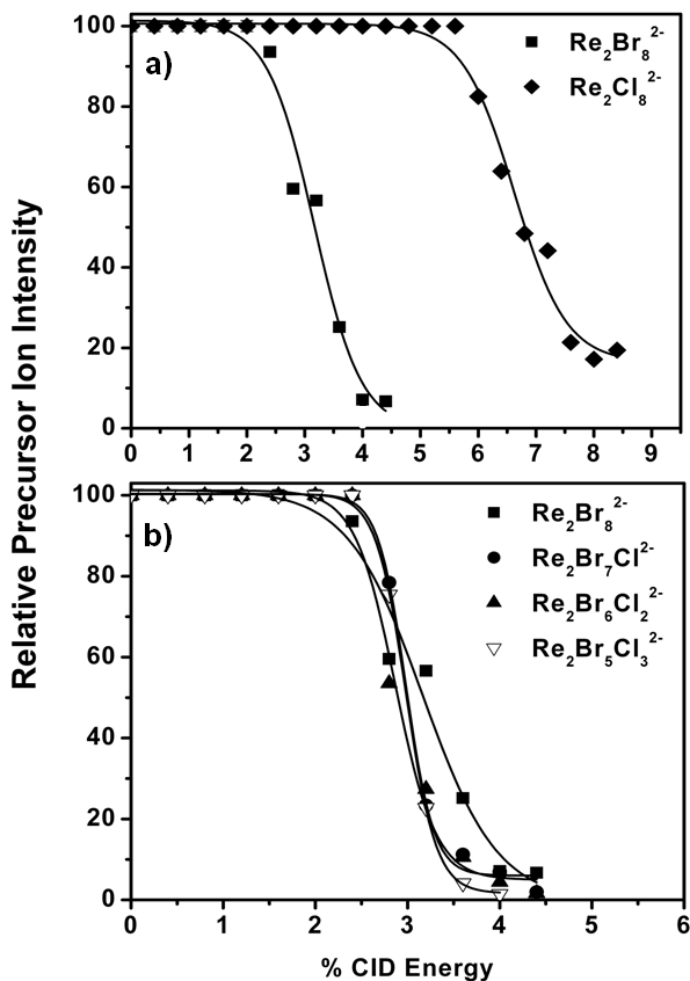


**Fig. 7.3** (a) Fragmentation curves for decay of the  $\text{Re}_2\text{Br}_8^{2-}$  and  $\text{Re}_2\text{Cl}_8^{2-}$  with production of  $\text{Re}_2\text{Br}_7^-$  and  $\text{Re}_2\text{Cl}_7^-$ , respectively. (b) Fragmentation curves for decay of the  $\text{Re}_2\text{Br}_8^{2-}$  and  $\text{Re}_2\text{Cl}_n\text{Br}_{8-n}^{2-}$  ( $n=1-3$ ), respectively (associated with loss of the  $\text{Br}^-$  fragment ion). Typical experimental errors (obtained from repeat runs) were  $\pm 3\%$ .

In general, however, the maximum collision energy converted to internal energy is proportional to the relative collision energy and inversely proportional to the parent ion mass. It is generally accepted that % CID curves can be directly compared if the  $m/z$  of the two species under consideration does not differ greatly.<sup>21,23</sup> Thus, the curves for  $\text{Re}_2\text{Cl}_n\text{Br}_{8-n}^{2-}$  ( $n=1-3$ ) and  $\text{Re}_2\text{Br}_8^{2-}$  presented in Fig. 7.3b can be directly compared, indicating that all of these ions fragment across potential energy surfaces with very similar activation barriers, in line with similar fragmentation energies.

It is notable that there is no evidence for decay *via* rupture of the dirhenium bond in any of the complexes studied, *i.e.*



In addition, since ionic fragmentation is the only decay pathway observed for all the systems investigated in this work, the RCB for ionic fragmentation ( $\text{RCB}_{\text{if}}$ ) must lie below the RCB for electron detachment ( $\text{RCB}_{\text{ed}}$ ) for all of the  $\text{Re}_2\text{X}_8^{2-}$  complexes.

### 7.3.2 Cryospray Ion Source

As part of this study, a cryospray source<sup>24</sup> was also used to produce the gas-phase dirhenium dianions to investigate whether this improved the ESI-MS signal strength ( $\text{Re}_2\text{X}_8^{2-}$  ion counts). For this system, cryospray had only a very marginal effect on the observed maximum ion counts, possibly because the  $\text{Re}_2\text{X}_8^{2-}$  is not susceptible to complexation with the bulky  $\text{Bu}_4\text{N}^+$  counterion. % CID fragmentation curves were also obtained using ions produced from the cryospray source, and compared to curves obtained using routine ESI. Fig. 7.4 displays a set of typical results obtained both with and without cryospray for the decay of  $\text{Re}_2\text{Br}_8^{2-}$  with production of  $\text{Re}_2\text{Br}_7^-$ .

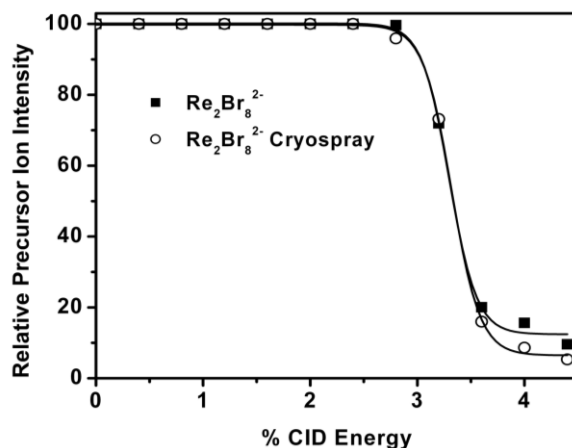


**Fig. 7.4** Fragmentation curves for decay of  $\text{Re}_2\text{Br}_8^{2-}$  with production of  $\text{Re}_2\text{Br}_7^-$ , produced both with and without cryospray.

These curves are identical within the experimental error, indicating that cryospray does not have a significant effect on the internal energy of the ions. This would be an interesting point to explore further in a system where cryospray has been observed to dramatically improve the ESI-MS signal of a particular molecular ion.<sup>24</sup>

### 7.3.3 Discussion of Ab initio calculations

*Ab initio* calculations carried out by Dr M.G.N. Nix are summarised here in order to enhance discussion of these results. These calculations were performed in order to investigate the potential energy surfaces for ionic fragmentation of  $Re_2X_8^{2-}$  ( $X=Cl, Br^-$ ). For both of the  $Re_2X_8^{2-}$  complexes, the calculated global energy minima corresponded to eclipsed  $D_{4h}$  structures in line with previous computational results and X-ray crystallography data.<sup>1,6,7</sup> The calculated structure of  $Re_2X_8^{2-}$  is illustrated on Fig. 7.5, with the calculated bond lengths for  $Re_2Cl_8^{2-}$  and  $Re_2Br_8^{2-}$  being listed in Table 7.1. The shorter Re-Cl bond distance is expected for the smaller halide, and is consistent with the stronger Re-Cl bond inferred from the data presented above.

**Table 7.1: Ab initio calculated parameters for the calculated global minimum energy structures and ionic fragmentation potential energy surfaces of the  $Re_2X_8^{2-}$  ( $X=Cl, Br^-$ ) dianions. See text for details of calculations.**

	Bond Lengths (Å)		RCB <sub>if(inner)</sub> (eV)	RCB <sub>if(outer)</sub> (eV)	$\Delta E_{if}^a$ (eV)	RCB <sub>ed(inner)</sub> <sup>b</sup> (eV)	RCB <sub>ed(outer)</sub> <sup>b</sup> (eV)
	Re-Re	Re-X					
$Re_2Cl_8^{2-}$	2.21	2.43	2.0	1.60	+0.37	3.5	~2.6
$Re_2Br_8^{2-}$	2.22	2.59	1.3	1.64	-0.39		-

a  $\Delta E$  For  $Re_2X_8^{2-} \rightarrow Re_2X_7^- + X^-$  ( $X=Cl, Br$ ).

b Experimental values from reference 17. RCB<sub>ed(inner)</sub> refers to the barrier measured from the dianion minimum energy structure. RCB<sub>ed(outer)</sub> refers to the barrier measured from the  $Re_2Cl_8^- + e^-$  asymptote.

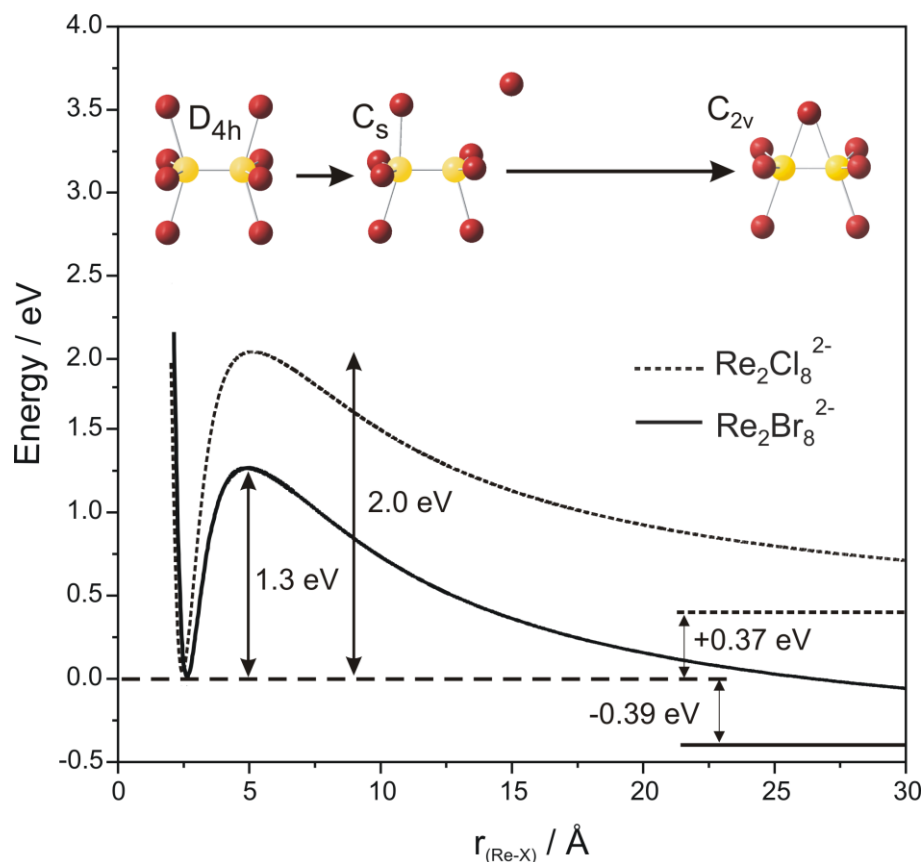


**Fig 7.5** Calculated potential energy curves (CASSCF(8,8)/LANL2DZ) for the ionic fragmentation of  $\text{Re}_2\text{X}_8^{2-} \rightarrow \text{Re}_2\text{X}_7^- + \text{X}^-$  ( $\text{X}=\text{Cl}$ ,  $\text{Br}$ ), obtained with geometries relaxed at each Re-X bond distance. The barrier heights for ionic fragmentation of each complex are illustrated on the figure, along with the calculated  $\text{D}_{4h}$  global minimum energy structure for  $\text{Re}_2\text{X}_8^{2-}$ , and the  $\text{C}_s$  symmetry transition state structure and  $\text{C}_{2v}$  symmetry  $\text{Re}_2\text{X}_7^-$  final product.

Fig. 7.5 displays the calculated potential energy curves for fragmentation of  $\text{Re}_2\text{X}_8^{2-}$  ( $\text{X}=\text{Cl}$ ,  $\text{Br}$ ) with loss of  $\text{X}^-$ , allowing for relaxation of the  $\text{Re}_2\text{X}_7^-$  moiety with increasing  $r_{\text{Re-X}}$ . The calculations clearly display a greater inner RCB height for ionic fragmentation of  $\text{Re}_2\text{Cl}_8^{2-}$  (2.0 eV) compared to  $\text{Re}_2\text{Br}_8^{2-}$  (1.3 eV), in line with the fragmentation results presented above. The higher fragmentation barrier of the Re-Cl bond in  $\text{Re}_2\text{Cl}_8^{2-}$  is consistent with the relatively shorter (and stronger) Re-Cl bond. Each complex rearranges through a  $\text{C}_s$  symmetry transition state at the RCB, to a novel  $\text{C}_{2v}$   $\text{Re}_2(\mu\text{-Cl})\text{Cl}_6^-$  bridging chloride final structure. It is notable that while the ionic fragmentation of  $\text{Re}_2\text{Cl}_8^{2-}$  is calculated to be endothermic, the value for  $\text{Re}_2\text{Br}_8^{2-}$  is exothermic indicating that gas-phase  $\text{Re}_2\text{Br}_8^{2-}$  dianion is metastable. This

reflects a general trend for RCB surfaces where the RCB height scales with the dissociation asymptote.<sup>25</sup>

The calculations further support the experimental observations since the calculated  $\text{RCB}_{\text{if}}(\text{inner})$  of 2.0 eV for  $\text{Re}_2\text{Cl}_8^{2-}$  is considerably lower than the value measured by Wang and Wang for the  $\text{RCB}_{\text{ed}}(\text{inner})$  of 3.5 eV,<sup>17</sup> hence the propensity of the system to decay *via* ionic fragmentation rather than electron detachment upon resonance excitation. In addition, the  $\Delta E_{\text{if}}$  values for Re-X fragmentation are considerably smaller than the energy required to fragment the Re-Re bond in such complexes ( $\sim 4.3$  eV),<sup>26</sup> thus explaining the absence of the  $\text{Re}_2\text{X}_8^{2-} \rightarrow 2\text{ReX}_4^-$  channel in the fragmentation mass spectra.

#### 7.4 Further Discussion

Wang and Wang isolated  $\text{Re}_2\text{Cl}_8^{2-}$  in the quadrupole ion-trap of their instrument, and found that the dianion decayed with a half-life of  $\sim 150$  s.<sup>17</sup> They deduced that this indicates that  $\text{Re}_2\text{Cl}_8^{2-}$  is unstable, *i.e.* subject to unimolecular decay *via* spontaneous ionic fragmentation. Even if the dianion is thermodynamically unstable with respect to ionic fragmentation, which our calculations suggest it is not, it will not be able to undergo spontaneous decay *via* ionic fragmentation since this would require a  $\text{Cl}^-$  to tunnel through the Repulsive Coulomb Barrier, an extremely inefficient process for a heavy chloride ion<sup>25,27</sup>. For example, a tunnelling lifetime of  $\sim 10^{10}$  years has been estimated for the  $\text{IrCl}_6^{3-}$  trianion which is thermodynamically unstable with  $\Delta E_{\text{if}} = -4.5$  eV.<sup>27</sup> It is notable that this situation differs dramatically from the case of electron loss where electron tunnelling is an extremely efficient process.<sup>28-30</sup> It is likely that the decay time measured by Wang and Wang represents a half-life for *activated* decay of  $\text{Re}_2\text{Cl}_8^{2-}$  within the quadrupole ion-trap as a result of collisions with the He trapping gas or residual solvent molecules.

### 7.5 Summary

A series of dirhenium dianion complexes have been studied in the gas phase using resonance excitation within a quadrupole ion trap to explore their intrinsic stability. The studies illustrate that the Re-Re bond is stable in the gas-phase, and that the lowest-energy gas-phase decay path of these dianions corresponds to ionic fragmentation with loss of a halide ion. The *ab initio* calculations performed for  $\text{Re}_2\text{Cl}_8^{2-}$  and  $\text{Re}_2\text{Br}_8^{2-}$  indicate that  $\text{Re}_2\text{Cl}_8^{2-}$  is intrinsically stable in the gas-phase, while for  $\text{Re}_2\text{Br}_8^{2-}$ , loss of  $\text{Br}^-$  is an exothermic process. However, gas-phase  $\text{Re}_2\text{Br}_8^{2-}$  is rendered metastable due to the presence of the repulsive coulomb barrier on the fragmentation potential energy surface.

While the structure of  $\text{Re}_2\text{Cl}_8^{2-}$  and the associated complexes are well-characterised in the condensed-phase, the measurements presented here illustrate that collision induced dissociation within a quadrupole ion-trap provides useful information on the structures of gas-phase inorganic ions, by providing a measure of the relative bond strengths within a complex. (Only the lowest energy fragmentation pathway or pathways are observed in this technique.<sup>18</sup>) Further examples are provided in the previous chapter by similar measurements on  $\text{Cr}_2\text{O}_7^{2-}$ , where the lowest energy pathway corresponds to electron detachment consistent with the ion's relatively strong covalent bonding,<sup>14</sup> and  $[\text{Fe}_4\text{S}_4\text{X}_4]^{2-}$  clusters which fragment into ions that are known structural sub-units of the parent clusters.<sup>31</sup> Finally, the intrinsic gas-phase stability displayed by the dirhenium complexes studied here indicates that they could usefully be investigated using more quantitative CID measurements to obtain accurate metal-ligand binding energies.<sup>10</sup>

References

47. F.A. Cotton, R.A. Walton, *Multiple Bonds Between Metal Atoms*; Clarendon Press: Oxford 1993
48. F.A. Cotton, C.B. Harris, *Inorg. Chem.* 6 (1967) 924
49. P.J. Hay, *J. Am. Chem. Soc.* 104 (1982) 7007
50. F.A. Cotton, C.B. Harris, *Inorg. Chem.* 4 (1965) 330
51. W.C. Trogler, H.B. Gray, *Acc. Chem. Res.* 11 (1978) 232
52. G. Cavigliasso, N. Kaltsoyannis, *Dalton Trans.* (2006) 5476, and references therein.
53. K. Saito, Y. Nakao, H. Sato, S. Sakaki, *J. Phys. Chem. A* 110 (2006) 9710
54. J. C. Traeger, *Int. J. Mass Spectrom.* 200 (2000) 387
55. T. Waters, X.B. Wang, L.S. Wang, *Coord. Chem. Rev.* 251 (2007) 474
56. P.B. Armentrout, *Ann. Rev. Phys. Chem.* 52 (2001) 423
57. R.A.J. O'Hair, *Chem. Comm.* (2006) 1469.
58. D. Schröder, H. Schwarz, *Ang. Chemie Int. Ed.* 34 (1995) 1973
59. R.J. Plowright, T.G. Wright, J.M.C. Plane, *J. Phys. Chem. A* 112 (2008) 6550
60. T.A. Salter, V.A. Mikhailov, C.J. Evans, A.M. Ellis, *J. Chem. Phys.* 125 (2006) 034302
61. W.E. Boxford, J.K. Pearce, C.E.H. Dessent, *Chem. Phys. Lett.* 399 (2004) 465
62. C.J. Taylor, B. Wu, C.E.H. Dessent, *Int. J. Mass Spectrom.* 276 (2008) 31
63. X.B. Wang, L.S. Wang, *J. Am. Chem. Soc.* 122 (2000) 2096
64. W.E. Boxford, C.E.H. Dessent, *Phys. Chem. Chem. Phys.* 8 (2006) 5151
65. F.A. Cotton, N.F. Curtis, W.R. Robinson, *Inorg. Chem.* 4 (1965) 1696
66. W.E. Boxford, J.K. Pearce, C.E.H. Dessent, *Chem. Phys. Lett.* 399 (2004) 465
67. M. Satterfield, J.S. Brodbelt, *Inorg. Chem.* 40 (2001) 5393
68. K.J. Hart, S.A. McLuckey, *J. Am. Soc. Mass Spectrom.* 5 (1994) 250
69. M.P. Ince, B.A. Perera, M.J. Van Stipdork, *Int. J. Mass Spectrom.* 207 (2001) 41
70. S. Sakamoto, M. Fujita, K. Kim, K. Yamaguchi, *Tetrahedron* 56 (2000) 955
71. W.E. Boxford, C.E.H. Dessent, *J. Phys. Chem. A* 109 (2005) 5836
72. L.R. Morss, R.J. Porcja, J.W. Nicoletti, J. San Filippo, H.D.B. Jenkins, *J. Am. Chem. Soc.* 102 (1980) 1923
73. W.E. Boxford, PhD thesis, University of York, (2007)
74. M. K. Scheller, R. N. Compton, L. S. Cederbaum, *Science* 270 (1995) 1160
75. X.B. Wang, C. F. Ding, L. S. Wang, *Chem. Phys. Lett.* 307 (1999) 391
76. M.N. Blom, O. Hampe, S. Glib, P. Weis, M.M. Kappes, *J. Chem. Phys.* 115 (2001) 3690

77. X. Yang, X.B. Wang, and L.S. Wang, *Int. J. Mass Spectrom.* 228 (2003) 797

## Chapter 8: Summary and Future Work

### 8.1 Summary and further experiments

Chapter 3 investigated how the precursor ion charge state and counter ion complexation effected the fragment ions produced from three Heparin disaccharides through low energy collisions. This study highlighted potential ‘marker’ fragments for each sugar that could be used in order to demonstrate which isomer was present, or to determine whether a particular sample contained a mixture. One notable result of this work was that while the minor fragmentation channels, such as loss water as a neutral molecule, could be affected by the presence of cation counter-ions, the primary low energy fragmentation routes remained relatively unchanged. Knowledge of the detailed fragmentation routes of these Heparin-counter ion complexes will prove useful in cases where significant cation contamination occurs from biological sources. The utility of Energy Resolved Mass Spectrometry in the analysis of these sugars has been discussed for these three isomeric examples. The results presented in Chapter 3 suggest that the dianionic  $[M-2H]^{2-}$  forms of these sulphated sugars are well suited to analysis that relies on this technique. The trianions  $[M-3H]^{3-}$  and the counter ion  $[M-2H.X^+]^-$  complexes are more challenging analytical targets since they are difficult to isolate at high signal intensity within an ion-trap. The natural extension of this work is the creation of a library of fragments for the most commonly encountered disaccharide Heparin fragments. It is doubtful whether a library based on a limited number of smaller molecules could be used to interpret the mass spectra of larger long chain examples simply because of the complexity of the Glycosaminoglycan family. Analysis based on ERMS is likely to be most useful in the testing of a synthesised or isolated product for purity, where the fragmentation characteristics of the product are previously known.

Chapter 4 reported the use of high energy (50-150 KeV) MIKE experiments to analyse mono and disaccharide examples of Heparin sulphated sugars. The high energy collisions produced abundant glycosidic and cross ring fragmentations that

are essential for the analysis of GAGs. An important result of this work was that numerous diagnostically useful fragments were produced independent of the charge state of the precursor sugar ion. At the present time, EDD based techniques are limited by the fact that as the number of charged sulphate groups increases, the more likely they are to be lost.<sup>1</sup> Raising the overall charge state of the precursor molecule allows for more carboxylate based electron detachment events, although this causes the overall numbers of glycosidic and cross ring fragments to fall.<sup>2</sup> An extension to the work carried out in Chapter 4 would involve repeating the experiments with much larger and densely negatively charged examples of Heparin. This would determine the usefulness of the method in ‘whole chain’ analysis, i.e. whether high energy collisions are capable of generating a complete set of cross ring and glycosidic fragments that would allow the positions of side groups along the entire molecule to be unambiguously assigned.

Chapter 5 presented the results of a combined molecular mechanics and quantum chemistry study into the three dimensional space available to a prototypical 2-O-sulfo- $\alpha$ -L-iduronate monosaccharide. This study compared the relative energies calculated using B3LYP, PW91PW91, MO5-2X and MP2 using the 6-31++G\*\* basis set for a series of optimized geometries of this molecule. The results show that MO5-2X method compares very favourably to the MP2 results, and that it provides improved relative energies over B3LYP. Additionally, the results presented demonstrate the need to study the three dimensional space available to sub conformers when assessing the relative energies of ring conformations. Due to the large size and flexibility of GAG structures, rigorous ab-initio studies are challenging. Future work involving the longer chain examples from this family will require the development of force fields specific to these sulphated sugars.

Chapter 6 displays the results of a low energy collision induced dissociation (CID) experiment on the dichromate  $\text{Cr}_2\text{O}_7^{2-}$  dianion.  $\text{Cr}_2\text{O}_7^{2-}$  was seen to fragment by two competing routes, either the loss of an electron, or by ionic fragmentation across the central Cr-O bond of the molecule. This result was unusual for a small molecular

dianion and the potential energy surfaces for electron loss and ionic fragmentation were modelled using density functional theory. The calculated inner barrier heights for the repulsive coulomb barrier were 3.5 eV and 3.6 eV for electron loss and ionic fragmentation respectively. This result is atypical for Multiply Charged Anions (MCAs) since the predominant lowest energy pathway in similar studies has been that of ionic fragmentation.<sup>3</sup> Zhai et al have made a detailed Photoelectron Spectroscopic (PES) study of  $M_2O_7^{2-}$  and  $MM'O_7^{2-}$  where M and M' may be Cr, Mo or W.<sup>4</sup> In this study the mixed  $MM'O_7^{2-}$  species were generated by electrospraying mixtures the salts  $(Bu_4N)_2[MO_4]$ . An extension of the CID technique used here to study these species is the next logical step for this work since Vertical Detachment Energies (VDEs) measured by PES are available for comparison with any theoretical results used to interpret mass spectrometric results.

Chapter 7 reported the CID technique being used to study the gas phase stability of the  $Re_2X_8^{2-}$  (X = Cl, Br) and  $Re_2X_nY_{8-n}^{2-}$  (X = Cl, Y=Br,  $n=1-3$ ) metal-metal bond complexes. Electron detachment was not observed during this study, with the lowest energy fragmentation pathway always represented by the loss of a singly negatively charged bromine or chlorine ion from the precursor dianion. The calculations performed to support this work suggest that  $Re_2Cl_8^{2-}$  is stable with respect to ionic fragmentation, i.e. that the loss of the  $Cl^-$  is an endothermic process. Wang and Wang have isolated this dianion in a quadrupole ion-trap and determined a half life of approximately 150 seconds and therefore it was susceptible to unimolecular decay via spontaneous ionic fragmentation<sup>5</sup>. In order to determine whether this loss of  $Cl^-$  is due to activated decay, i.e. through collisions with background helium or solvent molecules within the trap, a further experiment is necessary. The most effective way to rule out collision induced activated decay would be to isolate the  $Re_2Cl_8^{2-}$  dianion in a much higher vacuum. The Penning trap within a modern FT-ICR machine is kept at approximately  $10^{-10}$  Torr and so would be highly suitable for this work. The intrinsic gas-phase stability displayed by the dirhenium complexes studied indicated that they could be investigated using more quantitative CID measurements to obtain accurate metal-ligand binding energies.

## 8.2 References

30. F.E. Leach III, J.J. Wolff, T.N. Laremore, R.J. Linhardt, I.J. Amster, *Int. J. Mass Spec.* 276 (2008) 110
31. J.J. Wolff, T.N. Laremore, A.M. Busch, R.J. Linhardt, I.J. Amster, *J. Am. Soc. Mass Spec.* 19 (2008) 790
32. W. E. Boxford, J. K. Pearce, C. E. H. Dessent, *Chem. Phys. Lett.* 399 (2004) 465
33. H.-J. Zhai, X. Huang, T. Waters, X.-B. Wang, R. A. J. O'Hair, A.G. Wedd, L.-S. Wang, *J. Phys. Chem. A* 109 2005 10512
34. X.B. Wang, L.S. Wang, *J. Am. Chem. Soc.* 122 (2000) 2096

## Appendix 1: Glossary

**Basis Set** – Set of functions used to model atomic and molecular orbitals. A common form of notation is that used to describe Pople basis sets, an example being 6-31++G\*\*. In this case 6 primitive Gaussians comprise each core atomic orbital basis function, while the valence orbitals are represented by two basis functions each, one comprised of 3 primitive Gaussian functions and the other by one. The addition of ‘\*\*’ notation indicates the presence of extra polarisable functions on the heavy and light atoms, while the ‘++’ notation indicates diffuse functions are in use for both of these atom types. In general terms, polarisable functions allow orbitals to change shape to a greater extent, while diffuse functions model a greater three dimensional space.

**CID** – Collision Induced Dissociation, also known as Collision Activated Dissociation. The process of fragmenting positive or negatively charged ions through collisions with a neutral background gas, typically Helium.

**DFT** – Density Functional Theory. Quantum mechanical theory which allows for the properties of many electron systems to be known through the use of functionals to model electron density. Hybrid functionals used within this thesis include B3LYP, PW91PW91 and MO5-2X as referenced in Chapter 5.

**EDD** – Electron Detachment Dissociation. A technique which has proven useful in the fragmentation of negatively charged sugars. Low energy (10-20eV) beams of electrons are used to bombard gas phase anions. An electron, typically at an oxygen atom, is lost leading to the production of an unstable neutral radical which then causes the fragmentation of the molecule through a charge transfer process.

**ERMS** – Energy Resolved Mass Spectrometry. Mass spectral technique used to differentiate species that may produce very similar fragmentation patterns, i.e. chiral

isomers. This technique relies upon monitoring the intensity of product ions with increasing energy used to effect fragmentation.

**ESI** – Electrospray Ionization. Commonly used technique for the transfer of charged molecules from solution to the gas phase in mass spectrometry. The dissolved sample is sprayed through a needle which is biased at a high negative or positive voltage. The overall effect of the voltage bias is to cause the ions in solution to migrate to and break free of the solvent droplets as discussed in Chapter 2.

**MP2** – Second Order Møller–Plesset perturbation theory. An *ab initio* post Hartree-Fock computational method which includes the effects of electron correlation in attempts to provide solutions to the Schrödinger equation.

**MMFF 94** – Merck Molecular Force Field 1994. A force field developed by Merck Research Laboratories, referenced in Chapter 5. This force field was intended to provide good performance for a wide range of chemical species.